

INFORMATION TO USERS

This material was produced from a microfilm copy of the original document. While the most advanced technological means to photograph and reproduce this document have been used, the quality is heavily dependent upon the quality of the original submitted.

The following explanation of techniques is provided to help you understand markings or patterns which may appear on this reproduction.

1. The sign or "target" for pages apparently lacking from the document photographed is "Missing Page(s)". If it was possible to obtain the missing page(s) or section, they are spliced into the film along with adjacent pages. This may have necessitated cutting thru an image and duplicating adjacent pages to insure you complete continuity.
2. When an image on the film is obliterated with a large round black mark, it is an indication that the photographer suspected that the copy may have moved during exposure and thus cause a blurred image. You will find a good image of the page in the adjacent frame.
3. When a map, drawing or chart, etc., was part of the material being photographed the photographer followed a definite method in "sectioning" the material. It is customary to begin photoing at the upper left hand corner of a large sheet and to continue photoing from left to right in equal sections with a small overlap. If necessary, sectioning is continued again — beginning below the first row and continuing on until complete.
4. The majority of users indicate that the textual content is of greatest value, however, a somewhat higher quality reproduction could be made from "photographs" if essential to the understanding of the dissertation. Silver prints of "photographs" may be ordered at additional charge by writing the Order Department, giving the catalog number, title, author and specific pages you wish reproduced.
5. PLEASE NOTE: Some pages may have indistinct print. Filmed as received.

Xerox University Microfilms

300 North Zeeb Road
Ann Arbor, Michigan 48106

7815375

NICHOLS, HENRY FLOYD
INFRARED REFLECTIVITY, RAMAN SCATTERING, AND
THE VIBRATIONAL DYNAMICS OF UNIAXIAL CRYSTALS
AND MIXED CRYSTALS.

THE UNIVERSITY OF OKLAHOMA, PH.D., 1977

University
Microfilms
International

300 N. ZEEB ROAD, ANN ARBOR, MI 48106

THE UNIVERSITY OF OKLAHOMA

GRADUATE COLLEGE

INFRARED REFLECTIVITY, RAMAN SCATTERING,
AND THE VIBRATIONAL DYNAMICS OF
UNIAXIAL CRYSTALS AND MIXED CRYSTALS

A DISSERTATION

SUBMITTED TO THE GRADUATE FACULTY

in partial fulfillment of the requirements for the

degree of

DOCTOR OF PHILOSOPHY

BY

HENRY FLOYD NICHOLS

Norman, Oklahoma

1977

INFRARED REFLECTIVITY, RAMAN SCATTERING,
AND THE VIBRATIONAL DYNAMICS OF
UNIAXIAL CRYSTALS AND MIXED CRYSTALS

APPROVED BY

Roger French
Stanley C. Kelly
William J. Fogel
Sherril A. Curran
S. E. Bath Jr.

DISSERTATION COMMITTEE

Dedication

To Herbert and Falbie Westbrook

ACKNOWLEDGEMENTS

The author wishes to express his gratitude to Dr. Roger Frech for his direction and guidance of my graduate research. Integrity in research, leadership, knowledge of spectroscopy, dedication to research, and a personal interest in his students are but a few of the qualities I've seen in him. I shall always remember the unique role he has played in shaping my personal and professional life. It is an honor to be his first graduate student.

Some of the Raman spectra necessary for this work were obtained with the help of Dr. J. Paul Devlin at Oklahoma State University. His time and the use of his equipment is greatly appreciated.

I am grateful to Dr. Dick van der Helm, Dr. Steve Ealick, Mr. Don Washecheck, and Mr. Bob Baker for their help and facilities necessary for the X-ray work in this study.

Some of the crystals used in this work were provided by Mr. Steve Filmore, Mr. Lyle Lehman, and Mr. Dan Carter. Mr. Kip Hilshafer provided clues to the surface damage studies. Their contributions are fully appreciated.

The author wishes to express his thanks to Dr. Guo-Jen Wu, Mr. Dale Teeters, Mr. Robert Turner, and Mrs. Echung Chiang Wang. Their help and friendship will always be remembered.

I am grateful to the Chemistry Department and Dean Gordon Atkinson for providing financial assistance during the course of my studies.

I am sincerely grateful to Mr. Jerry Gibson for sharing his ideas and computer expertise. My close friendship with him and his wife, Susan, will always be remembered.

I would also like to express my gratitude to my grandparents, Herbert and Falbie Westbrook, for being my parents for twenty-five years and for their continued encouragement and support of my education. Their contribution cannot be overstated.

TABLE OF CONTENTS

	Page
LIST OF TABLES.....	viii
LIST OF FIGURES.....	ix
 Chapter	
I. OBLIQUE PHONON REFLECTIVITY IN CALCITE	
INTRODUCTION.....	1
GENERAL SOLUTION FOR THE REFLECTION COEFFICIENT AND SPECIAL EXPERIMENTAL GEOMETRIES.....	2
THE EXTRAORDINARY WAVE AND OBLIQUE PHONONS.....	2
THE REFLECTIVITY OF CALCITE: EXPERIMENTS AND DISCUSSION.....	8
REFERENCES.....	19
 II. THE ANOMALOUS INFRARED REFLECTIVITY MINIMUM IN NaNO ₃	
INTRODUCTION.....	20
EXPERIMENTAL.....	22
REFERENCES.....	27
 III. COMBINATION MODE ASSIGNMENTS IN NaNO ₃ USING MICROCRYSTALLINE REFLECTIVITY AND SINGLE CRYSTAL RAMAN SPECTRA	
INTRODUCTION.....	28
THEORY.....	29
EXPERIMENTAL.....	29
RESULTS AND DISCUSSION.....	30
CONCLUSION.....	35
REFERENCES.....	49
 IV. ABNORMALITIES IN THE INFRARED REFLECTION SPECTRA OF SINGLE CRYSTALS INDUCED BY MECHANICAL SURFACE DAMAGE	
INTRODUCTION.....	50
EXPERIMENTAL.....	51
NaNO ₃	52
KBrO ₃	57
REFERENCES.....	69

Chapter	Page
V. VIBRATIONAL STUDY OF THE OPTIC MODES OF SODIUM CHLORATE-SODIUM BROMATE MIXED CRYSTALS	
INTRODUCTION.....	70
THEORY.....	73
EXPERIMENTAL.....	76
NaClO ₃	77
NaBrO ₃	78
MICROCRYSTALLINE MIXED CRYSTALS.....	81
MIXED SINGLE CRYSTALS.....	93
DISCUSSION.....	116
REFERENCES.....	122
VI. VIBRATIONAL STUDY OF THE OPTIC MODES OF RbClO ₃ -RbBrO ₃ MIXED CRYSTALS	
INTRODUCTION.....	123
EXPERIMENTAL.....	125
PURE CRYSTALS.....	125
INTERNAL OPTIC MODES OF MIXED CRYSTALS.....	131
EXTERNAL OPTIC MODES IN MICROCRYSTALS.....	155
DISCUSSION.....	159
REFERENCES.....	160
Appendix	
A. SAMPLING ACCESSORIES.....	161

LIST OF TABLES

Table		Page
(3-1)	Infrared Active Fundamental and Combination Mode Frequencies for NaNO_3	46
(3-2)	Raman Active Fundamental and Combination Mode Frequencies for NaNO_3	48
(4-1)	Raman Frequencies, Static Crystal Field Frequencies, and Dipole Moment Derivatives for KBrO_3	62
(5-1)	Optic Mode Frequencies of NaClO_3	79
(5-2)	Optic Mode Frequencies of NaBrO_3	82
(6-1)	Frequencies of the Internal Optic Modes of RbClO_3 and RbBrO_3	127

LIST OF FIGURES

Figure	Page
(1-1) Special experimental geometries in near normal incidence infrared reflectivity measurements.	3
(1-2) Uniaxial crystal showing the orientation of the principal plane and phonon polarization plane with respect to the incident electric field.	5
(1-3) Decomposition of electric field incident upon a uniaxial crystal into ordinary and extraordinary wave components. . .	6
(1-4) Near normal incidence infrared reflectivity spectra of a calcite face cut with the optic axis at an angle of 0°. . . .	12
(1-5) Near normal incidence infrared reflectivity spectra of a calcite face cut with the optic axis at an angle of 18°. . .	13
(1-6) Near normal incidence infrared reflectivity spectra of a calcite face cut with the optic axis at an angle of 45°. . .	14
(1-7) Near normal incidence infrared reflectivity spectra of a calcite face cut with the optic axis at an angle of 63°. . .	15
(1-8) Near normal incidence infrared reflectivity spectra of a calcite face cut with the optic axis at an angle of 90°. . .	16
(1-9) Near normal incidence infrared reflectivity spectra with the optic axis at different angles.	17
(1-10) Graph of the angular dispersion of the $\nu_3(E_u)$ oblique phonon in calcite	18

Figure	Page
(2-1) Near normal incidence infrared reflectivity spectra of the ν_3 spectral region in $\text{Na}^{14}\text{NO}_3$ and $\text{Na}^{15}\text{NO}_3$	24
(2-2) Raman scattering spectra of the $2\nu_4$ overtone region of $\text{Na}^{14}\text{NO}_3$ and $\text{Na}^{15}\text{NO}_3$	25
(3-1) Unpolarized near normal incidence infrared reflectivity spectrum of a single crystal natural rhombohedral face of $\text{Na}^{14}\text{NO}_3$ and of microcrystalline $\text{Na}^{14}\text{NO}_3$	31
(3-2) Calculated and observed microcrystalline reflectivity spectra of $\text{Na}^{14}\text{NO}_3$	33
(3-3) Calculated and observed microcrystalline reflectivity spectra of $\text{Na}^{15}\text{NO}_3$	34
(3-4a) Microcrystalline reflectivity and single crystal transmission spectra of $\text{Na}^{14}\text{NO}_3$ in the $700\text{-}1200\text{cm}^{-1}$ region	36
(3-4b) Microcrystalline reflectivity and single crystal transmission spectra of $\text{Na}^{14}\text{NO}_3$ in the $1200\text{-}2000\text{cm}^{-1}$ region . .	37
(3-4c) Microcrystalline reflectivity and single crystal transmission spectra of $\text{Na}^{14}\text{NO}_3$ in the $2000\text{-}3000\text{cm}^{-1}$ region ...	38
(3-4d) Microcrystalline reflectivity and single crystal transmission spectra of $\text{Na}^{14}\text{NO}_3$ in the $3000\text{-}4000\text{cm}^{-1}$ region ...	39
(3-5a) Microcrystalline reflectivity spectrum of $\text{Na}^{15}\text{NO}_3$ in the $700\text{-}1500\text{cm}^{-1}$ region	40
(3-5b) Microcrystalline reflectivity spectrum of $\text{Na}^{15}\text{NO}_3$ in the $1500\text{-}2600\text{cm}^{-1}$ region	41

Figure	Page
(3-5c) Microcrystalline reflectivity spectrum of Na ¹⁵ NO ₃ in the 2600-4000cm ⁻¹ region	42
(3-6a) Raman spectra of Na ¹⁴ NO ₃ and Na ¹⁵ NO ₃ in the 1430-1550 cm ⁻¹ region	43
(3-6b) Raman spectra of Na ¹⁴ NO ₃ and Na ¹⁵ NO ₃ in the 2ν ₂ region . . .	44
(3-6c) Raman spectra of Na ¹⁴ NO ₃ and Na ¹⁵ NO ₃ in the 2050-2175cm ⁻¹ region	45
(4-1) Near normal incidence infrared reflectivity spectra of Na ¹⁵ NO ₃ with successive repolishing	53
(4-2) Near normal incidence infrared reflectivity spectra of Na ¹⁴ NO ₃ with successive repolishing.	54
(4-3) Near normal incidence infrared reflectivity spectrum of microcrystalline Na ¹⁴ NO ₃	55
(4-4) Near normal incidence infrared reflectivity spectra of Na ¹⁴ NO ₃ single crystals with successive repolishing	56
(4-5) Vibrational correlation diagram of KBrO ₃	58
(4-6) Infrared transmission spectra of KBrO ₃ in KBr pellets . . .	63
(4-7) Infrared transmission spectra of KBrO ₃ in KBr pellets . . .	64
(4-8) Near normal incidence polarized infrared reflectivity spectrum of KBrO ₃	65
(4-9) Polarized near normal incidence infrared reflectivity spectra of KBrO ₃ showing the effects of surface preparation	66
(4-10) Polarized near normal incidence infrared reflectivity spectra of KBrO ₃ showing the effects of surface preparation	67
(4-11) Polarized near normal incidence infrared reflectivity spectrum of KBrO ₃ before and after γ irradiation	68

Figure	Page
(5-1) Unit cell of NaClO_3 and NaBrO_3 as viewed along the C_3 axis of an anion	74
(5-2) Vibrational correlation diagram for NaClO_3 and NaBrO_3 . . .	75
(5-3) Crystallographic cartesian axes in relation to the pyramidal growth habit of NaBrO_3	80
(5-4) Coordinate system used in Raman experiments to separate the A and E symmetry phonons in NaBrO_3	80
(5-5) Raman spectra of the ν_1 - ν_3 spectral region of BrO_3^- and ClO_3^- in mixed NaClO_3 - NaBrO_3 microcrystals	84
(5-6) Raman spectra of the ν_1 - ν_3 spectral region of BrO_3^- and ClO_3^- in mixed NaClO_3 - NaBrO_3 microcrystals	85
(5-7) Graphs of Raman frequencies as a function of ClO_3^- concentration for the ν_1 - ν_3 spectral region of ClO_3^- in NaClO_3 - NaBrO_3 mixed microcrystals	86
(5-8) Graphs of Raman frequencies as a function of ClO_3^- concentration for the ν_1 - ν_3 spectral region of BrO_3^- in NaClO_3 - NaBrO_3 mixed microcrystals	87
(5-9) Raman spectra of the ν_2 - ν_4 spectral region of ClO_3^- in NaClO_3 - NaBrO_3 mixed microcrystals	89
(5-10) Raman spectra of the ν_2 - ν_4 spectral region of BrO_3^- in NaClO_3 - NaBrO_3 mixed microcrystals	90
(5-11) Graphs of Raman frequency as a function of ClO_3^- concentration for the ν_2 - ν_4 spectral region of NaClO_3 - NaBrO_3 mixed microcrystals	91

Figure	Page
(5-12) Graph of the fraction of Raman scattering intensity due to ClO_3^- as a function of the mole fraction of ClO_3^- for NaClO_3 - NaBrO_3 mixed microcrystals	92
(5-13) Infrared transmission spectra of nujol mulls of NaClO_3 - NaBrO_3 mixed microcrystals	94
(5-14) Graphs of absorption maxima in the ν_1 - ν_3 spectral region of BrO_3^- as a function of ClO_3^- concentration for NaClO_3 - NaBrO_3 mixed microcrystals suspended in nujol mulls	95
(5-15) Mixed NaClO_3 - NaBrO_3 single crystal Raman spectra in the x(zz)y scattering geometry for the ν_1 - ν_3 spectral region	97
(5-16) Mixed NaClO_3 - NaBrO_3 single crystal Raman spectra in the x(zx)y scattering geometry for the ν_1 - ν_3 spectral region	98
(5-17) Mixed NaClO_3 - NaBrO_3 single crystal Raman spectra in the x(zz)y scattering geometry for the ν_2 - ν_4 spectral region of ClO_3^-	99
(5-18) Mixed NaClO_3 - NaBrO_3 single crystal Raman spectra in the x(zx)y scattering geometry for the ν_2 - ν_4 spectral region of ClO_3^-	100
(5-19) Mixed NaClO_3 - NaBrO_3 single crystal Raman spectra in the x(zz)y scattering geometry for the ν_2 - ν_4 spectral region of BrO_3^-	101
(5-20) Mixed NaClO_3 - NaBrO_3 single crystal Raman spectra in the x(zx)y scattering geometry for the ν_2 - ν_4 spectral region of BrO_3^-	102

Figure	Page
(5-21) Graphs of Raman frequencies as a function of ClO_3^- concentration in the $\nu_1-\nu_3$ spectral region of ClO_3^- for mixed NaClO_3 - NaBrO_3 single crystals	103
(5-22) Graphs of Raman frequencies as a function of ClO_3^- concentration in the $\nu_1-\nu_3$ spectral region of BrO_3^- for mixed NaClO_3 - NaBrO_3 single crystals	104
(5-23) Graphs of Raman frequencies as a function of ClO_3^- concentration in the $\nu_2-\nu_4$ spectral region of mixed NaClO_3 - NaBrO_3 single crystals	105
(5-24) Mixed NaClO_3 - NaBrO_3 single crystal Raman spectra of the external optic modes in $x(\text{zz})y$ and $x(\text{zx})y$ scattering geometries	106
(5-25) Graphs of Raman frequencies as a function of ClO_3^- concentration in the external optic mode spectral region of mixed NaClO_3 - NaBrO_3 single crystals	107
(5-26) Near normal incidence infrared reflectivity spectra of mixed NaClO_3 - NaBrO_3 single crystals	110
(5-27) Near normal incidence infrared reflectivity spectra of mixed NaClO_3 - NaBrO_3 single crystals	111
(5-28) Graphs of infrared frequencies as a function of ClO_3^- concentration in the $\nu_1-\nu_3$ spectral region of ClO_3^- for mixed NaClO_3 - NaBrO_3 single crystals	112
(5-29) Graphs of infrared frequencies as a function of ClO_3^- concentration in the $\nu_1-\nu_3$ spectral region of BrO_3^- for mixed NaClO_3 - NaBrO_3 single crystals	113

Figure	Page
(5-30) Polarized Raman spectra in the ν_1 - ν_3 spectral region of BrO_3^- in NaClO_3 crystals grown in the presence of 1% and 0.1% BrO_3^-	114
(5-31) Infrared transmission spectra in the ν_1 - ν_3 spectral region of BrO_3^- in NaClO_3 crystals grown in the presence of 1% and 0.1% BrO_3^-	115
(5-32) Infrared transmission spectra in the ν_1 - ν_3 spectral region of ClO_3^- in a NaBrO_3 crystal grown in the presence of 0.1% ClO_3^-	117
(6-1) Vibrational correlation diagram for RbClO_3 and RbBrO_3 . . .	124
(6-2) Polarized near normal incidence infrared reflectivity spectrum of RbClO_3 single crystal	128
(6-3) Polarized near normal incidence infrared reflectivity spectrum of RbBrO_3 single crystal in the ν_1 - ν_3 spectral region	129
(6-4) Polarized near normal incidence infrared reflectivity spectrum of RbBrO_3 single crystal in the ν_2 - ν_4 spectral region	130
(6-5) Raman spectra of the ν_1 - ν_3 spectral region of ClO_3^- in RbClO_3 - RbBrO_3 mixed microcrystals	132
(6-6) Graphs of Raman frequencies in the ν_1 - ν_3 spectral regions of ClO_3^- and BrO_3^- as a function of ClO_3^- concentration for RbClO_3 - RbBrO_3 mixed microcrystals	133
(6-7) Raman spectra of the ν_1 - ν_3 spectral region of BrO_3^- in RbClO_3 - RbBrO_3 mixed microcrystals	134

Figure	Page
(6-8) Raman spectra of the ν_1 - ν_3 spectral region of BrO_3^- in RbClO_3 - RbBrO_3 mixed microcrystals	135
(6-9) Graph of the fraction of Raman scattering intensity due to ClO_3^- using the ν_1 - ν_3 spectral regions of ClO_3^- and BrO_3^- in RbClO_3 - RbBrO_3 mixed microcrystals	137
(6-10) Infrared reflectivity spectra of mixed RbClO_3 - RbBrO_3 single crystals	140
(6-11) Infrared reflectivity spectra of mixed RbClO_3 - RbBrO_3 single crystals	141
(6-12) Graphs of infrared frequencies as a function of ClO_3^- for the ν_1 - ν_3 spectral regions of ClO_3^- and BrO_3^- in mixed RbClO_3 - RbBrO_3 single crystals	142
(6-13) Polarized infrared reflectivity spectra for the ν_1 - ν_3 spectral region of BrO_3^- in mixed RbClO_3 - RbBrO_3 single crystals	143
(4-14) Polarized infrared reflectivity spectra for the ν_1 - ν_3 spectral region of BrO_3^- in mixed RbClO_3 - RbBrO_3 single crystals	144
(6-15) Infrared transmission spectra of the ν_1 - ν_3 spectral region of BrO_3^- for mixed RbClO_3 - RbBrO_3 microcrystals supported in nujol mulls	147
(6-16) Graph of infrared frequencies as a function of ClO_3^- concentration in the ν_1 - ν_3 spectral region of BrO_3^- for mixed RbClO_3 - RbBrO_3 microcrystals supported in nujol mulls .	148

Figure	Page
(6-17) Polarized Raman spectra of mixed $\text{RbClO}_3\text{-RbBrO}_3$ microcrystals containing 1% BrO_3^- in the $\nu_1\text{-}\nu_3$ spectral region of BrO_3^- and the infrared transmission spectrum of these microcrystals supported in nujol mulls	149
(6-18) Raman spectra of mixed $\text{RbClO}_3\text{-RbBrO}_3$ microcrystals in the $\nu_2\text{-}\nu_4$ spectral region of ClO_3^-	152
(6-19) Raman spectra of mixed $\text{RbClO}_3\text{-RbBrO}_3$ microcrystals in the $\nu_2\text{-}\nu_4$ spectral region of BrO_3^-	153
(6-20) Graphs of Raman frequencies of mixed $\text{RbClO}_3\text{-RbBrO}_3$ microcrystals as a function of ClO_3^- concentration in the $\nu_2\text{-}\nu_4$ spectral region	154
(6-21) Raman spectra of mixed $\text{RbClO}_3\text{-RbBrO}_3$ microcrystals in the external optic mode spectral region	156
(6-22) Graphs of Raman frequencies of mixed $\text{RbClO}_3\text{-RbBrO}_3$ microcrystals as a function of ClO_3^- concentration in the external optic mode spectral region	157
(A-1) Translation accessory for Raman experiments	162
(A-2) Backscattering accessory for Raman experiments	163

CHAPTER I

Oblique Phonon Reflectivity in Calcite

Introduction

The directional dependence of polar phonons in uniaxial crystals has been the subject of several experimental studies and theoretical treatments.^{1,2} Unger and Schaack³ described the mixed mechanical-electromagnetic resonances in these systems as consisting of either ordinary or extraordinary polaritons. In the electrostatic limit ($k \gg \omega/c$, $\vec{\nabla} \times \vec{E} = 0$) the ordinary polaritons become ordinary phonons whose frequencies are those of the transverse phonons and the extraordinary polaritons become extraordinary phonons in which all modes are coupled through the macroscopic electric field associated with the longitudinal component of the modes. The mixing of polar phonons propagating at general angles with respect to the optic axis (oblique phonons) was studied in KBrO_3 by Unger and Haussühl,⁴ in LiIO_3 by Porto and co-workers,⁵ and in RbClO_3 by Hwang and Solin.⁶ The frequency dependence of the directional dispersion was utilized by Belousov and co-workers to "tune" the extraordinary phonon into Fermi resonance with the biphonons resulting from a lower lying state in both calcite⁷ and sodium nitrate.⁸ The angular dispersion of the $\nu_3(E_u)$ phonon in calcite was observed by Ishigame *et al.*⁹ who studied the unpolarized reflectivity from faces cut at several angles to the optic axis and identified two independent components contributing to the reflectivity. However, they assumed these two components resulted from a removal of the degeneracy of the $\nu_3(E_u)$ mode rather than the separate contributions of the ordinary and extraordinary waves.

General Solution for the Reflection Coefficient
and Special Experimental Geometries

A solution for the Fresnel reflection coefficient in an absorbing uniaxial crystal whose optic axis is at some general orientation with respect to the plane of incidence has been given by Berek¹⁰ as well as Damany and Uzan¹¹ and has been rederived in a computationally convenient form.¹² An adequate description of the propagation of electromagnetic radiation in uniaxial systems is given in references 10 and 11 and the references contained therein.

The transverse magnetic (TM) reflectivity (R_{TM}) and the transverse electric (TE) reflectivity (R_{TE}) from the face of a uniaxial crystal whose optic axis is at some general orientation with respect to the plane of incidence each contain contributions from both the ordinary wave and the extraordinary wave. Referring to figure (1-1), when the plane of incidence as defined by the incident and reflected wave normals is perpendicular to the principal plane as defined by the optic axis and the transmitted wave normal, then the TM reflectivity consists entirely of the contribution from the ordinary wave (R_o) and the TE reflectivity consists entirely of the contribution from the extraordinary wave (R_e). Conversely, when the principal plane and the plane of incidence coincide, the TM reflectivity contains only the extraordinary wave contribution while the TE reflectivity contains only the ordinary wave component.

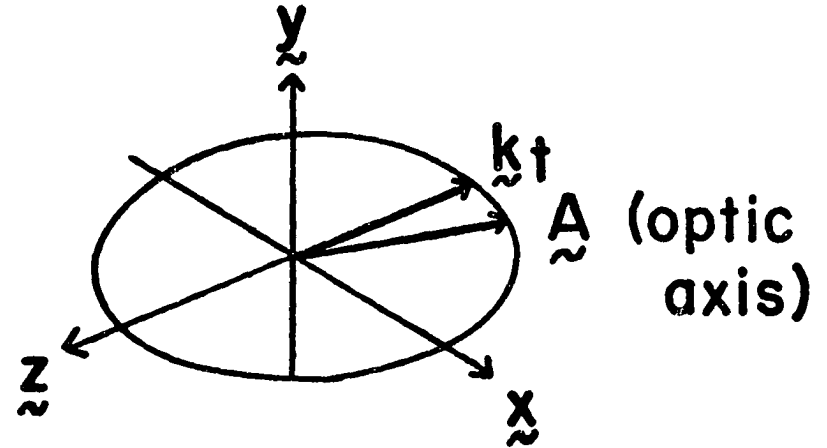
The Extraordinary Wave and Oblique Phonons

In the region of a polar double degenerate E type normal vibrational mode the extraordinary wave contains the dielectric response from an oblique phonon resonance whose frequency depends on the angle between the wave

Principal plane || plane of incidence

$$R_{TE} = R_o$$

$$R_{TM} = R_e$$



Principal plane \perp plane of incidence

$$R_{TE} = R_e$$

$$R_{TM} = R_o$$

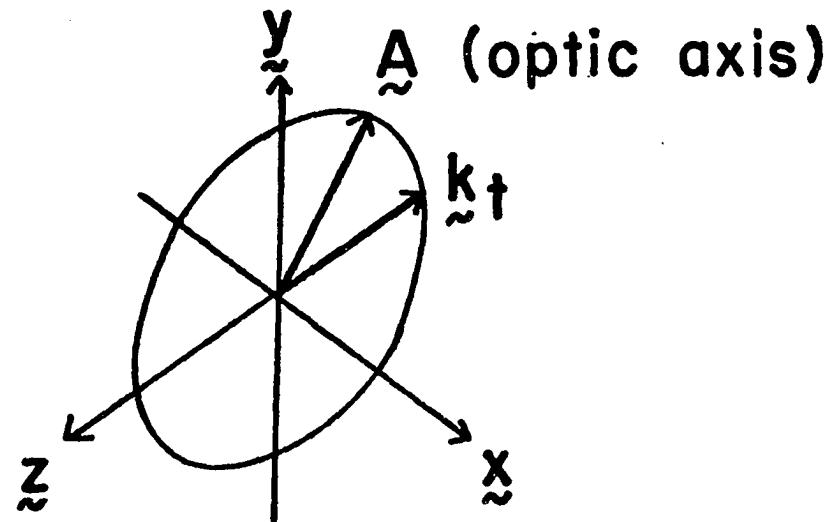


Figure (1-1). Special experimental geometries in near normal incidence infrared reflectivity measurements.

\tilde{k}_t is the transmitted wave vector.

vector and the polarization direction of the phonon. This may be seen more clearly in figures (1-2) and (1-3). In figure (1-2) an electromagnetic wave is incident on the xy face of a uniaxial crystal at normal incidence along the z axis. In this experiment the propagation wave vector of the light is assumed to make an infinitesimally small angle with the z axis to preserve the concept of the plane of incidence which is then the xz plane. The optic axis \underline{A} is in the yz plane and since the transmitted wave vector \underline{k}_t is along the z axis the principal plane is the yz plane. Also shown for convenience is the polarization plane of the doubly degenerate E type phonons which is orthogonal to the optic axis. The electric field of the incident wave \underline{E}_{inc} lies in the xy plane at an angle θ with respect to the y axis; the orientation of \underline{E}_{inc} in this plane can be chosen by a polarizer setting in a reflectivity measurement.

The interaction of the incident electric field with the phonons is shown in figure (1-3). The incident electric field can be decomposed into an ordinary wave component \underline{E}_o and an extraordinary wave component \underline{E}_e . The polarization of the doubly degenerate E type phonons can likewise be decomposed into an ordinary wave component \underline{P}_o and an extraordinary wave component \underline{P}_e . As is evident in figure (1-3) the ordinary wave polarization component is necessarily orthogonal to the direction of wave propagation \underline{k}_t resulting in pure transverse phonons. However, the extraordinary wave component \underline{P}_e is at some angle ψ with respect to \underline{k}_t , resulting in an oblique phonon. Of course, similar conclusions have been previously derived in these uniaxial systems on a macroscopic basis^{1,13} by an appropriate extension of Huang's description of the dispersion in a cubic crystal.^{14,15}

The angular dispersion of an oblique internal optic phonon in a

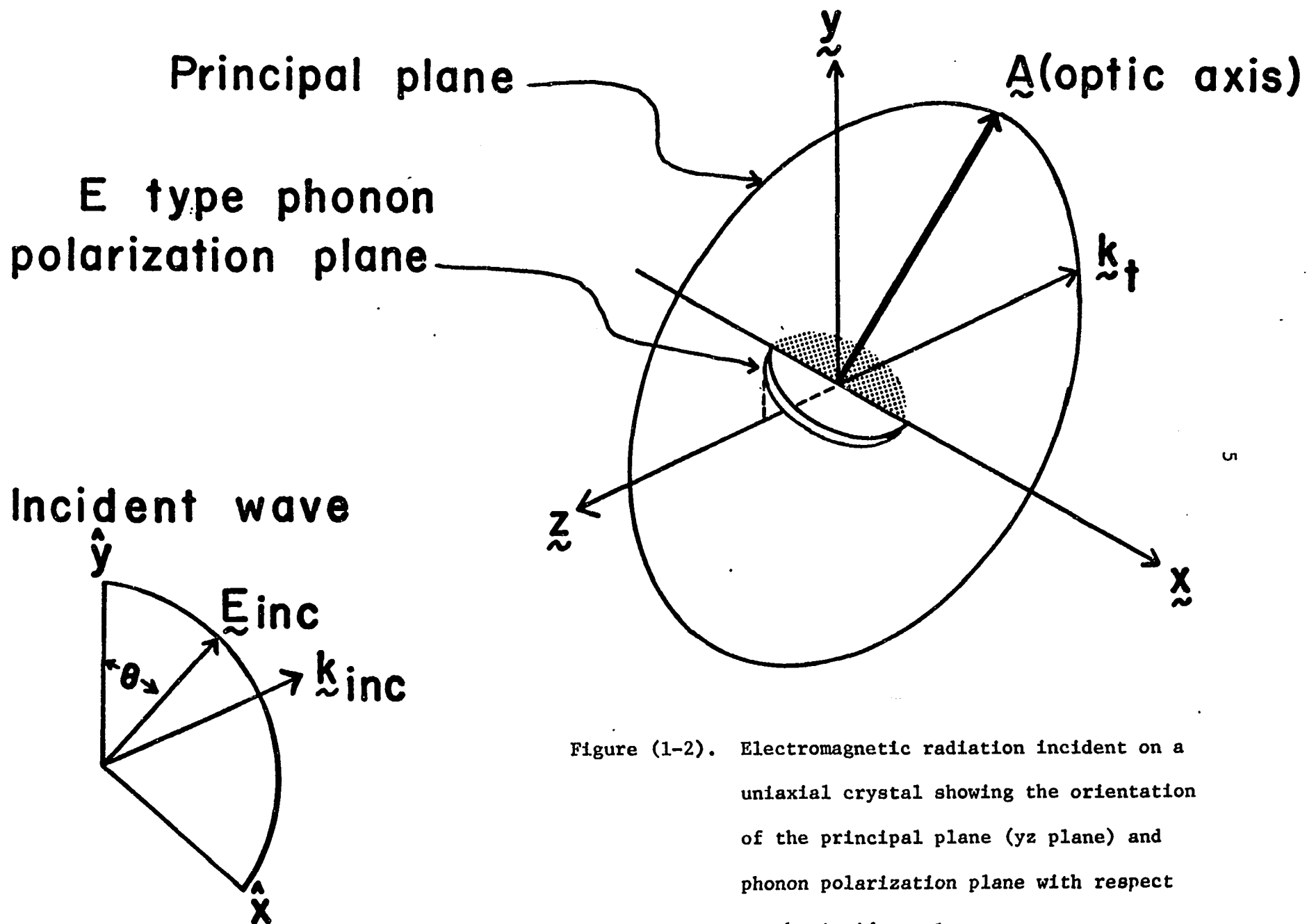


Figure (1-2). Electromagnetic radiation incident on a uniaxial crystal showing the orientation of the principal plane (yz plane) and phonon polarization plane with respect to the incident electric field.

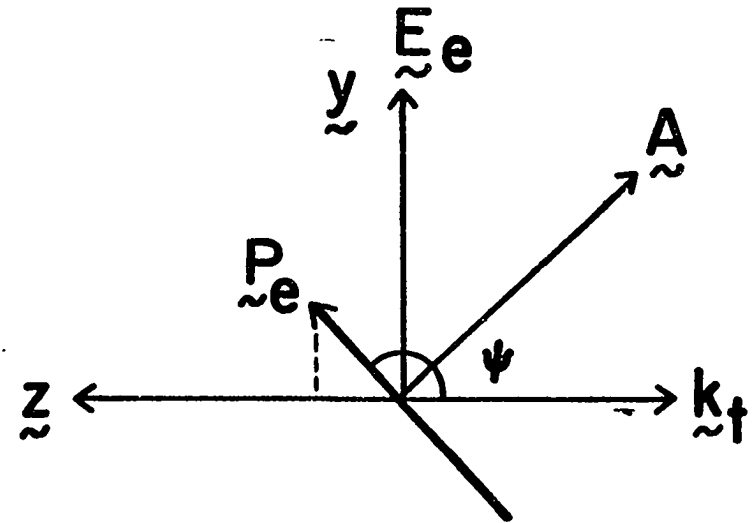
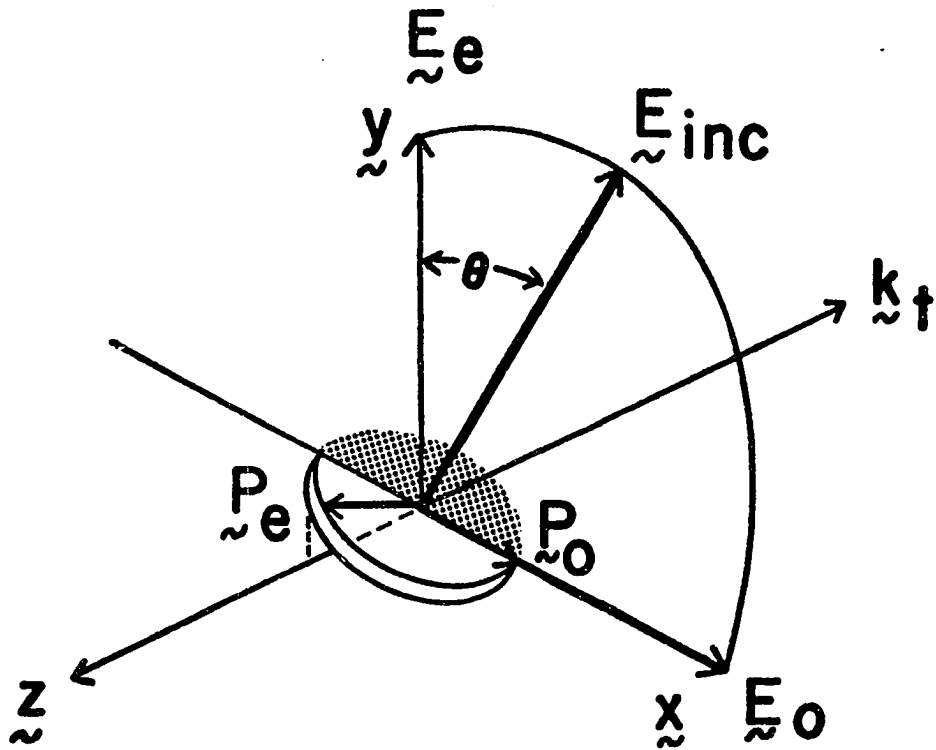


Figure (1-3). Decomposition of incident electric field and phonon polarization vectors into ordinary wave and extraordinary wave components. The angle ψ measures the angle between the oblique phonon polarization and propagation directions.

Ordinary wave: $\underline{k}_t \perp \underline{P}_o$
 \therefore pure transverse phonons

Extraordinary wave: $\underline{k}_t (\psi) \underline{P}_e$
 \therefore oblique phonons

Ordinary wave / Extraordinary wave
determined by θ (polarizer)

uniaxial crystal has been previously described in terms of a microscopic model.¹⁶ In that formalism the frequency of an oblique internal optic phonon polarized in the α Cartesian direction may be written as

$$\omega^2(\psi)(\vec{k})_{\gamma} = \omega_o^2 + \{S(\psi) [1 + \alpha_o S(\psi)]^{-1}\}_{\alpha\alpha}(\vec{k})_{\gamma} \{\partial\mu_{\alpha}/\partial q_j\}^2. \quad (1)$$

Here ψ is the angle between the direction of phonon polarization and the direction of phonon propagation, ω_o is the normal mode frequency in the absence of intermolecular dynamical coupling effects, $\partial\mu_{\alpha}/\partial q_j$ is the α Cartesian component of the vibrationally induced molecular dipole moment derivative with respect to the molecular normal coordinate q_j , γ is an irreducible representation label of the group of the wave vector \vec{k} , and S is a symmetrized linear combination of dipole sums. The quantity in square brackets includes the electronic polarization background and is a function of the components of the electronic polarizability tensor α_o . The calculation and significance of these quantities have been previously discussed.^{17,18}

When electromagnetic radiation is incident on the face of a uniaxial crystal such that the plane of incidence is perpendicular to the principal plane, then the reflectivity may be written

$$R = R_{TE} \cos^2 \theta + R_{TM} \sin^2 \theta = R_{ex} \cos^2 \theta + R_{ord} \sin^2 \theta \quad (2)$$

where θ is the angle between the incident electric field and the normal to the plane of incidence (here the y axis), R_{ord} is the reflectivity resulting from the extraordinary wave (oblique phonon resonance). R_{ord} is independent of the orientation of the crystal face from which reflection is occurring with respect to the optic axis. Furthermore, R_{ord} will be large between the longitudinal and transverse frequencies of the particular internal optic mode and will closely resemble the normal incidence reflection

spectrum observed from a crystal face containing the phonon polarization plane. On the other hand, R_{ex} depends on that orientation through the dependence of the oblique phonon resonant frequency on the angle between the phonon propagation direction and the polarization direction.

Specifically, R_{ex} will be large between the longitudinal optic mode frequency and the frequency of the oblique phonon resonance as given by equation (1). The relative contribution of these two reflectivity components to the observed reflectivity is determined by the angle θ which in a typical experiment depends on the setting of a polarizer.

The corresponding equation for the observed reflectivity from a crystal whose plane of incidence is parallel to the principal plane is

$$R = R_{\text{TE}} \cos^2 \theta + R_{\text{TM}} \sin^2 \theta = R_{\text{ord}} \cos^2 \theta + R_{\text{ex}} \sin^2 \theta. \quad (3)$$

The Reflectivity of Calcite:

Experiments and Discussion

Several crystals of optical quality calcite (CaCO_3) were obtained and faces were cut at various angles with respect to the optic axis. Reflectivity spectra were measured at room temperature on a Beckman IR-12 infrared spectrometer using a reflection accessory with a 4 to 1 linear image reduction at an average angle of incidence of 15 degrees.

Figure (1-4) is a set of near normal incidence reflection spectra from a crystal face which contains the optic axis perpendicular to the plane of incidence. At a polarizer setting of $\theta = 90^\circ$ the reflectivity (TE) consists entirely of the ordinary wave contribution which contains the pure transverse phonon resonance of $\nu_3(E_u)$. The reflectivity is large between 1410 cm^{-1} and 1550 cm^{-1} which correspond to the transverse and longitudinal mode frequencies, respectively. At $\theta = 0^\circ$ the reflectivity is entirely due to

the oblique phonon resonance. However, the angle ψ between the phonon propagation direction and polarization direction is 0° , or in other words the oblique phonon in this particular orientation becomes a pure longitudinal phonon and does not interact with the electric field of the incident light wave. Consequently, the reflectivity curve is more or less flat throughout the ν_3 spectral region. At intermediate polarizer settings ($90^\circ < \theta < 0^\circ$) the reflectivity is seen to consist of a mixture of ordinary wave and extraordinary wave contributions, leading to reflectivity curves which extend from 1410 cm^{-1} to 1550 cm^{-1} but with decreasing reflectivity as the ordinary wave contribution decreases (θ decreases).

In figure (1-5) the reflection spectra of a calcite face cut such that $\psi = 18^\circ$ are shown as a function of the angle θ as determined by the polarizer setting. At $\theta = 90^\circ$ the reflectivity is due to the pure transverse phonon resonance of the ordinary wave. As θ decreases the reflectivity component from the oblique phonon resonance in the extraordinary wave gradually becomes visible until $\theta = 0^\circ$ at which point the observed reflectivity is entirely due to the extraordinary wave. The resonant frequency of the oblique phonon is seen to occur at roughly 1530 cm^{-1} .

The reflectivity spectra of a crystal face cut such that $\psi = 45^\circ$ are shown in figure (1-6). Again the reflectivity at $\theta = 90^\circ$ is composed entirely of the pure transverse phonon resonance in the ordinary wave. The extraordinary wave component with an oblique phonon resonance estimated at 1480 cm^{-1} begins to contribute as θ decreases and finally dominates as θ approaches 0° .

A similar study of a crystal with a face cut to give a value of $\psi = 63^\circ$ is shown in figure (1-7) with results similar to those described in the

previous three figures. Now the oblique phonon resonance occurs at about 1430 cm^{-1} which is approaching the frequency of the pure transverse phonon. Consequently, the pure extraordinary wave reflectivity spectrum ($\theta = 0^\circ$) is somewhat similar in shape to the pure ordinary wave reflectivity spectrum ($\theta = 90^\circ$).

Finally, figure (1-8) is the reflectivity spectrum of a crystal whose reflection face is perpendicular to the optic axis and therefore $\psi = 90^\circ$. Here the oblique phonon is a pure transverse phonon, consequently the ordinary wave reflectivity and the extraordinary wave reflectivity are identical. The dependence of the extraordinary wave reflectivity on the orientation of the reflecting crystal face with respect to the crystallographic axes (through the orientation dependence of the frequency of the oblique phonon resonance) is summarized in figure (1-9). As the angle ψ between the phonon propagation direction and polarization direction decreases from 90° to 0° the oblique phonon successively goes from its pure transverse phonon limit to its pure longitudinal phonon limit and the reflectivity therefore decreases both in breadth and magnitude.

Infrared reflectivity data similar to that presented in figure (1-9) has been given for NaNO_3 by Ketelaar, Haas, and Fahrenfort.¹⁹ They interpreted their spectra in terms of a macroscopic model.^{14,15}

The angular dispersion of the $\nu_3(E_u)$ phonon as predicted by equation 1 is plotted in figure (1-10). The static crystal field frequency ($\omega_0 = 1430 \text{ cm}^{-1}$) and the magnitude of the molecular dipole moment derivative ($|\partial\mu_x/\partial q_3| = 281 \text{ cm}^{3/2} \text{ sec}^{-1}$) were calculated from the pure transverse and longitudinal frequencies of the ν_3 internal optic mode²⁰ and the electronic polarizability component $\alpha_{0,xx}$ was obtained from the optical refractive

index by a previously described method.²¹ The angular dispersion of the oblique phonon arises through the angular dispersion of the dipole sum $S(\psi)$ which are calculated using the standard techniques of Kornfeld and Ewald.^{22,23} Also shown are the frequencies of the oblique phonons as estimated from the inflection points of the experimental reflectivity curves. In view of the experimental uncertainty in estimating the values, the agreement must be regarded as semi-quantitative.

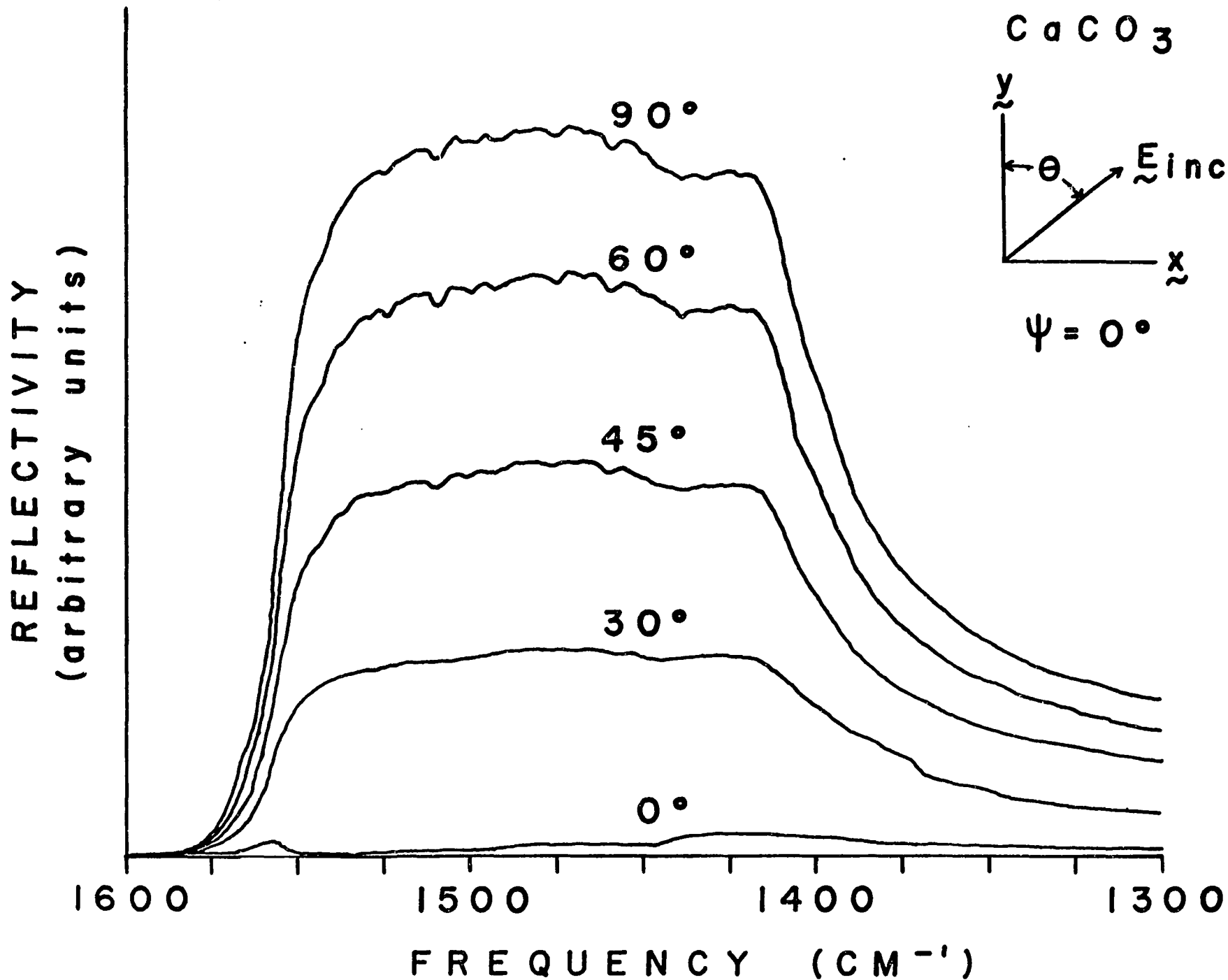


Figure (1-4). Near normal incidence reflectivity spectra of a calcite face cut with $\psi = 0^\circ$ shown as a function of θ as determined by the polarizer setting.

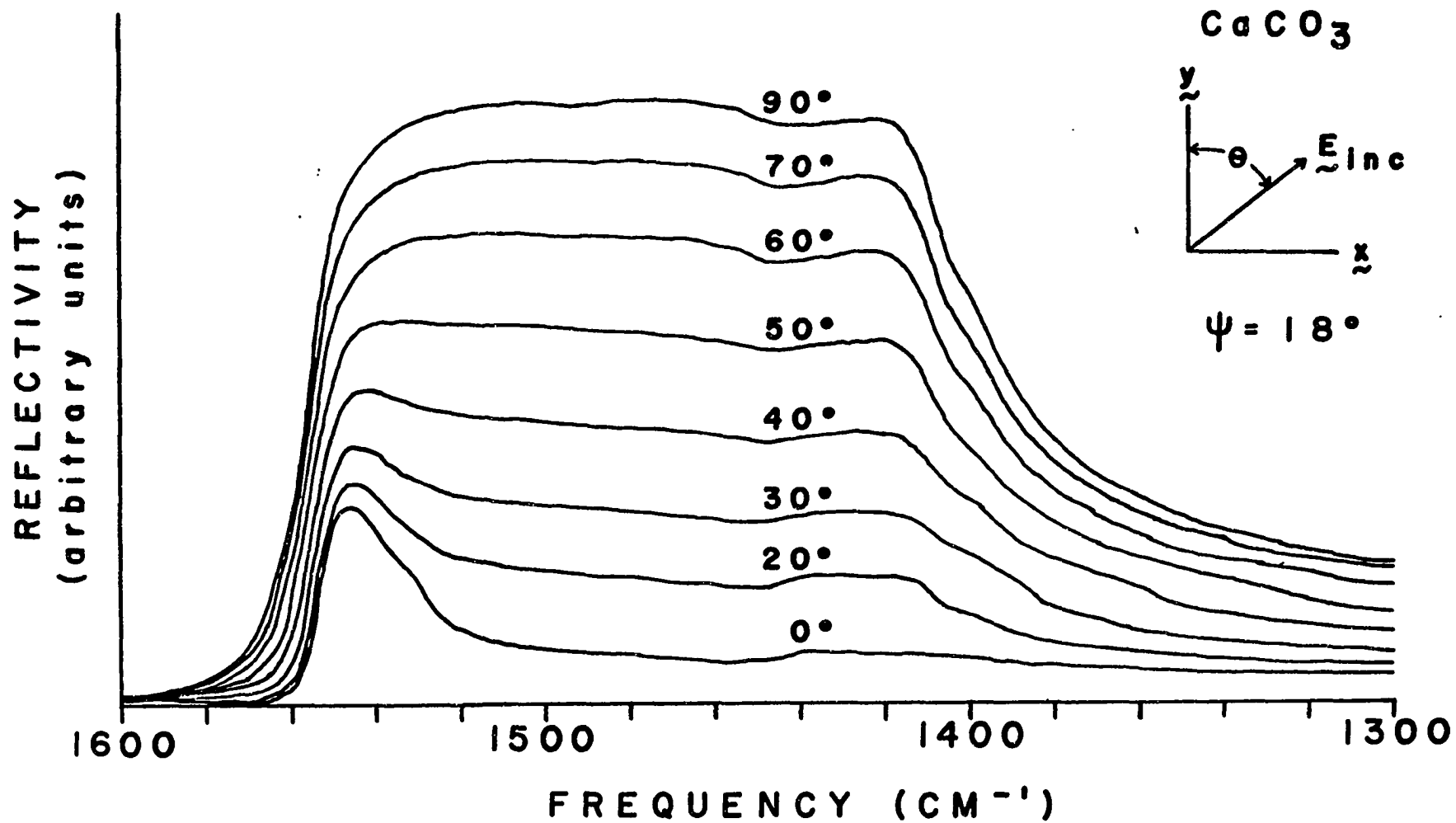


Figure (1-5). Near normal incidence reflectivity spectra of a calcite face cut with $\psi = 18^\circ$ shown as a function of θ as determined by the polarizer setting.

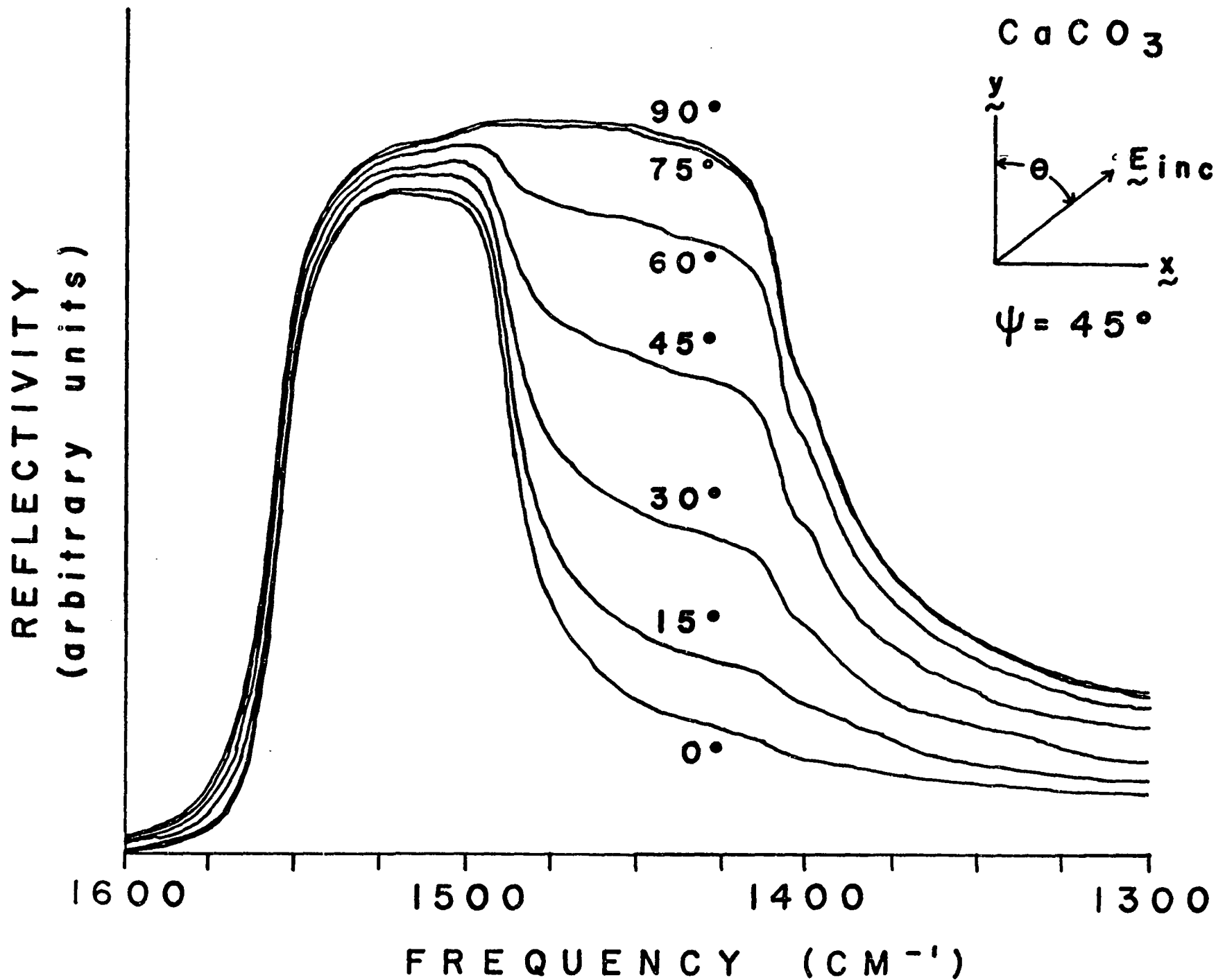


Figure (1-6). Near normal incidence reflectivity spectra of a calcite face cut with $\psi = 45^\circ$ shown as a function of θ as determined by the polarizer setting.

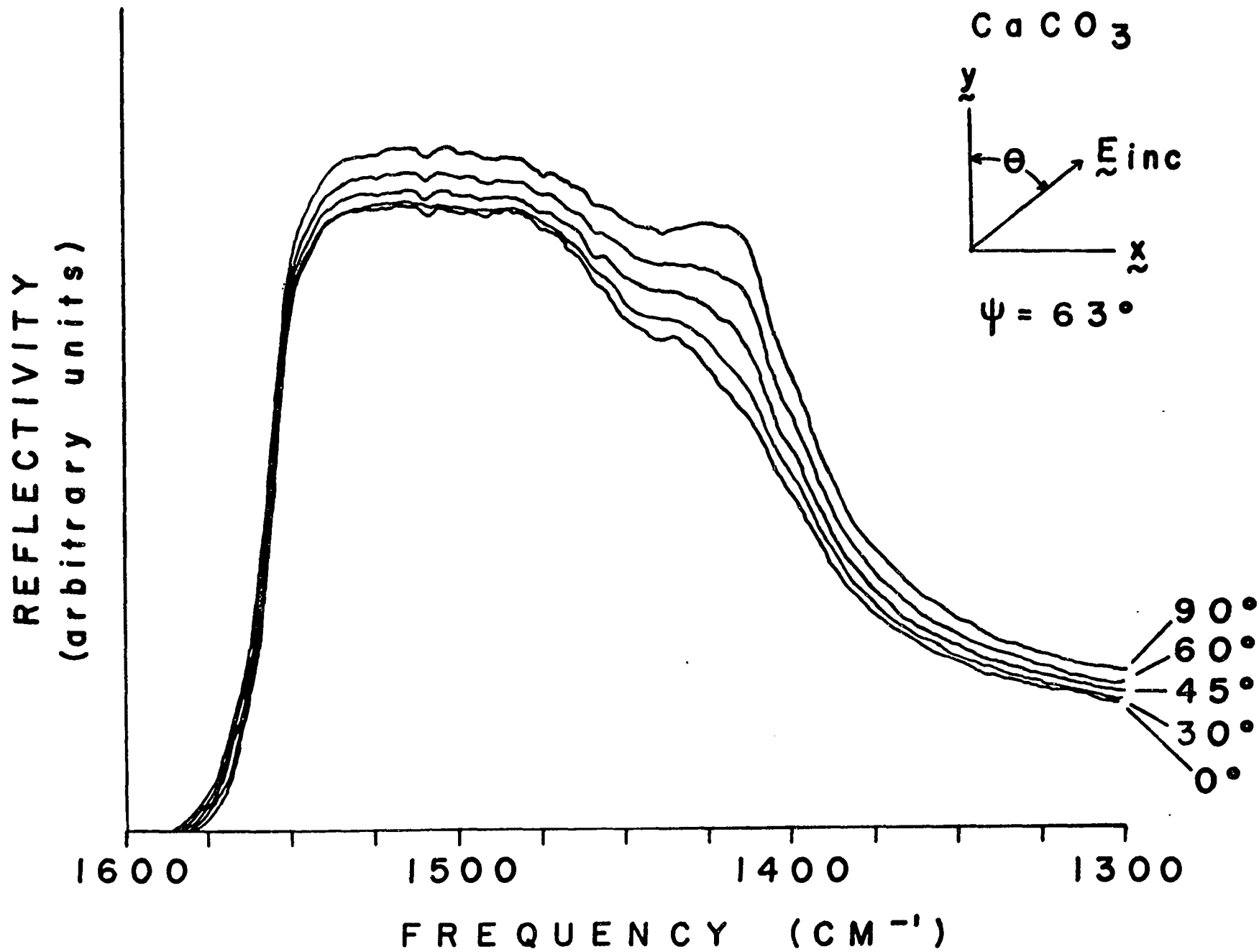


Figure (1-7). Near normal incidence reflectivity spectra of a calcite face cut with $\psi = 63^\circ$ shown as a function of θ as determined by the polarizer setting.

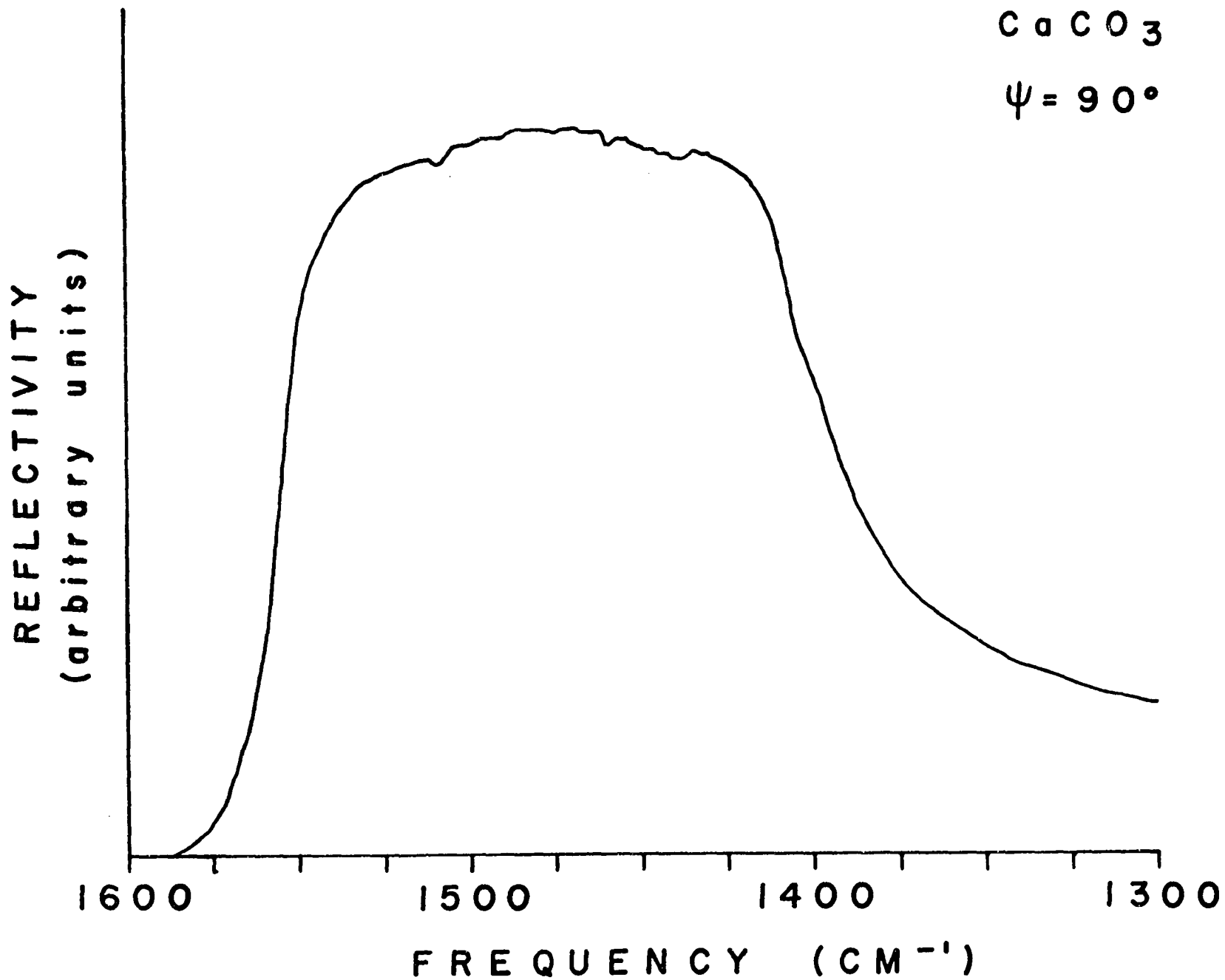


Figure (1-8). Near normal incidence reflectivity spectrum of a calcite face cut perpendicular to the optic axis ($\psi = 90^\circ$).

EXTRAORDINARY WAVE

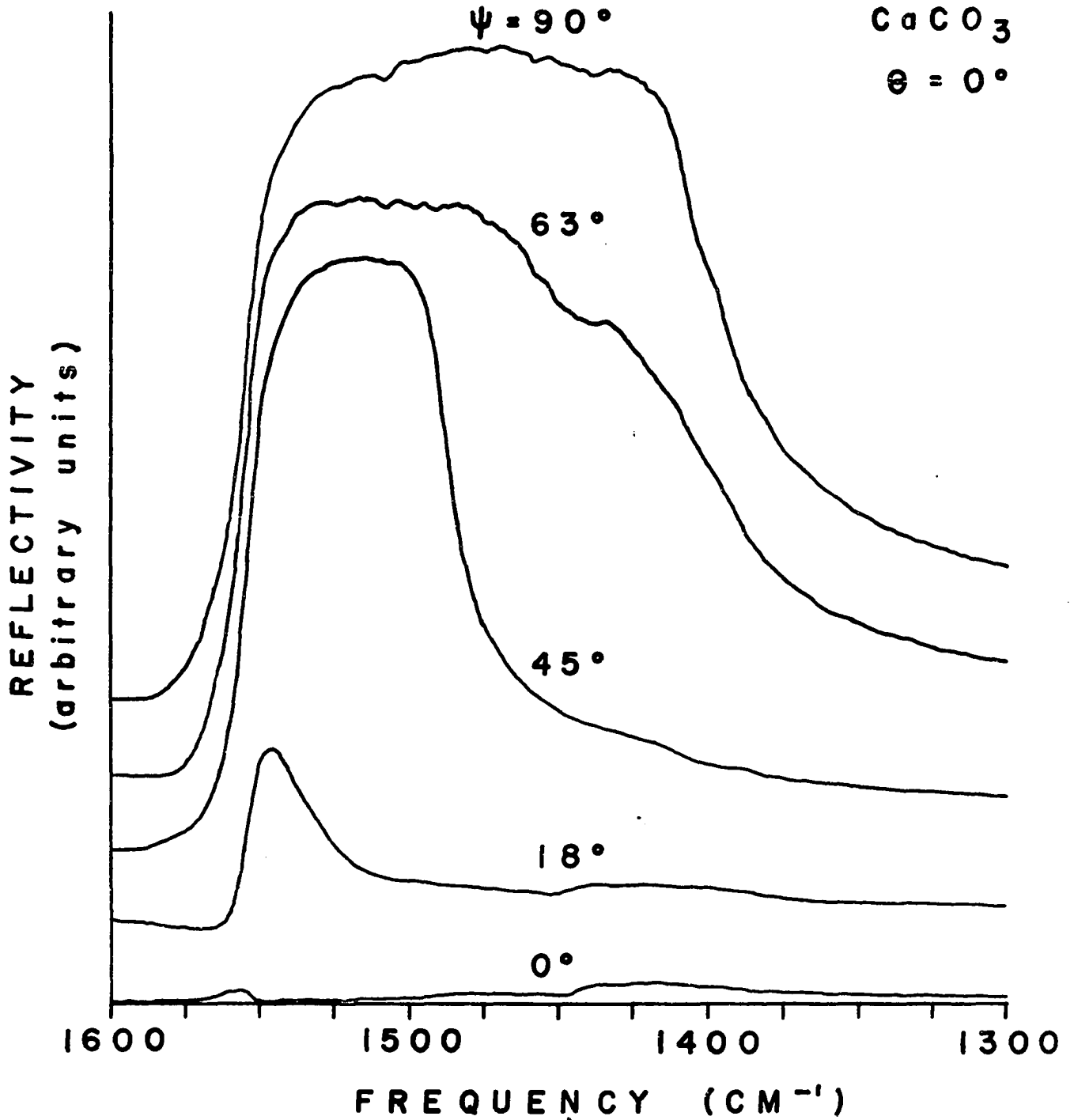


Figure (1-9). The extraordinary wave reflectivity components as a function of the angle ψ between the oblique phonon propagation and polarization directions.

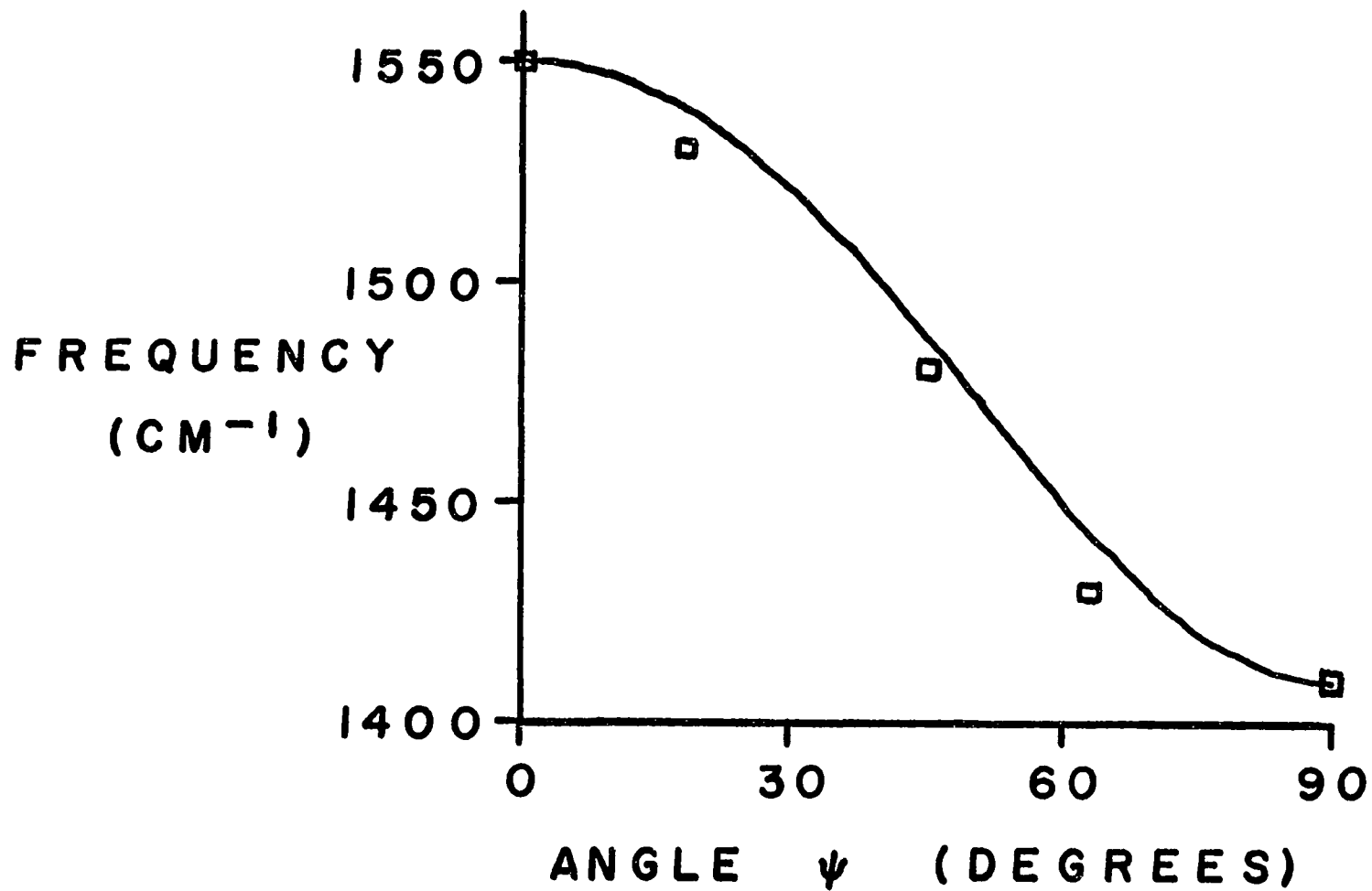


Figure (1-10). The angular dispersion of the $\nu_3(E_u)$ oblique phonon as calculated according to equation 1. The squares are experimental data points estimated from the inflection points of the near normal incidence extraordinary wave reflectivity spectra.

References

1. R. Loudon, *Advan. Phys.* 13, 423 (1964).
2. L. Merten, *Phys. Stat. Sol.* 30, 449 (1968).
3. B. Unger and G. Schaack, *Phys. Stat. Sol. B* 48, 285 (1971).
4. B. Unger and S. Haussühl, *Phys. Stat. Sol. B* 54, 183 (1972).
5. W. Otaguro, E. Wienar-Avneer, C. A. Arguello, and S. P. S. Porto, *Phys. Rev. B* 4, 4542 (1971).
6. D. M. Hwang and S. A. Solin, *Phys. Rev. B* 7, 843 (1973).
7. M. V. Belousov, D. E. Pogarev, and A. A. Shultin, *Fiz. Tverd. Tela.* 15, 2553 (1974), translated in *Sov. Phys. Solid State* 15, 1701 (1974).
8. M. V. Belousov, D. E. Pogarev, and A. A. Shultin, *Fiz. Tverd. Tela.* 16, 1136 (1974), translated in *Sov. Phys. Solid State* 16, 729 (1974).
9. M. Ishigame, T. Satō, and T. Sakurai, *Phys. Rev. B* 3, 4388 (1971).
10. M. Berek, *Z. Kristallogr.* 76, 396 (1931); 89, 144 (1934); 93, 116 (1936).
11. H. Damany and E. Uzan, *Opt. Acta* 17, 131 (1970).
12. R. Frech, *Phys. Rev. B* 13, 2342 (1976).
13. L. Merten, *Z. Naturforsch. A* 15, 47 (1960).
14. K. Huang, *Proc. Roy. Soc. (London) A* 208, 352 (1951).
15. M. Born and K. Huang, *Dynamical Theory of Crystal Lattices* (Oxford, London, 1956).
16. R. Frech, *J. Chem. Phys.* 67, 952 (1977).
17. J. C. Decius, *J. Chem. Phys.* 49, 1387 (1968).
18. R. Frech, *J. Chem. Phys.* 58, 5067 (1973).
19. J. A. A. Ketelaar, C. Haas, and J. Fahrenfort, *Physica* 20, 1259 (1954).
20. R. Frech and J. C. Decius, *J. Chem. Phys.* 54, 2374 (1971).
21. R. Frech and J. C. Decius, *J. Chem. Phys.* 51, 5315 (1969).
22. H. Kornfeld, *Z. Phys.* 22, 27 (1924).
23. P. P. Ewald, *Ann. Phys. (Leipzig)* 64, 253 (1921).

CHAPTER II

The Anomalous Infrared Reflectivity Minimum in NaNO_3

Introduction

In many crystals the measurement of the near normal incidence infrared reflectivity spectrum results in a smooth reflectivity curve which, in the vicinity of an infrared active vibrational mode, is large between the transverse optic mode frequency and the longitudinal optic mode frequency and exhibits a maximum between those two frequencies with no fine structure observable. This behavior is typical of most infrared active modes in most crystals. However, in a few crystals reflectivity bands have been observed which exhibit an anomalous minimum or "dip" in the spectral region between the transverse and longitudinal optic mode frequencies. The possible explanations which might be advanced to explain this phenomenon would include the observation of surface modes in the vicinity of the fundamental, a Fermi-like resonant interaction of the fundamental mode with nearby combination or overtone modes, or a frequency dependent damping constant sharply peaked in the vicinity of the reflectivity dip.

The existence of surface states in crystals has been discussed by Kliewer and Fuchs,^{1,2} Philpott,³ and others.^{4,5} Direct observations of surface states using attenuated total reflection techniques have been successfully made in a variety of systems including gallium phosphide (GaP)⁶ and calcium molybdate (CaMoO_4).⁷ These surface states are usually postulated to arise from two effects: first, the electric field seen by a molecule depends on its distance from the surface at least for a few atomic layers into the bulk material and second, the physical properties of the molecules

themselves may again depend on the distance of the molecule from the surface.

Philpott³ considers the crystal as consisting of planes of molecules within which the molecules are dynamically coupled through vibrationally induced dipolar interactions. Weak coupling between planes leads to the appearance of additional reflection minima located between the transverse and longitudinal optic modes in the crystal. Although Philpott's work treated electronic states in molecular crystals it was pointed out that the conclusions reached therein would be applicable to the problem of optical phonons in molecular crystals. Another interesting modification of the usual reflectivity behavior was reported by Berreman.⁸ The existence of bumps or pits on a plane dielectric surface was theoretically shown to produce a dip in the top of an ordinary reflection band, together with a rather sharp peak of enhanced reflectivity just below the frequency of the longitudinal optic mode.

An experimental spectroscopic study is reported here for sodium nitrate (NaNO_3) which exhibits an anomalous reflectivity minimum in the transverse-longitudinal band gap of the infrared active fundamental vibrational mode originating primarily in the asymmetric stretching motion of the nitrate ion, $\nu_3(E_u)$. This reflectivity minimum occurs in the immediate spectral vicinity of the combination mode resulting from $\nu_4(E_u) + \nu_4(E_g)$.

Raman active combination modes in $\text{Na}^{14}\text{NO}_3$ have been observed by Maksimov⁹ et al. in a study of the density function of two-phonon states obtained from second-order Raman scattering. In a related study of Fermi resonance of the $\nu_3(E_u)$ mode with the $\nu_4(E_u) + \nu_4(E_g)$ combination mode, Belousov et al.¹⁰ tuned the oblique phonon originating in $\nu_3(E_u)$ into the spectral region of the $\nu_4(E_u) + \nu_4(E_g)$ combination mode by taking advantage

of the angular dispersion of polar phonons in uniaxial crystals.¹¹ The reflectivity spectra of several crystals with faces cut at different angles with respect to the optic axis were reported and the reflectivity behavior was attributed to a Fermi-like resonant interaction between the fundamental and the combination modes. However some ambiguity remains, for the reflectivity behavior is that which one might expect from the extraordinary wave reflectivity of a fundamental modified by the presence of a constant "dip" in the reflectivity band. In other words the intensity variation of the two "Fermi components" may be only apparent since the reflectivity decreases as the oblique phonon becomes more longitudinal in character.

The $^{14}\text{N}/^{15}\text{N}$ isotopic shift of the various vibrational modes of sodium nitrate permit an important experiment which can clearly differentiate between a surface effect and the dependence of the reflectivity dip on the presence of nearby combination or overtone modes. The $\nu_3(\text{E}_u)$ mode of NaNO_3 undergoes an isotopic shift to a lower frequency of $\sim 33 \text{ cm}^{-1}$ upon substitution of ^{15}N for ^{14}N whereas the $\nu_4(\text{E}_u)$ mode undergoes a frequency shift of only $\sim 2 \text{ cm}^{-1}$.¹²

If the reflectivity dip found at 1448 cm^{-1} in the $\nu_3(\text{E}_u)$ mode of NaNO_3 (99.63% ^{14}N natural abundance) is due to the combination mode $\nu_4(\text{E}_u) + \nu_4(\text{E}_g)$ it should occur at 1445 cm^{-1} in the $\text{Na}^{15}\text{NO}_3$ crystal whereas if it is due to a surface effect it should follow $\nu_3(\text{E}_u)$ and be shifted by $\sim 33 \text{ cm}^{-1}$.

Experimental

Single crystals of $\text{Na}^{14}\text{NO}_3$ and $\text{Na}^{15}\text{NO}_3$ were grown by slow evaporation from aqueous solution at room temperature. The $\text{Na}^{15}\text{NO}_3$ (99.4% ^{15}N enriched) was obtained from Stohler Isotope Chemicals and reagent grade NaNO_3 was used for the $\text{Na}^{14}\text{NO}_3$ crystals without further purification. The crystals

were polished on ground glass using ethanol or water as a solvent followed by polishing on cloth using no solvent. Room temperature polarized infrared reflection spectra were recorded on a Beckman IR-12 using a 4:1 linear image reduction with an average angle of incidence of 15° . Raman frequencies were measured on a Spex Ramalog 5 Raman spectrometer using a two watt argon ion laser.

The near normal incidence infrared reflection spectra of the ν_3 region are shown in figure (2-1) for a face perpendicular to the optic axis in $\text{Na}^{14}\text{NO}_3$ and $\text{Na}^{15}\text{NO}_3$. The dips occur at 1448 and 1444 cm^{-1} with shoulders at 1455 and 1448 cm^{-1} respectively in the $\text{Na}^{14}\text{NO}_3$ and $\text{Na}^{15}\text{NO}_3$ crystals. Raman spectra for the $2\nu_4(\text{E}_u)$ and $2\nu_4(\text{E}_g)$ region are shown in figure (2-2). Only one $2\nu_4$ component at 1448 cm^{-1} in $\text{Na}^{14}\text{NO}_3$ and 1445 cm^{-1} in $\text{Na}^{15}\text{NO}_3$ is observed. The broad feature at 1490 cm^{-1} in the $\text{Na}^{14}\text{NO}_3$ spectrum is shifted by 35 cm^{-1} to 1455 cm^{-1} in the $\text{Na}^{15}\text{NO}_3$ spectrum which would indicate a lattice mode + ν_3 combination.

Slutsky et al.¹³ assigned the infrared active $\nu_4(\text{E}_u) + \nu_4(\text{E}_g)$ combination mode at 1449 cm^{-1} in $\text{Na}^{14}\text{NO}_3$ and 1447 cm^{-1} in $\text{Na}^{15}\text{NO}_3$ using single crystal transmission data. Based upon the sharpness of the combination mode he assumed that the dispersion of $\nu_4(\text{E}_u)$ is either very flat or that only the Brillouin zone center modes contribute to the spectrum. Both the $\nu_4(\text{E}_u) + \nu_4(\text{E}_g)$ combination mode and the $2\nu_4(\text{E}_u, \text{E}_g)$ overtones occur at the dip frequency in the $\text{Na}^{14}\text{NO}_3$ crystal which, along with the flat dispersion of $\nu_4(\text{E}_u)$ indicates that the shoulder at 1455 cm^{-1} is not due to the $\nu_4(\text{E}_u) + \nu_4(\text{E}_g)$ combination mode but is a part of $\nu_3(\text{E}_u)$. The presence of the combination mode between the transverse and longitudinal frequencies of the fundamental transition creates a minimum in the

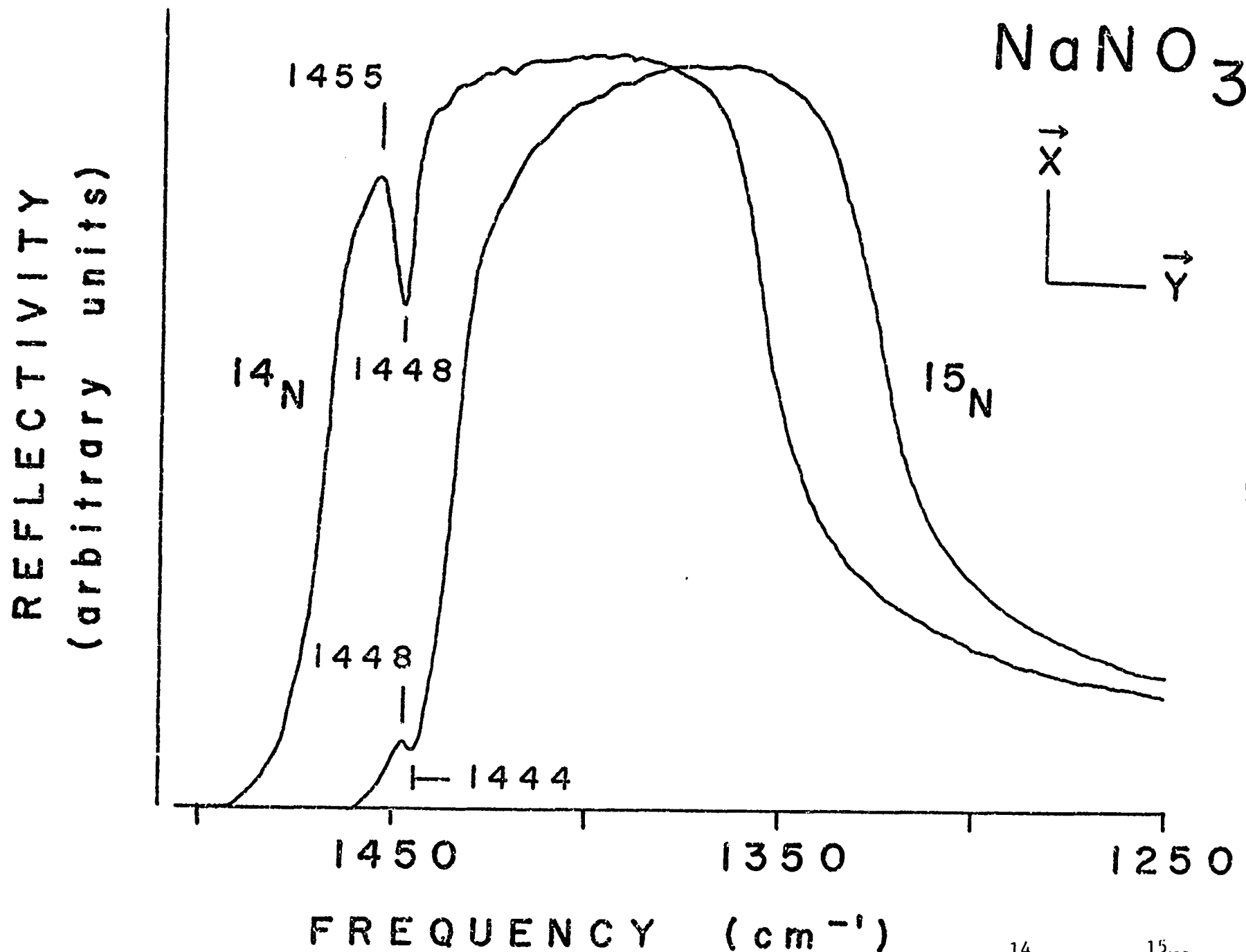
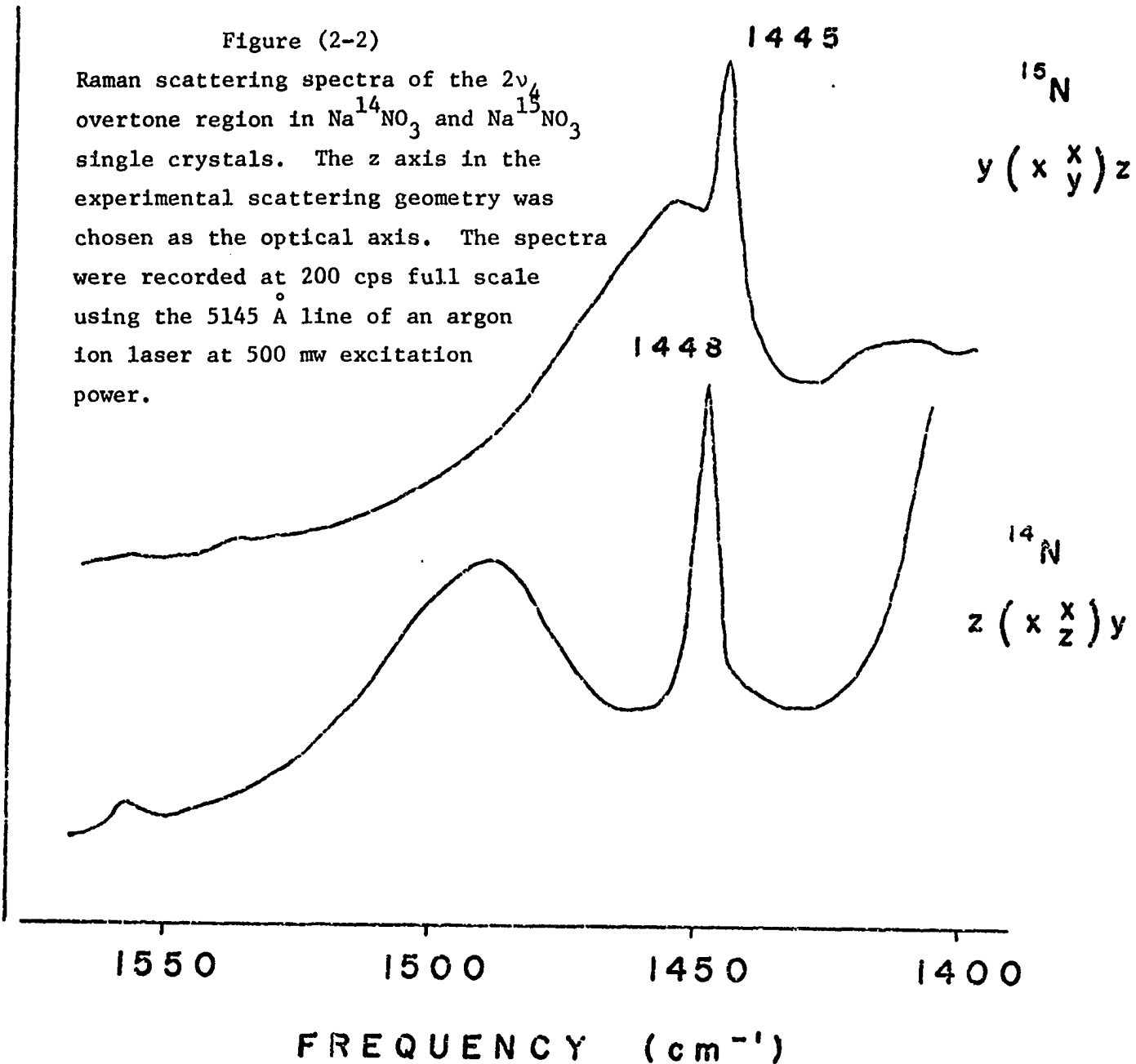


Figure (2-1). Near normal incidence infrared reflectivity spectra of the ν_3 region in $\text{Na}^{14}\text{NO}_3$ and $\text{Na}^{15}\text{NO}_3$ single crystals with faces cut perpendicular to the optical axis.

INTENSITY (arbitrary units)

Figure (2-2)

Raman scattering spectra of the $2\nu_4$ overtone region in $\text{Na}^{14}\text{NO}_3$ and $\text{Na}^{15}\text{NO}_3$ single crystals. The z axis in the experimental scattering geometry was chosen as the optical axis. The spectra were recorded at 200 cps full scale using the 5145 Å line of an argon ion laser at 500 mw excitation power.



reflectivity of $\nu_3(E_u)$. The dip in $\text{Na}^{15}\text{NO}_3$ occurs at the same frequency as the Raman active $2\nu_4(E_u, E_g)$ mode but is in disagreement with the $\nu_4(E_u) + \nu_4(E_g)$ combination mode frequency of 1447 cm^{-1} reported by Slutsky et al. Since the combination mode, dip, overtone, and shoulder all occur in the $1444\text{--}1448 \text{ cm}^{-1}$ range it is difficult to assign the reflectivity anomaly as being a dip caused by the combination mode or a shoulder which is the combination mode enhanced by Fermi resonance with $\nu_3(E_u)$. However, if the dip rather than the shoulder is attributed to the combination mode the $\text{Na}^{14}\text{NO}_3$ data and the $\text{Na}^{15}\text{NO}_3$ data are then consistent.

References for Chapter II

1. K. L. Kliewer and R. Fuchs, Phys. Rev. 144, 495 (1966); 150, 573 (1966).
2. R. Fuchs, K. L. Kliewer, and W. J. Pardee, Phys. Rev. 150, 589 (1966).
3. M. R. Philpott, J. Chem. Phys. 60, 1410, 2520 (1974).
4. D. P. Craig and L. A. Dissado, Proc. Roy. Soc. Lond. A325, 1 (1971); A332, 419 (1972).
5. V. I. Sugakov, Fiz. Tverd. Tela. 6, 1361 (1964). (Sov. Phys.-Solid State 6, 1064 (1964).)
6. N. Marshall and B. Fischer, Phys. Rev. Lett. 28, 811 (1972).
7. A. S. Barker, Jr., Phys. Rev. Lett. 28, 892 (1972).
8. D. W. Berreman in Localized Excitations in Solids, Proc. of the 1st Int. Conf. on Localized Excitations at the Univ. of Cal. at Irvine, Sept. 18-22, 1967. Pp. 420-5, Plenum Press, NY 1968.
9. O. P. Maksimov, V. S. Gorelik, and M. M. Sushchinskii, Fiz. Tverd. Tela 17, 2827 (1975). (Sov. Phys.-Solid State 17, 1892 (1976).)
10. M. V. Belousov, D. E. Pogarev, and A. A. Shultin, Fiz. Tverd. Tela 16, 1136 (1974). (Sov. Phys.-Solid State 16, 729 (1974).)
11. R. Loudon, Advan. Phys. 13, 423 (1964).
12. G. Hertzberg, Infrared and Raman Spectra (D. Van Nostrand, New York, 1945).
13. R. Eckhardt, D. Eggers and L. J. Slutsky, Spectrochimica Acta, 26A, 2033 (1970).

CHAPTER III

Combination Mode Assignments in NaNO_3 using Microcrystalline Reflectivity and Single Crystal Raman Spectra

Introduction

Single crystal infrared transmission and Raman spectra contain a wealth of information about multiphonon transitions. Slutsky and co-workers have reported the infrared transmission spectrum of $\text{Na}^{14}\text{NO}_3$ and $\text{Na}^{15}\text{NO}_3$ using very thin crystal slabs and have made assignments for many of the infrared active multiphonon transitions.¹ Most of the two-phonon Raman active vibrational modes for $\text{Na}^{14}\text{NO}_3$ have been made by Maksimov and co-workers in a two-phonon density of states study.²

One problem with a single crystal transmission study is that of obtaining a crystal large enough for use. Another problem is the strong absorption in the region of fundamental infrared active modes which leaves the crystal effectively opaque to infrared radiation and obscures the desired information. This problem can be eliminated by using crystals on the order of a few microns thick although these crystals are difficult to prepare.

In this work the Raman and infrared active two-phonon transitions are assigned for NaNO_3 using single crystal Raman scattering and microcrystalline reflectivity spectra.

Theory

Light scattering from a microcrystalline sample in a frequency range in which vibrational transitions do not occur will exhibit a broad flat background due to multiple reflection from the microcrystals. There is, in effect, transmission through the microcrystals with reflection from each surface characterized by the optical constants of a non-absorbing medium. In a region of very strong reflectivity such as that exhibited by the $\nu_3(E_u)$ mode of NaNO_3 the reflectivity at the first surface is so great that the first microcrystal surfaces reflect a large fraction of the incident light allowing very little to pass through to the second layer. However, in regions of weak absorption and hence weak reflectivity such as combination mode regions, the reflectivity from the first surface is not very large allowing the microcrystals to absorb part of the light transmitted through them. This transmitted light is subsequently reflected and contributes to the broad flat background. Therefore at these frequencies the reflection spectrum will resemble the single crystal transmission spectrum.

Experimental

Single crystals of NaNO_3 are easily grown by evaporation from aqueous solution at room temperature. Faces parallel and perpendicular to the optic axis were obtained for Raman measurements by grinding the crystals on emery paper followed by polishing on lens paper using small amounts of water as a solvent. Microcrystalline samples were prepared by grinding in an agate mortar and packing the powder in a slot in a metal plate using hand pressure. Single crystals were mounted with epoxy over a hole in a metal plate and ground as thin as possible on emery paper. Infrared transmission spectra were obtained by allowing the light to pass through the hole. Single crystal reflection spectra were obtained by

mounting the crystal so that the plane defined by the optic axis and the normal to the crystal face was perpendicular to the plane of incidence. In the experimental geometry the TM reflectivity is the ordinary wave reflectivity (which contains only contributions from transverse phonon resonances) and the TE reflectivity is the extraordinary wave reflectivity (which contains only contributions from oblique phonon resonances).

Raman spectra were recorded at room temperature on a Spex Ramalog 5 spectrometer equipped with a 2 watt argon ion laser. Near normal incidence infrared reflection spectra were recorded at room temperature on a Beckman IR-12 spectrometer using an average angle of incidence of 15° and a 4:1 linear image reduction.

Results and Discussion

The unpolarized microcrystalline reflectivity spectrum and the unpolarized single crystal reflectivity spectrum from a natural rhombohedral face for the $\nu_3(E_u)$ region of $\text{Na}^{14}\text{NO}_3$ are shown in figure (3-1). The two spectra are almost identical which may indicate that the microcrystal faces are primarily natural rhombohedral faces. The shape of $\nu_3(E_u)$ in the unpolarized single crystal reflection spectrum from a natural rhombohedral face is due to an oblique phonon of $\nu_3(E_u)$ at 1419 cm^{-1} propagating at an angle of 44 degrees from the optic axis and the $\nu_3(E_u)$ transverse phonon at 1353 cm^{-1} propagating in the plane perpendicular to the optic axis.

A theoretical treatment of the reflectivity spectrum from an anisotropic microcrystalline powder has been previously presented along with experimental data for $\text{Na}^{14}\text{NO}_3$.³ In that study the microcrystals were considered to be randomly oriented: any $\nu_4(E_u) + \nu_4(E_g)$ combination mode interactions were neglected. Reasonable agreement with the experimental data was obtained. Shown in figures (3-2) and (3-3) are the calculated and

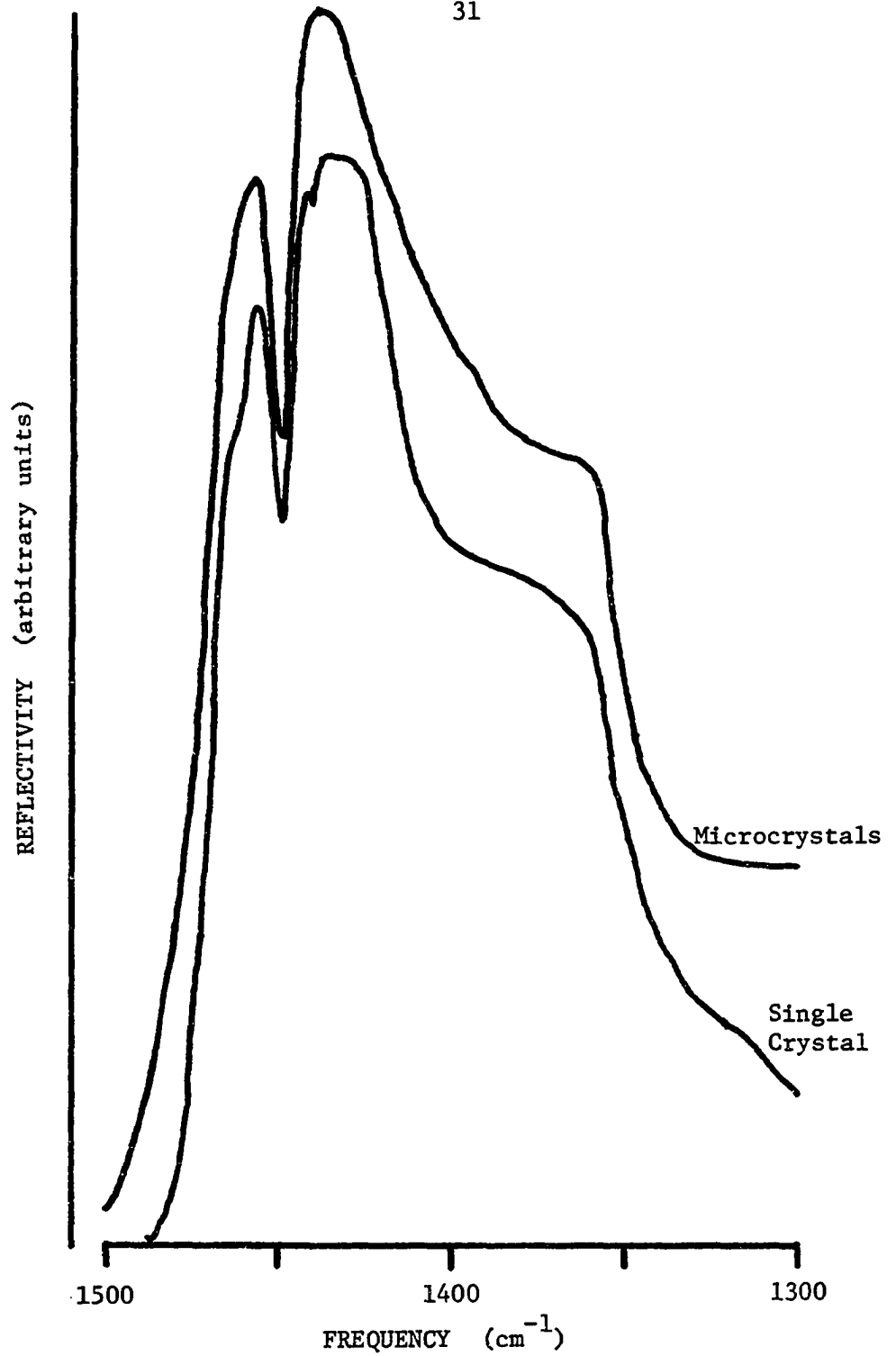
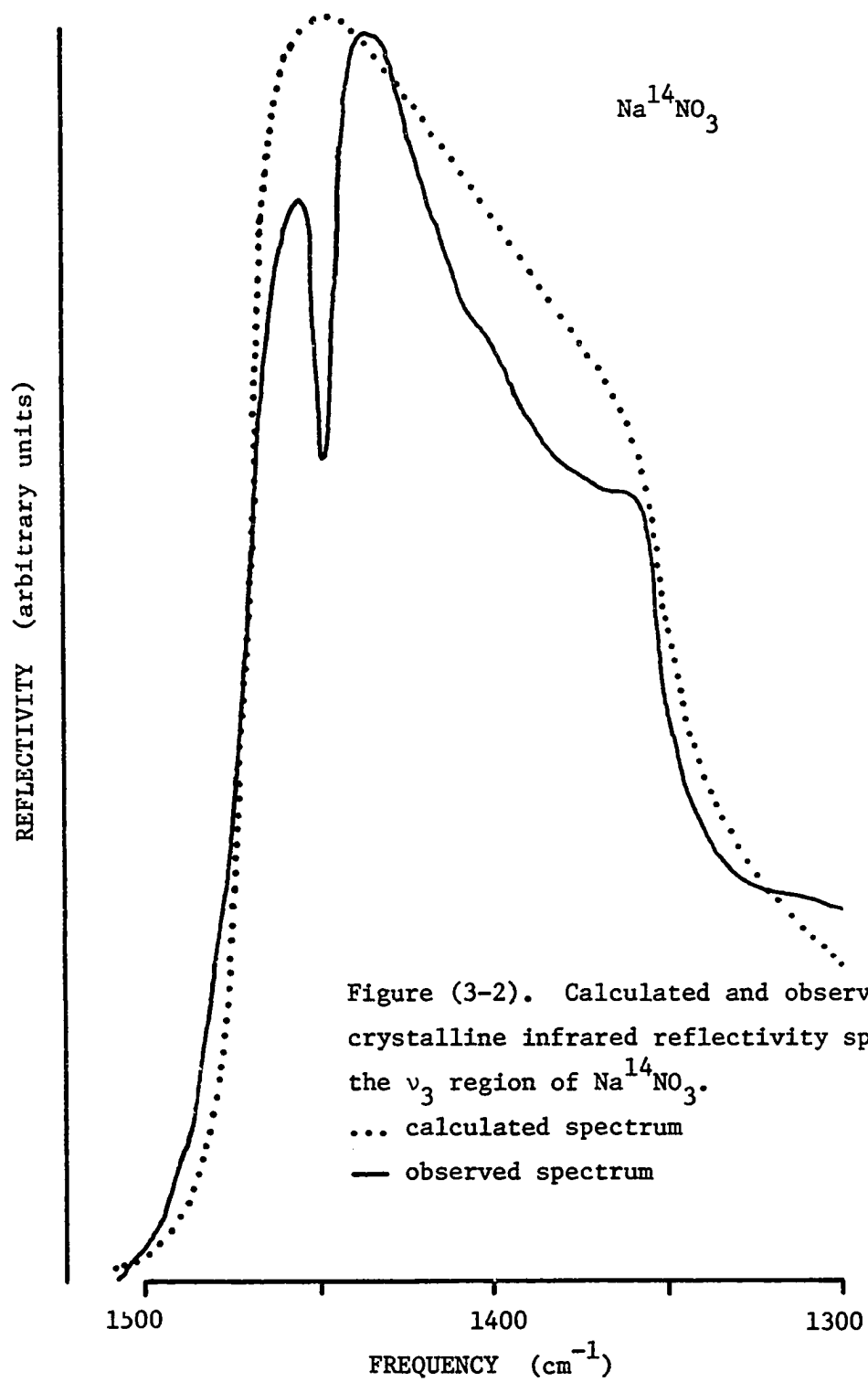


Figure (3-1). Unpolarized infrared reflectivity spectra from a microcrystalline powder and a single crystal natural rhombohedral face of Na¹⁴NO₃ in the ν_3 spectral region.

experimental microcrystalline reflectivity spectra for $\text{Na}^{14}\text{NO}_3$ and $\text{Na}^{15}\text{NO}_3$ respectively in the $\nu_3(E_u)$ region using the microcrystalline model. The calculated spectra reproduce the basic features of the experimentally observed spectra but the reflectivity of the low frequency side is calculated to be too high. This is probably due to the assumption that the microcrystals have random faces rather than primarily natural rhombohedral faces. The low frequency maximum observed in earlier experiments by Bates³ was not found here which enhances the agreement between theory and experiment. The low frequency maximum may be due to a particle size effect which would explain the discrepancy between this and earlier data though this apparent discrepancy was not pursued further. Another possibility is that the former samples were prepared by polishing the surface of the microcrystal layer which would create faces which are not the natural rhombohedral cleavage planes; this might reasonably be expected to produce some changes in the spectra.

The single crystal reflectivity spectrum revealed no structure in the combination mode region indicating that it cannot be used for studying multiphonon processes. The single crystal transmission and microcrystalline reflection spectra for $\text{Na}^{14}\text{NO}_3$ are shown in figure (3-4). These spectra are almost identical except in the immediate vicinity of $\nu_3(E_u)$ where the microcrystalline reflectivity spectrum is similar to the unpolarized single crystal reflectivity spectrum from a natural rhombohedral face. The absorption is so great in the $\nu_3(E_u)$ region of the single crystal transmission spectrum that the crystal is opaque revealing very little information about the $\nu_3(E_u)$ mode.

Group theory predicts the $\nu_4(E_u)$ mode to be infrared active, however, the dipole moment derivative is so small as to make it unobservable in single crystal reflectivity spectra. In both the microcrystalline



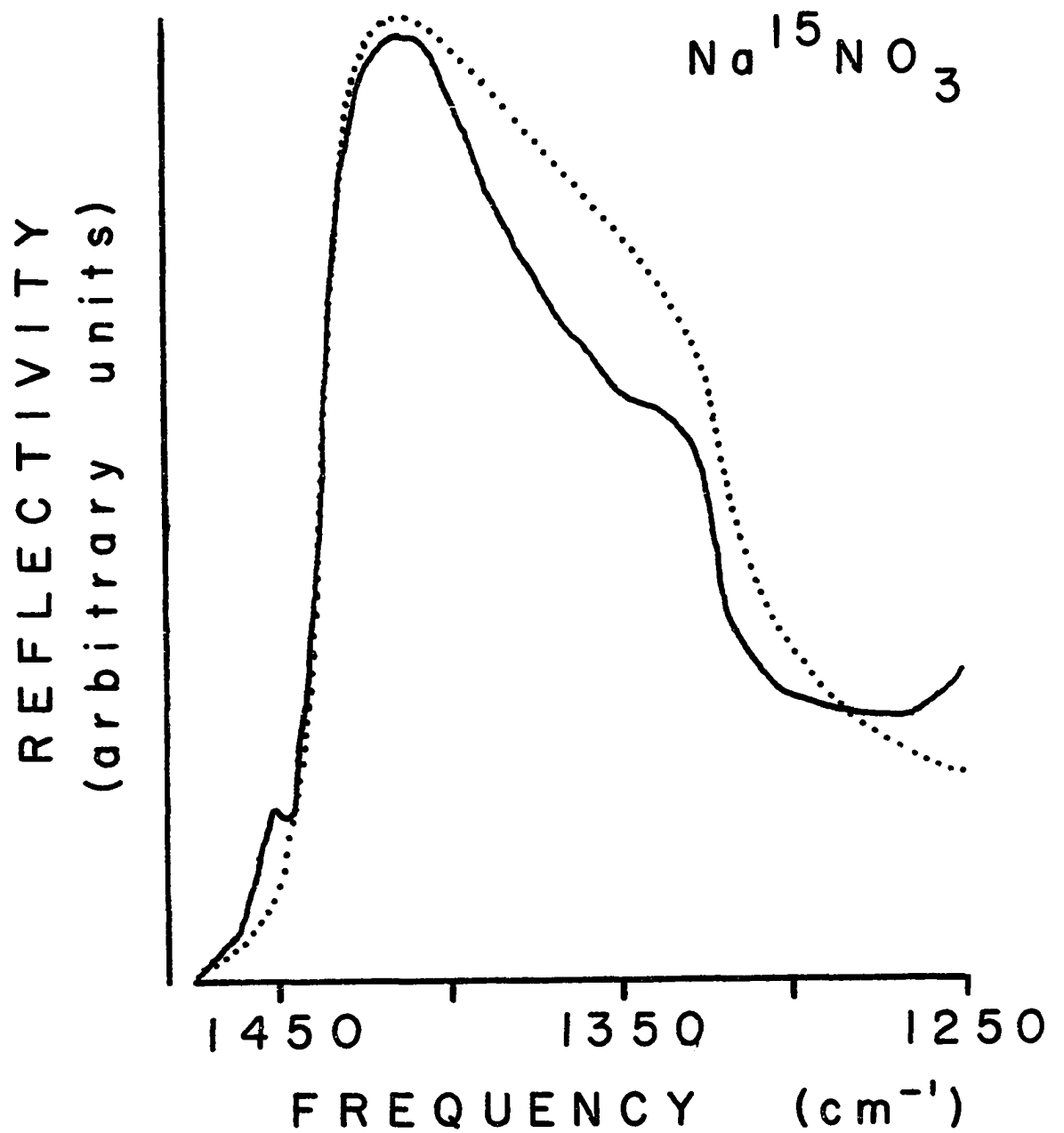


Figure (3-3). Calculated and observed microcrystalline infrared reflectivity spectra of the ν_3 region of $\text{Na}^{15}\text{NO}_3$.
... calculated spectrum
— observed spectrum

reflectivity spectrum and the single crystal transmission spectrum a very sharp absorption is found at 728 cm^{-1} corresponding to the $\nu_4(E_u)$ mode indicating that there is very little dipolar dispersion. The $\nu_2(A_{2u})$ mode is seen in single crystal reflectivity spectra but the absorption dominates in the microcrystalline reflectivity through the previously described mechanism of transmission loss. Only the very intense $\nu_3(E_u)$ mode shows any pronounced reflectivity in the microcrystalline reflectivity spectrum.

Shown in figure (3-5) is the microcrystalline reflectivity spectrum of $\text{Na}^{15}\text{NO}_3$. Infrared active multiphonon assignments are presented in table (3-1). The $\nu_3(E_u) + \nu_3(E_g)$ combination mode region has two maxima at 2765 cm^{-1} and 2855 cm^{-1} in $\text{Na}^{14}\text{NO}_3$ which shift by 63 cm^{-1} to 2703 and 2791 cm^{-1} respectively upon isotopic substitution. As the $\nu_3(E_u) + \nu_3(E_g)$ combination mode is the only mode in this frequency range that should shift by 63 cm^{-1} and this combination mode region is identical for both isotopic species these maxima are attributed to critical points in the $\nu_3(E_u) + \nu_3(E_g)$ two-phonon density of states. The multiphonon Raman spectra are shown in figure (3-6) with combination mode assignments in table (3-2).

Conclusion

Microcrystalline reflectivity circumvents much of the problem of obtaining a large single crystal for either single crystal reflectivity or single crystal transmission as well as the problem of very intense absorption with single crystal transmission spectra. However, the ability to observe polarized spectra, which is often desirable with non-cubic systems, is lost.

Figure(3-4a). Microcrystalline infrared reflectivity and single crystal infrared transmission spectra of $\text{Na}^{14}\text{NO}_3$ in the $700 - 1200 \text{ cm}^{-1}$ region. Upper spectrum is microcrystalline; lower spectrum is single crystal.

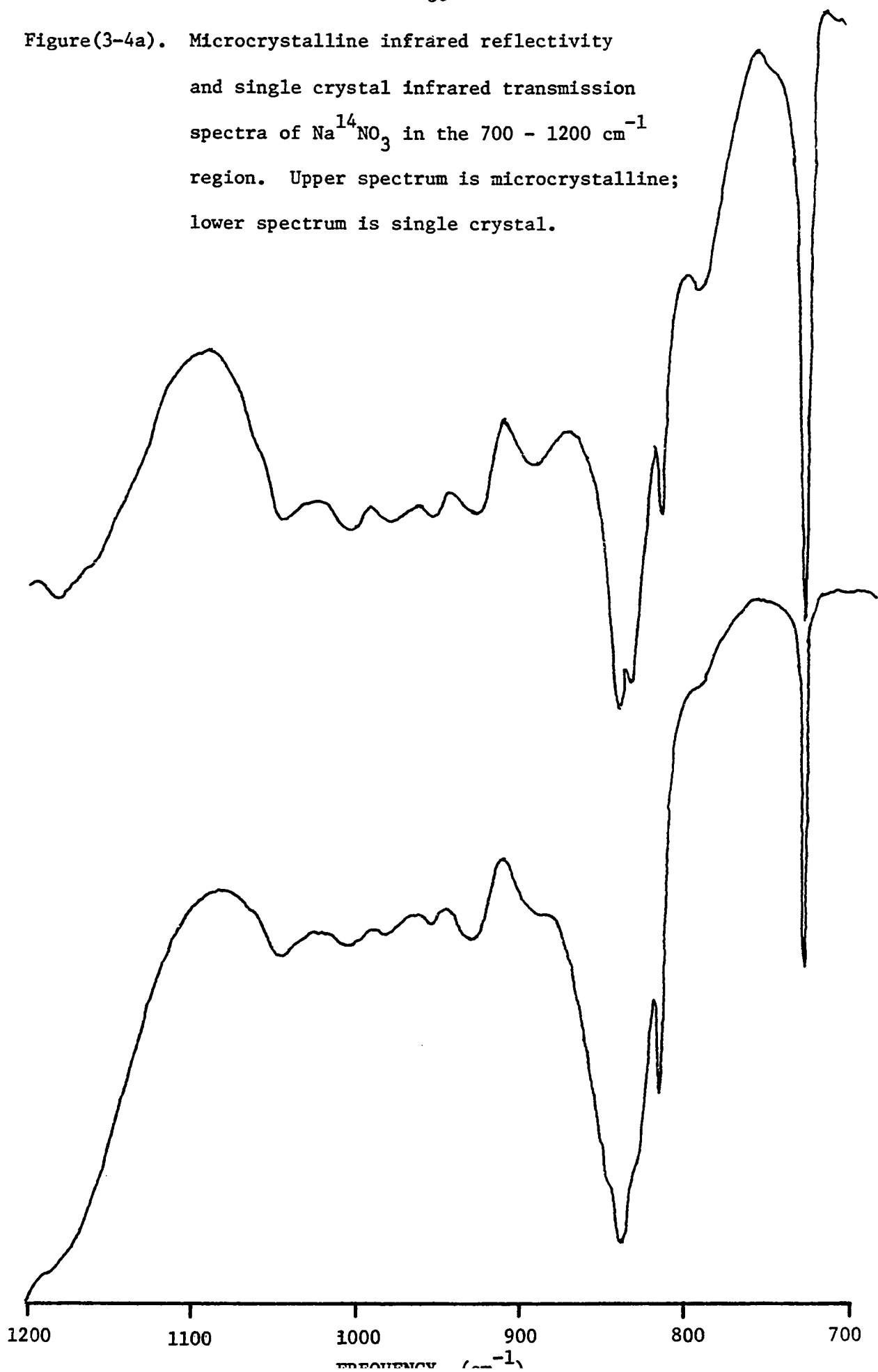


Figure (3-4b). Microcrystalline infrared reflectivity and single crystal infrared transmission spectra of $\text{Na}^{14}\text{NO}_3$ in the $1200 - 2000 \text{ cm}^{-1}$ region. Spectrum M is microcrystalline; spectrum C is single crystal.

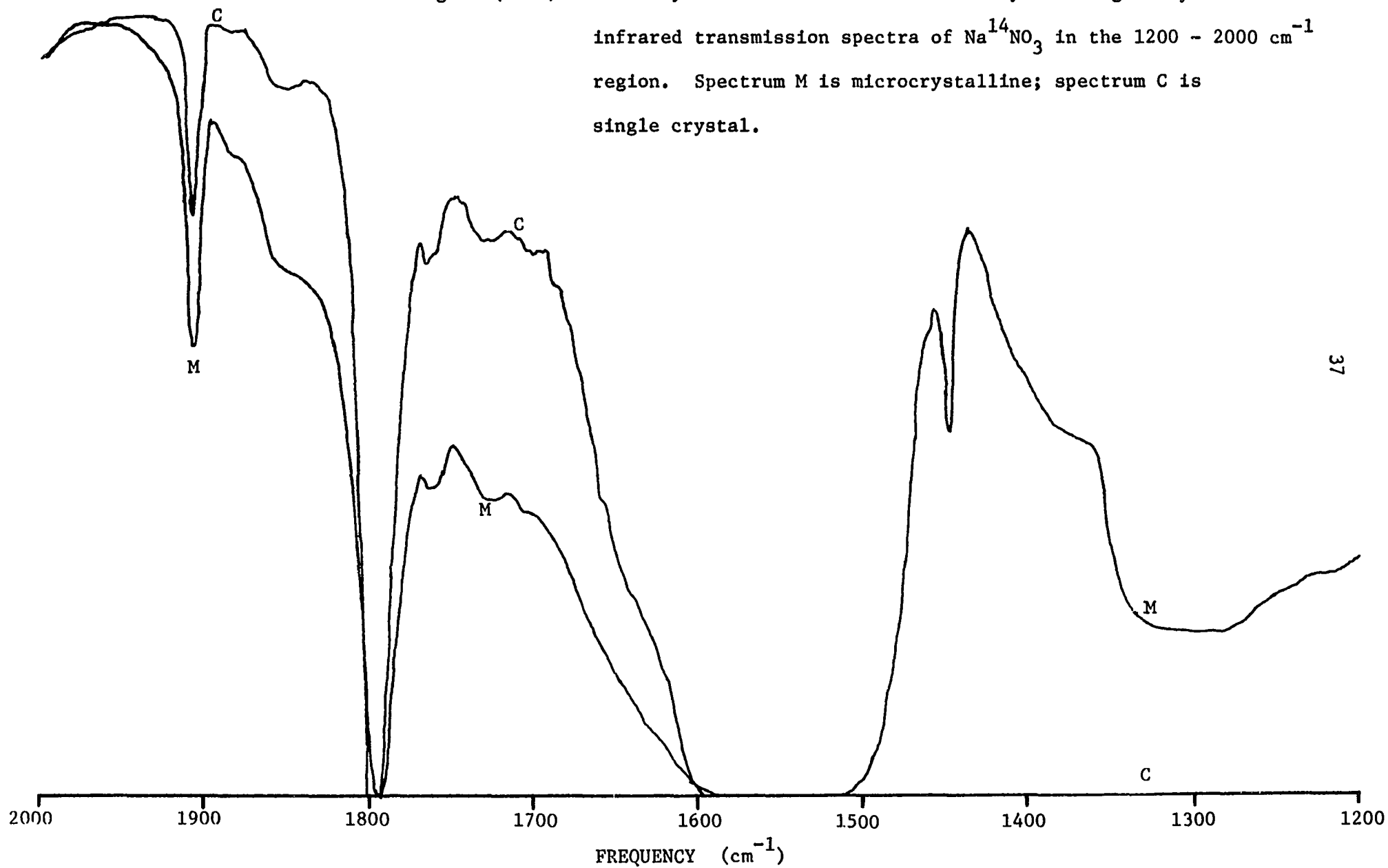


Figure (3-4c). Microcrystalline infrared reflectivity and single crystal infrared transmission spectra of $\text{Na}^{14}\text{NO}_3$ in the $2000 - 3000 \text{ cm}^{-1}$ region. Spectrum C is single crystal; spectrum M is microcrystalline and has been displaced upward.

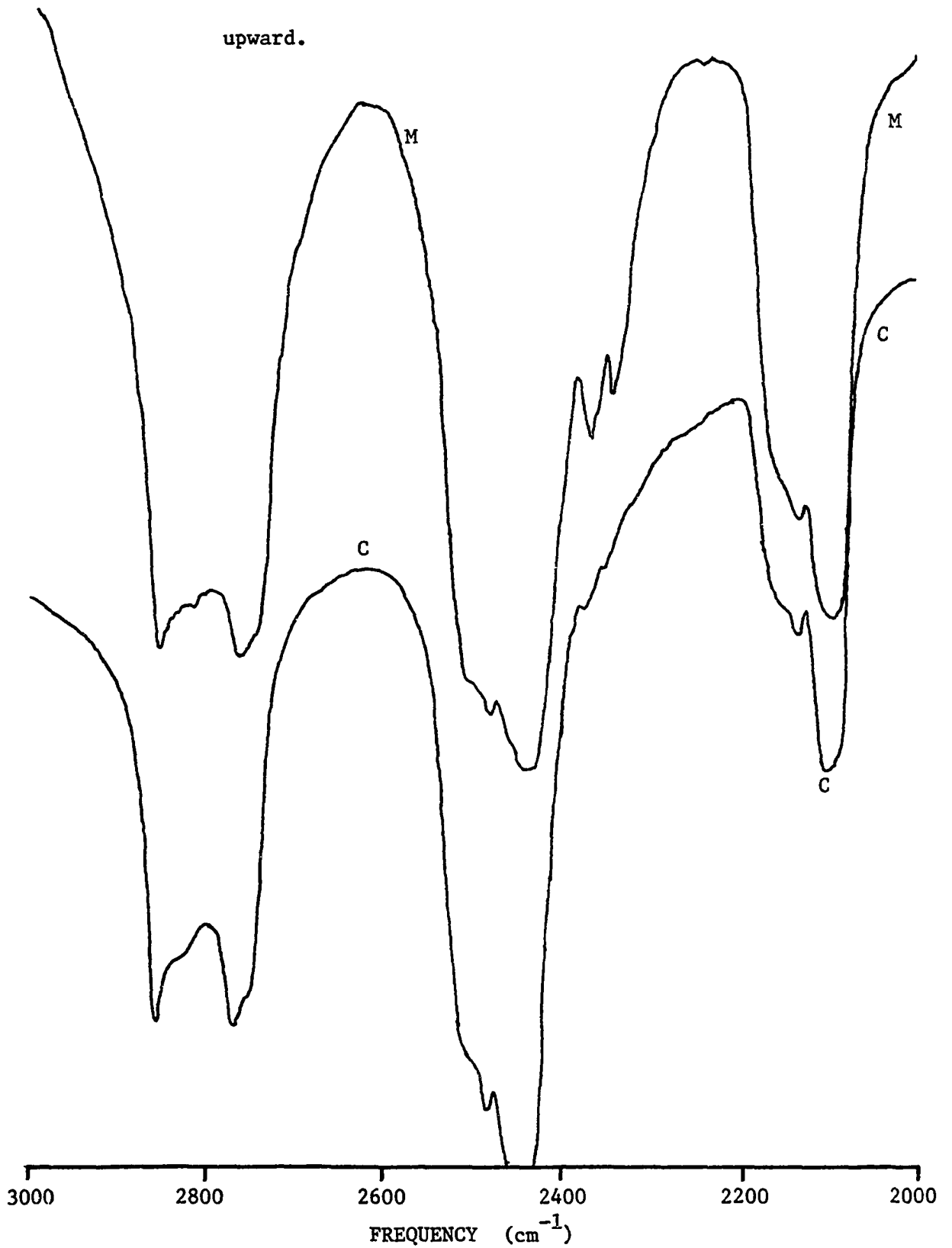


Figure (3-4d). Microcrystalline infrared reflectivity and single crystal infrared transmission spectra of $\text{Na}^{14}\text{NO}_3$ in the $3000 - 4000 \text{ cm}^{-1}$ region. Spectrum M is microcrystalline; spectrum C is single crystal.

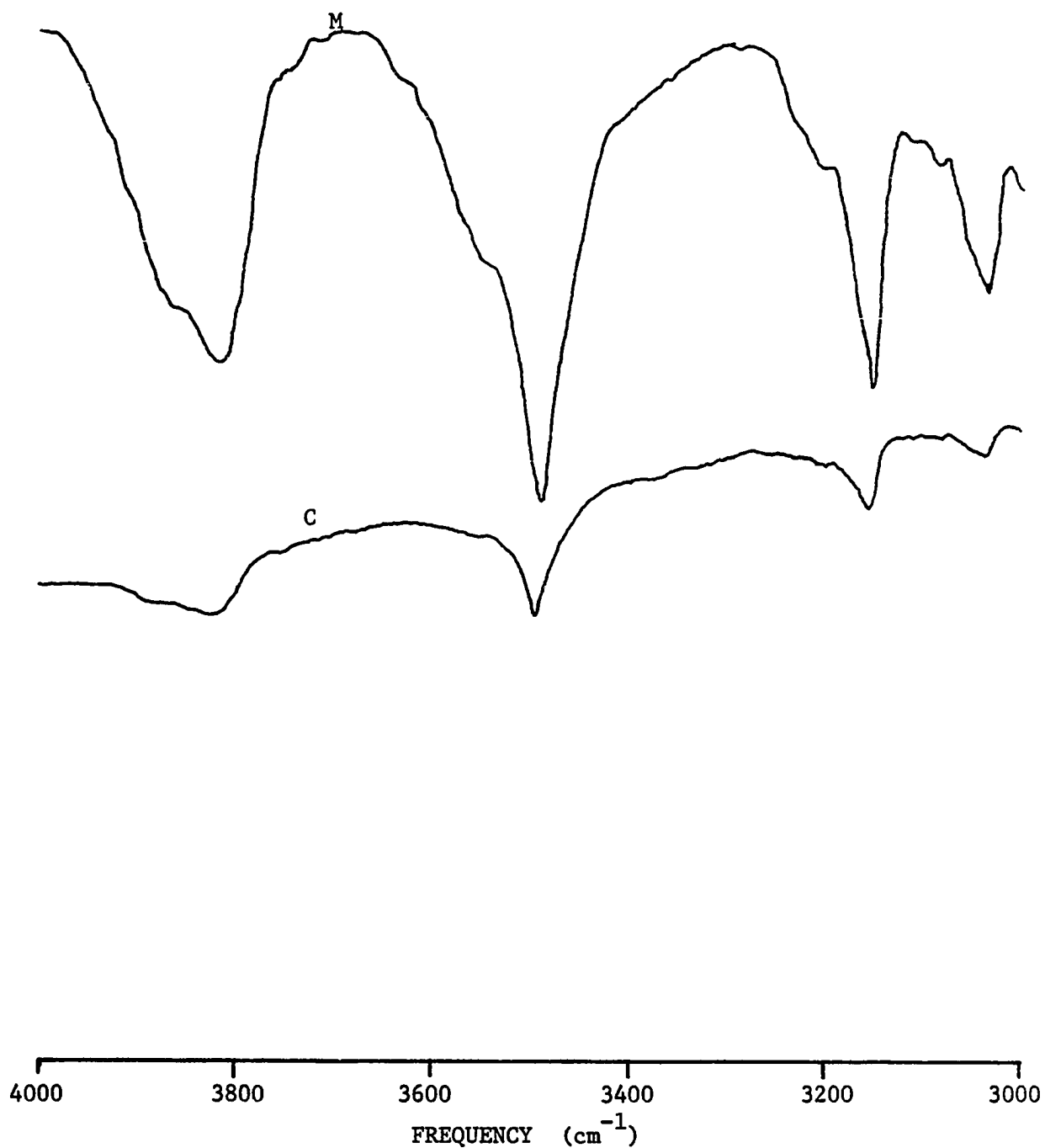


Figure (3-5a). Microcrystalline infrared reflectivity spectrum of $\text{Na}^{15}\text{NO}_3$ in the $700 - 1500 \text{ cm}^{-1}$ region.

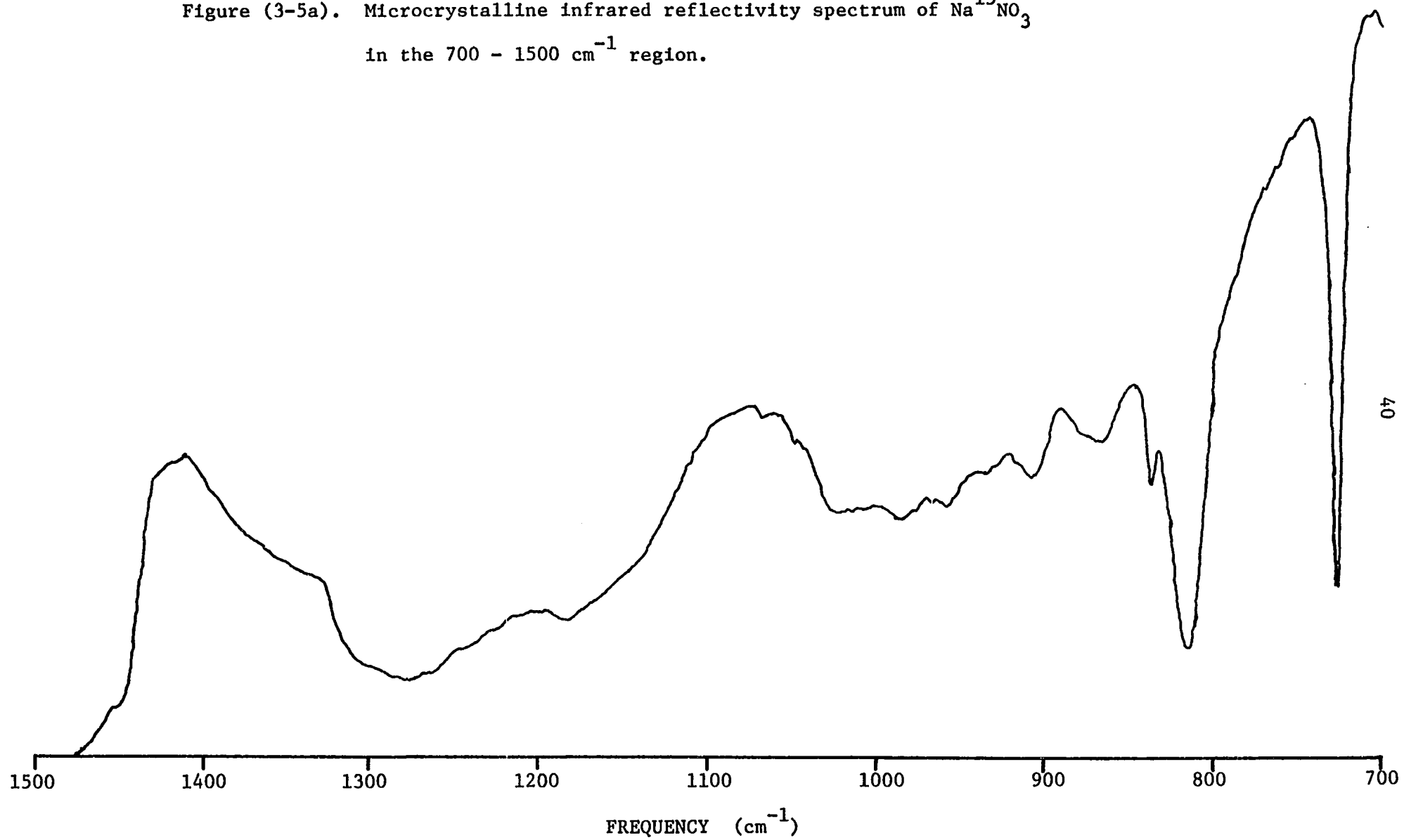


Figure (3-5b). Microcrystalline infrared reflectivity spectrum of $\text{Na}^{15}\text{NO}_3$ in the $1500 - 2600 \text{ cm}^{-1}$ region.

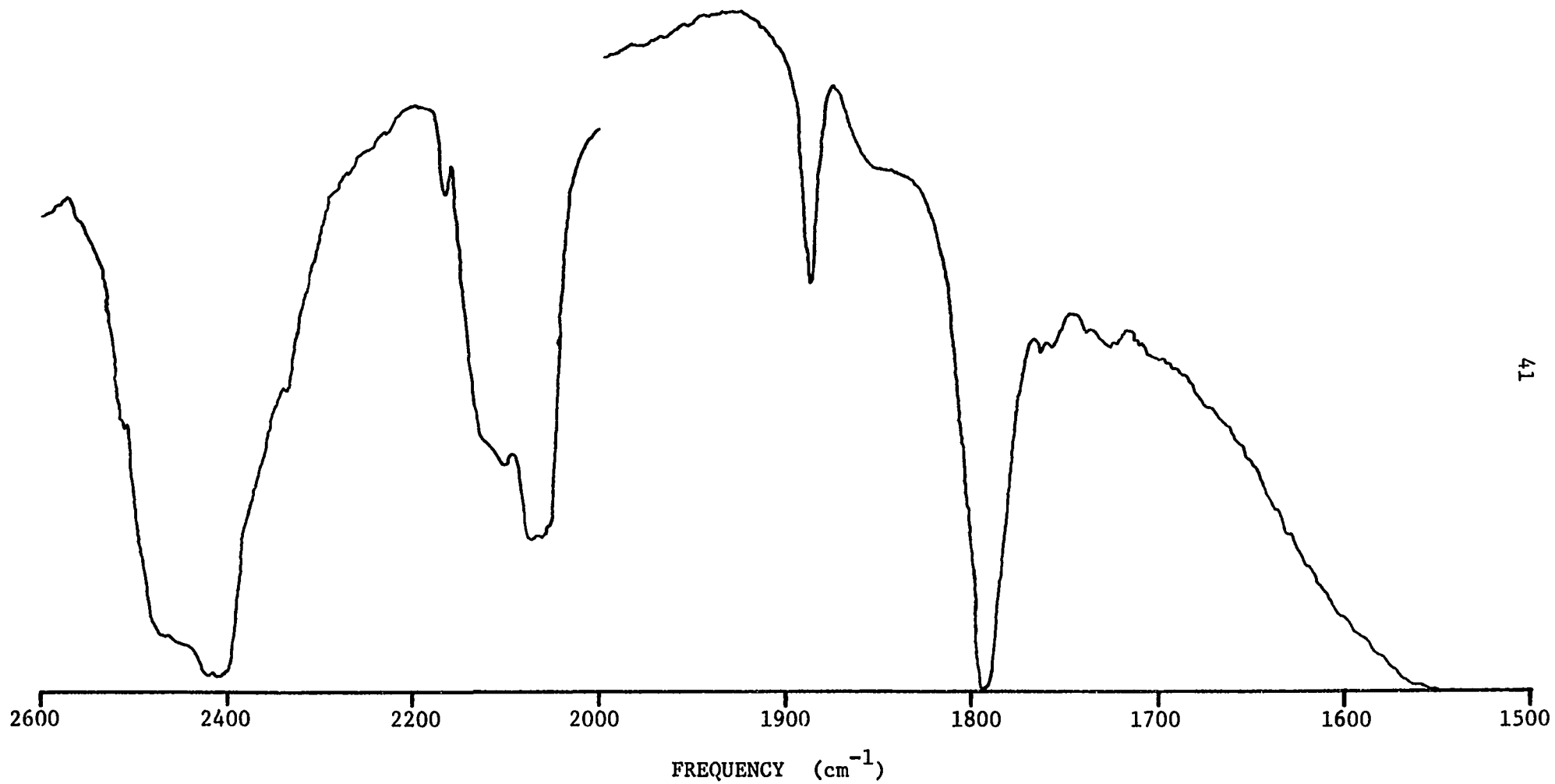


Figure (3-5c). Microcrystalline infrared reflectivity spectrum of $\text{Na}^{15}\text{NO}_3$ in the $2600 - 4000 \text{ cm}^{-1}$ region.

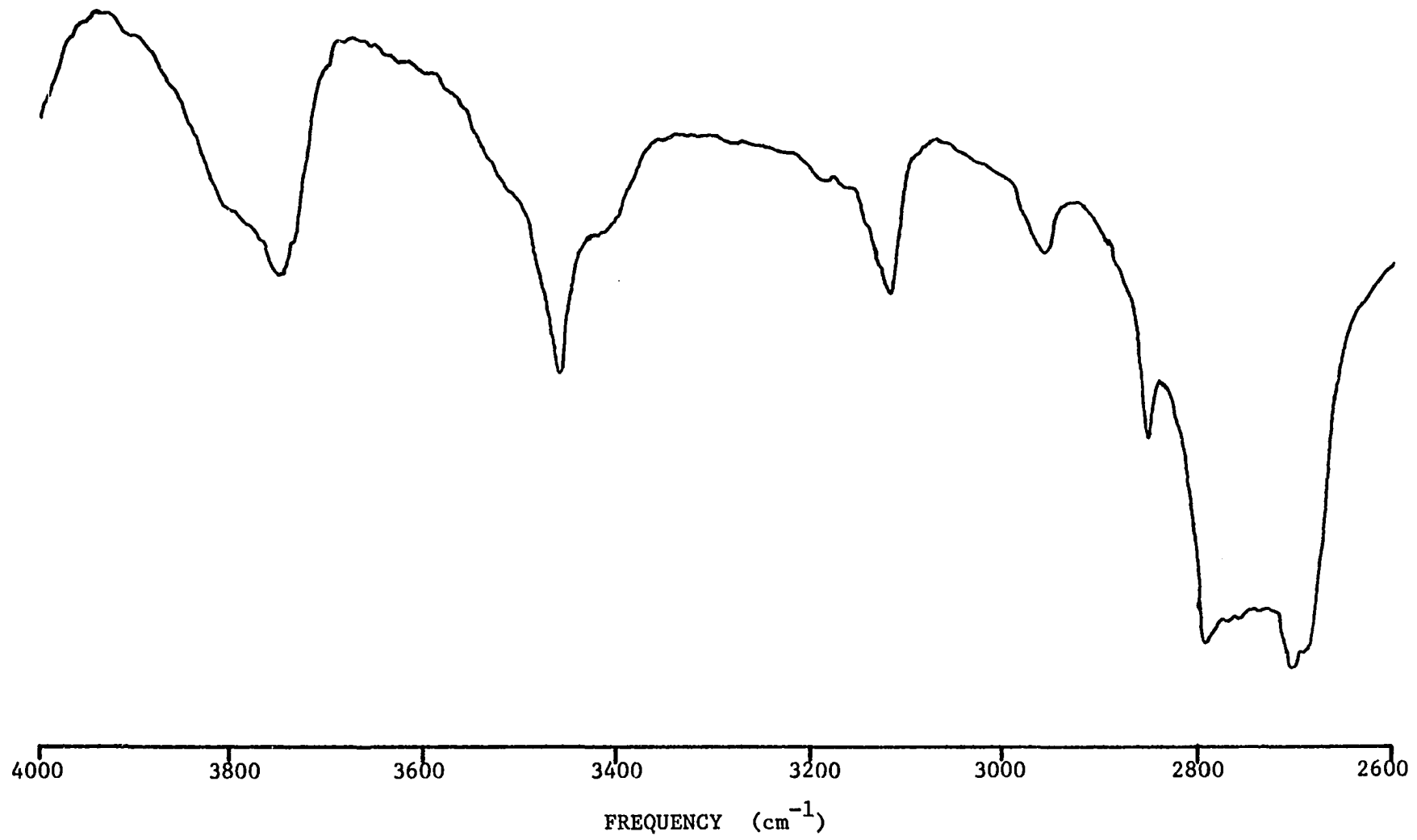


Figure (3-6a). Raman spectra of $\text{Na}^{14}\text{NO}_3$ and $\text{Na}^{15}\text{NO}_3$ single crystals in the $1430 - 1550 \text{ cm}^{-1}$ region.

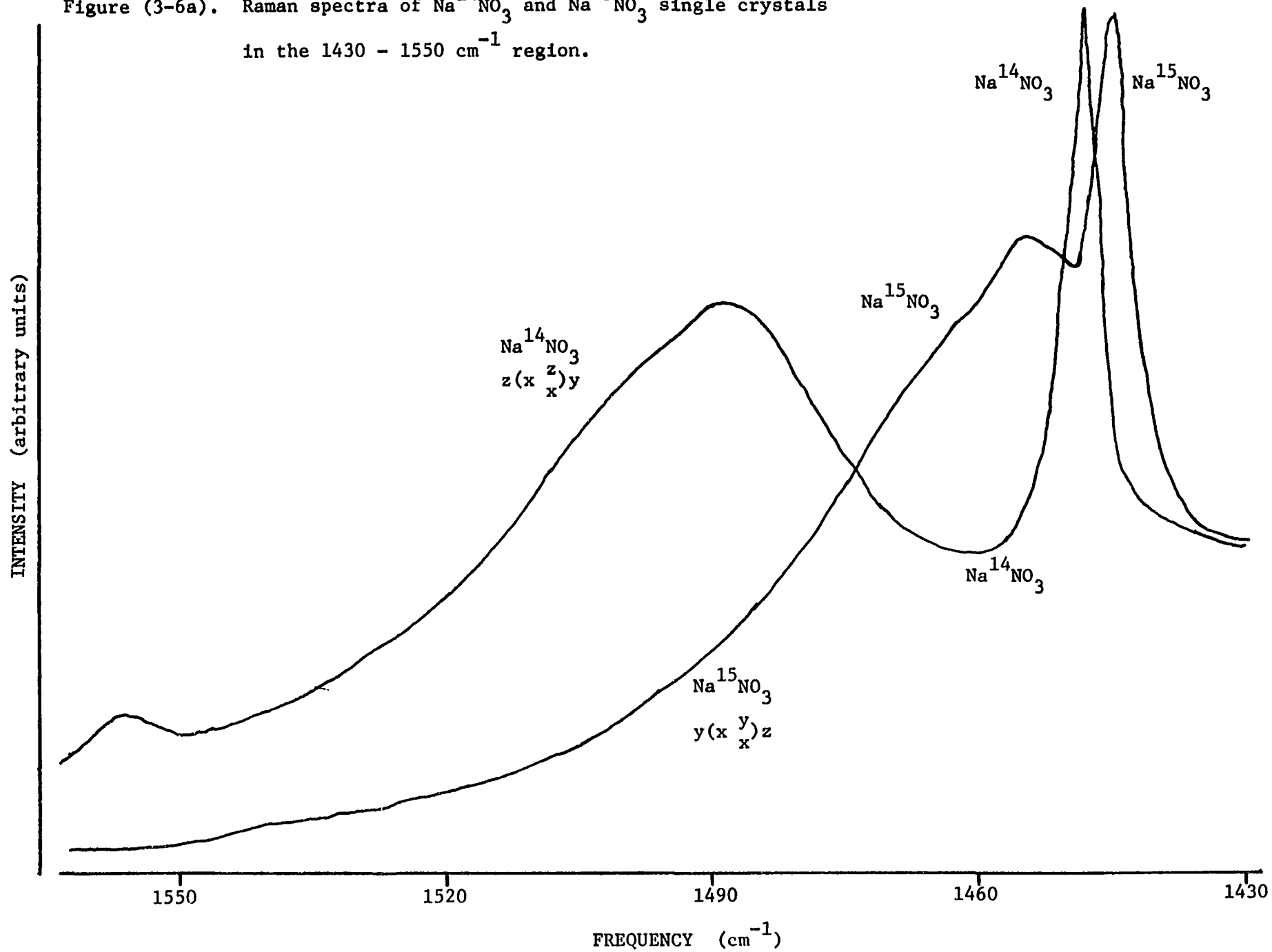


Figure (3-6b). Raman spectra of $\text{Na}^{14}\text{NO}_3$ and $\text{Na}^{15}\text{NO}_3$ in the $2\nu_2$ combination mode region.

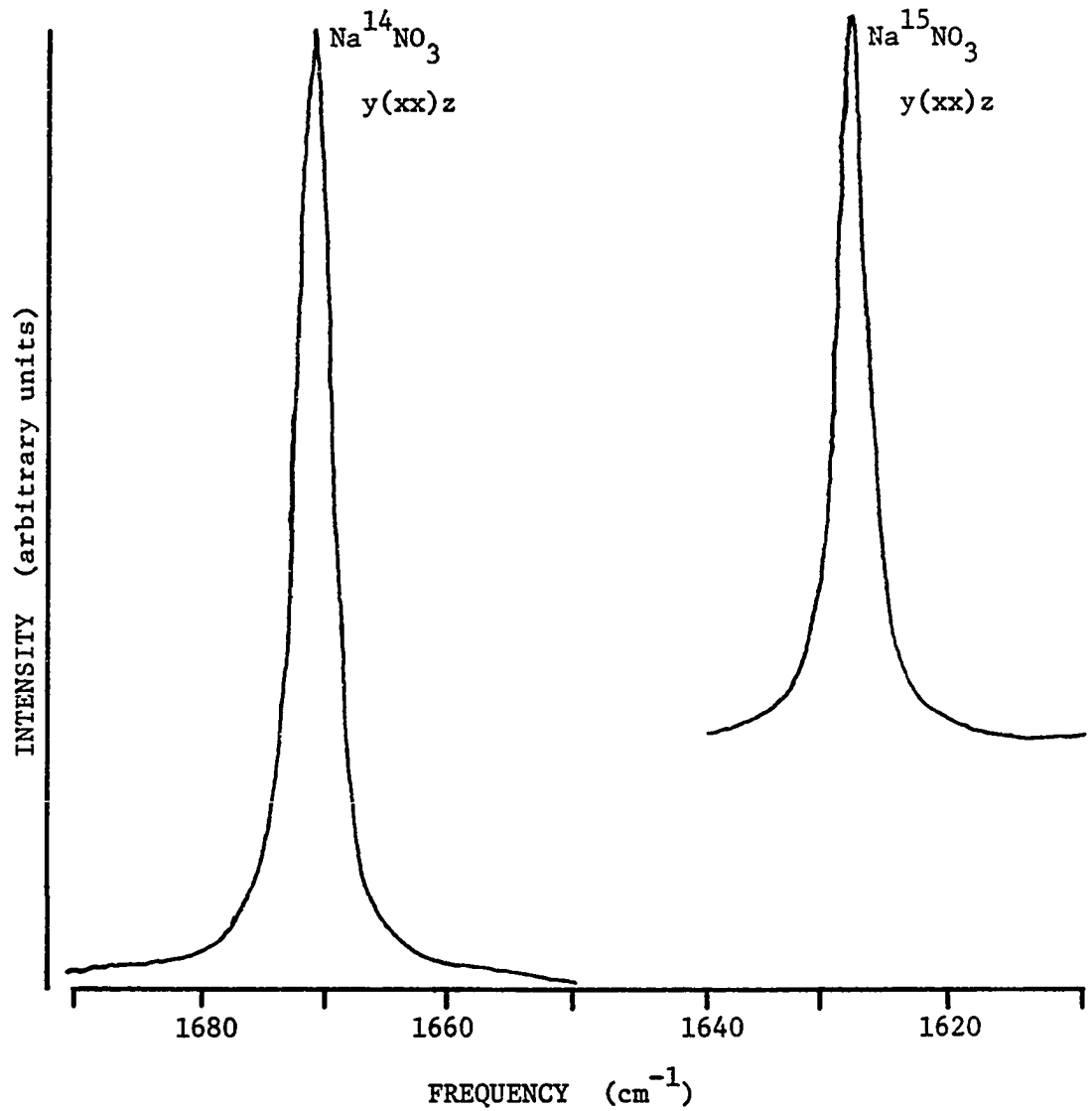


Figure (3-6c). Raman spectra of $\text{Na}^{14}\text{NO}_3$ and $\text{Na}^{15}\text{NO}_3$ single crystals in the 2050 - 2175 cm^{-1} region.

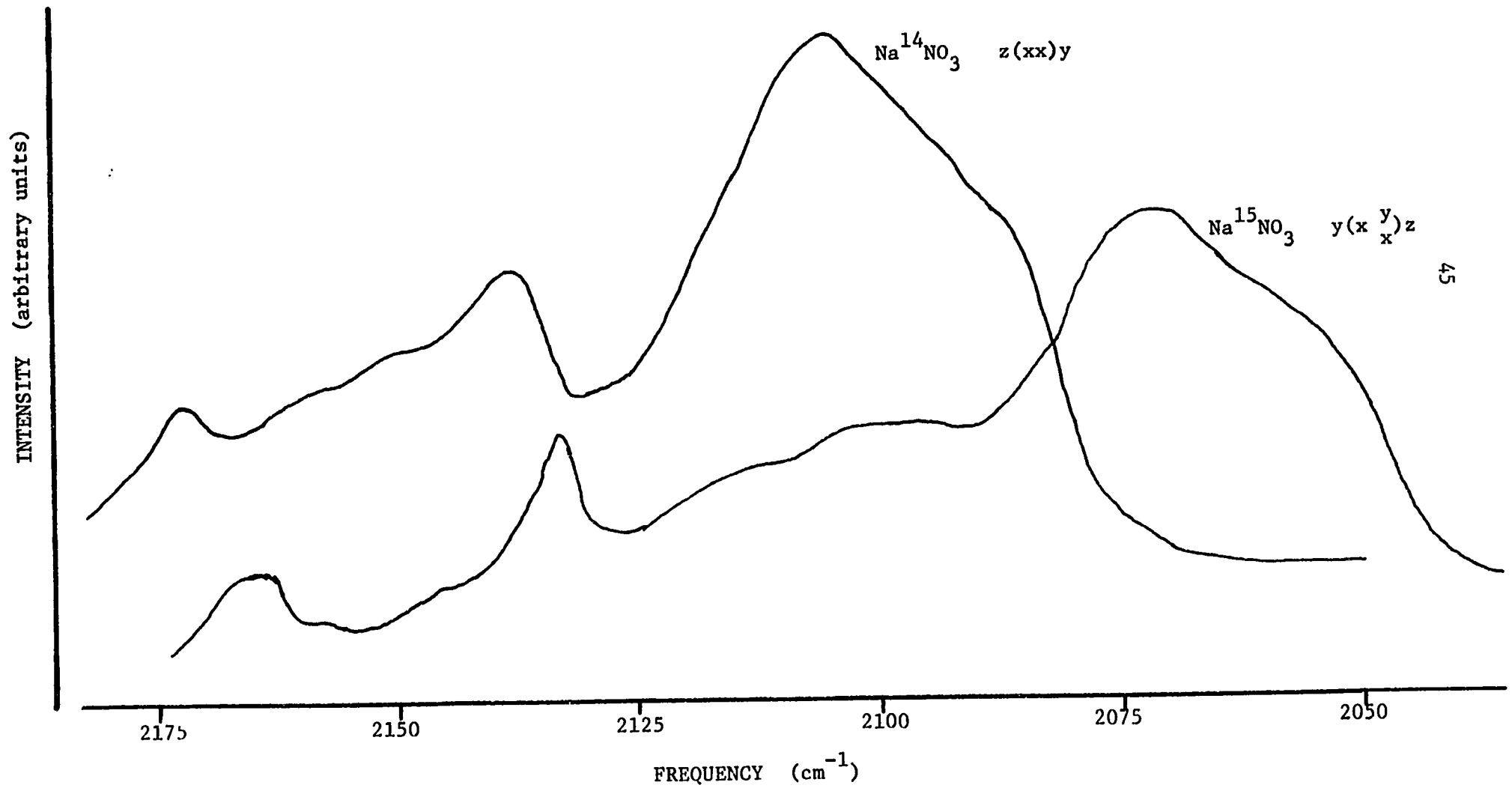


Table (3-1). Infrared active fundamental and combination mode frequencies for the internal optic modes of NaNO_3 . Frequencies are expressed in cm^{-1} .

Observed			Calculated			Assignments
^{14}N	^{15}N	$\Delta\nu$	^{14}N	^{15}N	$\Delta\nu$	
728	726	2				$\nu_4(\text{E}_u)$
837	813	24				$\nu_2(\text{A}_{2u})$
1068	1068	0				$\nu_1(\text{A}_{1u})^*$
1353	1323	30				$\nu_3(\text{E}_u)$
1450	1447	3	1452	1450	2	$\nu_4(\text{E}_u) + \nu_4(\text{E}_g)$
1795	1792	3	1796	1794	2	$\nu_4(\text{E}_u) + \nu_1(\text{A}_{1g})$
			1792	1792	0	$\nu_4(\text{E}_g) + \nu_1(\text{A}_{1u})$
1908	1886	22	1905	1881	24	$\nu_1(\text{A}_{1g}) + \nu_2(\text{A}_{2u})$
2096	2064	32	2077	2047	30	$\nu_3(\text{E}_u) + \nu_4(\text{E}_g)$
2134	2099	35	2114	2080	34	$\nu_3(\text{E}_g) + \nu_4(\text{E}_u)$
	2165			2174	2	$\nu_4(\text{E}_u) + 2\nu_4(\text{E}_g)$
2438	2410	28	2421	2391	30	$\nu_3(\text{E}_u) + \nu_1(\text{A}_{1g})$
	2509			2516		$\nu_1 + 2\nu_4$
2765	2703	62	2739	2677	62	$\nu_3(\text{E}_u) + \nu_3(\text{E}_g)$
2855	2791	64				

} due to critical points in two-phonon density of states

Table (3-1) cont.

Observed			Calculated			Assignments
^{14}N	^{15}N	$\Delta\nu$	^{14}N	^{15}N	$\Delta\nu$	
3036	2960	76	3027	2949	78	$\nu_3(\text{E}_u) + 2\nu_2$
3153	3120	33	3149	3117	32	$\nu_3(\text{E}_u) + \nu_1(\text{A}_{1u}) + \nu_4(\text{E}_u)$
			3145	3115	30	$\nu_3(\text{E}_u) + \nu_1(\text{A}_{1g}) + \nu_4(\text{E}_g)$
3491	3461	30	3489	3459	30	$\nu_3(\text{E}_u) + 2\nu_1$

* This mode is not infrared active. The frequency was taken from reference 1.

Table (3-2). Raman active fundamental and combination mode frequencies for the internal optic modes of NaNO_3 . Frequencies are expressed in cm^{-1} .

Observed			Calculated			Assignment
^{14}N	^{15}N	$\Delta\nu$	^{14}N	^{15}N	$\Delta\nu$	
724	724	0				$\nu_4(\text{E}_g)$
838	818	20				$\nu_2(\text{A}_{2g})^*$
1068	1068	0				$\nu_1(\text{A}_{1g})$
1386	1354	32				$\nu_3(\text{E}_g)$
			1448	1448	0	$2\nu_4(\text{E}_g)$
1448	1445	3	1456	1452	4	$2\nu_4(\text{E}_u)$
1671	1628	43	1674	1626	48	$2\nu_2$
2106	2073	33	2110	2078	32	$\nu_3(\text{E}_g) + \nu_4(\text{E}_g)$
2138	2134	4	2136	2136	0	$2\nu_1$
2172	2165	7	2180	2176	4	$2\nu_4(\text{E}_u) + \nu_4(\text{E}_g)$

* This mode is not Raman active. The frequency was taken from reference 1.

References for Chapter III

1. R. Eckhardt, D. Eggers, and L. J. Slutsky, *Spectrochimica Acta A* 26, 2033 (1970).
2. O. P. Maksimov, V. S. Gorelik, and M. M. Sushchinskii, *Fiz. Tverd. Tela* 17, 2827 (1975), translated in *Sov. Phys. Solid State* 17, 1892 (1976).
3. J. B. Bates, *Chem. Phys. Lett.* 22, 156 (1973).

CHAPTER IV

Abnormalities in the Infrared Reflection Spectra of Single Crystals Induced by Mechanical Surface Damage

Introduction

Grating ruled semiconductors produce reflectivity minima in the optic phonon T-L band gap which are found to be dependent upon the electric field polarization of the incident radiation. These minima are attributed to the excitation of surface plasmons. Marschall and co-workers have mapped the surface plasmon dispersion in InSb by varying the distance between grating lines and by varying the concentration of Te impurities.¹ The surfaces were diamond ruled and electron microscopy revealed that surface destruction was small compared to the grating spacing. Anderson and co-workers studied the same system but ruled the surface by spark cutting which produced reflectivity minima which were not dependent upon the electric field polarization of the incident radiation.² Spark cutting involves bombarding the sample with ~300ev electrons which generates enough heat to vaporize the InSb. After etching the semiconductor surface the authors observed that the reflectivity spectrum was identical to the spectrum before ruling. They argued that the spark cutting method produced a damage layer which was removed by etching. The presence of grating rules after etching played no important role in the reflectivity spectra.

In the course of this study it was observed that the reflectivity spectra which were obtained depended rather significantly on the method of

sample preparation. In particular, some of the spectra displayed a rather shallow and broad reflectivity minimum in the transverse-longitudinal band gap in samples with poorly prepared surfaces. The shape of the reflectivity curves suggested the presence of surface damage resulting in microcrystalline fragments either adsorbed on the surface or perhaps trapped in scratches on the surface. This was checked by deliberately damaging the surfaces of well characterized crystals of $\text{Na}^{14}\text{NO}_3$, $\text{Na}^{15}\text{NO}_3$, and KBrO_3 and then repolishing in successive stages while monitoring the polarized infrared reflectivity.

Experimental

NaNO_3 crystals were easily grown by slow evaporation from aqueous solution at room temperature. Many attempts were made to grow KBrO_3 single crystals from aqueous solution. Slow evaporation using twice recrystallized Analar Analytical grade KBrO_3 produced small clear crystals. A convection method was used to produce cloudy rhombohedral crystals 2-3mm along an edge. Larger irregular shaped crystals were grown by the addition of sodium nitrate to the solution. The addition of approximately 5 grams/liter of HNO_3 as suggested by Haussühl³ produced clear rhombohedral crystals 3-5mm along an edge. The solution was prepared in an Erlenmeyer flask with a ground glass stopper and placed in a water bath at 40°C. Evaporation took place by condensed water leaching between the ungreased ground glass joints.

Microcrystalline samples were prepared by grinding the material in an agate mortar and pressing the powder into a slot in a metal plate using hand pressure.

Infrared reflection spectra were recorded at room temperature on a

Beckman IR-12 spectrometer with an average angle of incidence of 15° and a 4:1 linear image reduction. Raman spectra were obtained on a Spex Ramalog 5 spectrometer equipped with a 2 watt argon ion laser.



Crystals of $\text{Na}^{14}\text{NO}_3$ and $\text{Na}^{15}\text{NO}_3$ were prepared by grinding on #600 emery paper to expose a face containing the optic axis. The $\text{Na}^{15}\text{NO}_3$ crystal was further polished on a frosted glass plate using no solvent and the infrared reflection spectra were recorded after successive repolishing on the frosted glass plate. An unusual reflectivity minimum was found in the $\nu_3(\text{E}_u)$ spectral region and changed with successive repolishing in the order 1, 2, 3, etc. as indicated in figure (4-1). Infrared reflection spectra for the $\text{Na}^{14}\text{NO}_3$ crystal shown in figure (4-2) were obtained in a similar manner with the exception that spectrum 1 was recorded after grinding on emery paper but before polishing on frosted glass and spectrum 4 after polishing on lens paper dampened with water which produced a very smooth, clean surface.

The spectrum labeled 1 of figure (4-2) resembles that obtained from the near normal incidence reflectivity of a microcrystalline powder shown in figure (4-3). It is apparent from figure (4-4) that polarization parallel to the optic axis cannot eliminate the reflectivity of $\nu_3(\text{E}_u)$ from a mechanically damaged surface, suggesting that the surface contains microcrystalline fragments exposing crystal faces other than the particular bulk crystal face to the incident beam. Polishing on damp lens paper dissolves the microcrystals yielding spectrum number 4 in both figures (4-2) and (4-4) which is the expected behavior of the $\nu_3(\text{E}_u)$ reflectivity band.

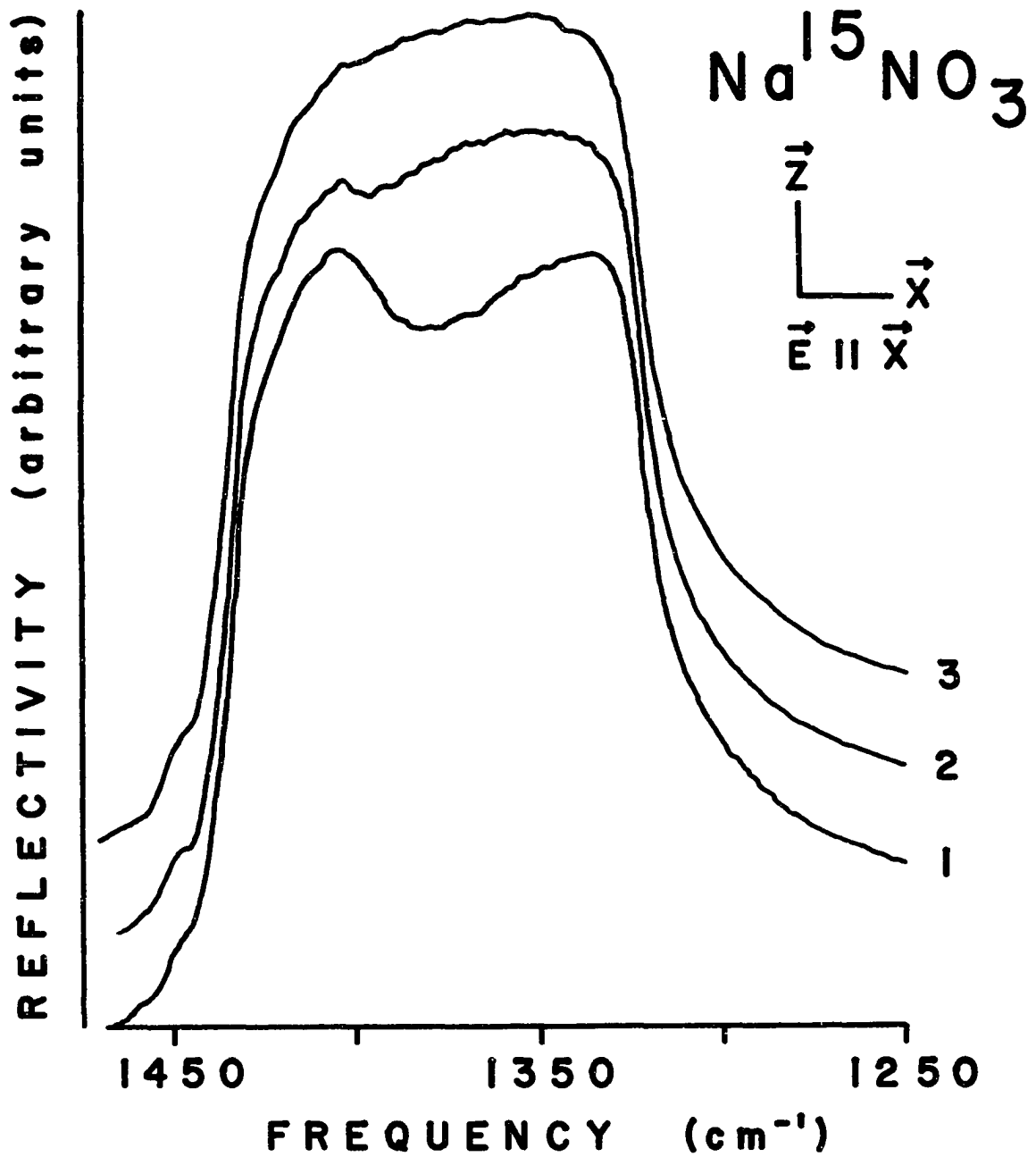


Figure (4-1). Near normal incidence infrared reflectivity spectra of $\text{Na}^{15}\text{NO}_3$ with successive repolishing in the order 1, 2, 3. The optic axis is parallel to z .

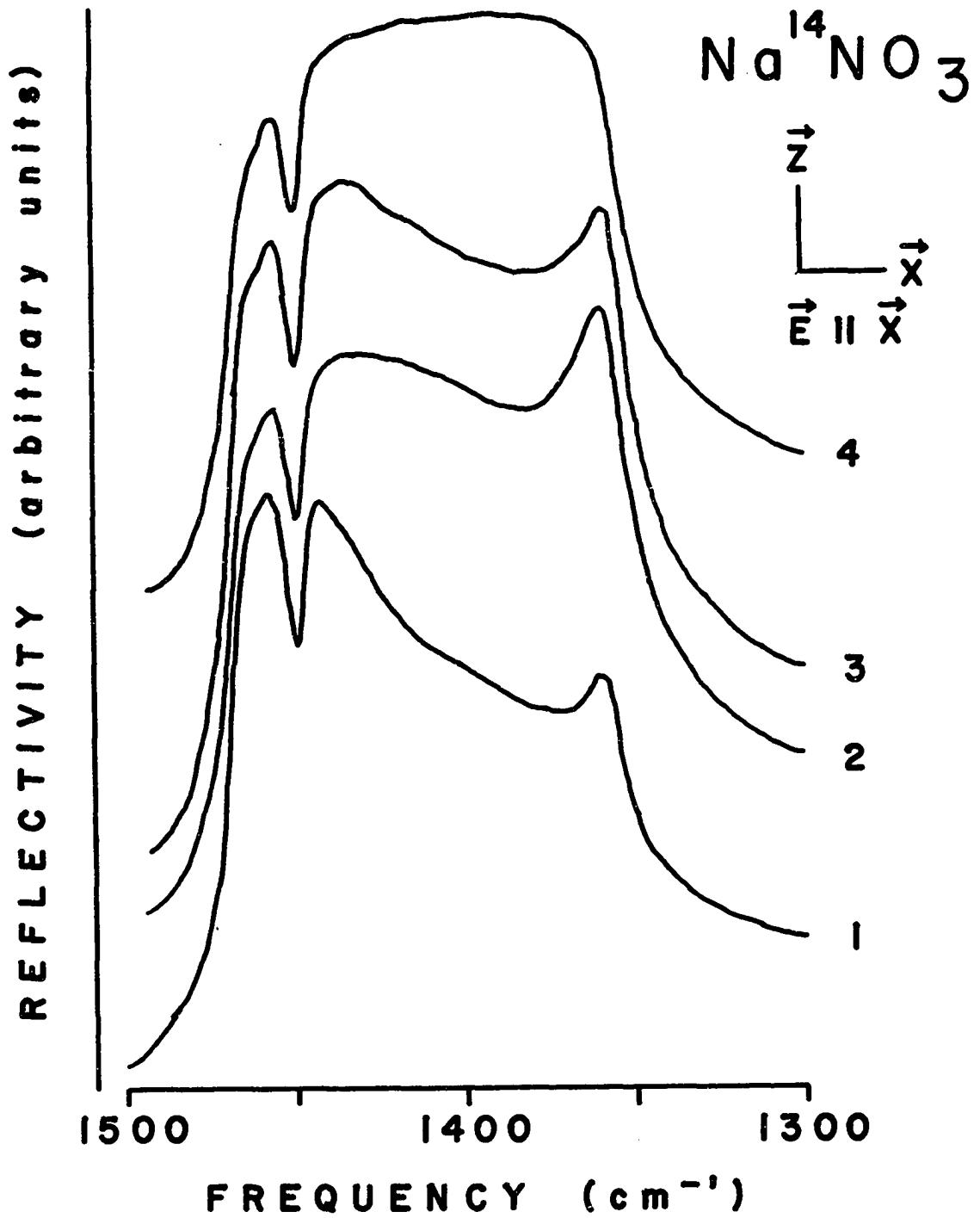


Figure (4-2). Near normal incidence infrared reflectivity spectra of $\text{Na}^{14}\text{NO}_3$ with successive repolishing in the order 1, 2, 3, 4. The optic axis is parallel to z

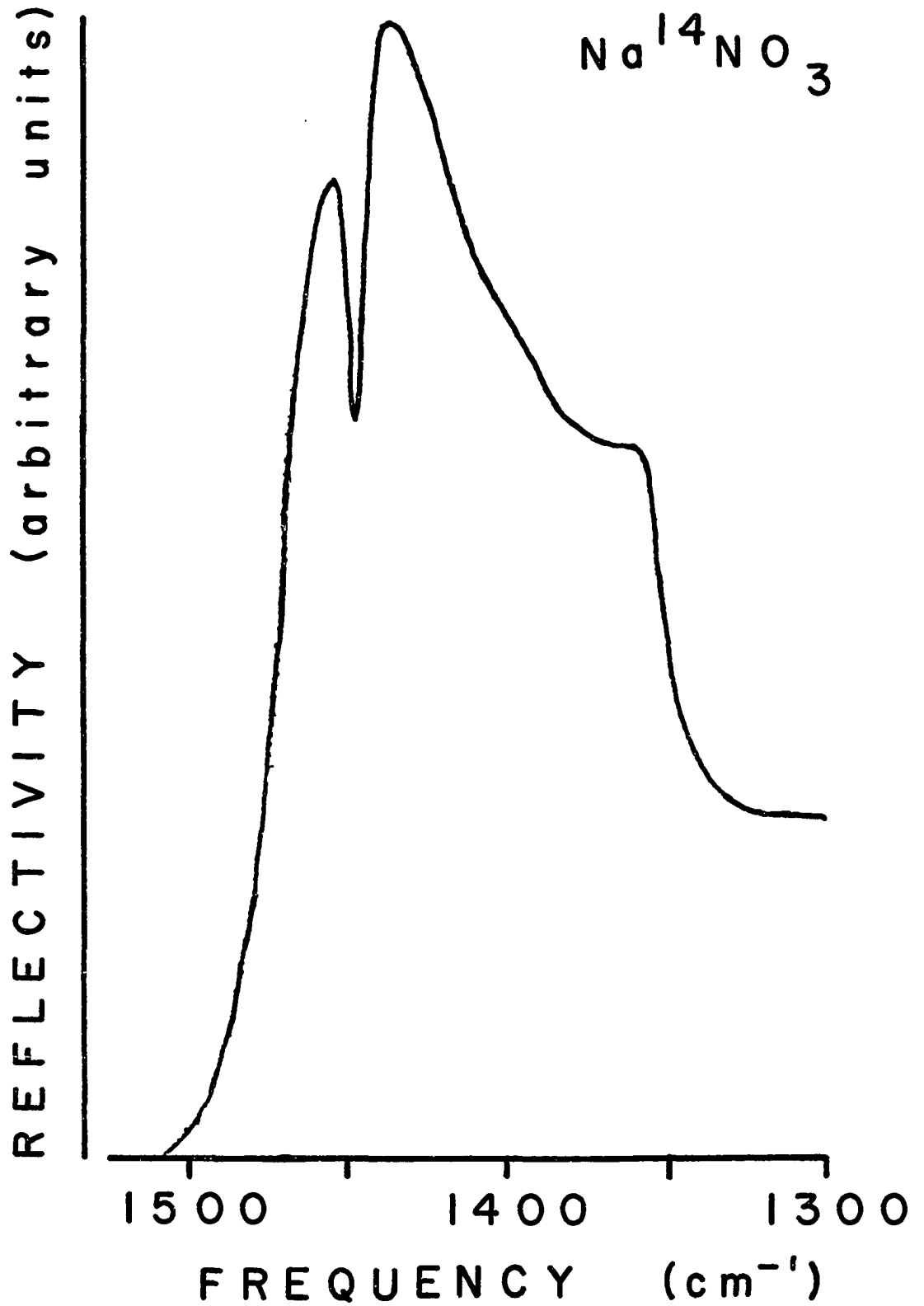


Figure (4-3). Near normal incidence infrared reflectivity spectrum of microcrystalline $\text{Na}^{14}\text{NO}_3$ in the ν_3 spectral region.

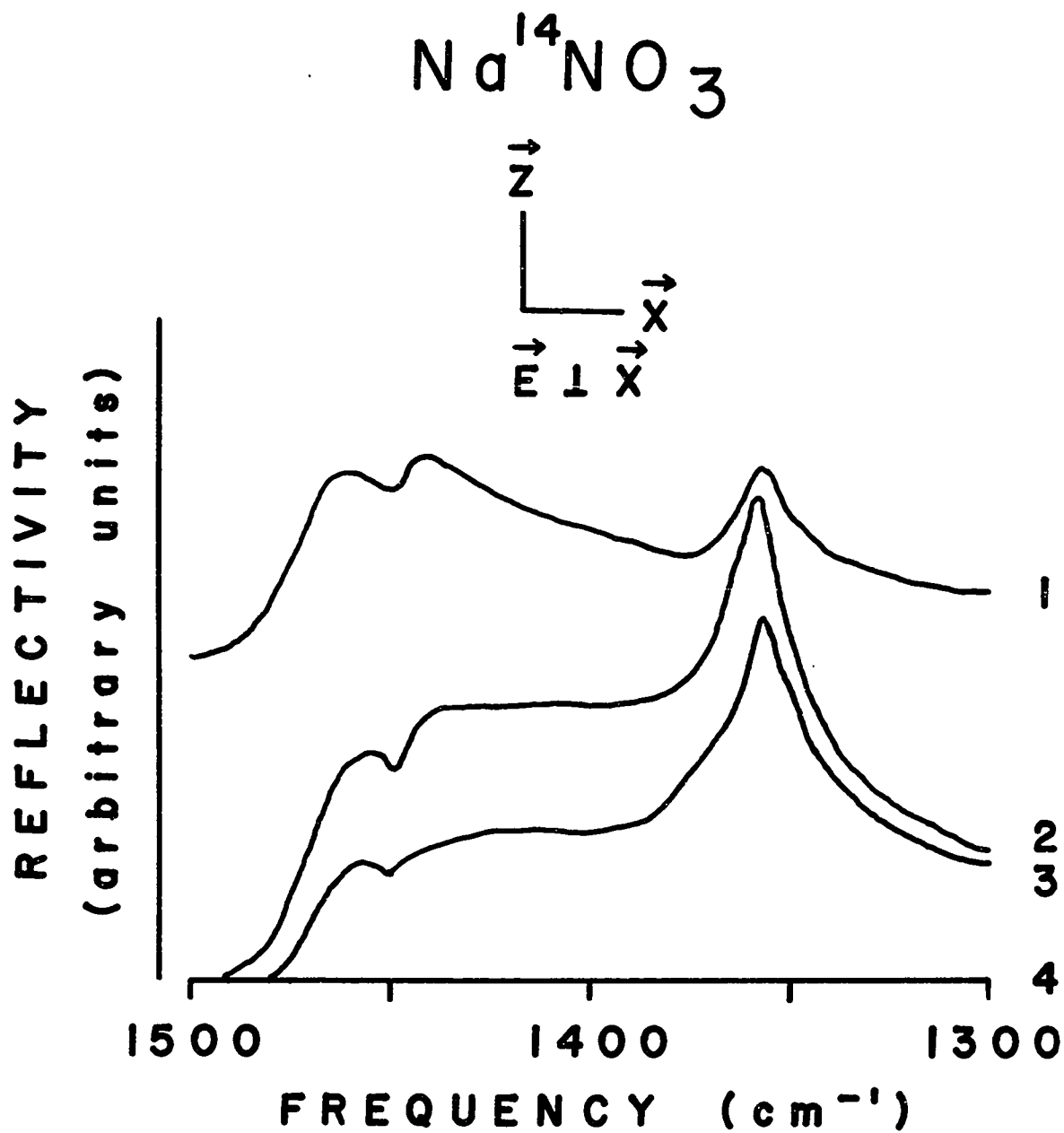


Figure (4-4). Near normal incidence infrared reflectivity spectra of $\text{Na}^{14}\text{NO}_3$ with successive repolishing in the order 1, 2, 3, 4. The optic axis is parallel to z

KBrO₃

Potassium bromate (KBrO₃) belongs to space group C_{3v}⁵ (R3m) with one molecule per rhombohedral unit cell. Both the potassium ion and the bromine atom occupy sites of C_{3v} symmetry.⁴ The correlation diagram of figure (4-5) shows that there is no site group or factor group splitting and all internal optic modes are simultaneously infrared and Raman active.

Polarized infrared reflection and Raman spectra were reported for KBrO₃ by Unger and co-workers in a study of the angular dispersion of polar phonons.⁵ No abnormal reflectivity minima were found in the ν₃(E) T-L band gap as with the ν₃(E_u) mode of Na¹⁴NO₃ (see chapter II) although the infrared active combination mode ν₂(A₁) + ν₄(E) should occur in this region. It is possible that the dispersion of the ν₂(A₁) + ν₄(E) combination mode is so broad that its effect would be a general raising or lowering of the reflectivity in the ν₃(E) region rather than creating a pronounced dip as observed in Na¹⁴NO₃. Another possibility is that the intensity of the combination mode is so weak that it produces no observable effect in the ν₃(E) spectral region.

As the crystals used in this study were grown with the presence of NO₃⁻ ion in solution an attempt was made to check the crystals for the presence of NO₃⁻ as an impurity. A small crystal was ground in an agate mortar with KBr and the infrared transmission spectrum of a pressed pellet was obtained. No absorption bands were found for the NO₃⁻ ion, however, it was observed that BrO₃⁻ reacted in the KBr matrix producing a time dependent change in the BrO₃⁻ spectrum. The ν₂(A₁) mode was found to undergo the most drastic change and the behavior of this mode was further investigated. Initial spectra revealed one mode at 431cm⁻¹ which



Figure (4-5). Vibrational correlation diagram for KBrO₃

POINT GROUP	C _{3v}	C _{3v}	C _{3v}	VIBRATIONS
SITE GROUP	C _{3v}	C _{3v}	C _{3v}	FACTORS
GROUP	C _{3v}	C _{3v}	C _{3v}	GROUP
ν_1, ν_2	A ₁	A ₁	A ₁	z, zz, xx + yy
	A ₂	A ₂	A ₂	
ν_3, ν_4	E	E	E	(x, y), (yz, zx) (xx - yy, xy)

decreased in intensity while new modes at 445 and 454cm^{-1} appeared and increased in intensity with time as shown in figure (4-6). The mode at 454cm^{-1} gradually became less pronounced and in later stages merged with the 445cm^{-1} mode to give it an asymmetric appearance. A small peak was also observed to appear at 417cm^{-1} after several hours. The process could not be reversed by repressing the pellet or by regrinding the pellet before repressing as shown in figure (4-7).

Using the peak heights at 445 and 431cm^{-1} as a measure of the respective relative intensities the reaction did not seem to obey simple zero, first, or second order kinetics although for times less than 30 minutes the 431cm^{-1} mode appeared to be second order. As it is not the purpose of this work to study the chemistry of the $\text{BrO}_3^- - \text{Br}^-$ system no attempts were made to assign the modes or to refine the kinetic data.

Figure (4-8) shows the polarized infrared reflection spectrum of KBrO_3 from a crystal face containing the optic axis. Raman frequencies are presented in table (4-1) along with the calculated values of the static crystal field frequencies, ω_0 , and dipole moment derivatives, $|\partial\mu/\partial q|$, using a molecular dipole model.⁶⁻¹⁰ The Raman frequencies agree with those obtained by Unger and Haussühl,⁵ as does the infrared reflection spectrum.

The infrared reflection spectra of figures (4-9) & (4-10) were obtained using a natural rhombohedral face with the surface prepared as follows:

Spectrum #	Preparation
1	no polishing
2	brief polishing on #500 emery paper to damage the surface
3	brief polishing on #600 emery paper
4	polishing for a few minutes on frosted glass using no solvent

<u>Spectrum #</u>	<u>Preparation</u>	(continued)
5	further polishing for a few minutes on frosted glass using no solvent	
6	polishing for a few minutes on frosted glass using ethanol as a solvent	
7	further polishing for a few minutes on frosted glass using ethanol as a solvent	
8	polishing on lens paper for a few minutes using ethanol as a solvent	
9	polishing for a few seconds on lens paper using a small amount of water as a solvent	
10	further polishing on lens paper for a few seconds using a small amount of water as a solvent	

An experimental reflection geometry with the electric field polarized perpendicular to the plane containing the optic axis should produce a pure $\nu_3(E)$ reflectivity spectrum while polarization parallel to the plane containing the optic axis should reveal the $\nu_1(A_1)$ mode and an oblique phonon of $\nu_3(E)$. This has been described in chapter I and is seen in the spectra labeled 1 of figures (4-9) & (4-10). Spectra 2-8 show that for a mechanically damaged surface the $\nu_1(A_1)$ mode is observed in the ordinary ray reflectivity at 790cm^{-1} in figure (4-9) and new features are observed at 781 and 814cm^{-1} in the extraordinary ray reflectivity shown in figure (4-10).

Assuming the $\nu_2(A_1) + \nu_4(E)$ combination mode frequency may be obtained by adding transverse frequency components, the $\nu_2(A_1) + \nu_4(E)$ combination mode dispersion may range from 777cm^{-1} to 820cm^{-1} using frequencies taken from table (4-1). The feature at 781cm^{-1} may be due to the $\nu_3(E)$ transverse mode or to the $\nu_2(A_1) + \nu_4(E)$ combination mode. The feature at 814cm^{-1} may also be due to the $\nu_2(A_1) + \nu_4(E)$ combination mode. The intensity of the

features at 781 and 814cm^{-1} decreased as the crystal was further polished which is expected if microcrystalline fragments are being removed. Final polishing on lens paper using water as a solvent dissolves the microcrystals leaving a very smooth surface and the expected ordinary and extraordinary ray reflectivity of spectrum 10 in figures (4- 9) & (4-10) is obtained.

Gamma irradiation produces fragments of BrO_3^- ions and scatters them throughout the crystal creating a bulk crystal disorder. Figure (4-11) shows the ordinary ray reflectivity spectra for KBrO_3 before and after being irradiated with gamma rays for 44 hours in a 15000 curie source. The bulk crystal damage was sufficient to change the crystal from colorless to brown, however, the surface appeared very smooth to the naked eye. As the two spectra appear to be identical the indication is that all the aforementioned irregularities are apparently surface related.

Table (4-1). Table of Raman frequencies, static crystal field frequencies, and dipole moment derivatives for KBrO_3 , where ω_T is the transverse frequency, ω_L is the longitudinal frequency, ω_o is the static crystal field frequency, and $|\partial\mu/\partial q|$ is the dipole moment derivative.

Mode	$\omega_T(\text{cm}^{-1})$	$\omega_L(\text{cm}^{-1})$	$\omega_o(\text{cm}^{-1})$	$ \partial\mu/\partial q (\text{cm}^{3/2}\text{sec}^{-1})$
ν_1	792	803	798	67.9
ν_2	419	450	438	84.1
ν_3	778	840	814	163
ν_4	358	370	365	48.1

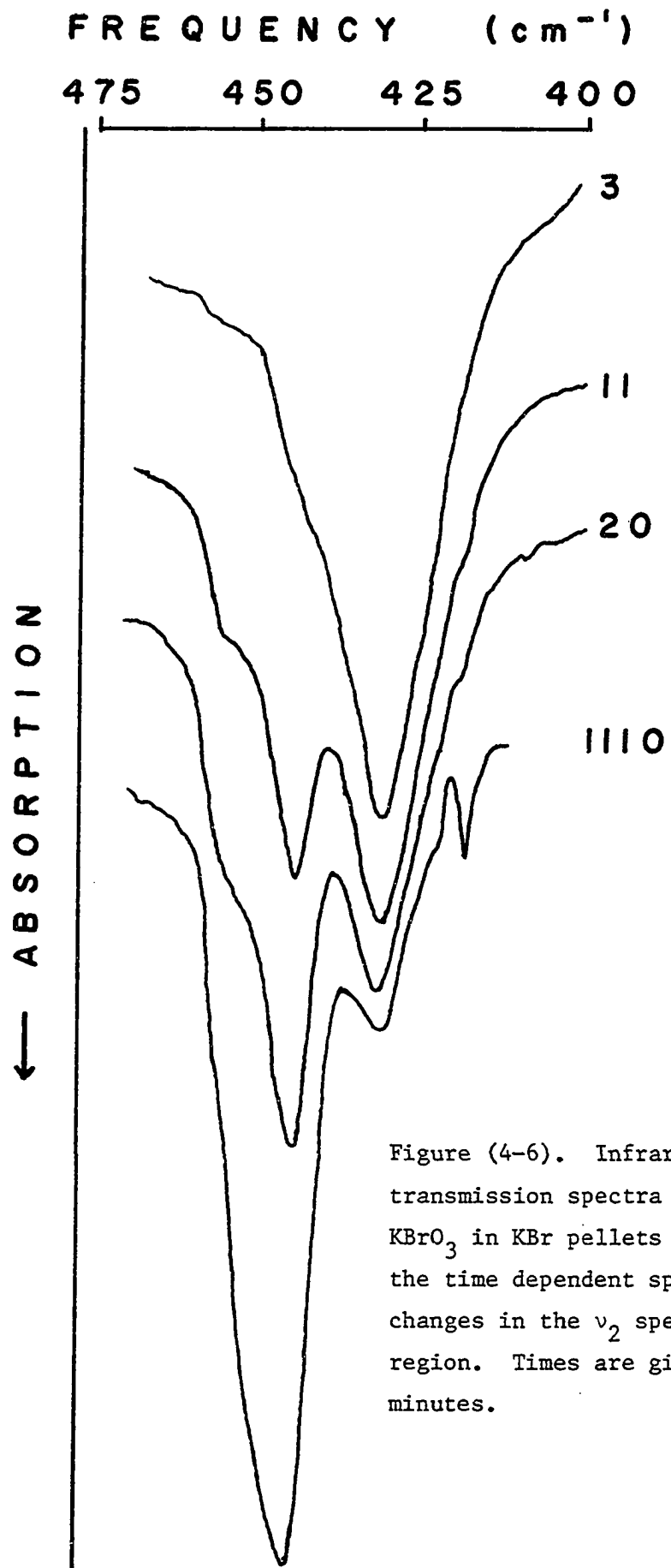
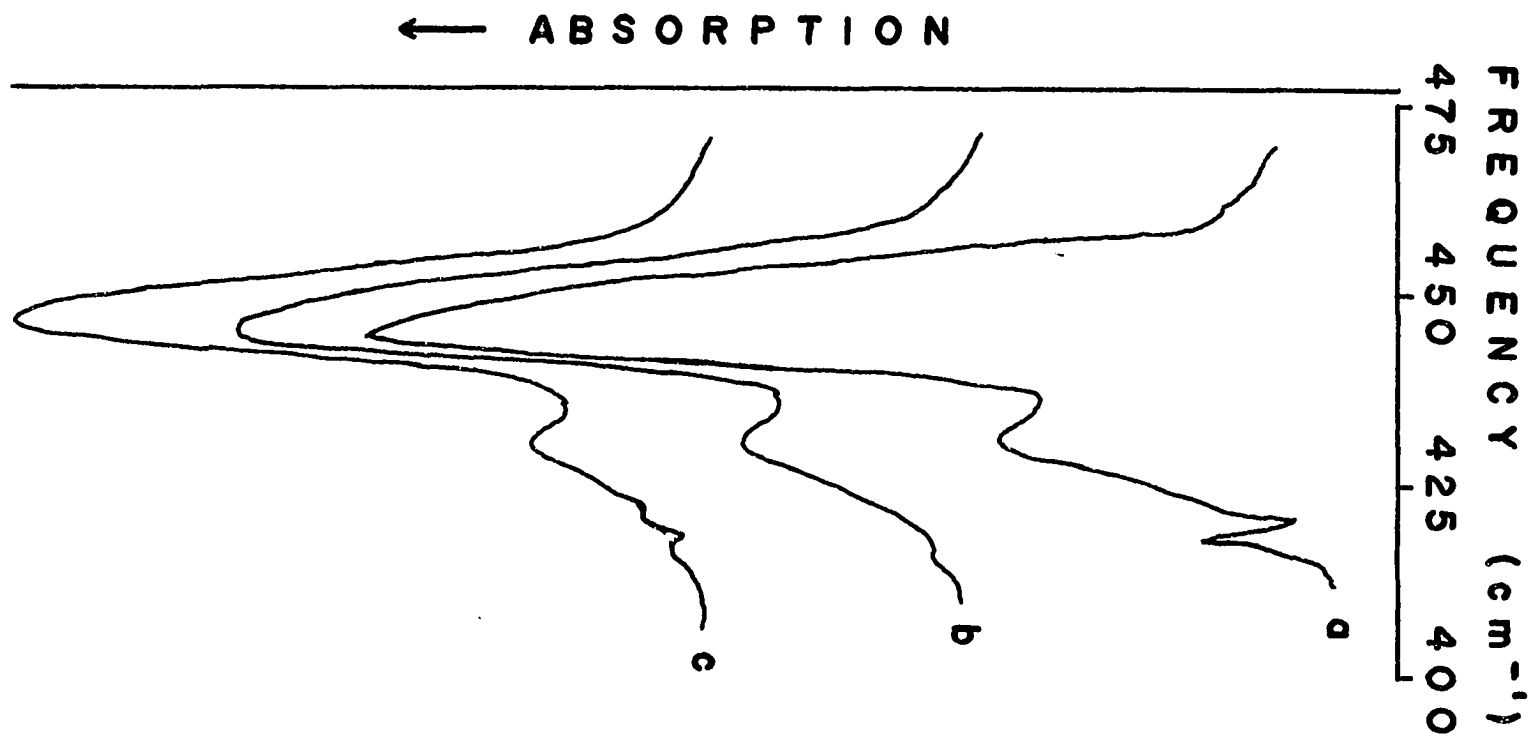


Figure (4-6). Infrared transmission spectra of KBrO_3 in KBr pellets showing the time dependent spectral changes in the ν_2 spectral region. Times are given in minutes.

Figure (4-7). Infrared transmission spectra of KBrO_3 in KBr pellets showing the effect of repressing and regrinding. Spectrum a is a pellet aged for 1110 minutes. Spectrum b is this same pellet after repressing. Spectrum c is this same pellet after regrinding and repressing.



INFRARED REFLECTION SPECTRA OF KBrO_3

Figure (4-8). Polarized near normal incidence infrared reflectivity spectrum of a KBrO_3 single crystal. The optic axis is parallel to z

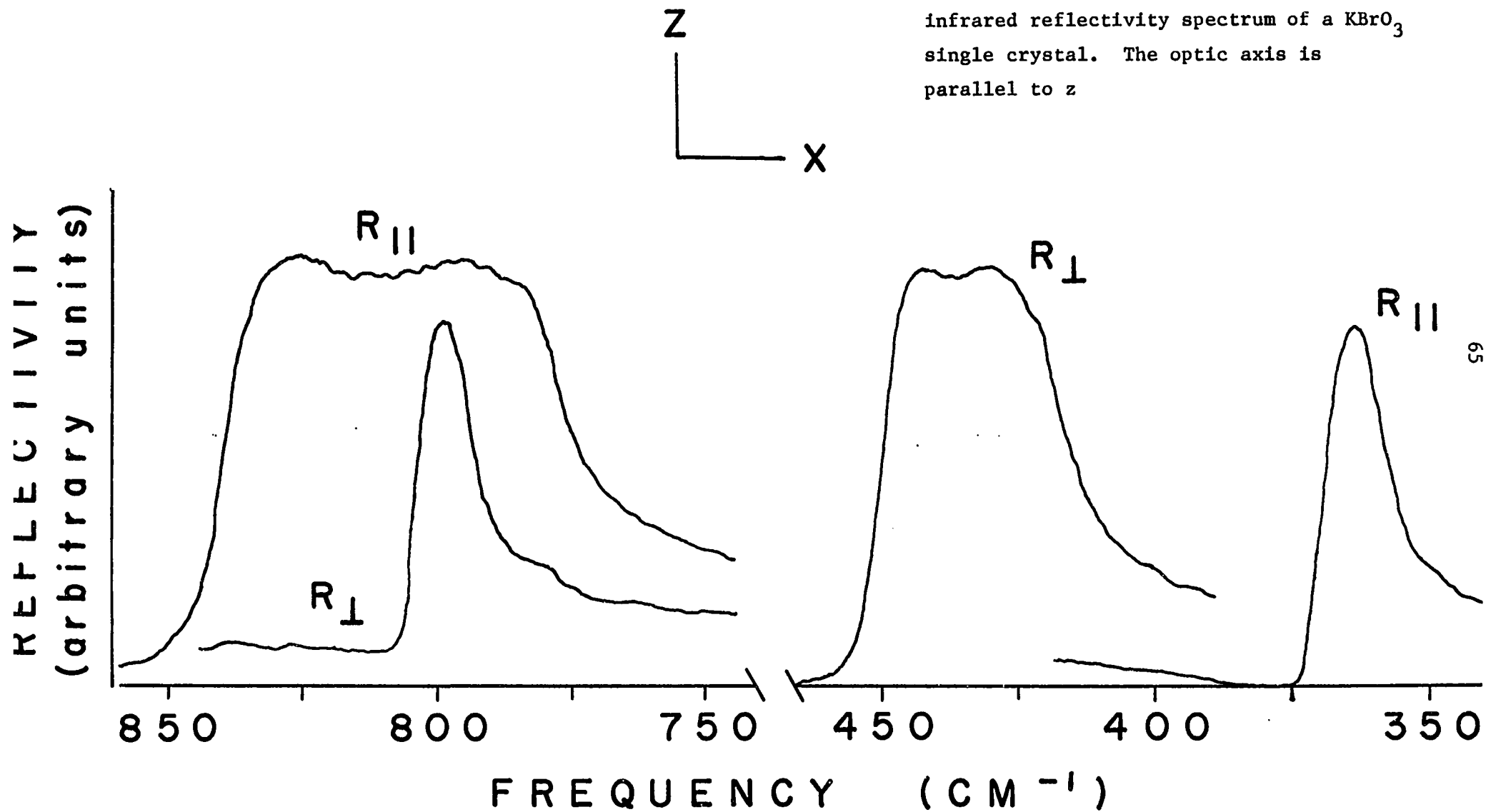
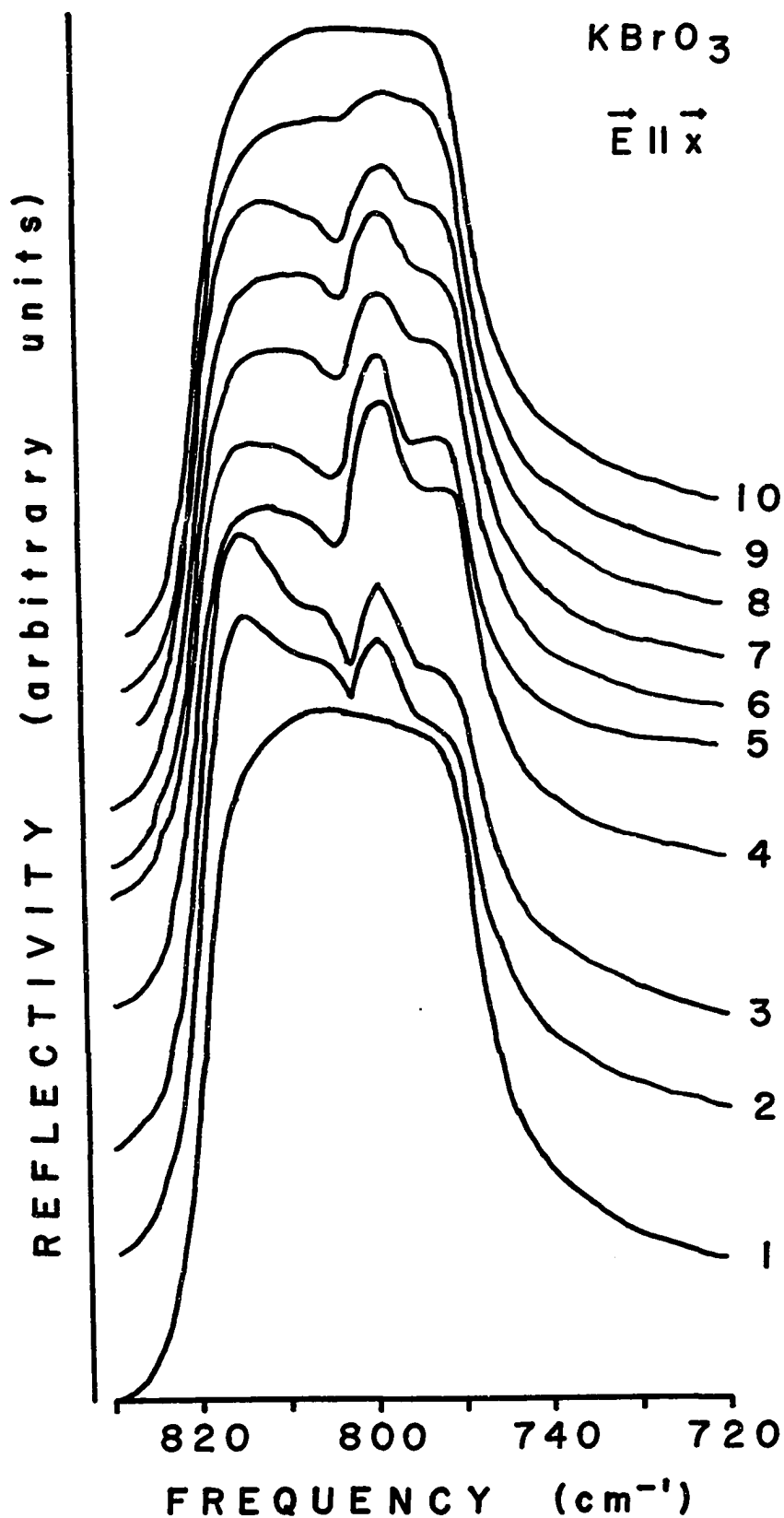


Figure (4-9). Polarized near normal incidence infrared reflectivity spectra of KBrO_3 showing the effects of successive repolishing in the order 1, 2, 3, ... A natural rhombohedral crystal face was used with the optic axis in the plane perpendicular to x .



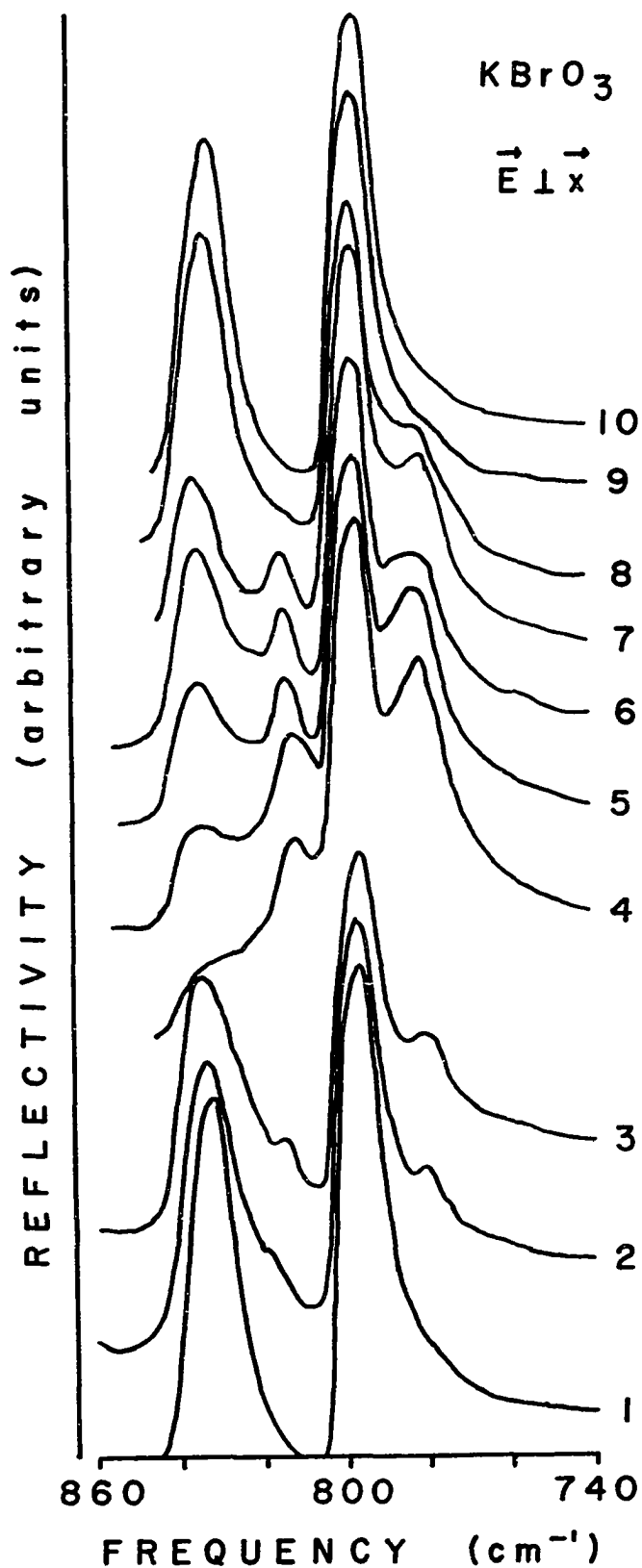


Figure (4-10). Polarized near normal incidence infrared reflectivity spectra of KBrO₃ showing the effects of successive repolishing in the order 1, 2, 3, ... A natural rhombohedral crystal face was used with the optic axis in the plane perpendicular to x.

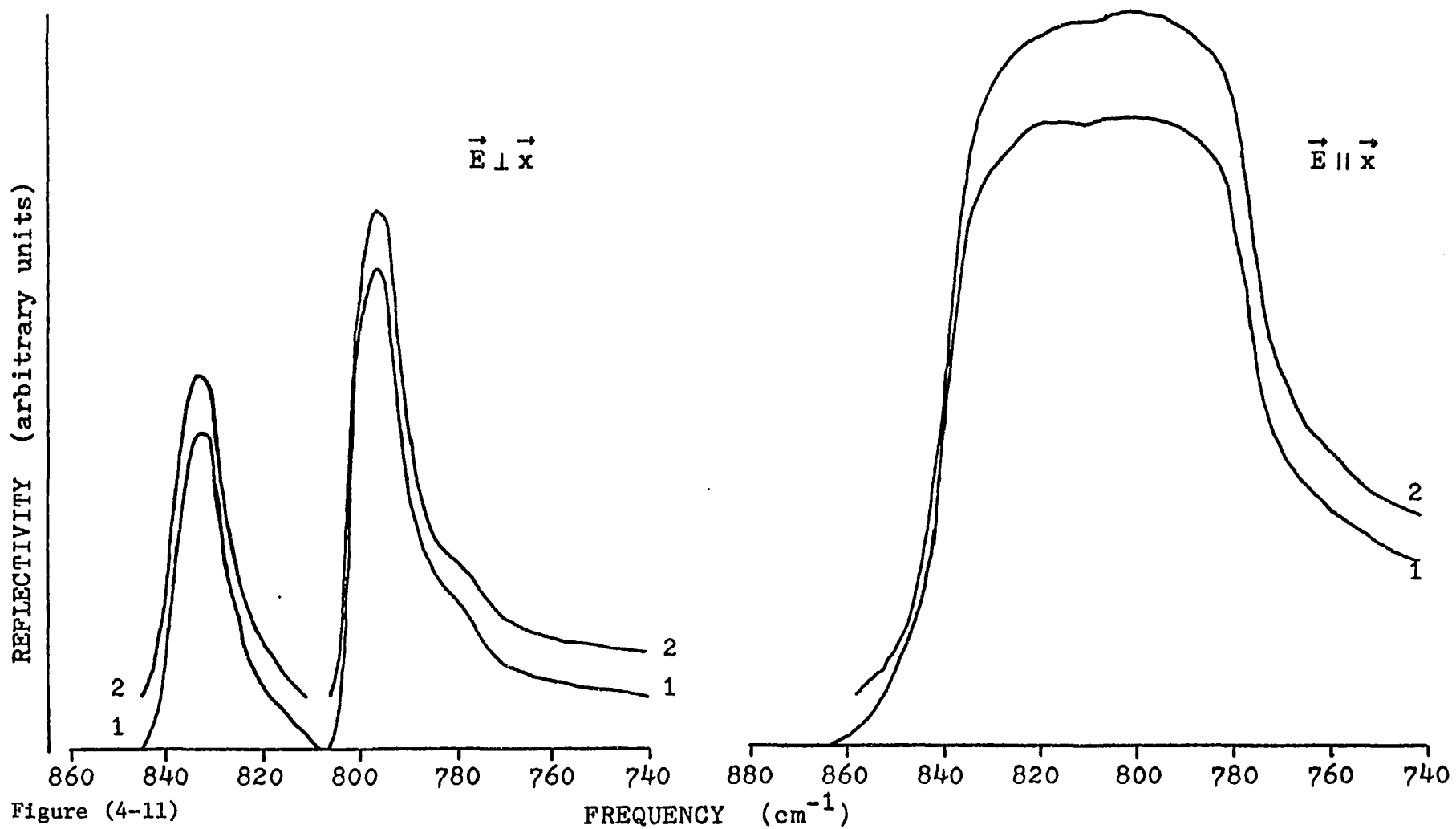


Figure (4-11)

Polarized near normal incidence infrared reflectivity spectra of a KBrO_3 single crystal. Spectrum 1 was obtained before irradiating the crystal in a γ -ray source and spectrum 2 is after irradiation. A natural rhombohedral crystal face was used with the optic axis in the plane perpendicular to x .

References for Chapter IV

1. N. Marschall, B. Fischer, and H. J. Queisser, Phys. Rev. Lett. 27, 95 (1971).
2. W. E. Anderson, R. W. Alexander, Jr., and R. J. Bell, Phys. Rev. Lett. 27, 1057 (1971).
3. S. Haussühl, Phys. Stat. Sol. 6A, K23 (1971).
4. Ralph W. G. Wyckoff, Crystal Structures, vol. 2 (Interscience publishers, New York, 1960).
5. B. Unger and S. Haussühl, Phys. Stat. Sol. B 54, 183 (1972).
6. J. C. Decius, J. Chem. Phys. 49, 1387 (1968).
7. Roger Frech and J. C. Decius, J. Chem. Phys. 51, 1536 (1969).
8. Roger Frech and J. C. Decius, J. Chem. Phys. 51, 5315 (1969)..
9. Roger Frech and J. C. Decius, J. Chem. Phys. 54, 2374 (1971).
10. R. E. Carlson and J. C. Decius, J. Chem. Phys. 58, 4919 (1973).

CHAPTER V

Vibrational Study of the Optic Modes of Sodium Chlorate - Sodium Bromate Mixed Crystals

Introduction

The influence of defects introduced into a host crystal has been the subject of numerous studies. If the impurity concentration is small, new modes may be observed which are characteristic of the intermolecular interactions and the properties of the impurity. The addition of defects also destroys the translational symmetry of the host crystal which may allow symmetry forbidden modes to be observed. As the impurity concentration increases, the effects of impurity-impurity interactions also become important.

When atoms A and B of different chemical species are randomly substituted on periodic lattice sites the resulting solid is termed a mixed crystal. Other types of disordered crystals, such as those exhibiting orientational disorder or spatial disorder, will not be described as mixed crystals. It is obvious that this random substitution of atoms of type A and B destroys the translational symmetry of the lattice which, in a strict sense, means that the resulting solid is not a true crystal. X-ray diffraction methods, however, show that many of these systems have a characteristic "unit cell" with an effective site occupancy $x_A + (1-x)B$ (where $0 < x < 1$). That is, the disordered system appears to have a periodic lattice in which an atom with a scattering intensity intermediate between those of atoms A and B occupies each site. This is probably due to an average of scattering intensities

from the two types of atoms. Both $\text{Sr}_{1-x}\text{Ba}_x\text{F}_2$ and $\text{Ni}_x\text{Co}_{1-x}\text{O}$ exhibit this behavior and the lattice parameters of the mixed crystals were found to be linear with concentration.^{1,2} In certain mixed crystal systems substitution of one ion for another can be made over the complete range of concentrations. In some of these systems only one vibrational mode is observed which is found to vary in frequency between the end frequencies of the two pure components with an intensity intermediate between the two pure crystal intensities. This is usually termed "one-mode" behavior. Fuller and co-workers found this behavior in $\text{Li}_x\text{Na}_{1-x}\text{Br}$, $\text{LiCl}_x\text{Br}_{1-x}$, $\text{Na}_x\text{Rb}_{1-x}\text{I}$, and $\text{Na}_x\text{K}_{1-x}\text{I}$ systems using infrared transmission of films evaporated onto polyethylene substrates.³ Other systems, $\text{KCl}_x\text{Br}_{1-x}$,⁴ $\text{Ni}_x\text{Co}_{1-x}\text{O}$,² $\text{Ca}_x\text{Sr}_{1-x}\text{F}_2$,¹ and $\text{Sr}_x\text{Ba}_{1-x}\text{F}_2$ ¹ also show one-mode behavior.

In some mixed crystal systems, two vibrational modes with frequencies close to those of the pure components are found at intermediate concentrations and whose intensities depend upon the relative concentrations of the components. This is termed "two-mode" behavior. Some systems having two-mode behavior are $\text{K}_x\text{Rb}_{1-x}\text{I}$,⁴ $\text{Ga}_x\text{Al}_{1-x}\text{As}$,⁵ $\text{GaAs}_x\text{P}_{1-x}$,^{6,7} $\text{CdS}_x\text{Se}_{1-x}$,⁸ and $\text{ZnS}_x\text{Se}_{1-x}$.⁹

There have been several methods developed for predicting whether a mixed crystal system will exhibit one-mode or two-mode behavior. These methods are usually based on the qualifying conditions that if both local modes (impurity modes above the optic modes of the host) and gap modes (impurity modes between the optic modes and acoustic modes to the host) are allowed then two mode behavior will result. Using a one dimensional random element isodisplacement model, which assumes the anions B and C are randomly substituted and anions of like species vibrate in phase against a cation (A) sublattice for the system $\text{AB}_x\text{C}_{1-x}$, Chang and Mitra found that

local modes and gap modes would be observed if $m_B < \mu_{AC} < m_A, m_C$ and $m_C > \mu_{AB}$; where m represents the mass of an ion and μ represents the reduced mass of an ion pair.¹⁰ Fertel and Perry have pointed out that Chang and Mitra's model was derived using a linear chain, not a three dimensional crystal, which implies that the local mode may be above the transverse optical mode of the host but below the longitudinal optic mode.⁴ In that case the reststrahlen bands would overlap which invariably means the system would exhibit one mode behavior.

In an infrared reflectivity study of the mixed crystal system $\text{Ga}_x\text{In}_{1-x}\text{Sb}$, Brodsky and co-workers found that the system exhibits two-mode behavior over only part of the concentration range.¹¹ This behavior was explained by the local mode being allowed but the gap mode being forbidden.

Most of the mixed crystal systems studied involve systems of the type $\text{A}_x\text{B}_{1-x}\text{C}$ where both end members, AC and BC, have the same crystal structure. Perry and Tornberg, however, have studied the mixed crystal system $\text{Na}_x\text{K}_{1-x}\text{TaO}_3$ which has different crystal structures for the end members.¹² KTaO_3 has a cubic structure whereas NaTaO_3 is monoclinic. The system was found to remain essentially cubic up to 70% Na but a sharp distortion in c/a , which increased with Na concentration, was found to occur after 70% Na.

In this work the mixed crystal system $\text{Na}(\text{ClO}_3)_x(\text{BrO}_3)_{1-x}$ is studied. This system differs from the aforementioned systems in that the anions are molecular and have internal degrees of freedom. Since this system has a multiply occupied unit cell the internal modes exhibit a rich multiplet structure through factor group correlations. Therefore, this system is excellent for studying the disorder induced breakdown of the space group selection rules. Also, long range dipolar coupling plays an important role

in the interactions of the modes originating in the ν_3 intramolecular motion of the anions.

Theory

Both NaClO_3 ¹³ and NaBrO_3 ¹⁴ crystallize in the T^4 ($P2_13$) space group with four molecules per unit cell. The unit cell basis vector is 6.575\AA for NaClO_3 and 6.705\AA for NaBrO_3 . The pure crystal unit cell has the C_3 axes of the anions parallel to the body diagonals although the C_3 axes do not intersect. There are four equivalent positions for anion substitution and these positions are arranged so that the C_3 axes of the anions are parallel to the C_3 axes of a tetrahedron. The unit cell is shown in figure (5-1).

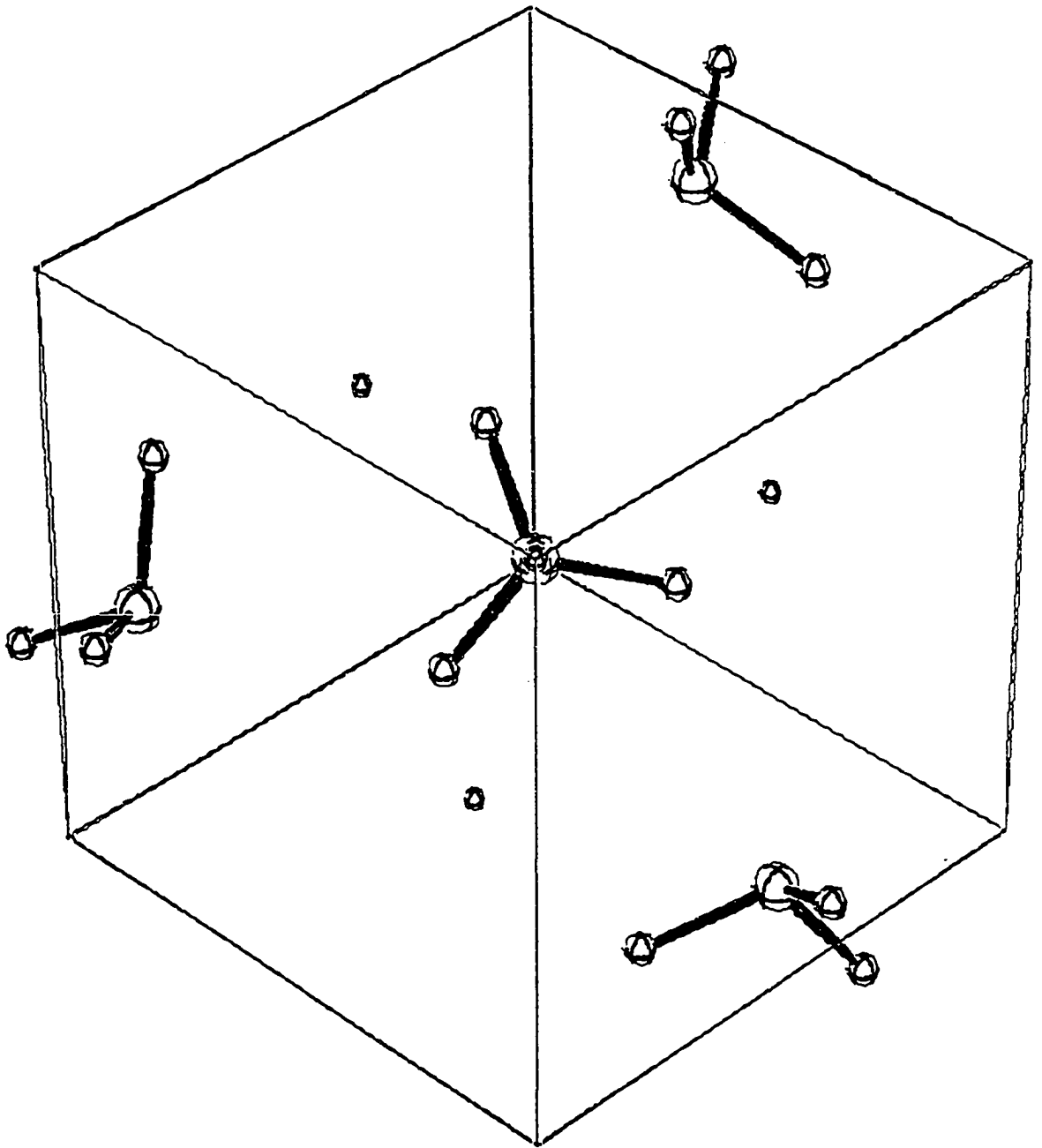
Figure (5-2) shows the vibrational correlation diagram for the pure crystals. All optic modes are Raman active while only the F symmetry modes have infrared activity. By factor group analysis there should be $3A+3E+8F$ external optic modes and $2A+2E+6F$ internal optic modes. In the crystallographic cartesian coordinate system the Raman tensors for the A, E, and F symmetry species of the pure crystals are:¹⁵

$$A \equiv \begin{bmatrix} a & 0 & 0 \\ 0 & a & 0 \\ 0 & 0 & a \end{bmatrix}$$

$$E \equiv \begin{bmatrix} b & 0 & 0 \\ 0 & b & 0 \\ 0 & 0 & -2b \end{bmatrix}, \begin{bmatrix} \sqrt{3}b & 0 & 0 \\ 0 & -\sqrt{3}b & 0 \\ 0 & 0 & 0 \end{bmatrix}$$

$$F \equiv \begin{bmatrix} 0 & 0 & 0 \\ 0 & 0 & c \\ 0 & c & 0 \end{bmatrix}, \begin{bmatrix} 0 & 0 & c \\ 0 & 0 & 0 \\ c & 0 & 0 \end{bmatrix}, \begin{bmatrix} 0 & c & 0 \\ c & 0 & 0 \\ 0 & 0 & 0 \end{bmatrix}$$

Figure (5-1). Unit cell of NaClO_3 and NaBrO_3 as viewed along the C_3 axis of an anion. The smallest atoms are Na, largest atoms are Cl or Br, and atoms of intermediate size are O.



NaClO₃ & NaBrO₃
CORRELATION DIAGRAM

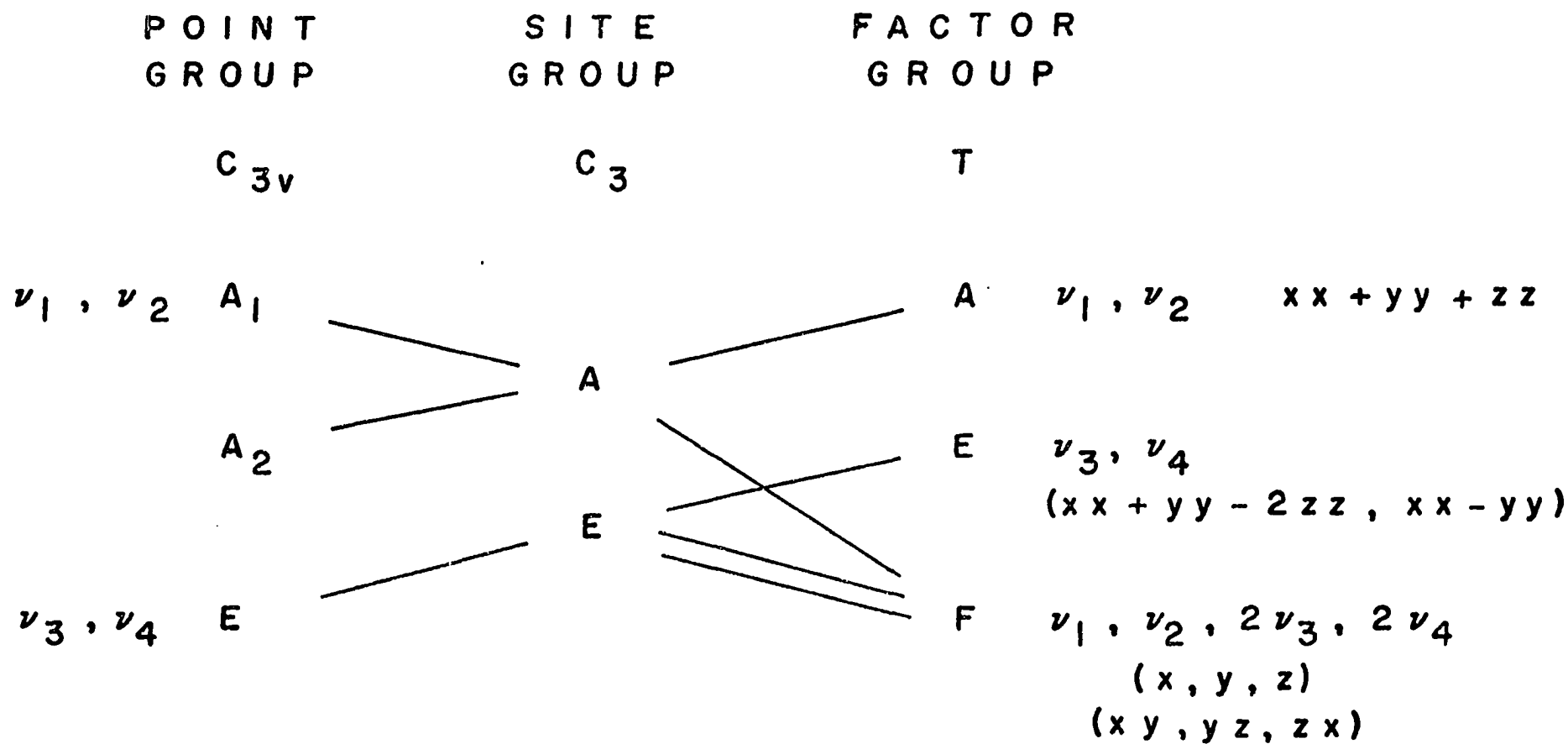


Figure (5-2). Vibrational correlation diagram for NaClO₃ and NaBrO₃

In this coordinate system both the A and E symmetry species have only diagonal components while the F symmetry species have only off-diagonal components. Rotation of the crystal, however, allows the E symmetry Raman tensors to acquire off-diagonal elements while the A symmetry Raman tensor remains unchanged. This allows separation of the A and E symmetry species by experimental scattering geometries.

In very dilute samples, the impurity may be treated as being matrix isolated provided the impurity is homogeneously distributed. A method for determining the symmetry of matrix isolated species has been developed by Miller and Decius.¹⁶ If the impurity ions are not allowed to rotate in the site and are aligned to allow the maximum symmetry possible, then the effective impurity symmetry will be isomorphous to C_3 . The matrix isolated ion will have four internal optic modes due to the ν_1 , ν_2 , ν_3 , and ν_4 intramolecular motions.

The addition of impurities destroys the translational symmetry of the lattice so that the symmetry designations of the vibrational modes are no longer valid. They are retained here only as an aid in labeling the origin of the mixed crystal modes. They are not to be taken as the true symmetry label of the mixed crystal mode.

Experimental

Pure NaBrO_3 and NaClO_3 crystals were grown by slow evaporation from aqueous solution at room temperature. Mixed crystals were grown in like manner using weighed amounts of materials. Microcrystalline mixed crystals were prepared by dissolving weighed amounts of NaBrO_3 and NaClO_3 in distilled water and evaporating under an aspirator vacuum while stirring. The microcrystals were then ground in an agate mortar and packed in glass

capillary tubes for Raman measurements. Single crystals were prepared for transmission measurements by epoxying the crystals over a hole in a metal plate and grinding on emery paper. Final polishing was on lens paper using ethanol as a solvent.

All infrared spectra were recorded at room temperature with a Beckman IR-12 spectrometer. Near normal incidence infrared reflection spectra were recorded with an average angle of incidence of 15° and a 4:1 linear image reduction. Room temperature Raman spectra were obtained using a Spex Ramalog 5 spectrometer equipped with a two watt argon ion laser. Raman integrated intensities were determined by weighing the chart paper in the ν_1 - ν_3 spectral regions of BrO_3^- and ClO_3^- on an analytical balance.

NaClO_3

At room temperature NaClO_3 grows with the 100, 010, and 001 crystallographic faces exposed, as determined by X-ray diffraction. Two crystal orientations were used for obtaining Raman spectra; one having the crystallographic cartesian axes coinciding with the laboratory axes and the other having the crystallographic cartesian axes rotated through an angle of 45° with respect to the laboratory axes. The Raman tensors associated with the latter coordinate system are given below.

$$\begin{aligned}
 A' &\equiv \begin{bmatrix} a & 0 & 0 \\ 0 & a & 0 \\ 0 & 0 & a \end{bmatrix} ; E' \equiv \begin{bmatrix} -b/2 & 0 & 3b/2 \\ 0 & b & 0 \\ 3b/2 & 0 & -b/2 \end{bmatrix} , \begin{bmatrix} 0 & -\sqrt{(3/2)}b & 0 \\ -\sqrt{(3/2)}b & 0 & -\sqrt{(3/2)}b \\ 0 & -\sqrt{(3/2)}b & 0 \end{bmatrix} \\
 F' &\equiv \begin{bmatrix} -c/\sqrt{2} & -c/2 & 0 \\ -c/2 & 0 & c/2 \\ 0 & c/2 & c/\sqrt{2} \end{bmatrix} , \begin{bmatrix} -c/\sqrt{2} & c/2 & 0 \\ c/2 & 0 & -c/2 \\ 0 & -c/2 & c/\sqrt{2} \end{bmatrix} , \begin{bmatrix} c/2 & 0 & c/2 \\ 0 & -c & 0 \\ c/2 & 0 & c/2 \end{bmatrix}
 \end{aligned}$$

The Raman frequencies are listed in table (5-1). A discrepancy is found between this work and the results reported by Porto and co-workers.¹⁷ The $\nu_1(\text{A})$ mode is assigned here at 936cm^{-1} and the $\nu_1(\text{F})$ mode at 937cm^{-1} , which is opposite to the assignments of those authors.

NaBrO₃

Sodium bromate grows with a trigonal pyramidal habit at room temperature in aqueous solution. Using X-ray diffraction, the crystallographic cartesian axes were shown to be related to the pyramidal geometry as shown in figure (5-3). Each axis bisects opposite edges of the trigonal pyramid. A crystal was ground on emery paper to expose faces parallel and perpendicular to the crystallographic cartesian coordinates. The crystal was oriented so that the crystallographic cartesian coordinates coincided with the laboratory axes. Another crystal was ground to expose faces parallel and perpendicular to the primed axes as shown in figure (5-4). The x' - y' plane coincides with one of the crystal faces. The y' axis coincides with an edge of the trigonal pyramid. Raman spectra were obtained with the crystal oriented so that the primed axes coincided with the laboratory axes. The Raman tensors associated with the primed coordinate system are given below.

$$\begin{aligned}
 \text{A}' &\equiv \begin{bmatrix} a & 0 & 0 \\ 0 & a & 0 \\ 0 & 0 & a \end{bmatrix} ; & \text{E}' &\equiv \begin{bmatrix} -b & 0 & \sqrt{2}b \\ 0 & b & 0 \\ \sqrt{2}b & 0 & 0 \end{bmatrix} , & & \begin{bmatrix} 0 & -b & 0 \\ -b & 0 & -\sqrt{2}b \\ 0 & -\sqrt{2}b & 0 \end{bmatrix} \\
 \text{F}' &\equiv \begin{bmatrix} -0.667c & -0.577c & -0.236c \\ -0.577c & 0 & 0.408c \\ -0.236c & 0.408c & 0.667c \end{bmatrix} , & & \begin{bmatrix} -0.667c & 0.577c & -0.236c \\ 0.577c & 0 & -0.408c \\ -0.236c & -0.408c & 0.667c \end{bmatrix} , \\
 & & & & \begin{bmatrix} 0.333c & 0 & 0.471c \\ 0 & -c & 0 \\ 0.471c & 0 & 0.667c \end{bmatrix}
 \end{aligned}$$

Table (5-1). Optic mode frequencies (in cm^{-1}) of NaClO_3 .

assignment	Symmetry			
	<u>A</u>	<u>E</u>	<u>F_T</u>	<u>F_L</u>
[65		
			73	79
	84			
			94	
	external		121	
[128	129
		131		
		177		
	ν_4		480	
	ν_4		482*	487*
ν_4		488	488	
ν_2	618			
ν_2			624	629
ν_1	936			
ν_1			937	940
ν_3		957		
ν_3			966	983
ν_3			987	1027

* inflection point of infrared reflectivity spectrum.

Figure (5-3).
 Crystallographic cartesian
 axes in relation to the
 pyramidal growth habit
 of NaBrO_3

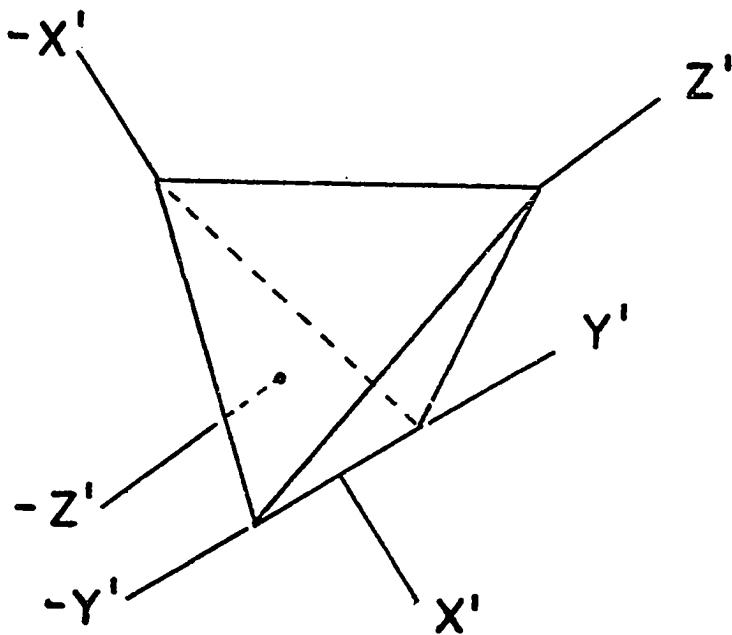
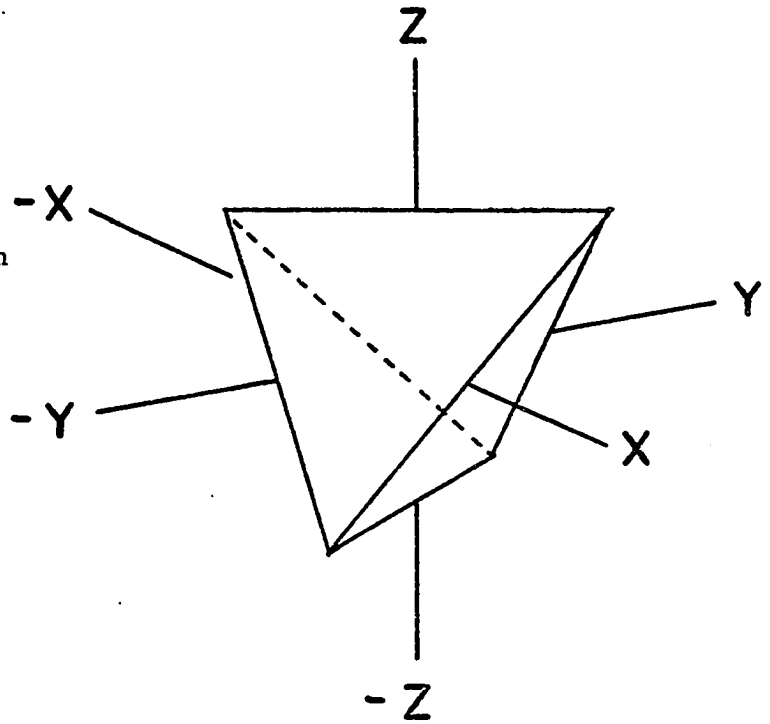


Figure (5-4).
 Coordinate system used
 in Raman experiments to
 separate the A and E
 symmetry phonons of
 NaBrO_3

In this coordinate system the A symmetry Raman tensor remains unchanged, however, Raman tensors for the E symmetry species acquire off-diagonal elements and those of the F symmetry species acquire diagonal elements. Raman frequencies are given in table (5-2). These values agree favorably with those obtained by D'Andrea and co-workers.¹⁸ Four of the external F symmetry modes reported in that study were not found here.

Microcrystalline Mixed Crystals

Figures (5-5) & (5-6) show the Raman spectra of the ν_1 - ν_3 spectral region of BrO_3^- and ClO_3^- in the microcrystalline samples. The $\nu_{3a}(\text{F}_T)$, $\nu_{3a}(\text{F}_L)$, and $\nu_{3b}(\text{F}_T)$ modes of NaClO_3 were found to shift to lower frequencies as the concentration of BrO_3^- increased. At $\sim 55\%$ ClO_3^- the $\nu_{3b}(\text{F}_T)$ mode began to increase in frequency and at $\sim 20\%$ ClO_3^- the modes originating from $\nu_{3a}(\text{F}_T)$ and $\nu_{3b}(\text{F}_T)$ converged to the limiting frequency of the matrix isolated ion at 967cm^{-1} . As the $\nu_{3a}(\text{F}_T)$ and $\nu_{3b}(\text{F}_T)$ modes are the result of the factor group correlation, this multiplet cannot be maintained upon destruction of the factor group. In the matrix isolation limit only one ν_3 component can be allowed so that the merging of the $\nu_{3a}(\text{F}_T)$ and $\nu_{3b}(\text{F}_T)$ modes is expected. The $\nu_{3a}(\text{F}_L)$ mode persisted to ~ 20 mole percent ClO_3^- with a continuing drop in frequency. Surprisingly, the longitudinal mode did not merge at a common frequency with the transverse mode. The transverse-longitudinal frequency separation arises from the electric field induced by the collective motion of like ions throughout the crystal. As the concentration of these ions is decreased, the collective nature of the motion is progressively destroyed and the transverse-longitudinal frequency separation should decrease. In the limit of matrix isolated ions the transverse and longitudinal modes should merge at one common frequency.

Table (5-2). Optic mode frequencies (in cm^{-1}) of NaBrO_3 from Raman spectra

assignment	Symmetry			
	<u>A</u>	<u>E</u>	<u>F_T</u>	<u>F_L</u>
[external]		65		
			76	79
	85			
			98	98
			113	116
			130	132
		134		
	148			
		179		
	189			
ν_4		358		
ν_4			373	
			374	
ν_2	443			
ν_2			443	
			457	
ν_3		791		
ν_1			795	
			796	
ν_3			798	
			821	
ν_1	799			
ν_3			821	
			845	

At 10 mole percent ClO_3^- only two modes were found in the ν_1 - ν_3 spectral region of ClO_3^- at 936 and 967cm^{-1} corresponding to the $\nu_1(\text{A})$ and $\nu_3(\text{E})$ modes respectively in the C_3 site group approximation. Figure (5-7) shows the frequency vs. concentration curves for the ClO_3^- ion.

At low BrO_3^- concentrations two modes were found at 801 and 814cm^{-1} with the mode at 814cm^{-1} having the greater scattering intensity. As evident in figures (5-5) & (5-6) the mode at 814cm^{-1} dropped in intensity relative to that of the 801cm^{-1} mode as the BrO_3^- concentration increased so that at ~ 30 mole percent BrO_3^- the mode originating at 801cm^{-1} had the greater intensity. The intensity change was accompanied by a shift to lower frequencies for both modes as the BrO_3^- ion concentration increased. The frequencies of the BrO_3^- modes as a function of concentration are described in figure (5-8). At ~ 35 mole percent BrO_3^- the longitudinal mode of $\nu_{3a}(\text{F})$ became observable and at $\sim 45\%$ BrO_3^- the mode originating at 814cm^{-1} split into two components. As the BrO_3^- concentration increased, one component approached the $\nu_{3a}(\text{F}_\text{T})$ frequency of pure NaBrO_3 at 822cm^{-1} while the other component approached a limiting frequency of 832cm^{-1} . This mode was not found in the single crystal spectra. Its frequency is too high to be the $\nu_{3a}(\text{F}_\text{T})$ mode; if it is assigned as a combination mode of $\nu_2 + \nu_4$ it would be expected to appear in the single crystal spectra. Therefore no assignment will be proposed here. Unlike the ClO_3^- modes, the $\nu_{3b}(\text{F}_\text{T})$ and $\nu_{3a}(\text{F}_\text{T})$ modes of BrO_3^- were not found to undergo a smooth frequency shift converging to one common frequency as the BrO_3^- concentration decreased. As the intensity of the $\nu_1(\text{A})$ mode is much greater than that of the $\nu_{3b}(\text{F}_\text{T})$ mode and these modes are almost coincident in frequency, the $\nu_{3b}(\text{F}_\text{T})$ mode was not resolved in the pure NaBrO_3 powder. The one mode observed was

Figure (5-5). Raman spectra of the ν_1 - ν_3 spectral region of BrO_3^- and ClO_3^- in mixed NaClO_3 - NaBrO_3 microcrystals.

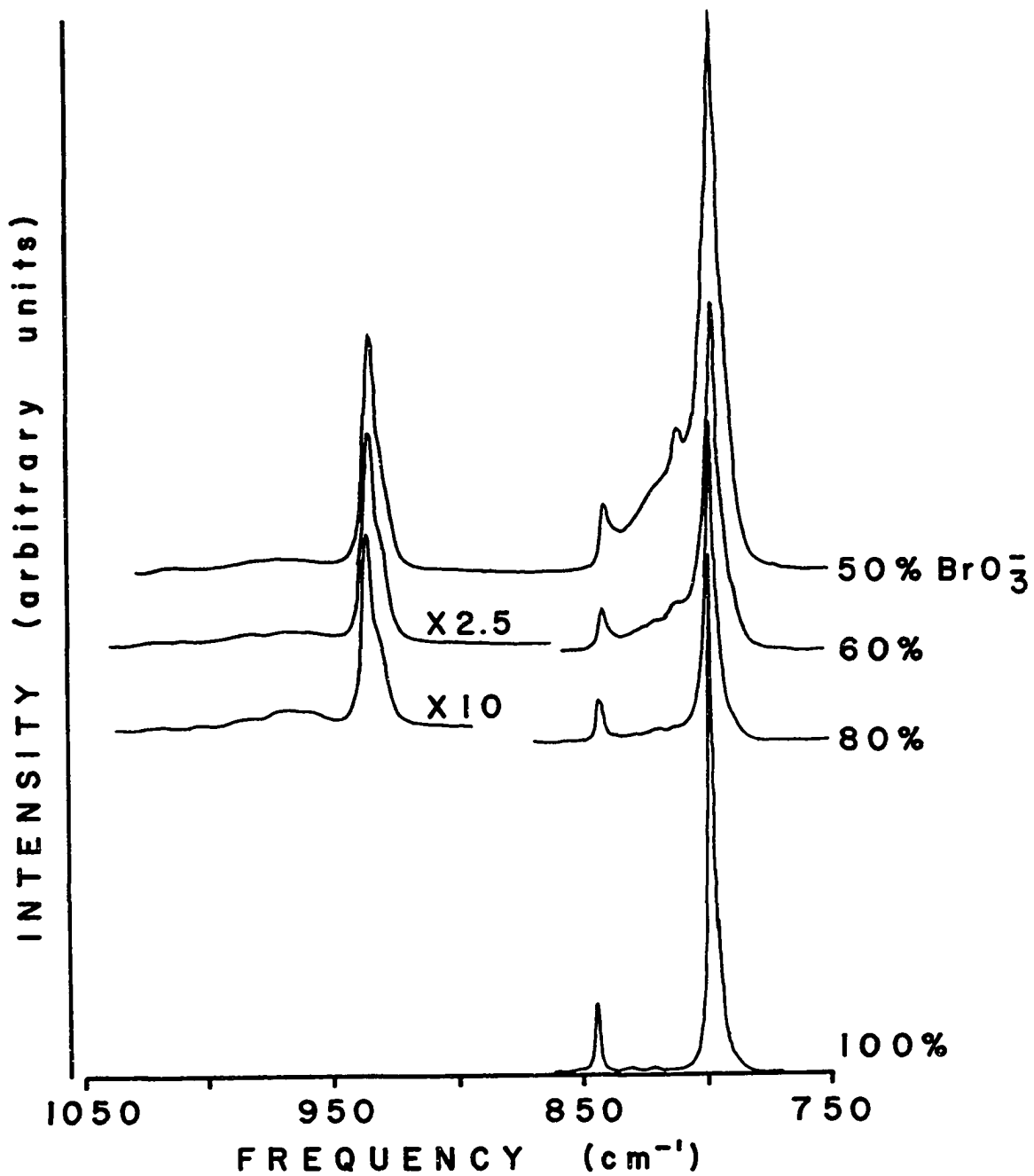
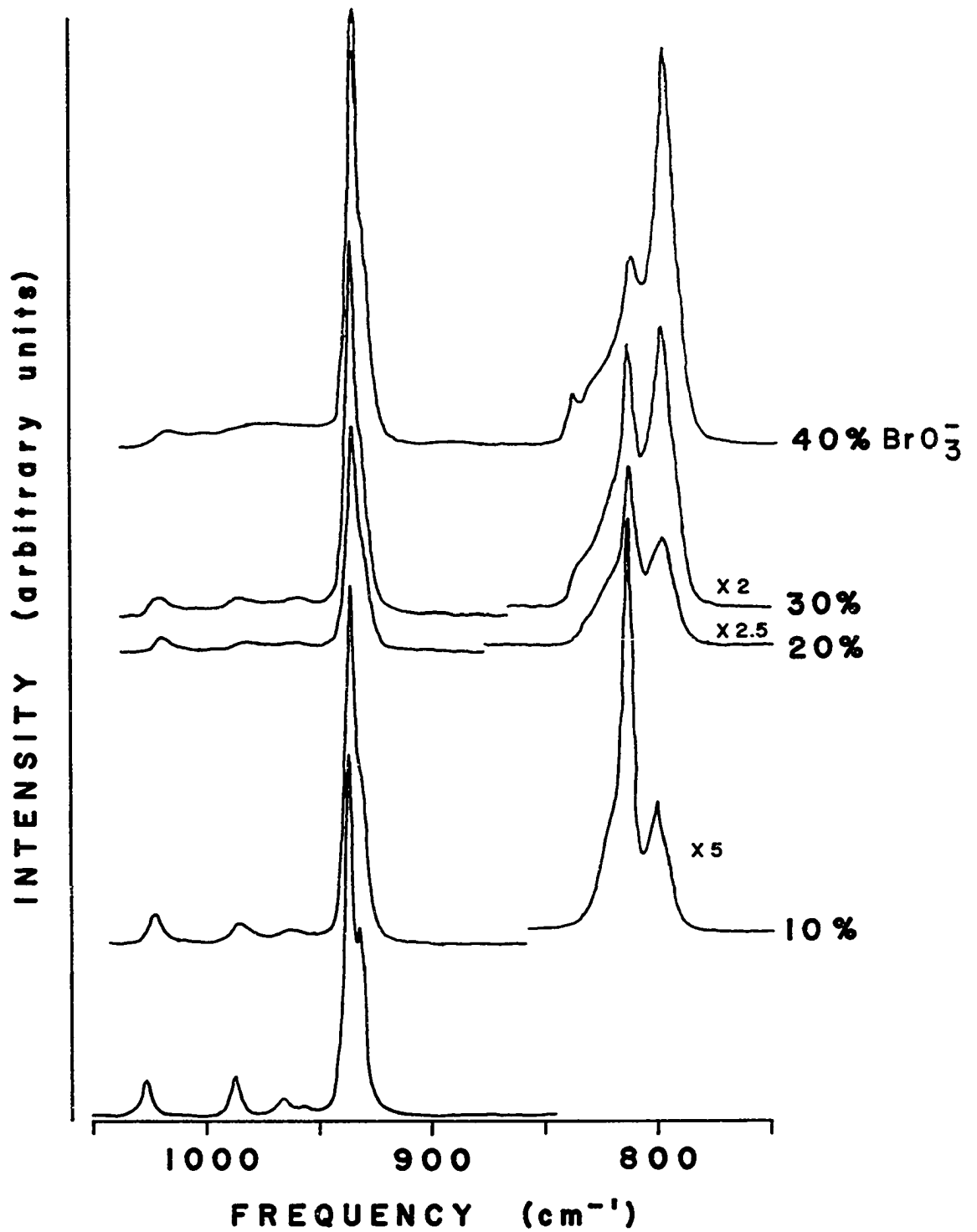


Figure (5-6). Raman spectra of the ν_1 - ν_3 spectral region of BrO_3^- and ClO_3^- in mixed NaClO_3 - NaBrO_3 microcrystals.



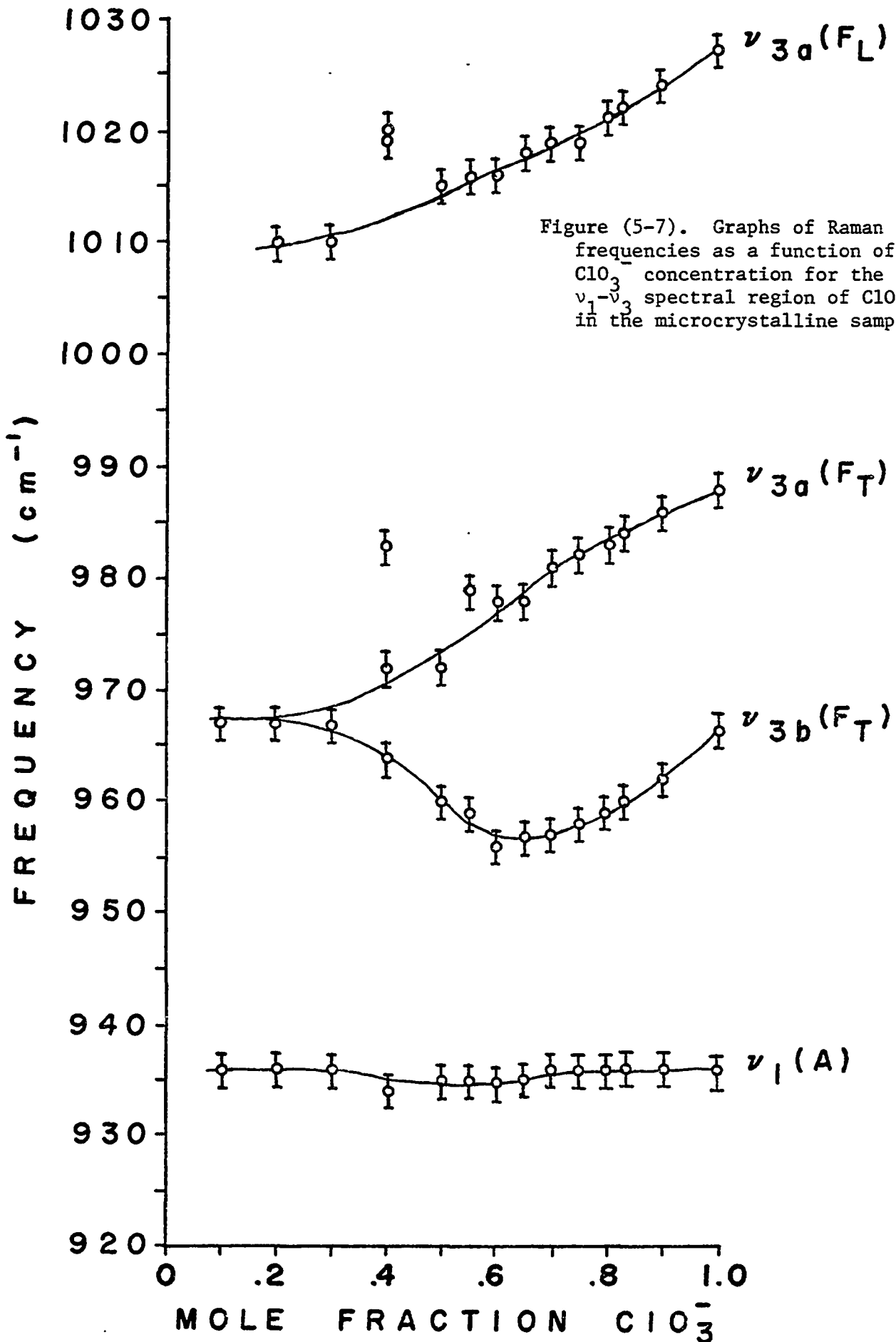
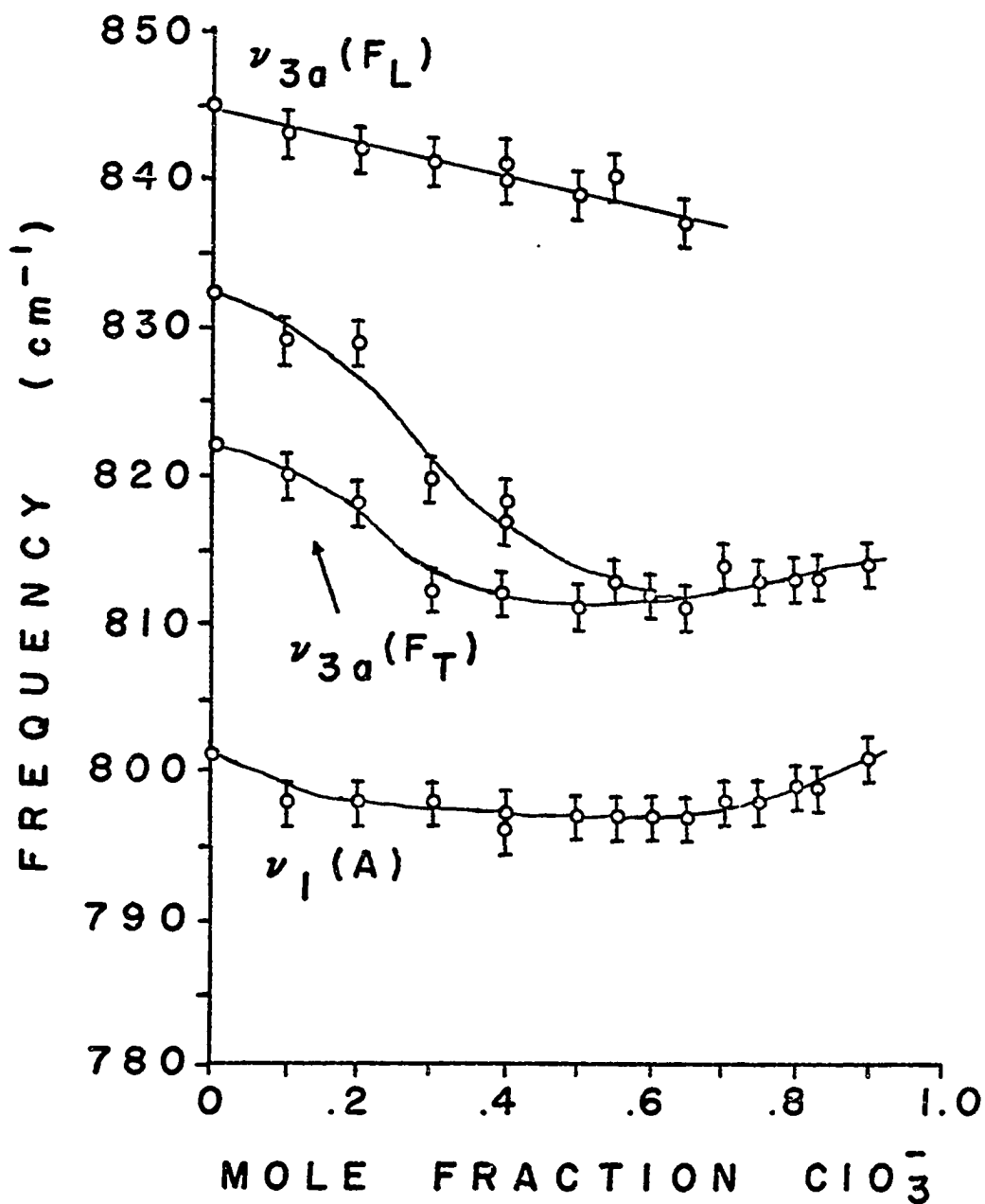


Figure (5-8). Graphs of Raman frequencies as a function of ClO_3^- concentration for the ν_1 - ν_3 spectral region of BrO_3^- in the microcrystalline samples.



followed to 10% BrO_3^- . No component was found to increase in frequency to merge with the mode originating from $\nu_{3a}(\text{F}_T)$.

Figures (5-9) & (5-10) show the ν_2 - ν_4 spectral regions of ClO_3^- and BrO_3^- in the microcrystalline samples and figure (5-11) shows the frequency vs. concentration curves for these modes. The $\nu_{4a}(\text{F}_T)$ and $\nu_4(\text{E})$ modes of BrO_3^- originating in the pure microcrystalline powder were found to merge to one common frequency at ~25 mole percent BrO_3^- . The $\nu_2(\text{A})$ and $\nu_2(\text{F}_T)$ modes at 443cm^{-1} in the pure NaBrO_3 sample merged with the $\nu_2(\text{F}_L)$ mode at ~35% BrO_3^- . The convergence of these modes is in agreement with the C_3 site symmetry approximation. The $\nu_2(\text{A})$ component of ClO_3^- was not detected in the powder samples. The $\nu_2(\text{F}_T)$ mode was found to shift linearly to lower frequencies as the ClO_3^- concentration decreased. The splitting of the $\nu_4(\text{E})$ and $\nu_{4a}(\text{F}_T)$ components of ClO_3^- decreased with decreasing ClO_3^- concentration but even at 10% ClO_3^- two modes could be resolved, a somewhat surprising result. The $\nu_{4b}(\text{F}_T)$ mode was not found.

Using the Raman scattering intensities of the ν_1 - ν_3 spectral regions of BrO_3^- and ClO_3^- a graph, shown in figure (5-12), of intensity percent ClO_3^- vs. mole percent ClO_3^- was obtained. This graph was used to determine mixed crystal concentrations.

The Raman spectra of the microcrystalline mixed crystals differ from the spectra obtained from a simple mechanical mixture of the two pure microcrystals with respect to the frequencies and relative intensities of the modes. Mechanically mixing the two pure microcrystals gave rise to a Raman spectrum which closely resembled a simple superposition of the two pure components.

Figure (5-9). Raman spectra of the ν_2 - ν_4 spectral region of ClO_3^- in the microcrystalline samples. The spectra are displaced vertically.

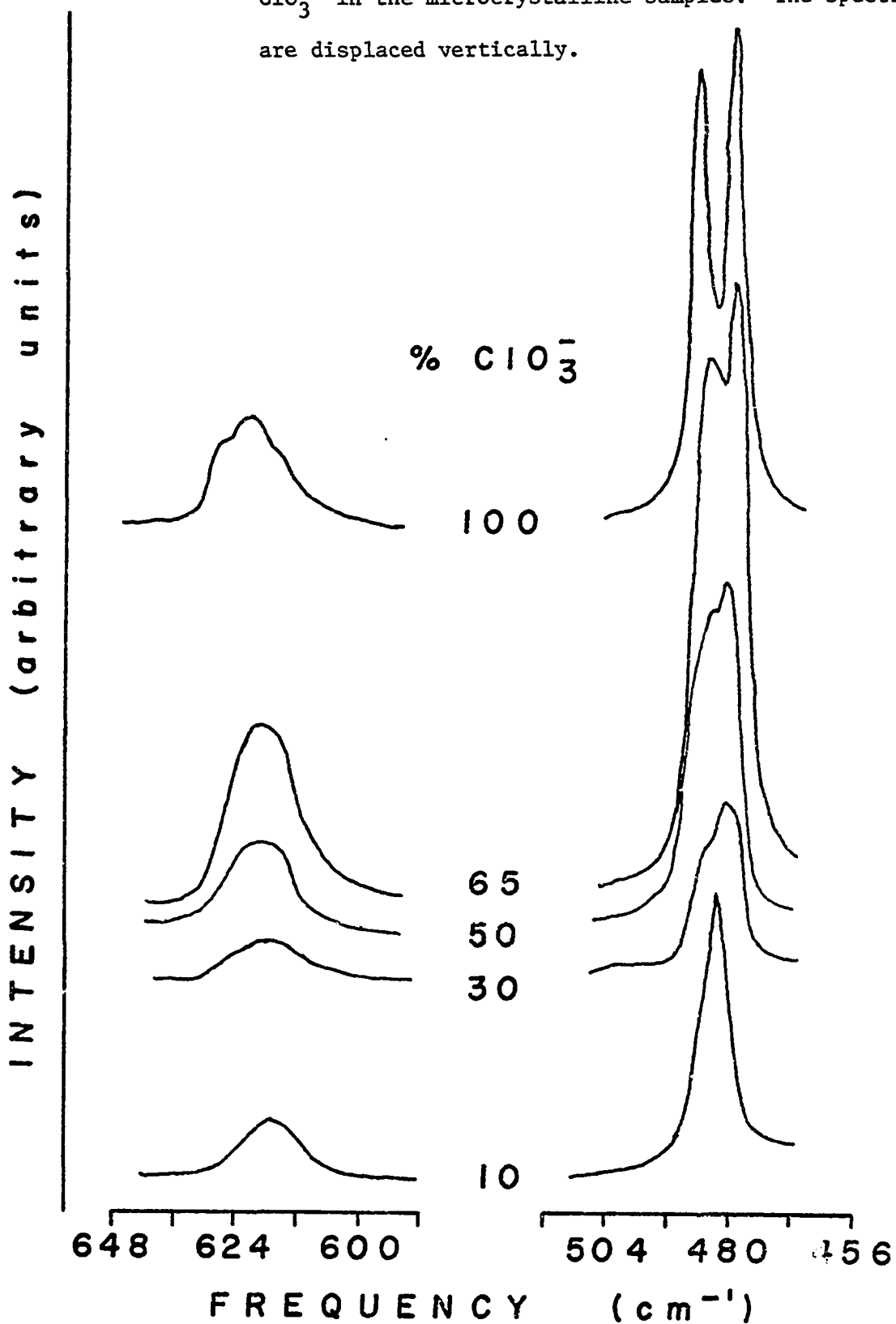
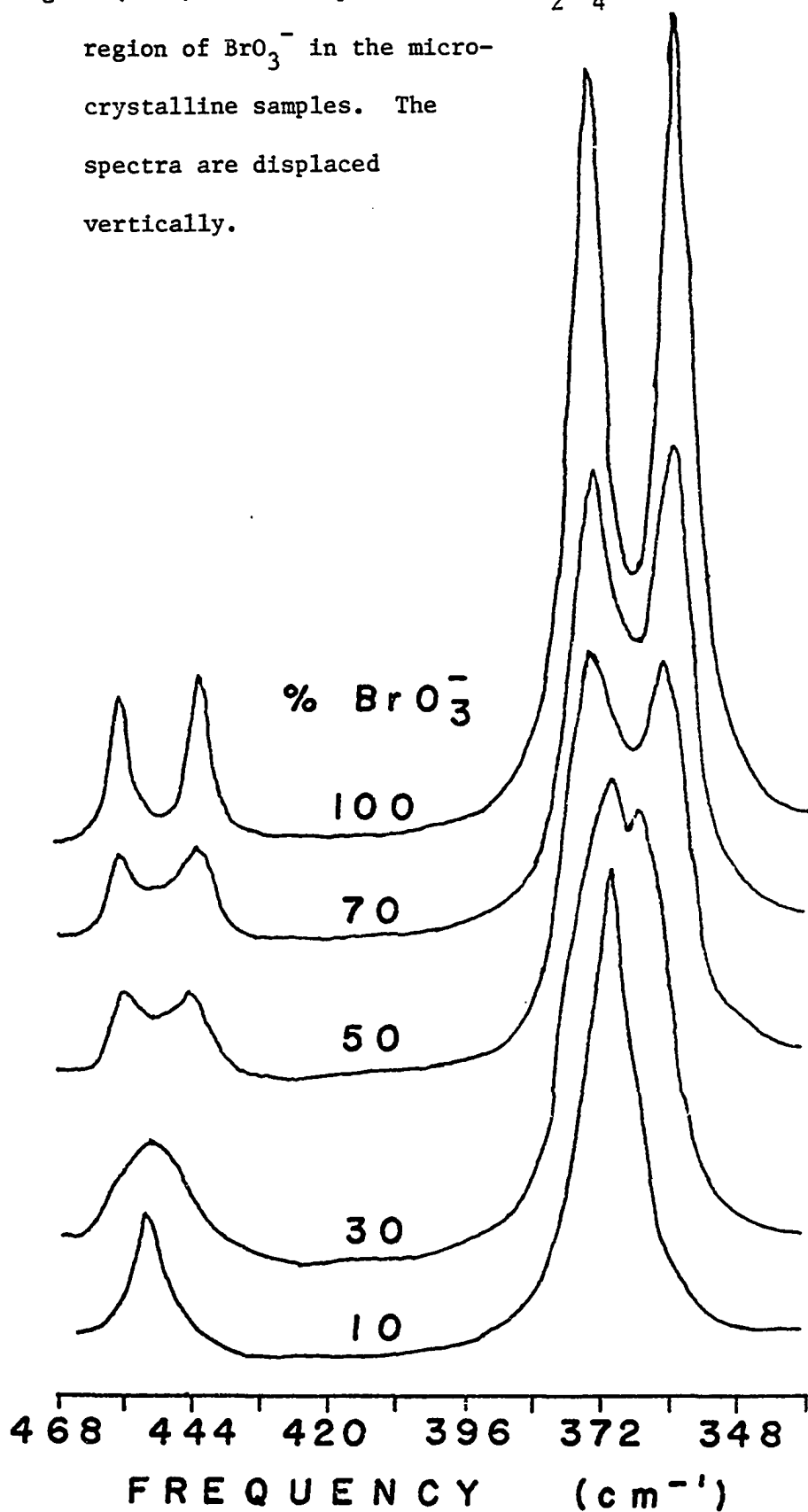


Figure (5-10). Raman spectra of the $\nu_2-\nu_4$ spectral region of BrO_3^- in the microcrystalline samples. The spectra are displaced vertically.

INTENSITY (arbitrary units)



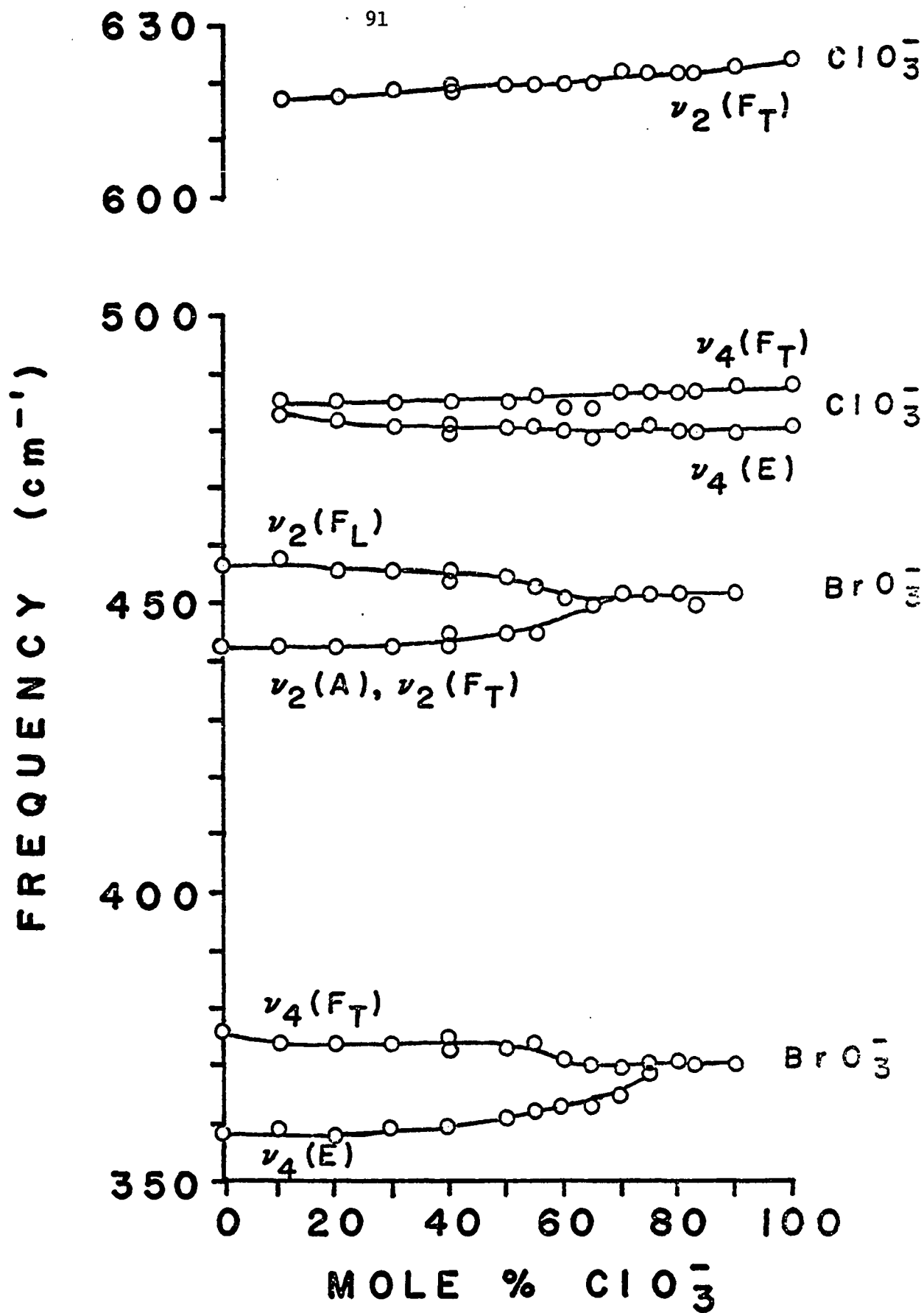


Figure (5-11). Graphs of Raman frequency as a function of ClO_3^- concentration for the ν_2 - ν_4 spectral regions of ClO_3^- and BrO_3^- in the microcrystalline samples.

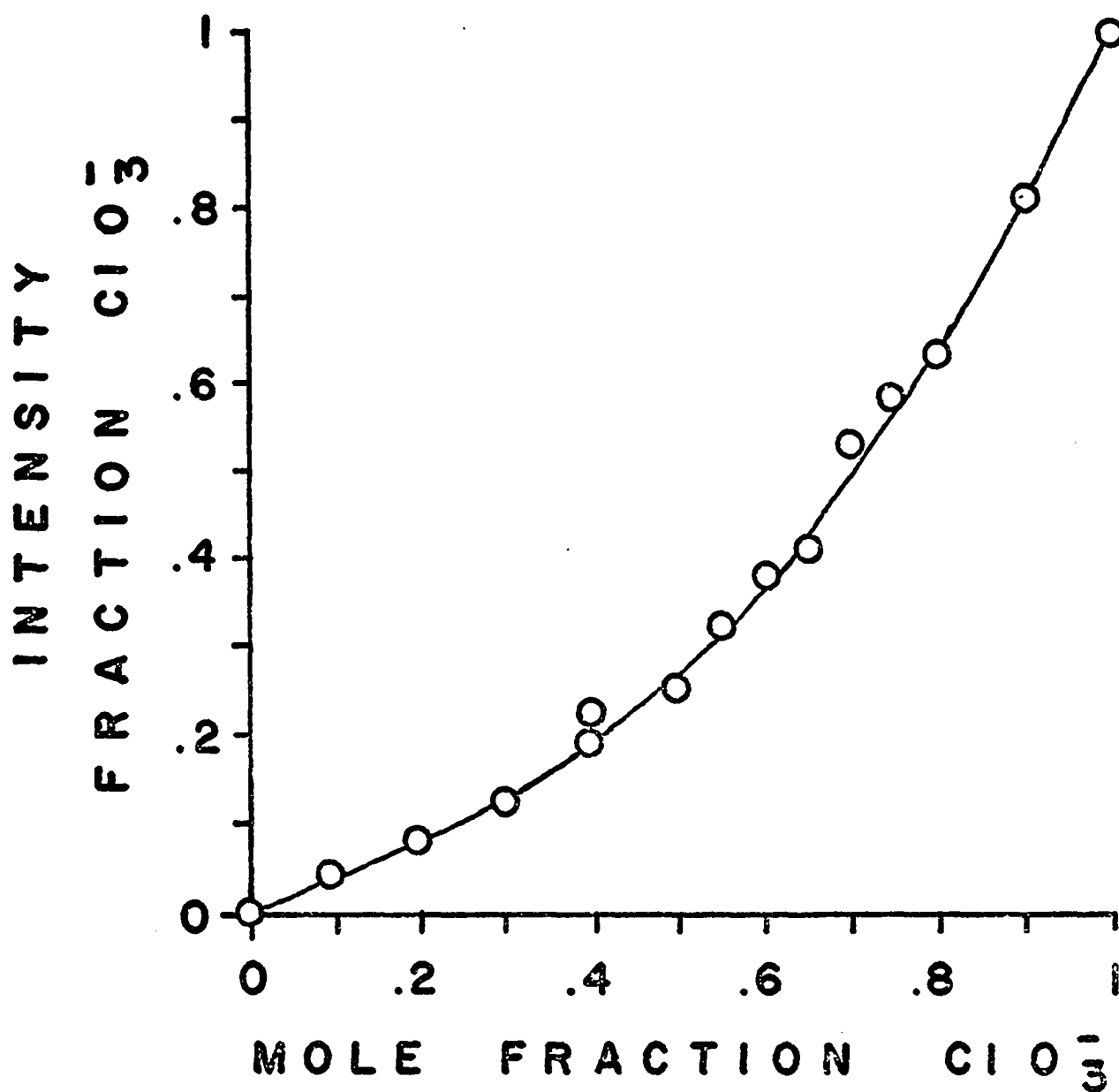


Figure (5-12). Graph of the fraction of the Raman scattering intensity due ClO_3^- as a function of the mole fraction of ClO_3^- for the microcrystalline samples. The ν_1 - ν_3 spectral regions of ClO_3^- and BrO_3^- were used.

Infrared transmission spectra of nujol mulls of the microcrystalline powders are shown in figure (5-13) for the ν_1 - ν_3 spectral region of BrO_3^- . A number of small spectral features were found which could be followed over the complete concentration range, although the significance of these features is uncertain. Frequency vs. concentration curves are shown in figure (5-14) for the absorption maxima. As the concentration of ClO_3^- increased, a mode originating at $\sim 804\text{cm}^{-1}$ was found to increase in frequency, finally merging with the mode originating at 821cm^{-1} at $\sim 35\%$ BrO_3^- . Another component of the mode originating at 804cm^{-1} was found to decrease in frequency, merging with a mode originating at 793cm^{-1} at $\sim 25\%$ BrO_3^- . The absorption maxima at 815cm^{-1} which appears in the 90% BrO_3^- sample is believed to be a combination mode arising from $\nu_2 + \nu_4$.

Mixed Single Crystals

The concentration of BrO_3^- or ClO_3^- in large crystals grown by slow evaporation was found to be almost independent of the solution concentration. Crystals having different infrared and Raman spectra could be harvested from the same solution and homogeneous crystals were difficult to obtain. Single crystal concentrations were found by filing the faces of the crystals and packing the removed material in glass capillaries. The Raman intensities of these powders and the intensity vs. concentration calibration graph in figure (5-12) enabled the single crystal concentrations to be determined.

The Raman spectra of crystals grown by slow evaporation are shown in figures (5-15) + (5-20). The mixed crystals appear to lose most of their polarization properties as evident from the similarity of the $x(zx)y$ and $x(zz)y$ spectra. This may be attributed to polarization losses by the optical activity of these crystals. That is, as plane polarized light enters the

Figure (5-13). Infrared transmission spectra of nujol mulls of the micro-crystalline samples. Only the ν_1 - ν_3 spectral region of BrO_3^- is shown and the spectra are displaced vertically.

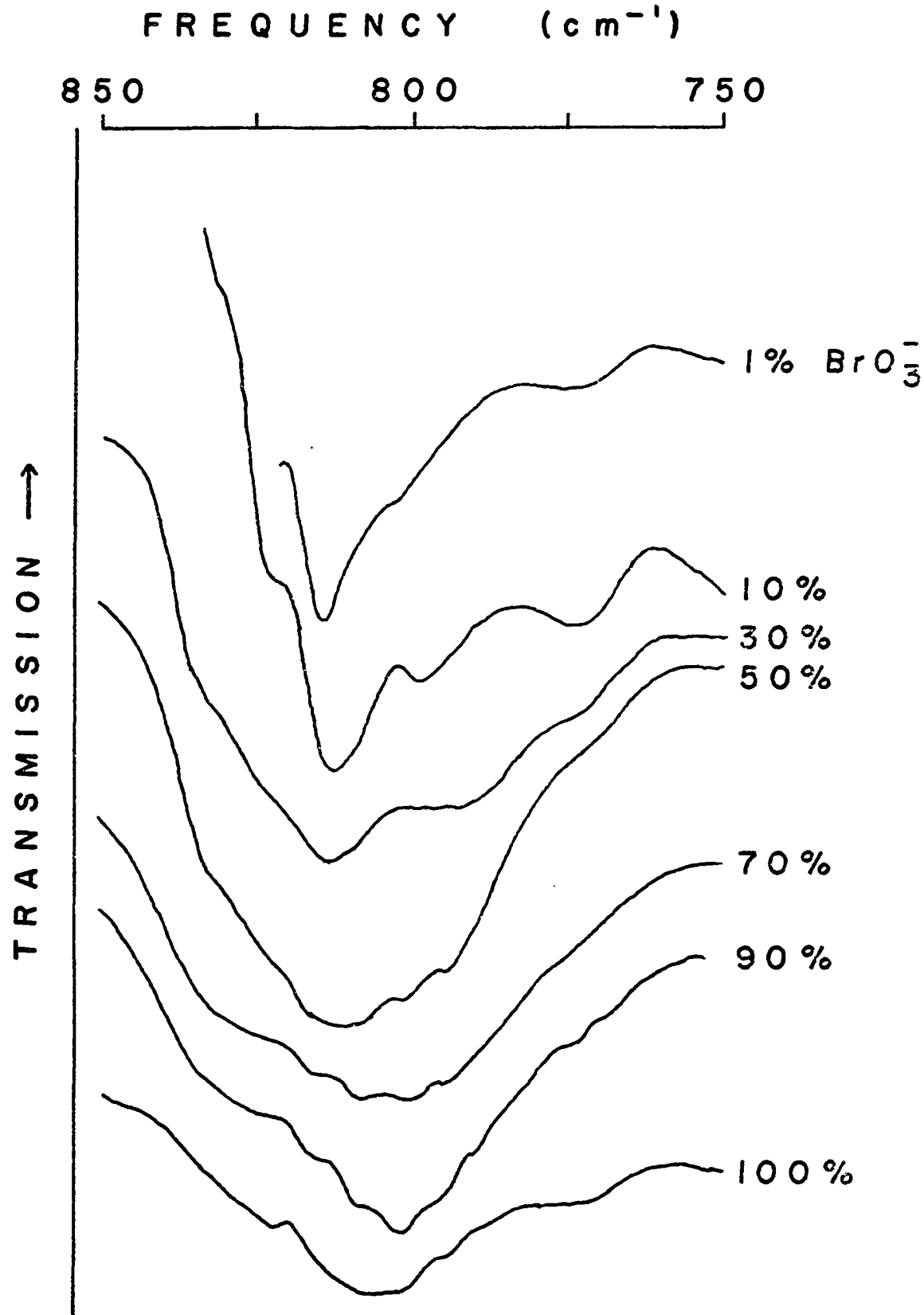
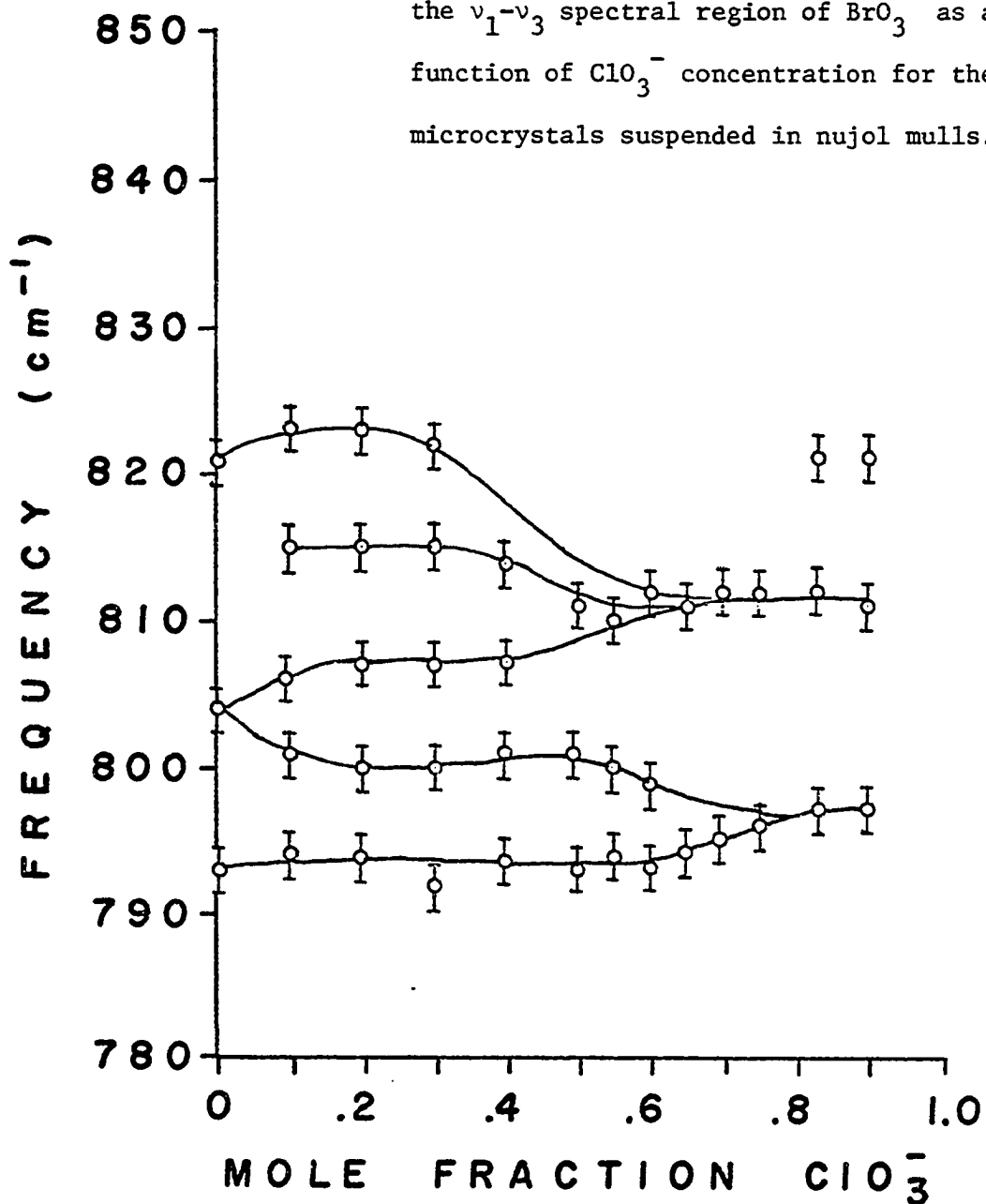


Figure (5-14). Graphs of absorption maxima in the ν_1 - ν_3 spectral region of BrO_3^- as a function of ClO_3^- concentration for the microcrystals suspended in nujol mulls.



crystal the direction of polarization rotates about the direction of propagation. The light is then scattered by the Raman effect and the polarization direction is again rotated before it leaves the crystal.

Raman spectral behavior similar to that found in microcrystals prepared by fast evaporation from solution was observed although there were some differences in the frequency vs. concentration curves. These curves are shown in figures (5-21) - (5-23). The initial frequency decrease of the ν_3 modes of ClO_3^- occurred at a much greater rate in the single crystal samples compared with the microcrystalline samples as the BrO_3^- concentration increased. The $\nu_{3a}(\text{F}_T)$ and $\nu_{3b}(\text{F}_T)$ modes merged at $\sim 50\%$ ClO_3^- in the single crystal samples as compared with $\sim 20\%$ ClO_3^- in the microcrystalline samples. The $\nu_{3a}(\text{F}_T)$ mode of BrO_3^- in the single crystal samples did not undergo the initial drop in frequency observed with the microcrystalline samples as ClO_3^- was added, although the latter spectra were complicated by the additional mode between $\nu_{3a}(\text{F}_T)$ and $\nu_{3a}(\text{F}_L)$. The $\nu_4(\text{E})$ and $\nu_4(\text{F}_T)$ modes of ClO_3^- were found to merge in the single crystal data, unlike the microcrystalline data.

Figure (5-24) shows the Raman spectra of the external lattice mode region in the mixed crystals and figure (5-25) shows the frequency vs. concentration curves. As the frequency ordering of the modes is the same in both pure crystals there is no mode which originates in NaBrO_3 and becomes a mode of different symmetry in NaClO_3 .

Unpolarized near normal incidence infrared reflection spectra are shown in figures (5-26) & (5-27) for the ν_1 - ν_3 spectral region of BrO_3^- in the pure and mixed crystals. The pure NaBrO_3 spectrum shows two maxima. The low frequency maximum is due to $\nu_{3b}(\text{F}_T)$ and $\nu_1(\text{F}_T)$ while the high

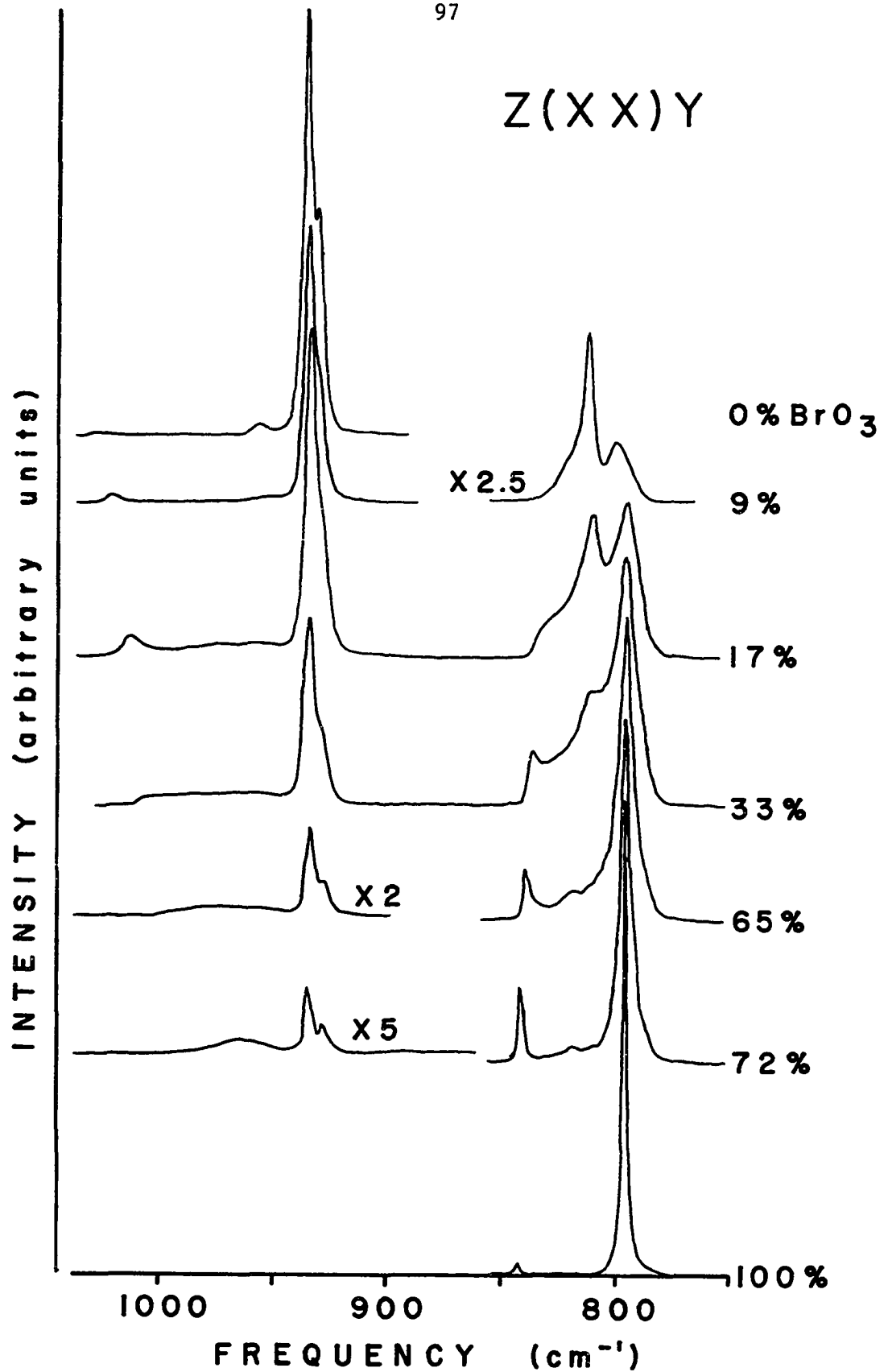


Figure (5-15). Mixed NaClO_3 - NaBrO_3 single crystal Raman spectra in ν_1 - ν_3 spectral region.

Figure (5-16). Mixed NaClO_3 - NaBrO_3 single crystal Raman spectra in the ν_1 - ν_3 spectral region.

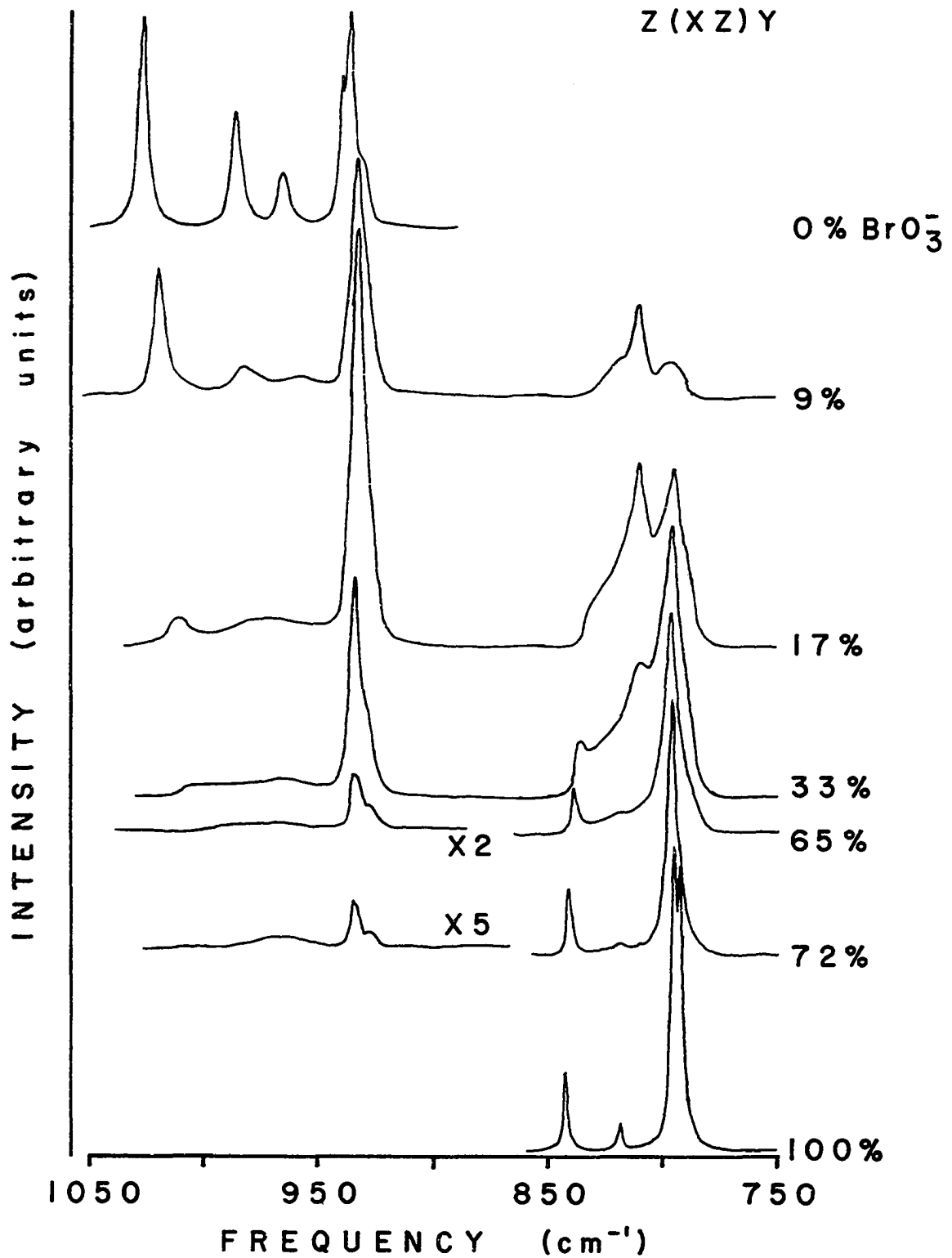


Figure (5-17). Raman spectra of the ν_2 - ν_4 spectral region of ClO_3^- in the $x(zz)y$ scattering geometry for the single mixed crystals. The spectra are displaced vertically.

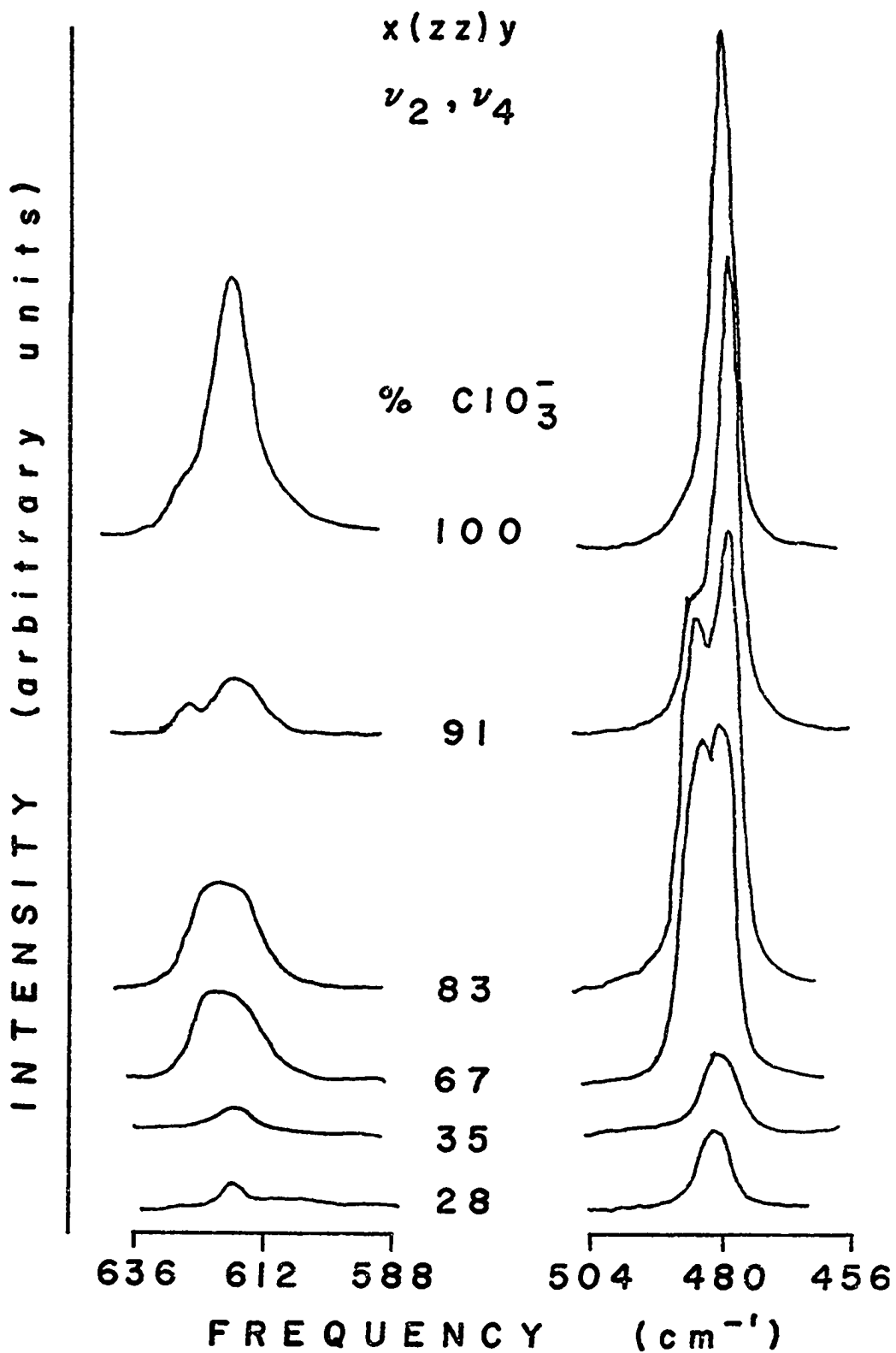


Figure (5-18). Raman spectra of the ν_2 - ν_4 spectral region of ClO_3^- in the $x(zx)y$ scattering geometry for the single mixed crystals. The spectra are displaced vertically.

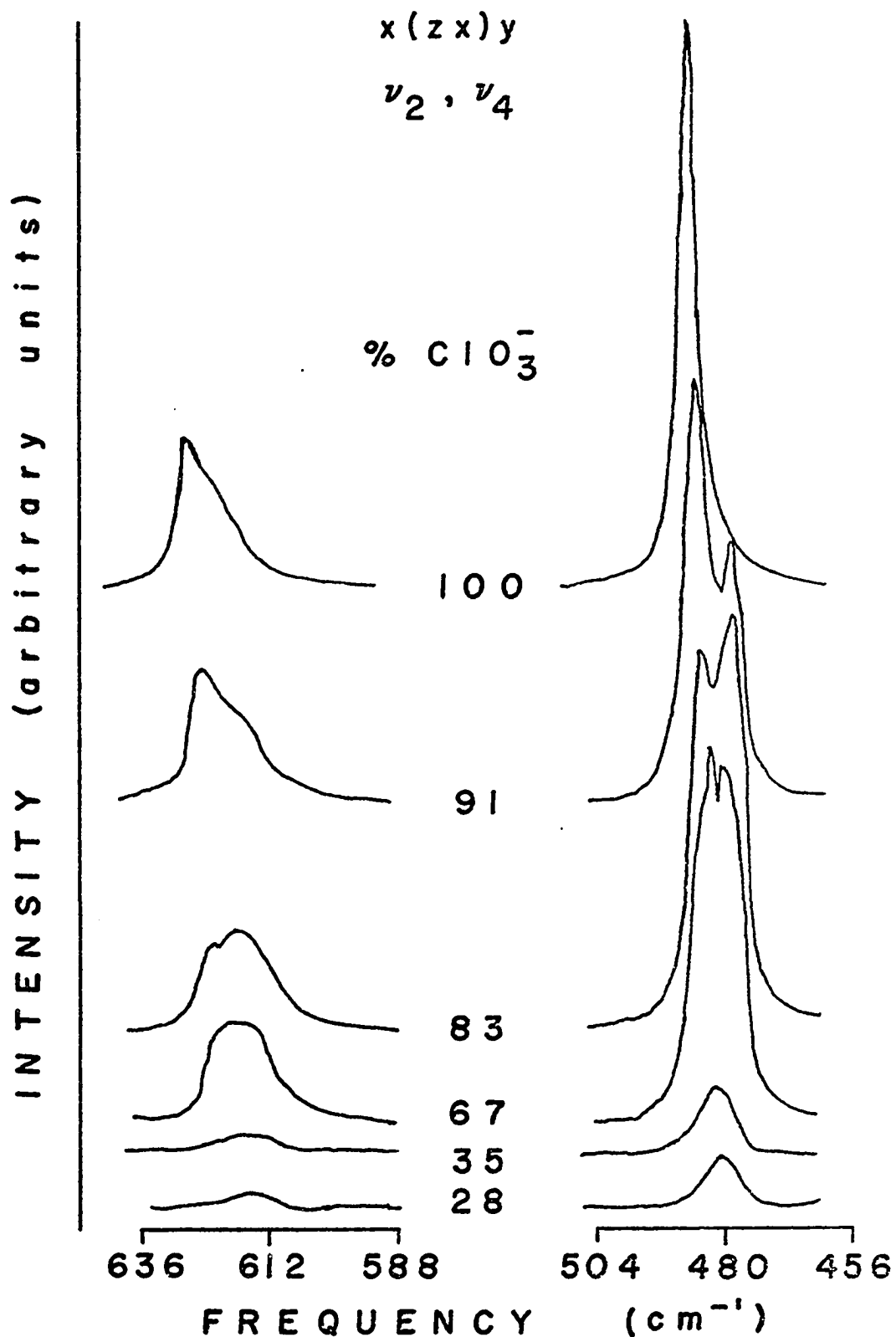


Figure (5-19). Raman spectra of the ν_2 - ν_4 spectral region of BrO_3^- in the $x(zz)y$ scattering geometry for the single mixed crystals. The spectra are displaced vertically.

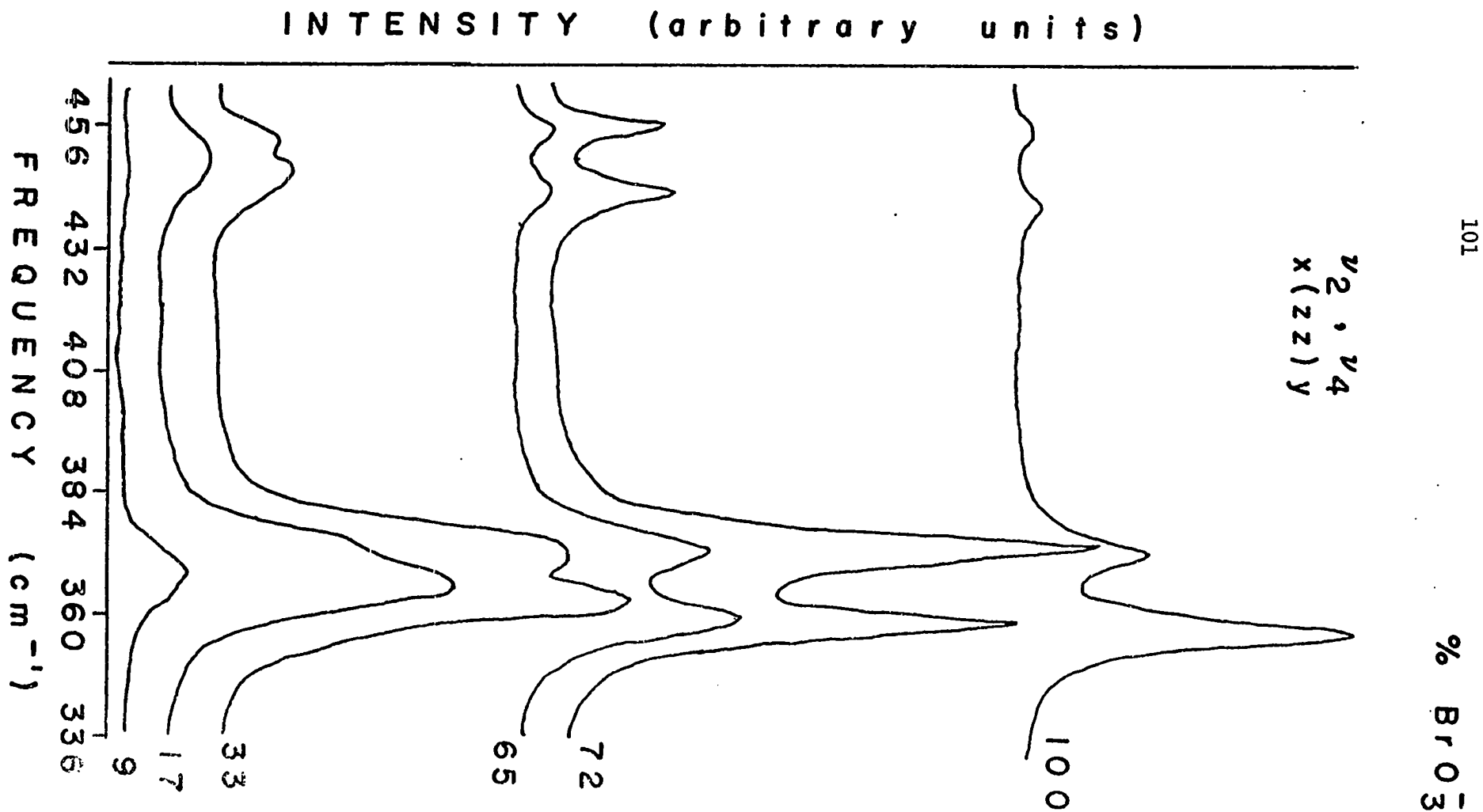
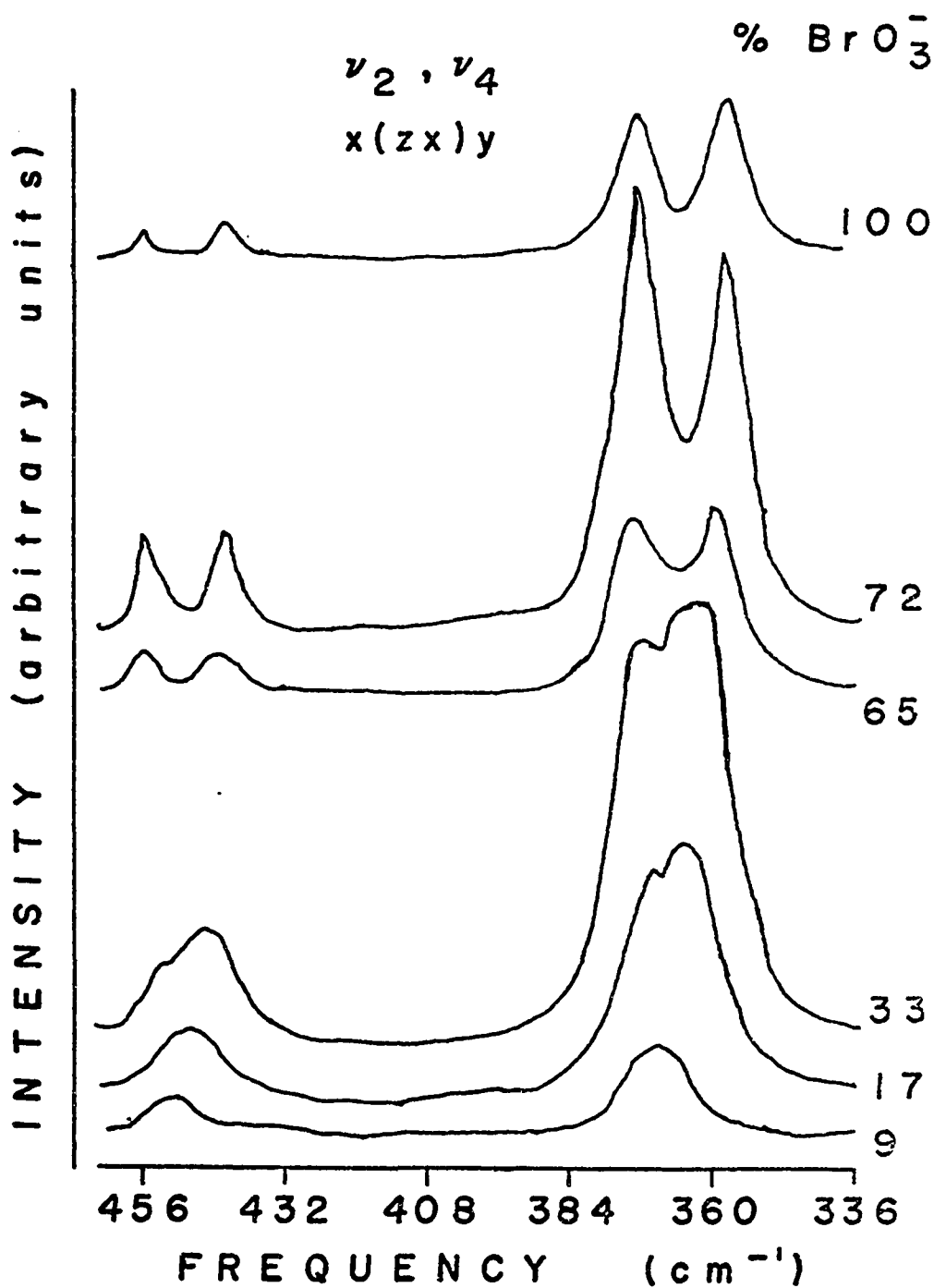


Figure (5-20). Raman spectra of the ν_2 - ν_4 spectral region of BrO_3^- in the $x(zx)y$ scattering geometry for the single mixed crystals. The spectra are displaced vertically.



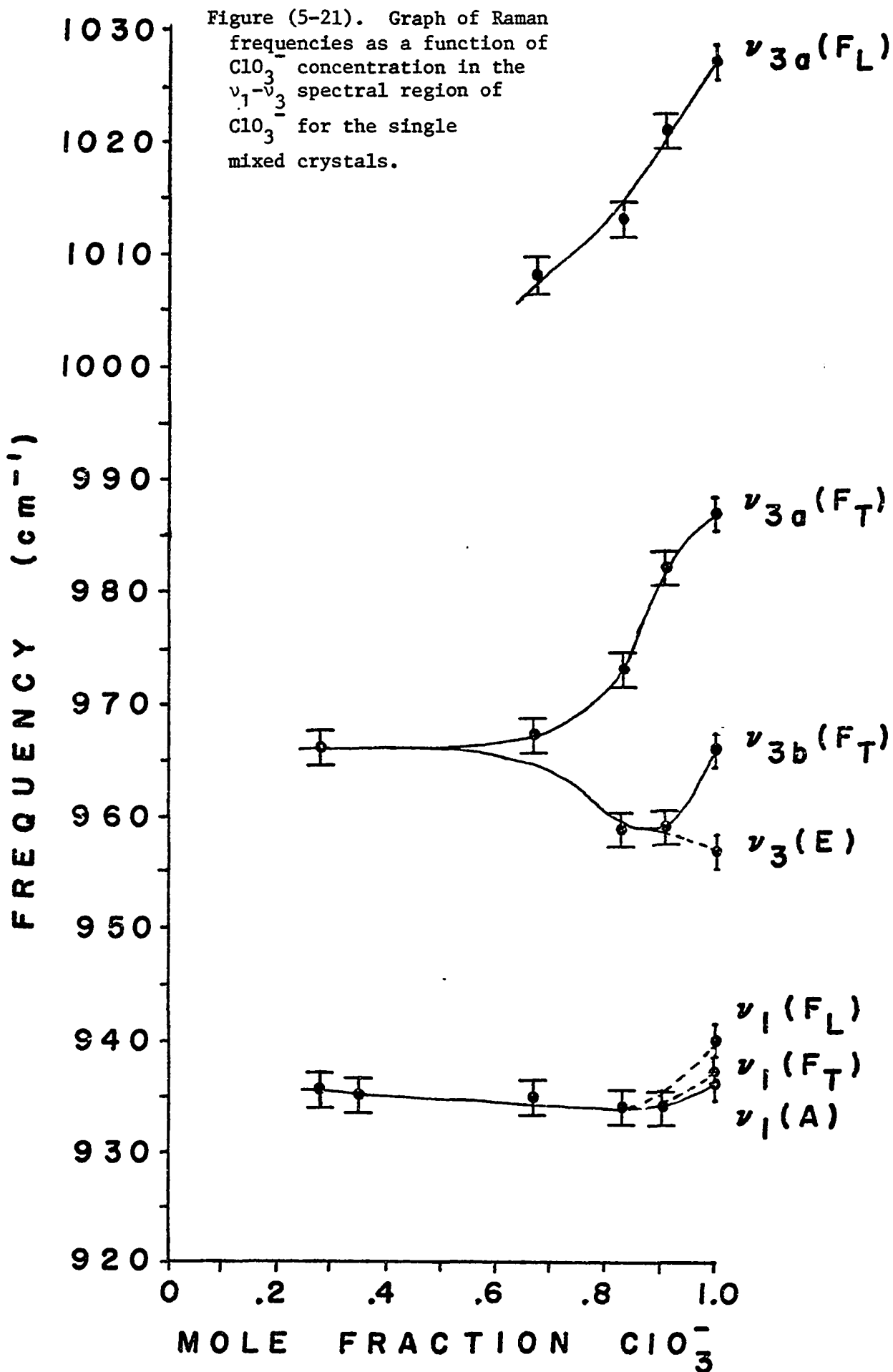
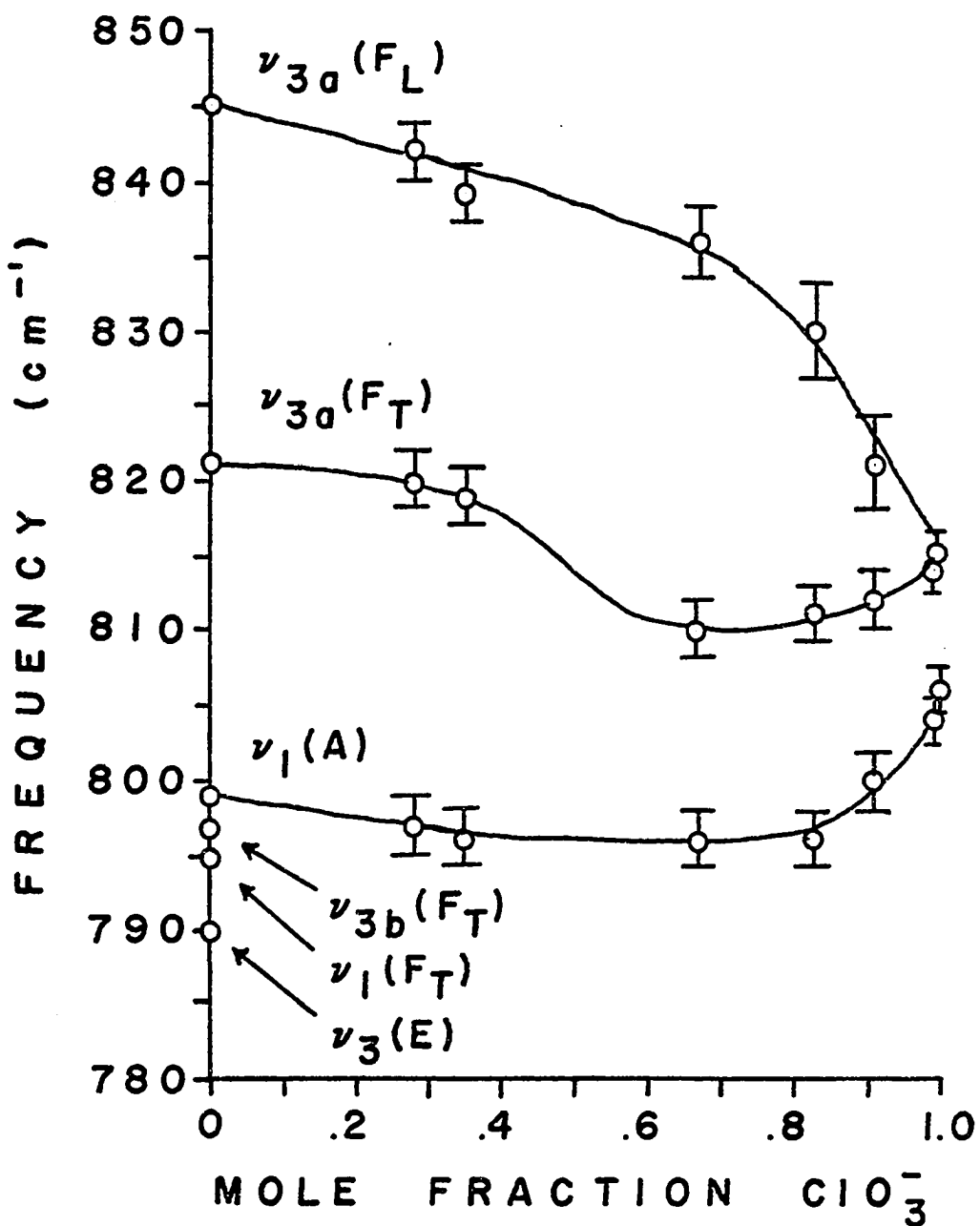


Figure (5-22). Graph of Raman frequencies as a function of ClO_3^- concentration in the ν_1 - ν_3 spectral region of BrO_3^- for the single mixed crystals.



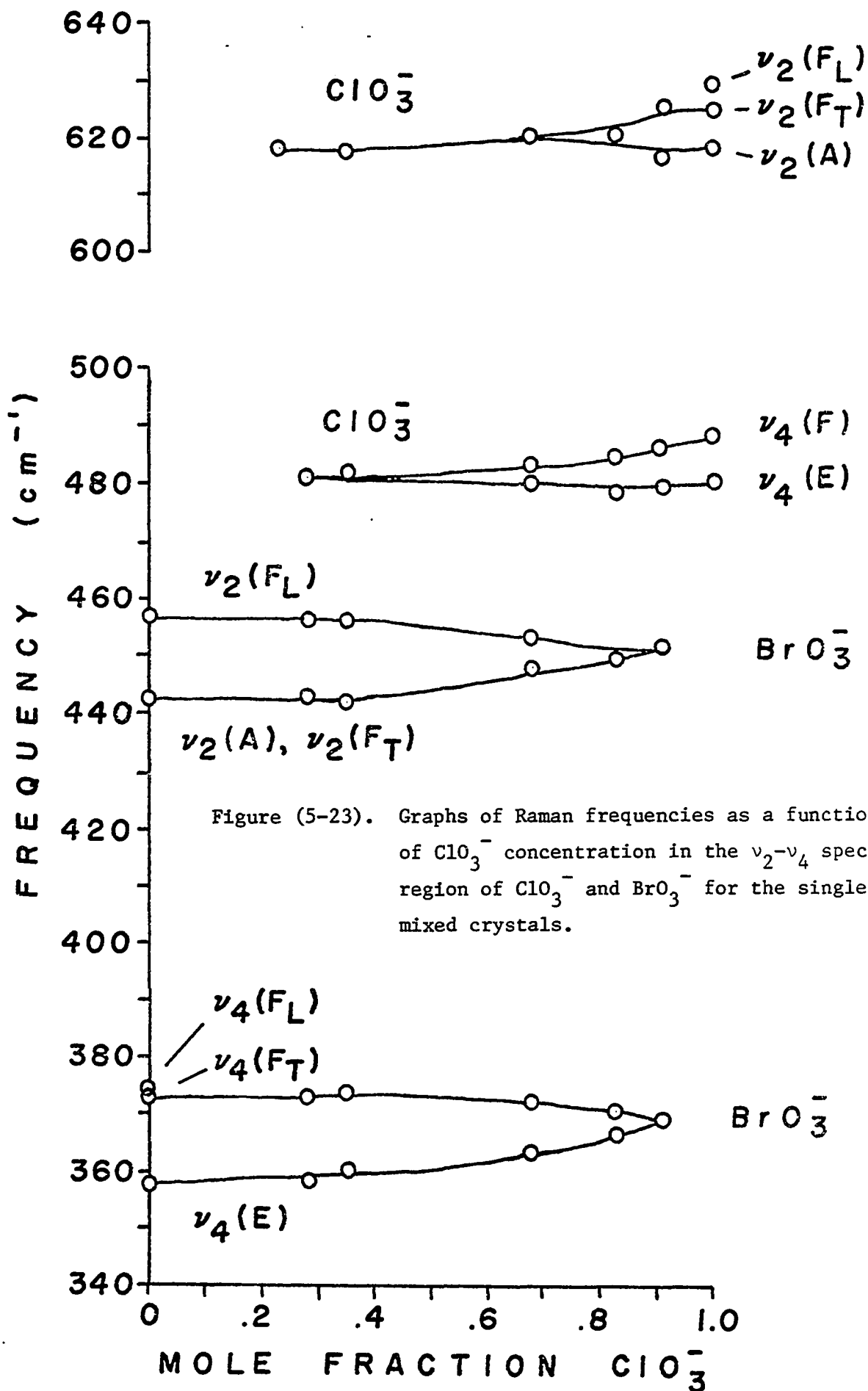


Figure (5-23). Graphs of Raman frequencies as a function of ClO_3^- concentration in the ν_2 - ν_4 spectral region of ClO_3^- and BrO_3^- for the single mixed crystals.

Figure (5-24). Mixed NaClO_3 - NaBrO_3 single crystal Raman spectra of the external optic modes.

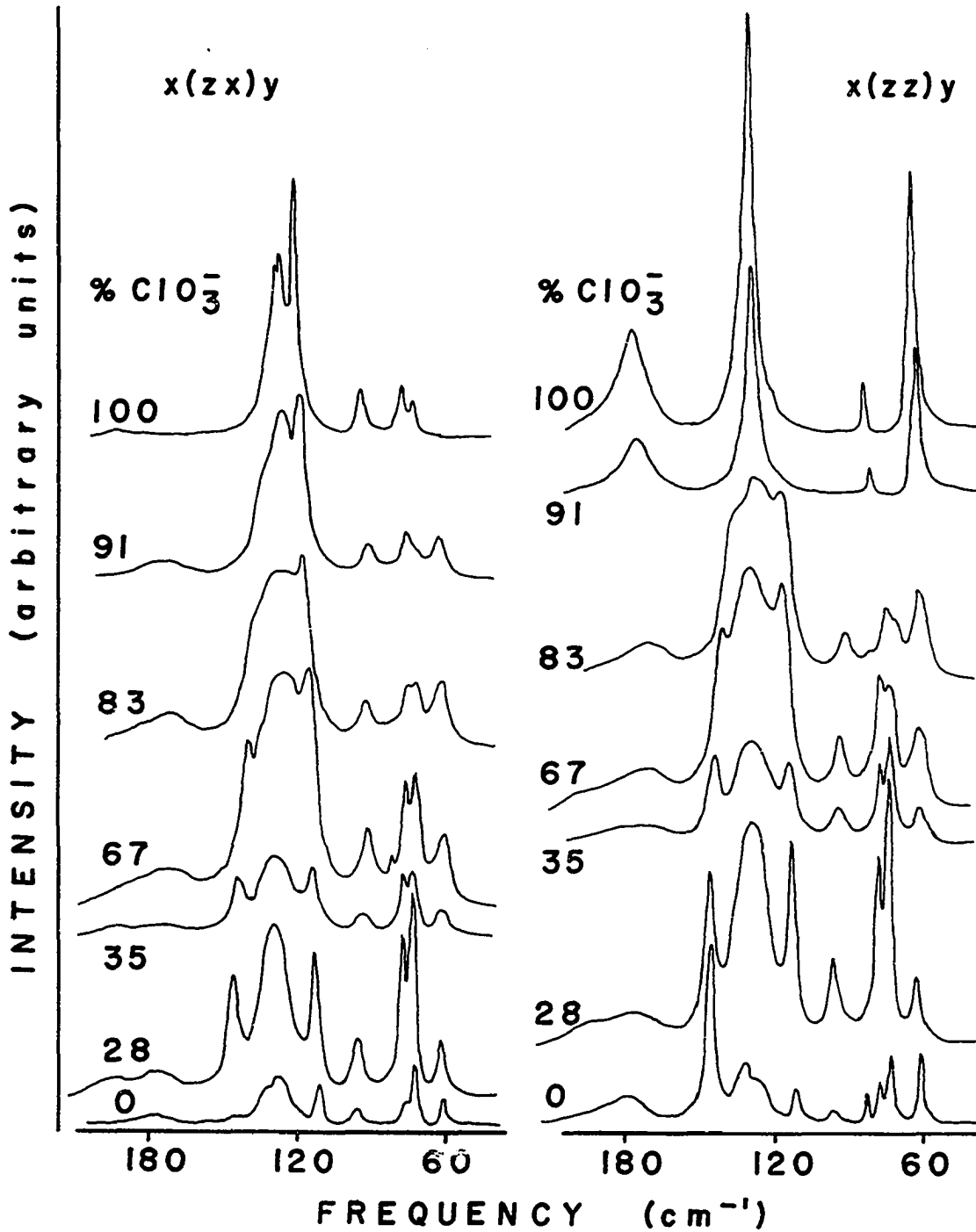
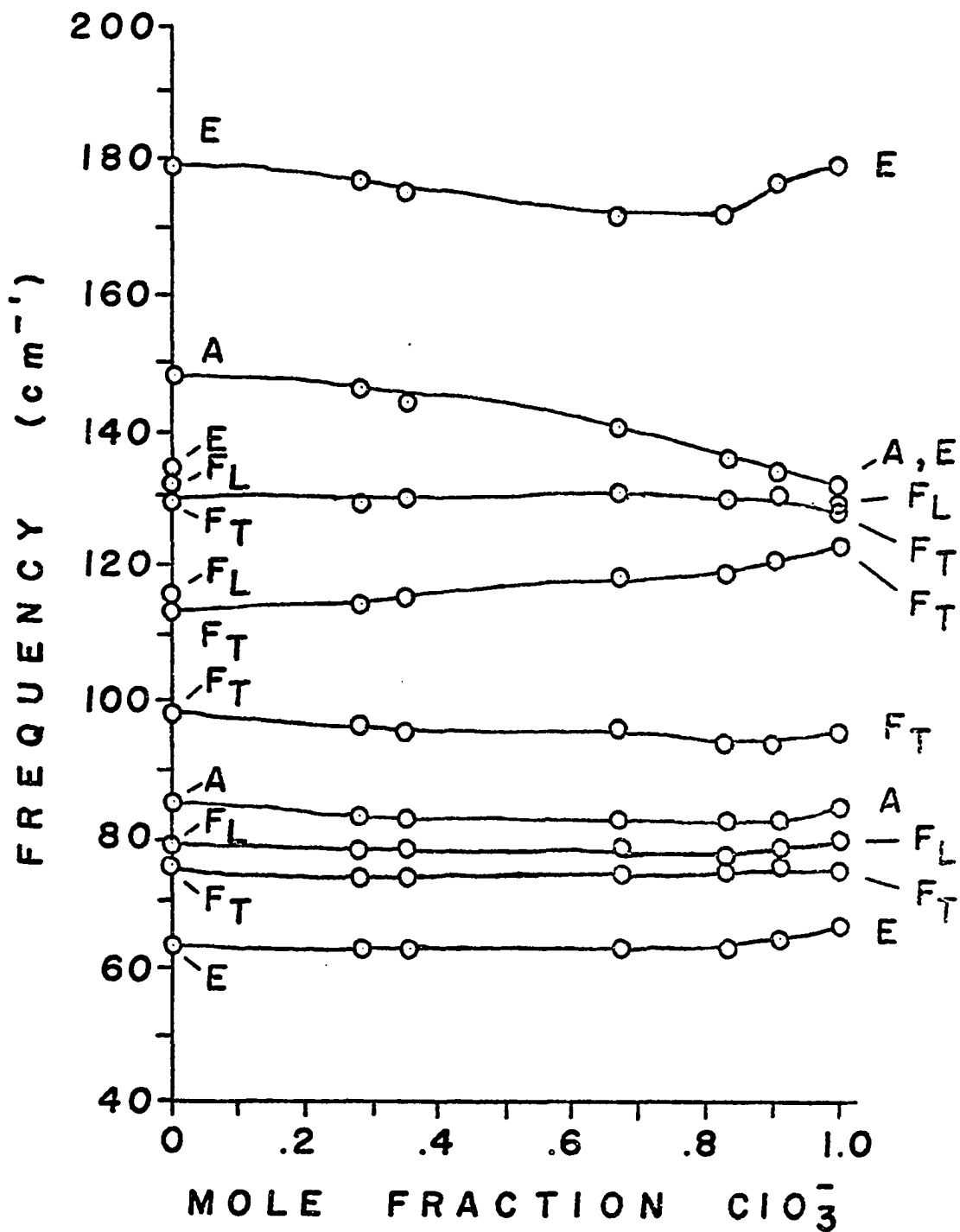


Figure (5-25). Graphs of Raman frequencies as a function of ClO_3^- concentration in the external optic mode spectral region of the single mixed crystals.



frequency maximum is due to $\nu_{3a}(F_T)$. The transverse-longitudinal frequency difference was found to be $\sim 1\text{cm}^{-1}$ in Raman measurements of $\nu_1(F)$, hence the dipole moment derivative and the reflectivity of this mode should be small. Therefore, almost all of the reflectivity of the low frequency maximum should be due to $\nu_{3b}(F_T)$. The pure crystals did not show any fine structure in this spectral region but the addition of ~ 2 mole percent ClO_3^- induced a number of fine structural features, primarily in the region of $\nu_{3b}(F)$. Three maxima were observed at 804, 810, and 817cm^{-1} in the ν_{3b} spectral region and a shoulder at $\sim 830\text{cm}^{-1}$ was observed in the ν_{3a} spectral region. At this impurity concentration no ClO_3^- modes were observed in the infrared reflectivity spectrum. As the concentration of ClO_3^- increased these features became more pronounced, but frequency shifts were minimal.

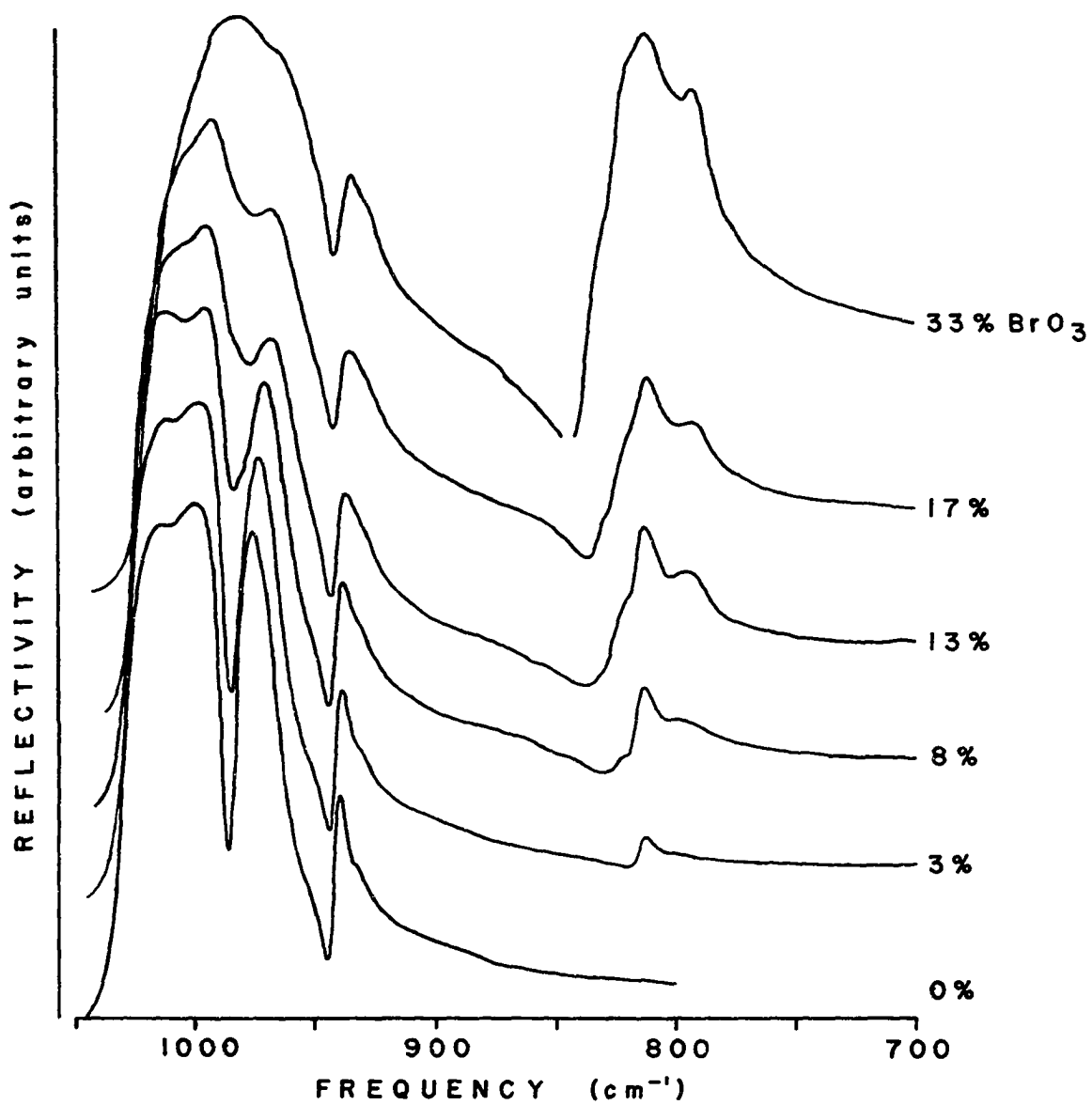
The pure NaClO_3 crystal has three maxima in the infrared reflectivity spectrum in the $\nu_1-\nu_3$ spectral region. These maxima are due to $\nu_1(F_T)$, $\nu_{3b}(F_T)$, and $\nu_{3a}(F_T)$ in order of increasing frequency. As BrO_3^- ions are substituted no major structural changes were observed in this spectral region as found in the BrO_3^- modes upon ClO_3^- substitution but the reflectivity between $\nu_{3a}(F_T)$ and $\nu_{3b}(F_T)$ begins to increase. This is accompanied by a frequency shift to lower frequencies with increasing BrO_3^- concentration.

The $\nu_1-\nu_3$ spectral region of the ClO_3^- ion changes smoothly and continuously with concentration whereas the $\nu_1-\nu_3$ spectral region of the BrO_3^- ion appears to have a discontinuity between 30 and 65 mole percent ClO_3^- . No crystals were obtained in order to bridge this spectral gap. Figures (5-28) & (5-29) show graphs of frequency vs. concentration for the $\nu_1-\nu_3$ spectral regions of ClO_3^- and BrO_3^- respectively, as measured in the near normal incidence reflectivity spectra. Frequencies were determined

by estimating the inflection points on the spectra and these curves are in agreement with the curves obtained from the Raman single crystal data. The infrared reflectivity data show a mode originating in the $\nu_{3b}(F_T)$ and $\nu_1(F_T)$ spectral region increasing in frequency to converge with the mode originating in $\nu_{3a}(F_T)$. This was probably masked in the Raman data by the intensity of the $\nu_1(A)$ mode. The modes originating in $\nu_{3a}(F_T)$ and $\nu_{3a}(F_L)$ of both the ClO_3^- and BrO_3^- ions could be followed to ~ 3 mole percent of the respective ions. The concentration dependence of the $\nu_{3a}(F_L)$ mode of the ClO_3^- ion was found to be approximately linear.

In the matrix isolation limit of BrO_3^- in $NaClO_3$, the $\nu_1(A)$ and $\nu_3(E)$ modes have essentially the same frequency. Figure (5-30) shows the polarized Raman spectra of a $NaClO_3$ crystal grown with the presence of 1% $NaBrO_3$ in solution. The crystal was cut and polished as a very thin plate to eliminate the effects of optical activity. These spectra clearly show that the $\nu_1(A)$ mode occurs at $814.5cm^{-1}$. The $z(xz)y$ spectrum shows that another mode occurs at about the same frequency which is identified as $\nu_3(E)$. The width at half height of the mode appearing in the $z(xz)y$ spectrum is $\sim 6.6cm^{-1}$. This is about twice the width of the mode appearing in the $z(xx)y$ spectrum, which is $\sim 3.3cm^{-1}$. Figure (5-30) also shows the Raman spectrum of a $NaClO_3$ crystal grown in the presence of 0.1% $NaBrO_3$. Infrared transmission spectra of these crystals reveal the strongest absorption at $814cm^{-1}$ in the 1% crystal and $816cm^{-1}$ in the 0.1% crystal with shoulders at 806 and $807cm^{-1}$ respectively. These spectra are shown in figure (5-31). As the $\nu_3(E)$ mode should have the greater intensity in the infrared experiment and the $\nu_1(A)$ mode should have the greater intensity in the Raman experiment, these spectra verify that there is almost an accidental degeneracy in these modes.

Figure (5-26). Near normal incidence infrared reflectivity spectra of mixed NaClO_3 - NaBrO_3 single crystals.



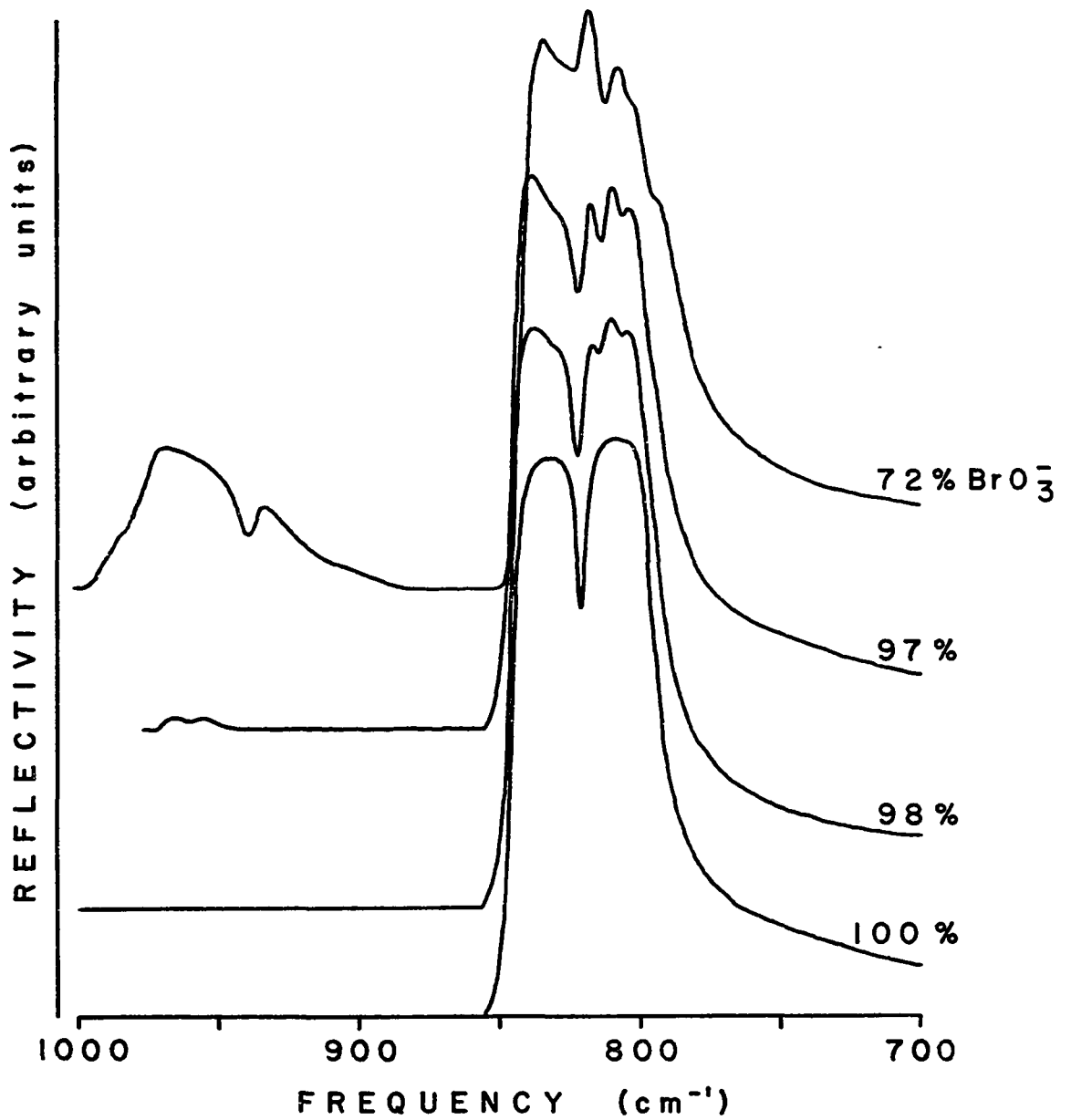


Figure (5-27). Near normal incidence infrared reflectivity spectra of mixed NaClO_3 - NaBrO_3 single crystals.

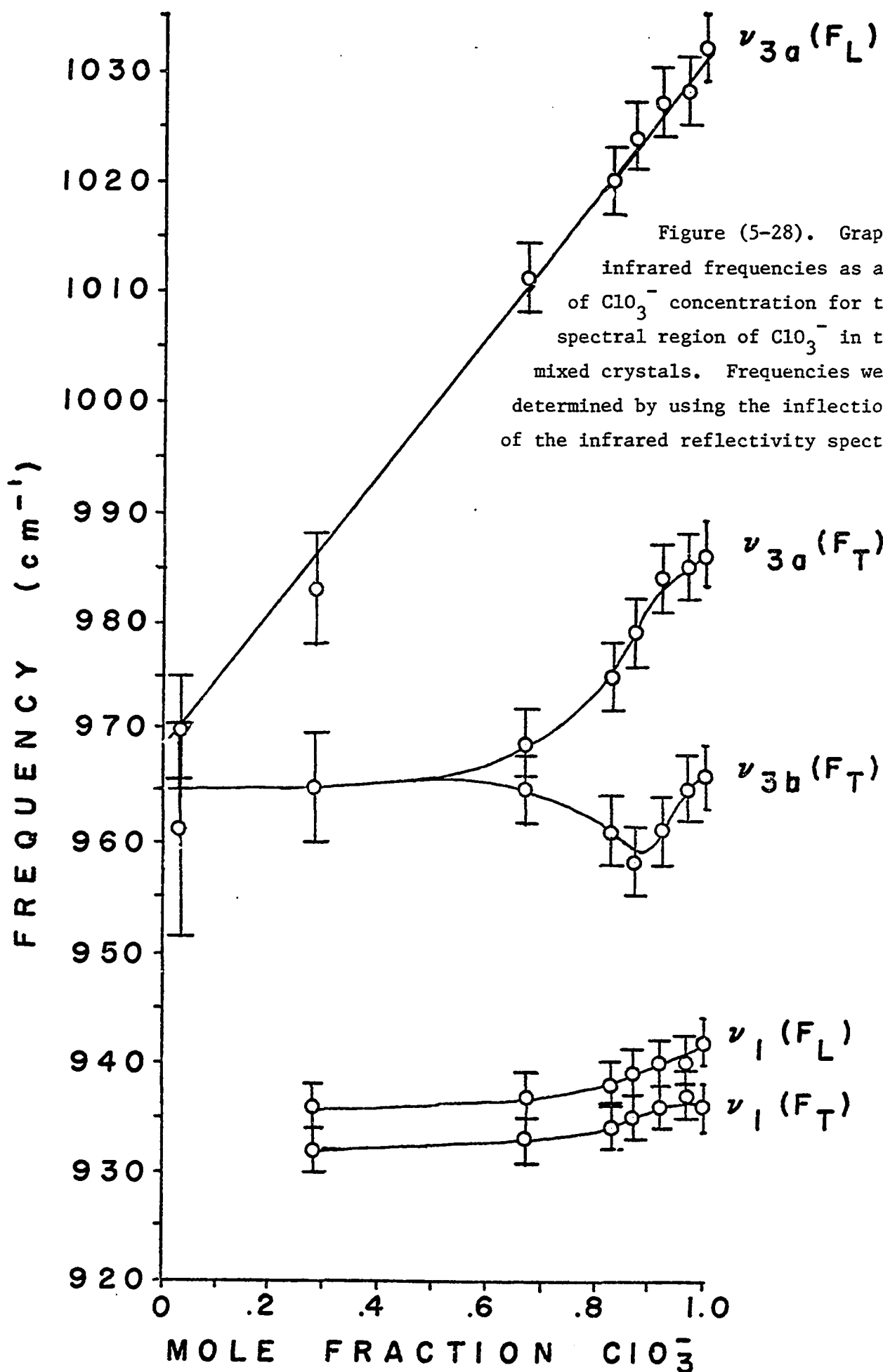


Figure (5-29). Graphs of infrared frequencies as a function of ClO_3^- concentration for the ν_1 - ν_3 spectral region of BrO_3^- in the single mixed crystals. Frequencies were determined by using the inflection points of the infrared reflectivity spectra.

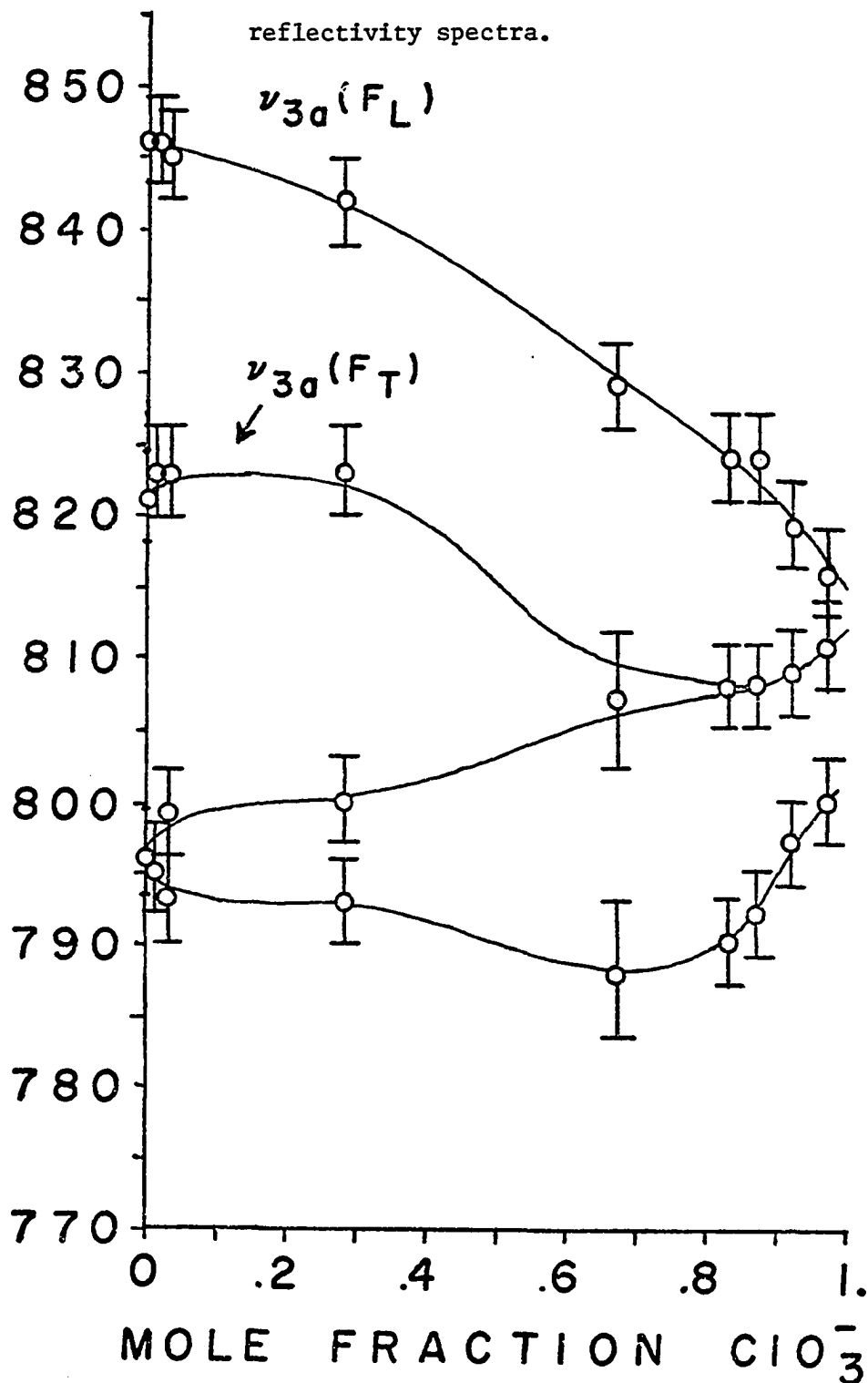


Figure (5-30). Polarized Raman spectra in the ν_1 - ν_3 spectral region of BrO_3^- of NaClO_3 crystals grown in the presence of 1% and 0.1% BrO_3^- .

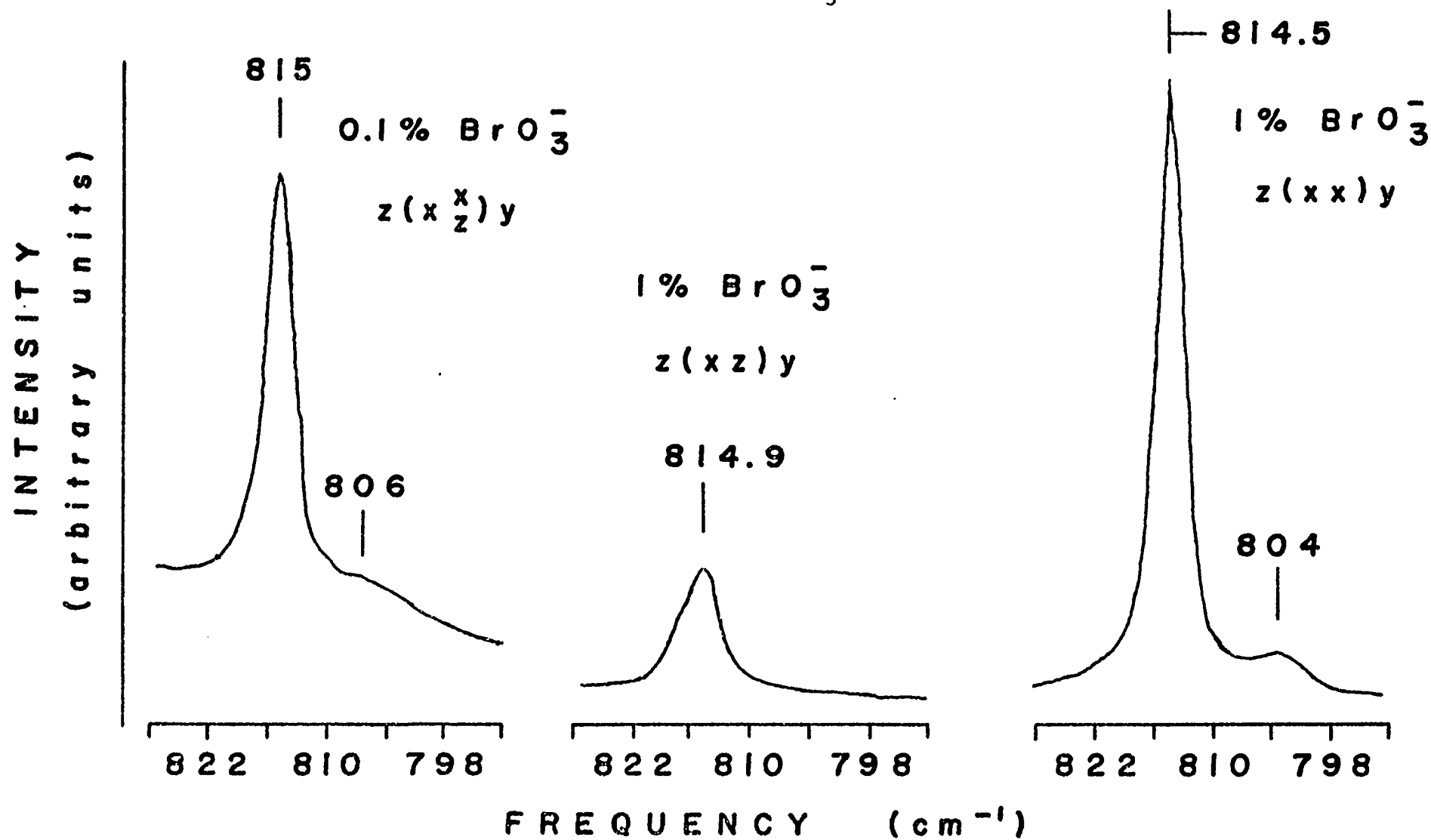
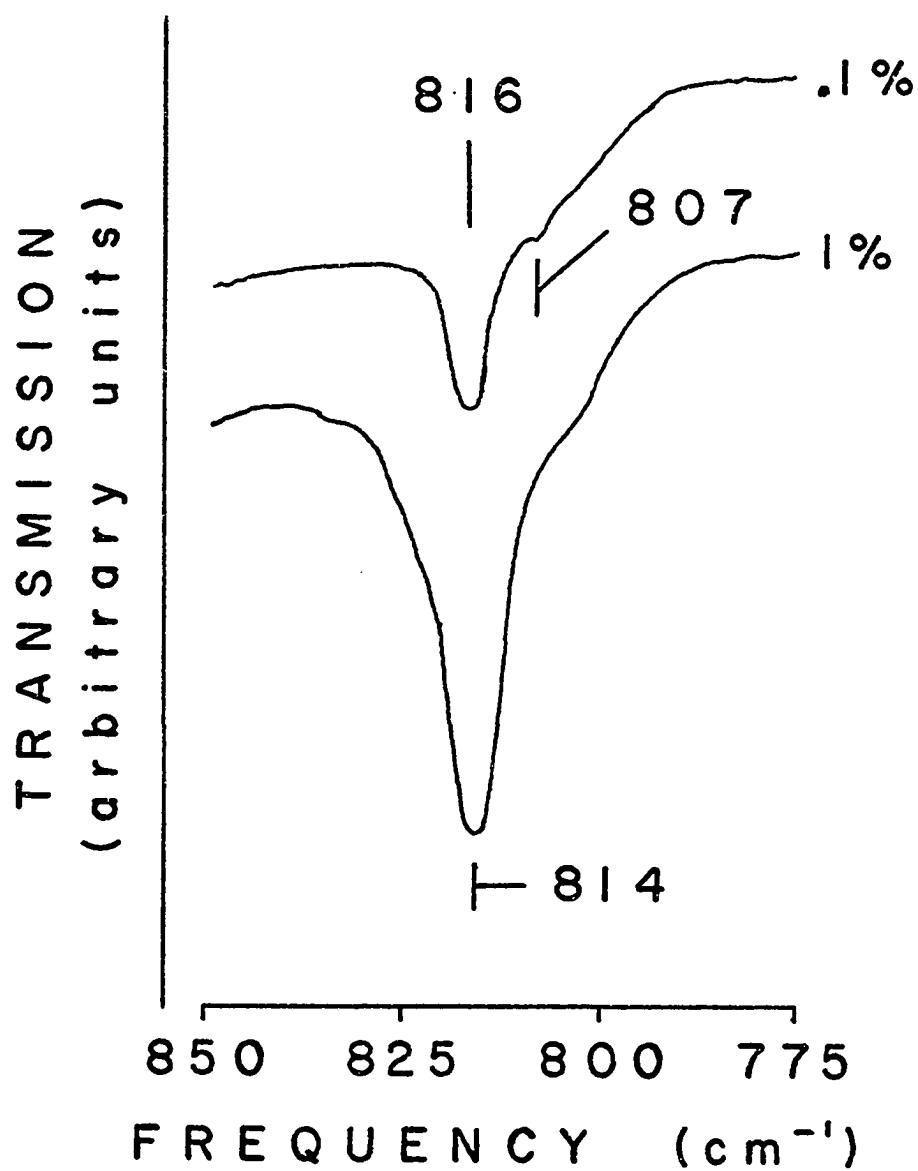


Figure (5-31). Infrared transmission spectra in the ν_1 - ν_3 spectral region of BrO_3^- in NaClO_3 crystals grown with the presence of 1% and 0.1% BrO_3^- in solution.



The lower frequency feature in the $\text{BrO}_3^- \nu_1-\nu_3$ spectral region which occurs at 807cm^{-1} is followed to 0.1% BrO_3^- concentration in the Raman spectrum. The Raman experiments indicate that it is of A symmetry in the C_3 matrix isolation limit. This may be attributed to a residual factor group component of ν_1 , although it is quite surprising to find a factor group remnant at such a dilute concentration.

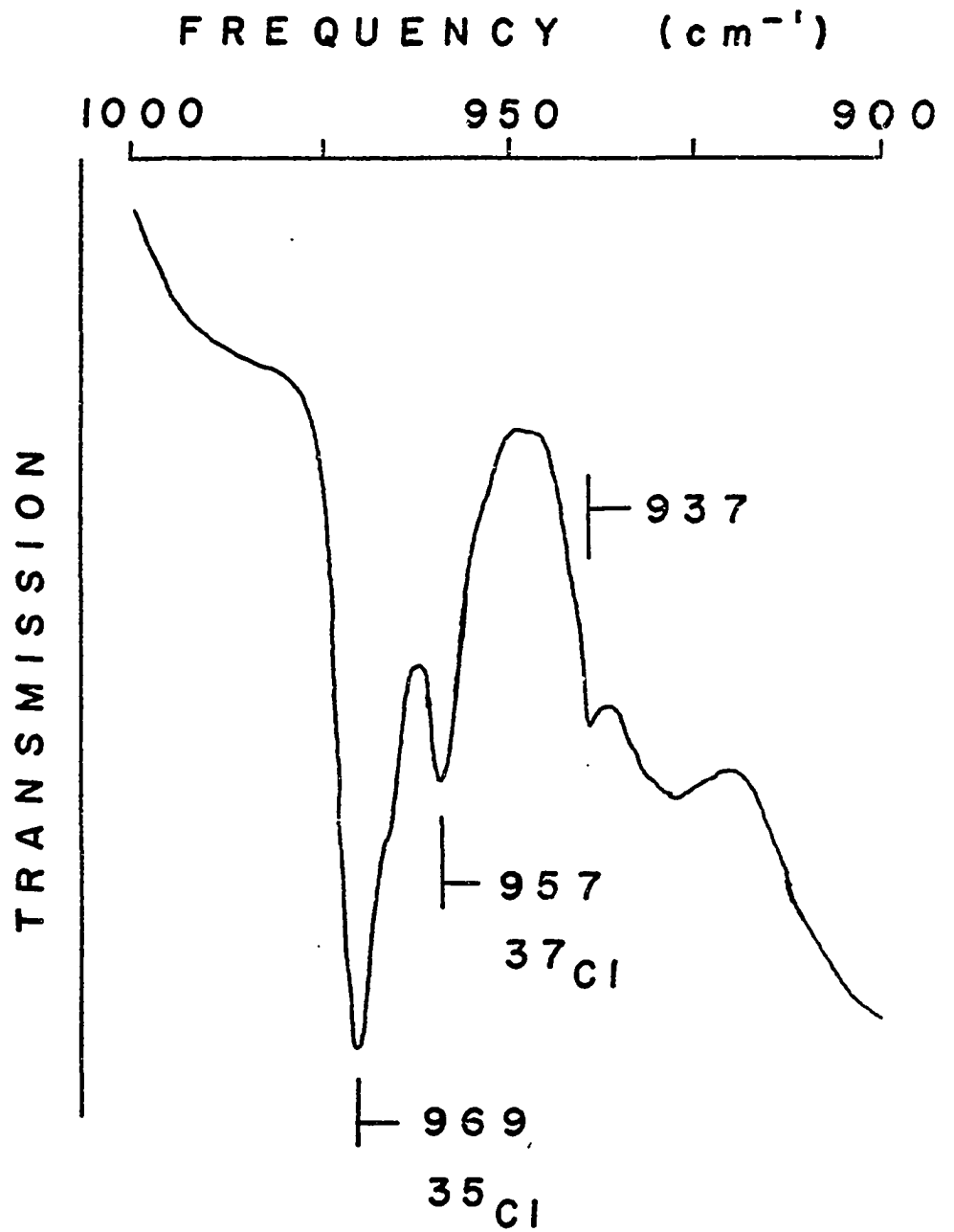
Figure (5-32) shows the infrared transmission spectrum of a NaBrO_3 crystal grown in the presence of 0.1% ClO_3^- . Two modes are found in the ν_3 spectral region of ClO_3^- . The highest frequency mode at 969cm^{-1} is attributed to the $\nu_3(\text{E})$ mode of $^{35}\text{ClO}_3^-$ in the C_3 matrix isolation limit while the mode at 957cm^{-1} is attributed to the $^{37}\text{ClO}_3^- \nu_3(\text{E})$ mode. A weak mode at 937cm^{-1} is attributed to $\nu_1(\text{A})$ in the matrix isolation limit.

Discussion

If the major interaction between anions is assumed to be due to long range dipolar coupling and the dipolar coupling between like anions is much greater than between unlike anions, then the addition of impurities will decrease the dipolar coupling between host ions and a frequency shift should result which is dependent upon the magnitude of the dipole moment derivative, $\partial\mu/\partial q$, of the mode. This frequency shift should be different for modes of different symmetry as the nature of the dipolar coupling differs for modes of different symmetry.

The $\nu_1(\text{A})$ and $\nu_1(\text{F})$ modes of NaClO_3 have a smaller $\partial\mu/\partial q$ than the ν_3 modes as indicated by the transverse-longitudinal splitting of the $\nu_1(\text{F})$ mode being substantially less than the $\nu_3(\text{F})$ modes. It was observed in NaClO_3 that upon dilution with BrO_3^- to ~9% BrO_3^- the $\text{ClO}_3^- \nu_3(\text{F})$ modes shifted by $\sim 7\text{cm}^{-1}$ to a lower frequency whereas the $\text{ClO}_3^- \nu_1(\text{F})$ mode shifted

Figure (5-32). Infrared transmission spectrum in the ν_1 - ν_3 spectral region of ClO_3^- in a NaBrO_3 crystal grown with the presence of 0.1% ClO_3^- in solution.



to a lower frequency by only $\sim 1\text{cm}^{-1}$. The $\nu_1(\text{A})$ mode also shifted by only $\sim 1\text{cm}^{-1}$ to a lower frequency. This initial frequency shift is attributed to a loss of the long range dipolar coupling. The $\nu_{3a}(\text{F}_\text{T}) - \nu_{3b}(\text{F}_\text{T})$ frequency separation remained very nearly constant during the initial stages of dilution. Upon further dilution the factor group symmetry is disrupted and the crystal can no longer sustain the ν_3 multiplet. This is marked by the convergence in frequency of the $\nu_{3a}(\text{F}_\text{T})$ and $\nu_{3b}(\text{F}_\text{T})$ components. The $\nu_3(\text{E})$ mode was found to be very weak in the Raman spectrum and was observed only in the pure crystal.

Another factor which should influence the frequencies of the ClO_3^- modes is the effective size of the unit cell. As BrO_3^- is added to the lattice the effective unit cell becomes larger and the ClO_3^- modes should decrease in frequency. This explains the observation that the BrO_3^- modes did not undergo the initial drop in frequency which occurs in the ClO_3^- ν_1 ν_3 modes.

In the usual normal mode analysis for the point group of BrO_3^- , the symmetric stretching (ν_1) and asymmetric stretching (ν_3) motions are decoupled by symmetry. For the pure NaBrO_3 crystal these modes are still decoupled under the site group analysis. The factor group, however, determines the contribution of each site to the unit cell symmetrized modes and in this case produces modes originating in symmetric stretching motions with the same symmetry as those originating in asymmetric stretching motions, e.g. $\nu_1(\text{F})$, $\nu_{3b}(\text{F})$, and $\nu_{3a}(\text{F})$. In the pure NaBrO_3 crystal the modes originating in the free ion ν_1 and ν_3 modes occur at very nearly the same frequency and interactions between them cannot be neglected. The observed pure crystal frequencies labeled $\nu_1(\text{F})$, $\nu_{3a}(\text{F})$, and $\nu_{3b}(\text{F})$ are mixtures of the two types

of intramolecular motion. The T-L splitting of the $\nu_1(F)$ mode is only $\sim 1\text{cm}^{-1}$ which indicates that this mode has a small dipole moment derivative. During the initial stages of dilution in which some of the long range dipolar coupling is lost this mode should shift very little. Since the $\nu_{3b}(F_T)$ mode cannot cross the $\nu_1(F_T)$ mode it cannot drop in frequency as did the $\nu_{3b}(F_T)$ mode of ClO_3^- , which in turn means that the $\nu_{3a}(F_T)$ mode cannot drop in frequency. At higher concentrations of ClO_3^- the effective factor group symmetry is destroyed which is marked by the decrease in frequency of $\nu_{3a}(F_T)$ and the increase in frequency of $\nu_{3b}(F_T)$, as seen in figures (5-22) & (5-28). The ν_1 mode was not found to shift smoothly from its pure crystal frequency to its matrix isolation frequency, but rather, between 50 and 90% ClO_3^- the totally symmetric component seems to decay at $\sim 796\text{cm}^{-1}$ and reappear at $\sim 811\text{cm}^{-1}$. This behavior was found in both the single crystal and micro-crystalline Raman data, as shown in figures (5-9) & (5-23). This could be explained in terms of the high frequency component developing more symmetric stretching character whereas the low frequency component loses some of its symmetric stretching character as the BrO_3^- concentration decreases.

An alternative explanation is that the pure crystal mode labeled ν_{3b} already contains part of the symmetric stretching motion. This mode was observed in the infrared reflectivity data to increase in frequency to merge with the $\nu_{3a}(F_T)$ mode at ~ 70 to 80% ClO_3^- . If this mode contains most of the symmetric stretching motion, which is usually assigned to $\nu_1(F)$, then disruption of the factor group could allow this mode to increase in Raman scattering intensity and eventually become the $\nu_1(A)$ mode in the matrix isolation limit. The original $\nu_1(A)$ component of the pure crystal would then gradually lose intensity to become a decaying factor group component.

The pure crystal mode labeled $\nu_1(F)$ contains mostly asymmetric stretching motions and eventually becomes a decaying factor group component as did $\nu_1(A)$.

At very dilute concentrations of BrO_3^- the frequencies of both the $\nu_1(A)$ and $\nu_3(E)$ modes (C_3 site group approximation) and the residual factor group components underwent a sharp increase in frequency. This is probably due to a decrease in the effective unit cell volume which should increase the frequencies of the BrO_3^- modes. Another factor may be that the $\text{BrO}_3^- - \text{BrO}_3^-$ nearest neighbor interactions, which are dominated by dipolar coupling, are very important in lowering the frequencies of the BrO_3^- modes.

Mixed crystal systems are usually classified as having one-mode or two-mode behavior which is determined by the existence of local modes and gap modes. The terms used for local modes and gap modes must be used with caution as a gap mode is taken to be an impurity mode observed between the acoustic modes and the optic modes of the host crystal and a local mode is taken to be an impurity mode above the optic modes of the host. The system studied here does not belong to the usual class of mixed crystals in that some of the impurity modes occurred between the optic modes of the host crystal and in the usual sense cannot be classified as local modes or gap modes. The definitions for one-mode and two-mode behavior will be modified here. "One-mode" behavior will be taken to mean that one mode is observed in the mixed crystal whose frequency varies continuously with concentration between a normal mode frequency of one pure component and a normal mode frequency of the other pure component. Its intensity will be intermediate between the intensities of the two pure crystal normal modes. "Separated-mode" behavior will be taken to mean that a mixed crystal mode varies continuously with concentration between a normal mode frequency of one

pure constituent to the matrix isolation frequency of that component. Its intensity will be dependent upon the concentration of that constituent. Each mode in a particular crystal must be examined independently as it is possible for some modes to exhibit one-mode behavior and other modes to exhibit separated-mode behavior.

In terms of the above definition, the external lattice modes of the $\text{Na}(\text{ClO}_3)_x(\text{BrO}_3)_{1-x}$ mixed crystal system were found to exhibit one-mode behavior while the internal optic modes were found to exhibit separated-mode behavior.

References for Chapter V

1. R. K. Chang, B. Lacina, and P. S. Pershan, Phys. Rev. Lett. 17, 755 (1966).
2. P. J. Gielisse, J. N. Plendl, L. C. Mansur, R. Marshall, S. S. Mitra, R. Mykolajewycz, and A. Smakula, J. Appl. Phys. 36, 2446 (1965).
3. R. M. Fuller, C. M. Randall, and D. J. Montgomery, Bull. Am. Phys. Soc. 9, 644 (1964).
4. J. H. Fertel and C. H. Perry, Phys. Rev. 184, 874 (1969).
5. I. F. Chang and S. S. Mitra, Phys. Rev. B 2, 1215 (1970).
6. Y. S. Chen, W. Shockley, and G. L. Pearson, Phys. Rev. 151, 648 (1966).
7. H. W. Verleur and A. S. Barker, Phys. Rev. 149, 715 (1966).
8. H. W. Verleur and A. S. Barker, Jr., Phys. Rev. 155, 750 (1967).
9. O. Brafman, I. F. Chang, G. Lengyel, S. S. Mitra, and E. Carnall, Jr., Phys. Rev. Lett. 19, 1120 (1967).
10. I. F. Chang and S. S. Mitra, Phys. Rev. 172, 924 (1968).
11. M. H. Brodsky, G. Lukovsky, M. F. Chen, and T. S. Plaskett, Phys. Rev. 2, 3303 (1970).
12. C. H. Perry and N. E. Tornberg, Phys. Rev. 183, 595 (1969).
13. C. Aravindakshan, Zeitschrift für Kristallographie 111, 241 (1959).
14. Ralph W. G. Wyckoff, Crystal Structures, vol. 2, Pp 380 (Interscience Publishers, New York, 1960).
15. R. Loudon, Advan. Phys. 13, 423 (1964).
16. Ralph E. Miller and J. C. Decius, J. Chem. Phys. 59, 4871 (1973).
17. C. M. Hartwig, D. L. Rousseau, and S. P. S. Porto, Phys. Rev. 188, 1328 (1969); Phys. Rev. B 2, 1216 (1970).
18. A. D'Andrea, B. Fornari, G. Mattei, M. Pagannone, and M. Scrocco, Phys. Stat. Sol. B 53, 577 (1972).

CHAPTER VI

Vibrational Study of the Optic Modes of RbClO_3 - RbBrO_3 Mixed Crystals

Introduction

Both rubidium chlorate (RbClO_3) and rubidium bromate (RbBrO_3) crystallize in the C_{3v}^5 ($R3m$) space group with one molecule per rhombohedral unit cell. The crystallographic parameters are $\alpha = 86.63^\circ$ and $a = 4.440\text{\AA}$ for RbClO_3 ¹, and $\alpha = 87.60^\circ$ and $a = 4.492\text{\AA}$ for RbBrO_3 .² The Rb atom and Cl or Br atoms occupy sites of C_{3v} symmetry. The correlation diagram in figure (6-1) shows that there is no point group, site group, or factor group splitting and all internal optic modes are both infrared and Raman active.

As the unit cell parameters are similar and the space groups of these crystals are identical, it seemed plausible that this system would undergo isomorphous substitution of the anions over the complete concentration range. This would provide a mixed crystal system having internal optic modes with long range dipolar coupling playing an important role in its lattice dynamics. Since all of the pure crystal internal and external optic modes are simultaneously infrared and Raman active, with the exception of one external libration mode of A_2 symmetry, this system should offer a large amount of spectroscopic information about the dynamics of mixed crystals. It should also lend itself to future theoretical studies due to the simplicity of the unit cell.

In this work the mixed crystal system $\text{Rb}(\text{ClO}_3)_x(\text{BrO}_3)_{1-x}$ is investigated with emphasis on the ν_1 - ν_3 internal optic modes of ClO_3^- and BrO_3^- .

RbClO₃ & RbBrO₃
CORRELATION DIAGRAM

POINT GROUP	C _{3v}	SITE GROUP	C _{3v}	FACTOR GROUP	C _{3v}	
ν_1, ν_2	A ₁	—————	A ₁	—————	A ₁	z, xx + yy, zz
	A ₂	—————	A ₂	—————	A ₂	
ν_3, ν_4	E	—————	E	—————	E	(x, y), (xx - yy, xy), (yz, zx)

Figure (6-1). Vibrational correlation diagram for RbClO₃ and RbBrO₃.

Experimental

Many attempts were made to grow pure RbClO_3 and RbBrO_3 crystals from aqueous solution. Slow evaporation from aqueous solution proved to be the best method although the results were not easily reproduced. The solutions were prepared using recrystallized RbClO_3 and RbBrO_3 obtained from Atomergic Chemetals Company. The solutions were contained in small jars covered with aluminum foil. Several small holes were punched in the foil to allow evaporation and the jars were placed in an oven at $47.0 \pm 0.1^\circ\text{C}$. Greater temperature fluctuations resulted in polycrystalline masses. Mixed crystals were prepared in a similar manner using weighed amounts of materials.

Microcrystalline samples were prepared using weighed amounts of solute and evaporated under an aspirator vacuum while being stirred. The microcrystals were packed in glass capillaries for Raman measurements.

Infrared reflectivity spectra were recorded at room temperature on a Beckman IR-12 spectrometer with an average angle of incidence of 15° and a 4:1 linear image reduction. Room temperature Raman spectra were obtained using a Spex Ramalog 5 spectrometer equipped with a 2 watt argon ion laser. Integrated Raman intensities were obtained by weighing the chart paper in the ν_1 - ν_3 spectral regions of BrO_3^- and ClO_3^- .

Pure Crystals

Hwang and Solin reported the Raman spectrum of RbClO_3 in an oblique phonon study.³ The spectra obtained by those authors were recorded using an immersion technique in which the crystal is immersed in a fluid having an index of refraction similar to that of the crystal in order to reduce the solid angle of refraction.⁴ The Raman frequencies obtained in this study for RbClO_3 are presented in table (6-1) and agree favorably with

those reported by Hwang and Solin.

Crystal faces parallel and perpendicular to the optic axis were obtained by grinding the crystal on emery paper, followed by polishing on frosted glass. Figure (6-2) shows the polarized infrared reflectivity spectrum of RbClO_3 in the internal optic mode spectral region. An anomalous "dip" is observed in the reflectivity of the $\nu_3(\text{E})$ mode at $\sim 983\text{cm}^{-1}$. Using frequencies taken from table (6-1) the $2\nu_4(\text{E})$ overtone should occur in the $\nu_3(\text{E})$ T-L band gap, however, the frequency of the dip is greater than the expected frequency of the overtone. This should rule out the possibility that the dip is caused by the $2\nu_4(\text{E})$ overtone, as was found with NaNO_3 in chapter 2. Another explanation is that the dip is caused by surface damage, which was discussed in chapter 4. The reflectivity loss at $\sim 983\text{cm}^{-1}$ was found to vary with different crystals and surface preparation adding evidence that surface damage is the primary cause of this reflectivity loss.

The Raman frequencies for RbBrO_3 are presented in table (6-1). It is interesting to note that the internal optic mode frequencies of RbBrO_3 are almost identical to those reported by Unger and Haussühl for the isomorphous crystal KBrO_3 .⁵ The polarized infrared reflectivity spectra of RbBrO_3 are shown in figures (6-3) & (6-4). The anomalous dip in the reflectivity of $\nu_3(\text{E})$ is attributed to surface damage, as was shown to be the case with the isomorphous crystal KBrO_3 in chapter 4.

Using the inflection points of the infrared reflectivity spectrum as a measure of the transverse and longitudinal frequencies is a common practice among solid state vibrational spectroscopists. As the internal optic modes of RbClO_3 and RbBrO_3 are simultaneously infrared and Raman

Table (6-1). Frequencies of the internal optic modes of RbClO_3 and RbBrO_3 from Raman scattering and infrared inflection points.

RbClO_3				
	Raman		Infrared	
	ω_T	ω_L	ω_T	ω_L
	<u>ω_T</u>	<u>ω_L</u>	<u>ω_T</u>	<u>ω_L</u>
ν_1	925		926	936
ν_2	611		613	621
ν_3	941	1011	940	1014
ν_4	485	491	484	491

RbBrO_3				
	Raman		Infrared	
	ω_T	ω_L	ω_T	ω_L
	<u>ω_T</u>	<u>ω_L</u>	<u>ω_T</u>	<u>ω_L</u>
ν_1	793	803	793	803
ν_2	419	448	423	452
ν_3	779	838	777	838
ν_4	358	369	363	373

Frequencies are in cm^{-1} .

INFRARED REFLECTION SPECTRA OF RbClO_3

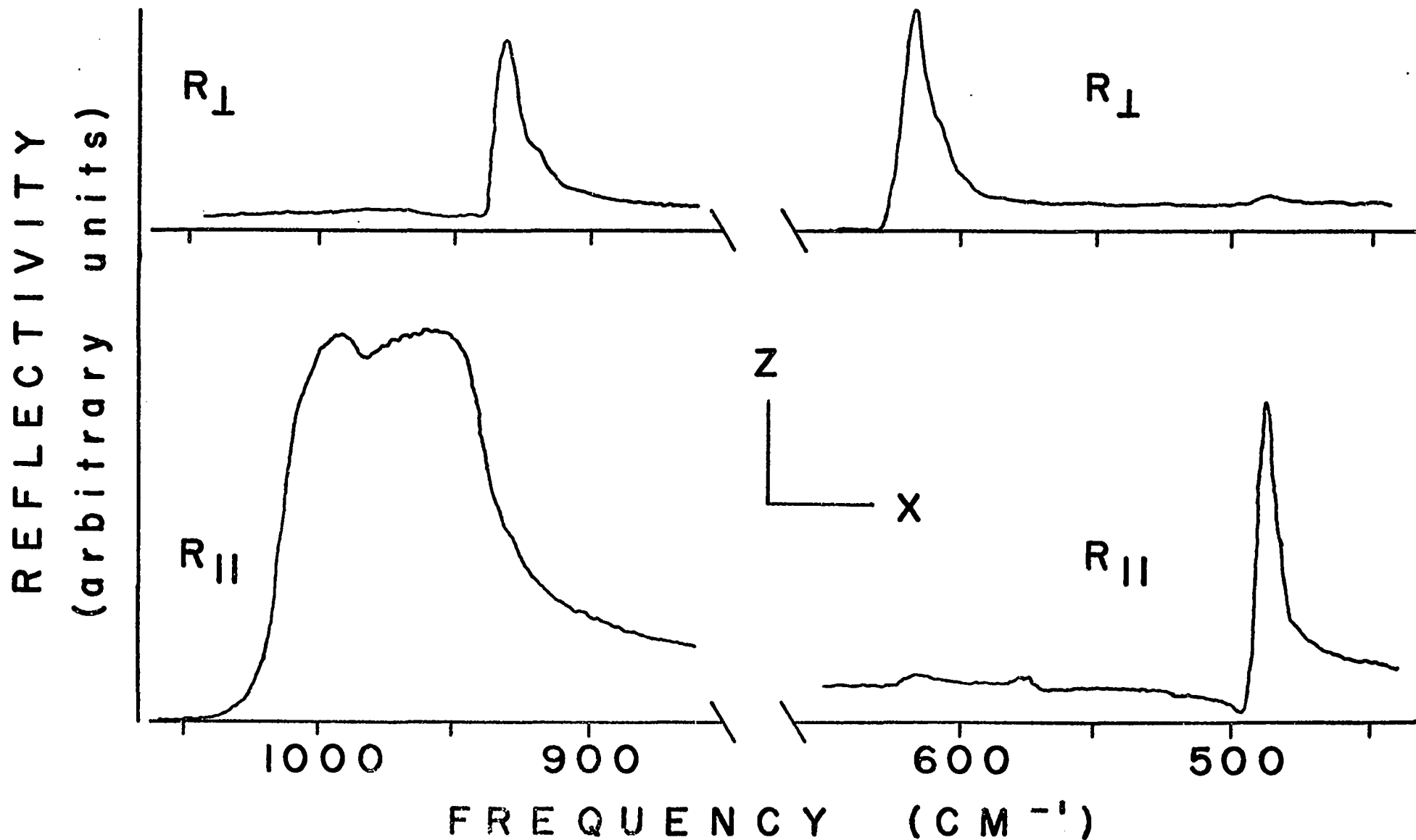


Figure 6-3 Polarized near-normal incidence infrared reflectivity spectra of RbClO_3 single crystals. The optic axis is parallel to z.

Figure (6-3). Polarized near normal incidence infrared reflectivity spectrum of RbBrO_3 in the ν_1 - ν_3 spectral region. The optic axis is parallel to z.

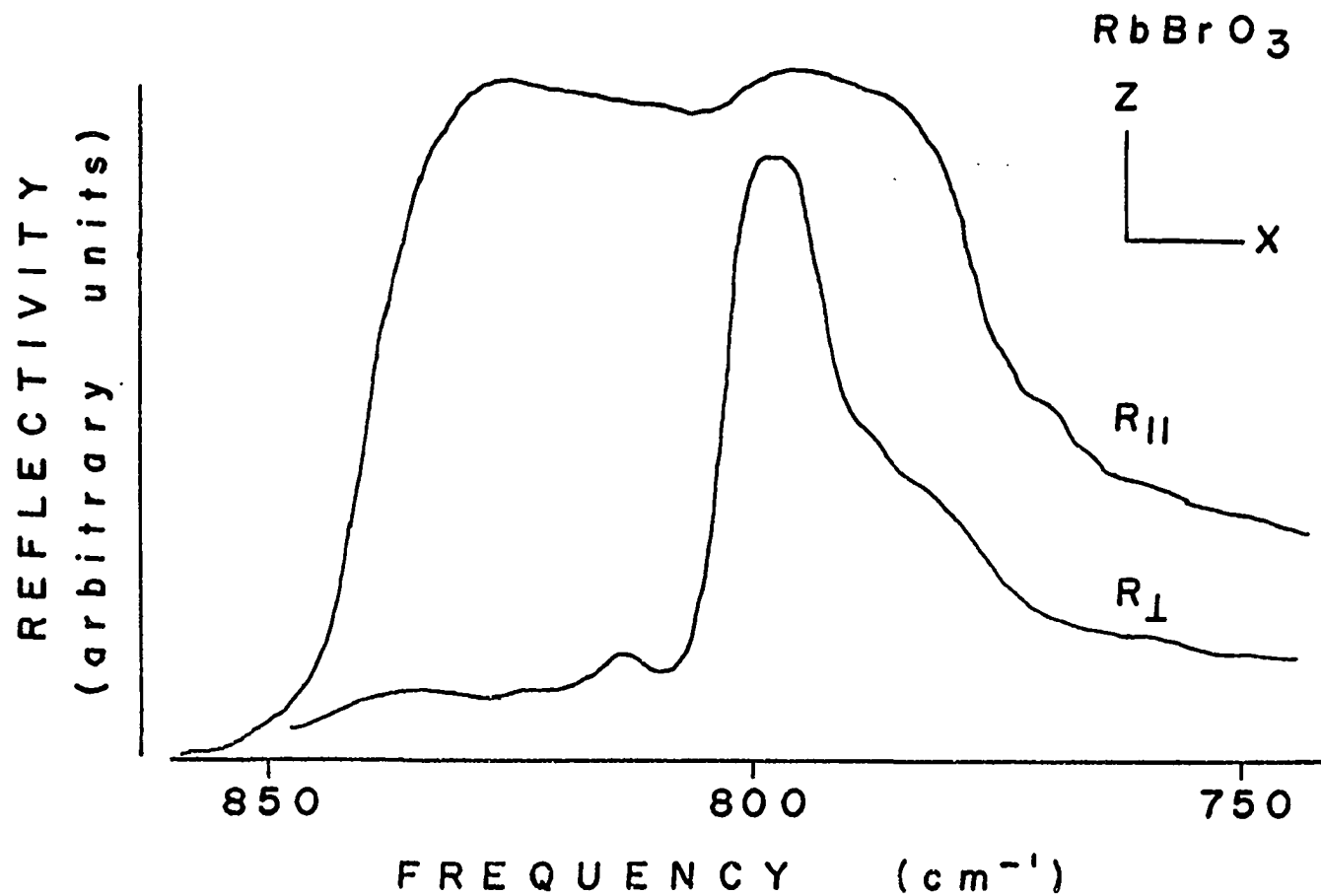
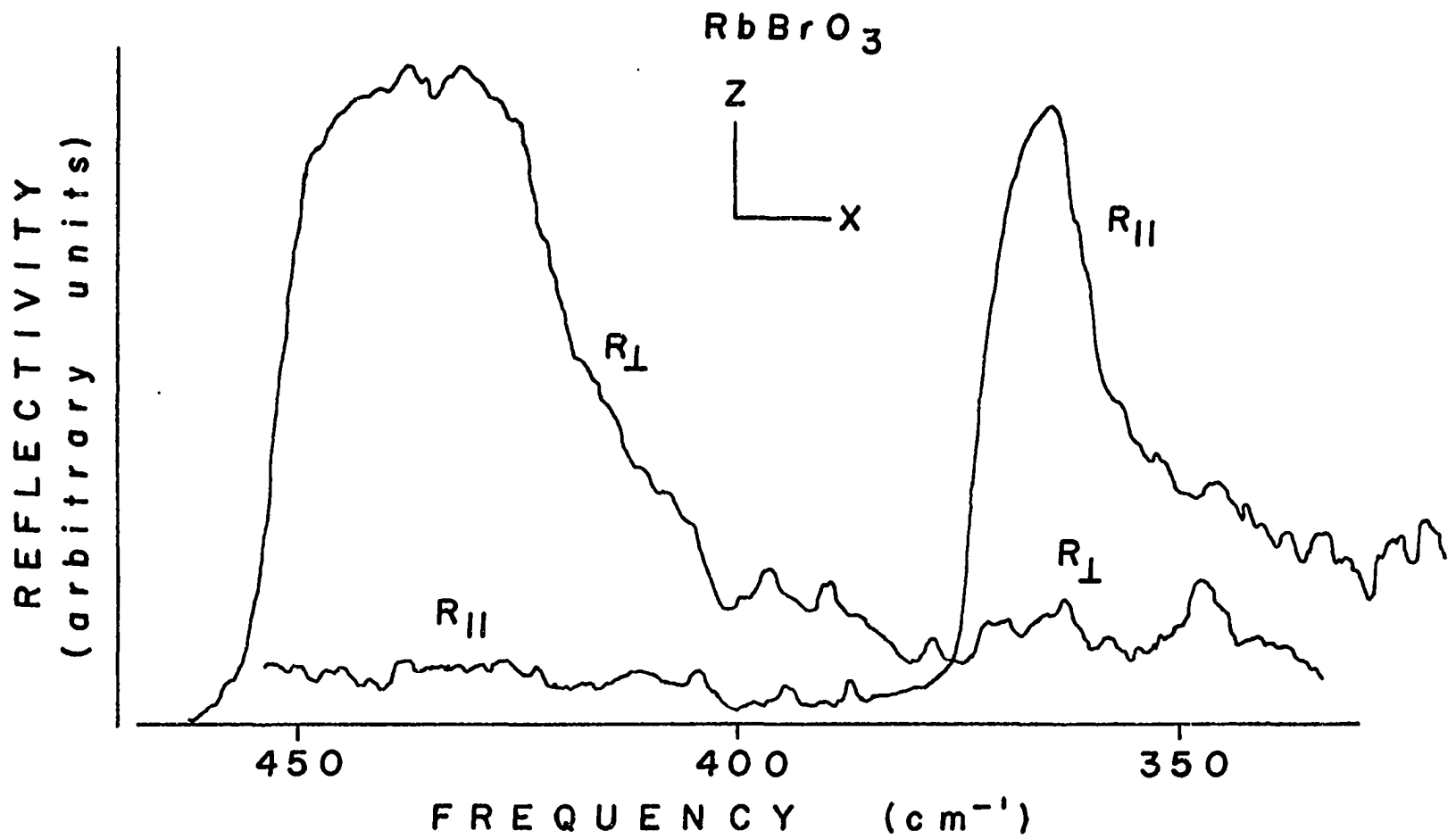


Figure (6-4). Polarized near normal incidence infrared reflectivity spectrum of RbBrO_3 in the ν_2 - ν_4 spectral region. The optic axis is parallel to z.



active a useful comparison can be made between the infrared reflectivity inflection points and the true transverse and longitudinal frequencies directly measured by Raman spectroscopy. These values are presented in table (6-1). The favorable agreement between these values suggests that the inflection points may be used as an estimation of transverse and longitudinal frequencies, at least for these crystals.

Internal Optic Modes of Mixed Crystals

The addition of impurities destroys the factor group of the host crystal which means that the symmetry labels of the pure crystals are no longer valid for the mixed crystals. These labels are retained here only as an aid in labeling the modes; they are not to be taken as the true symmetries of the mixed crystal modes.

Shown in figure (6-5) are the Raman spectra of the ν_1 - ν_3 spectral region of ClO_3^- for the microcrystalline samples. As the BrO_3^- concentration increases, the $\nu_3(\text{E}_L)$ mode at 1008cm^{-1} is seen to drop to lower frequencies. The $\nu_1(\text{A}_{1T})$ mode at 926cm^{-1} and $\nu_3(\text{E}_T)$ mode at 940cm^{-1} maintain the same frequency over the complete concentration range. Graphs of frequency vs. concentration are shown in figure (6-6).

Figures (6-7) & (6-8) show the Raman spectra of the ν_1 - ν_3 spectral region of BrO_3^- for the microcrystalline samples. A number of spectral changes were observed as the concentration of BrO_3^- decreased. These spectral changes were primarily intensity changes, although the $\nu_3(\text{E}_L)$ mode at 832cm^{-1} was found to shift to lower frequencies as the concentration of BrO_3^- decreased. Graphs of frequency vs. concentration are shown in figure (6-6). A mode originating in the $\nu_1(\text{A}_{1T})$ mode of pure RbBrO_3 was found to decrease in intensity relative to the other BrO_3^- modes but did

Figure (6-5). Raman spectra of the ν_1 - ν_3 spectral region of ClO_3^- in RbClO_3 - RbBrO_3 mixed microcrystals.

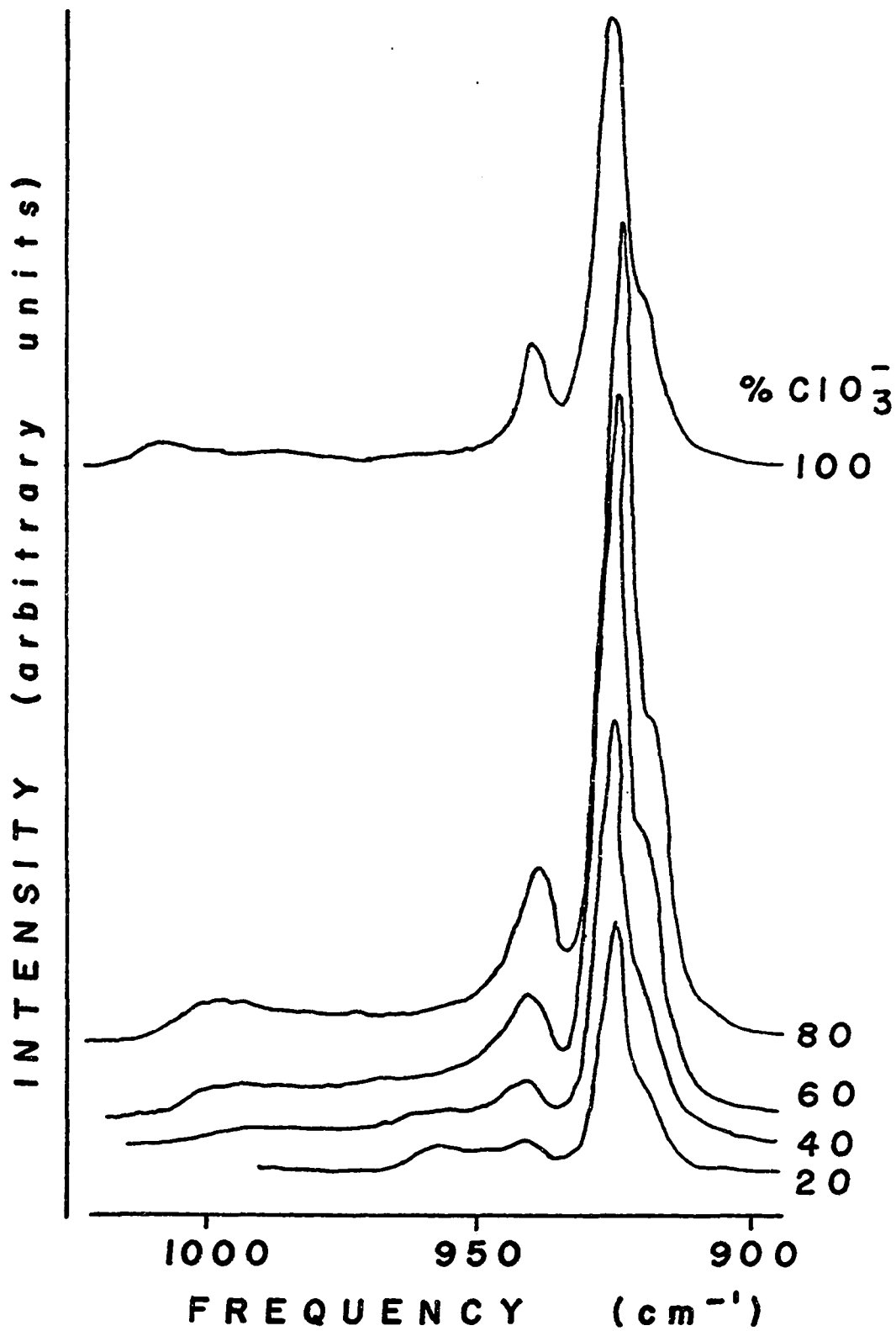
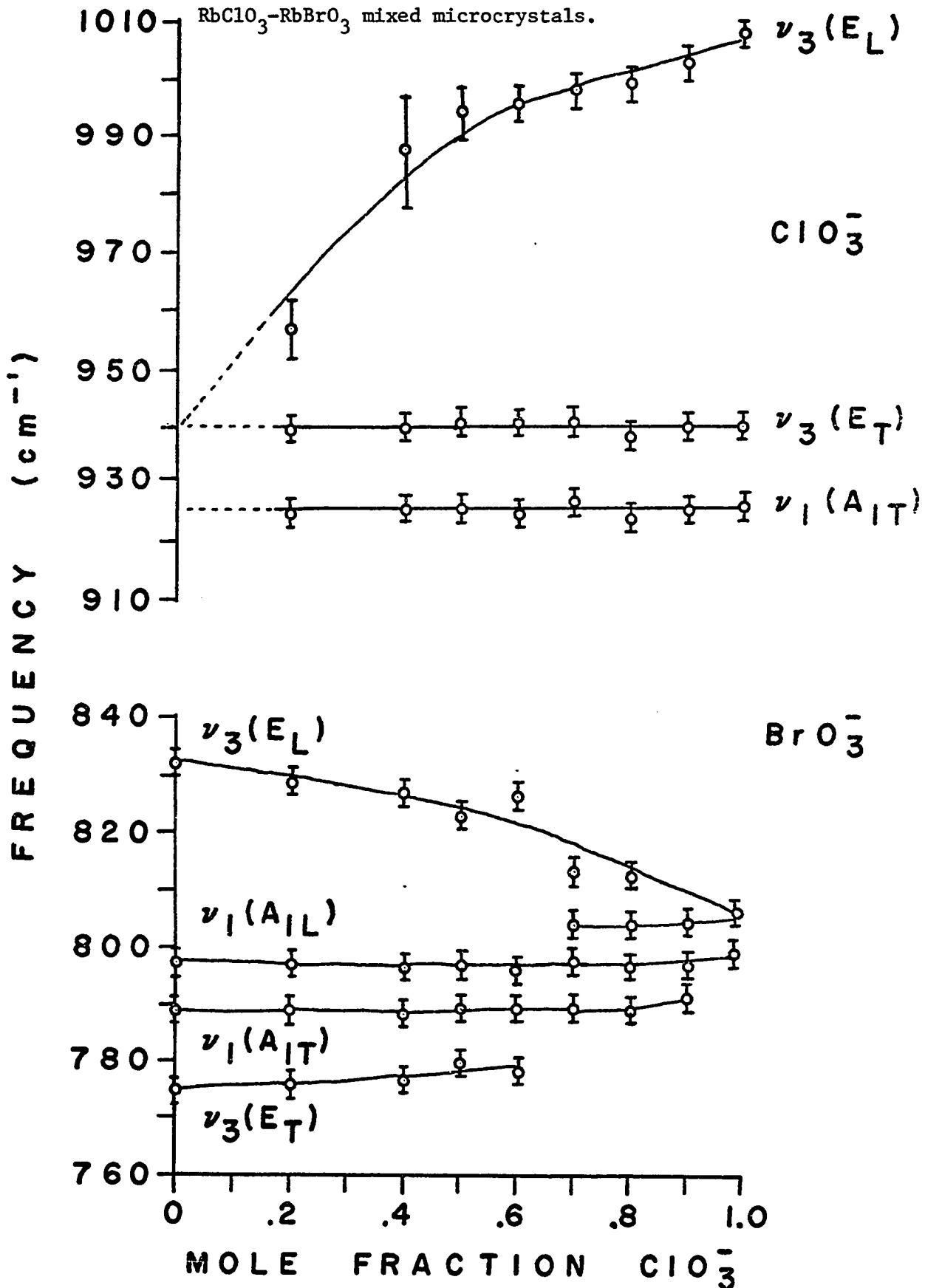
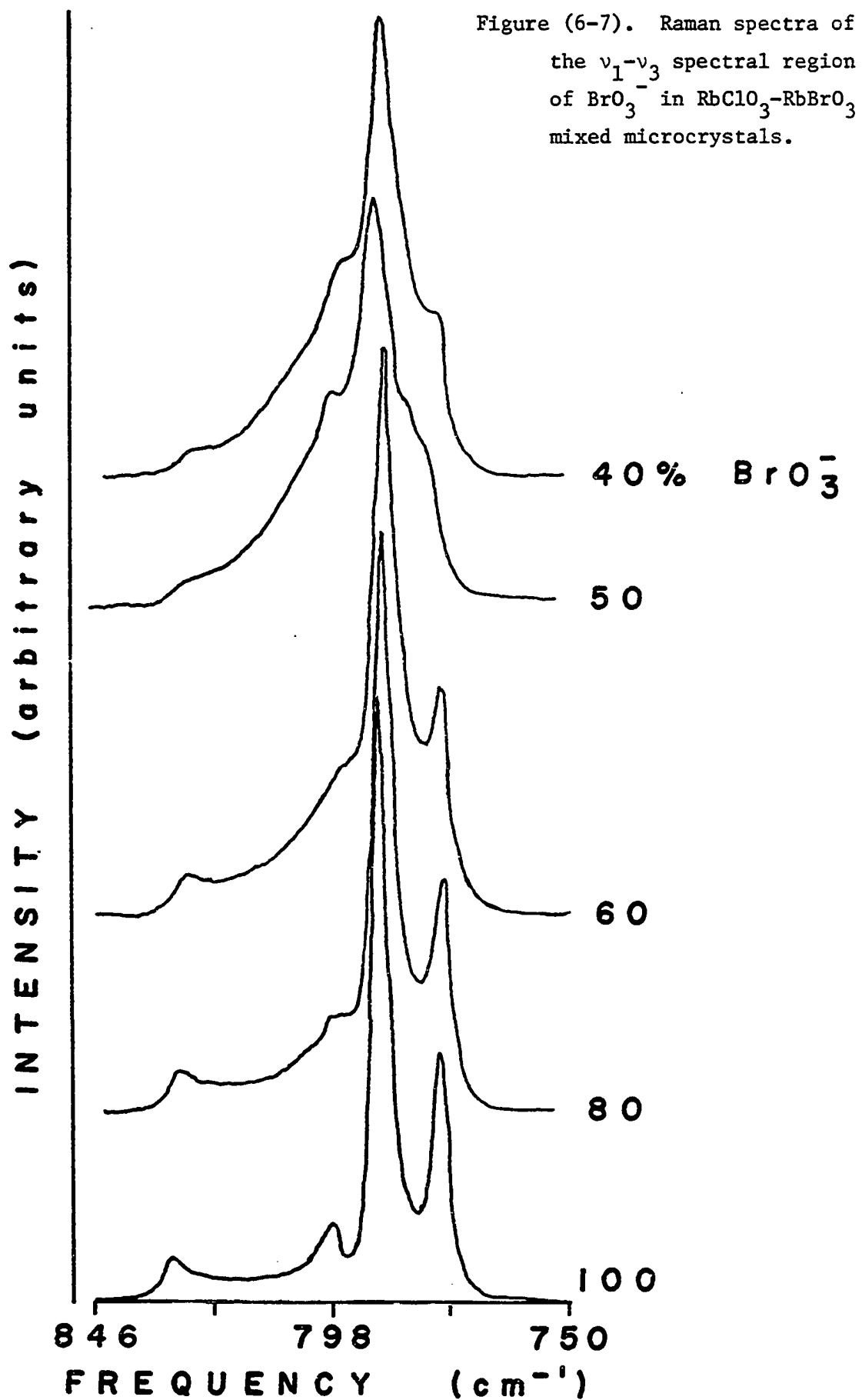
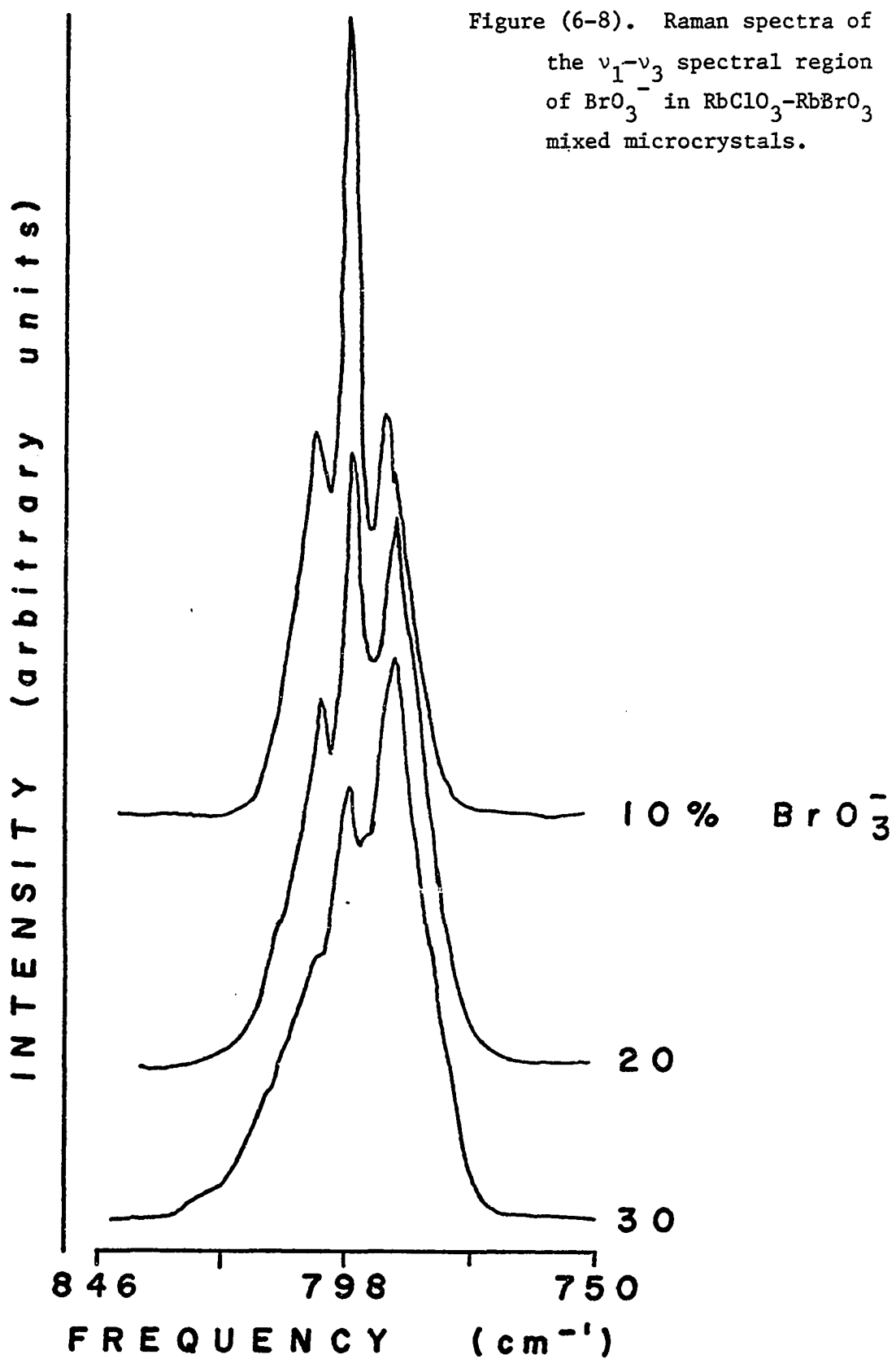


Figure (6-6). Graphs of Raman frequencies in the ν_1 - ν_3 spectral regions of ClO_3^- and BrO_3^- as a function of ClO_3^- concentration for RbClO_3 - RbBrO_3 mixed microcrystals.







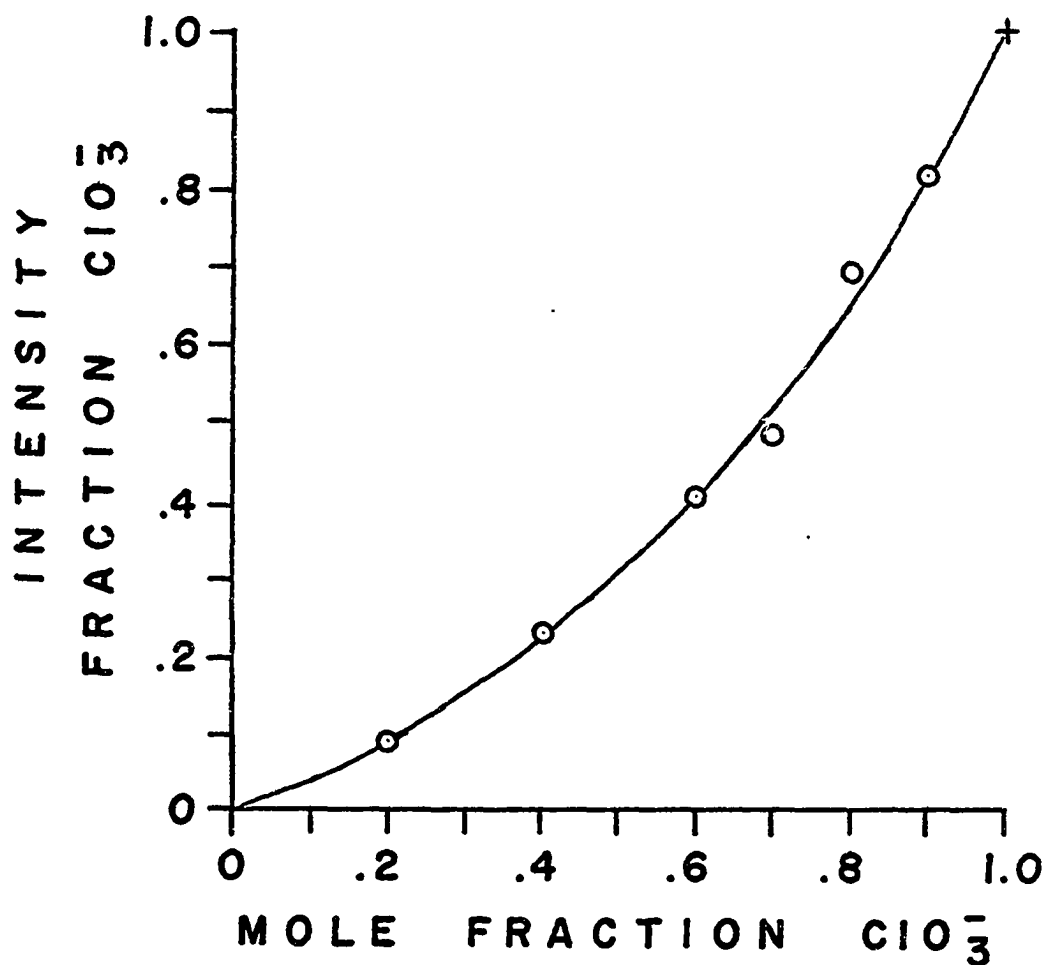
not change frequency as the concentration of BrO_3^- decreased. This mode was followed to 10% BrO_3^- but was not found in the 1% BrO_3^- sample. A mode originating in $\nu_1(\text{A}_{1\text{L}})$ exhibited an initial decrease in intensity followed by an increase in intensity upon further dilution. At BrO_3^- concentrations of less than ~ 20 mole percent this mode had the greatest intensity. The mode originating in $\nu_3(\text{E}_\text{T})$ was found to decrease in intensity and finally disappeared at BrO_3^- concentrations less than 40%. A mode appeared at $\sim 804\text{cm}^{-1}$ in the 30% BrO_3^- sample and persisted to 1% BrO_3^- with increasing intensity relative to the other modes.

In order to determine the concentrations of the mixed crystals grown by slow evaporation, a graph of intensity percent ClO_3^- vs. mole percent ClO_3^- was made for the microcrystalline samples by using the integrated intensities in the ν_1 - ν_3 spectral regions of ClO_3^- and BrO_3^- . This graph is shown in figure (6-9).

Infrared reflection spectra were obtained for several crystals grown from solutions containing 25-75%, 50-50%, and 75-25% RbClO_3 - RbBrO_3 . The faces of these crystals were then ground and the removed material packed in glass capillaries for Raman measurements. The integrated intensities and the graph in figure (6-9) enabled the crystal concentrations to be determined. The 75-25% solution produced crystals which had approximately the same concentration as the solution whereas the 50-50% solution produced crystals having $\sim 75\%$ RbClO_3 . The crystals examined from the 25-75% solution were found to have between 8 and 27% ClO_3^- .

A precise orientation of the crystallographic axes with respect to the incoming laser beam is required for single crystal Raman measurements as any misalignment will produce oblique phonon scattering. In the case of

Figure (6-9). Graph of the fraction of Raman scattering intensity due to ClO_3^- using the $\nu_1-\nu_3$ spectral regions of ClO_3^- and BrO_3^- of the $\text{RbClO}_3\text{-RbBrO}_3$ mixed microcrystals.



RbClO₃, scattering from phonons with frequencies intermediate between the transverse and longitudinal frequencies will be observed. This directional dispersion of phonons in RbClO₃ has been studied by Hwang and Solin.³ In RbBrO₃ the directional dispersion is further complicated as the $\nu_1(A_1)$ mode is within the $\nu_3(E)$ transverse-longitudinal band gap. In this crystal, the oblique phonons will appear to be of mixed A_1 and E symmetry and will be found between the $\nu_3(E_T)$ and $\nu_1(A_{1T})$ frequencies and between the $\nu_1(A_{1L})$ and $\nu_3(E_L)$ frequencies. This behavior has been observed in LiIO₃ by Otaguro and co-workers,⁶ and in KBrO₃ by Unger and Haussühl.⁵ This behavior was discussed by Frech using a microscopic model.⁷ Since the crystals used in this study were too small and, in general, of poor optical quality they could not be cut to expose faces parallel and perpendicular to the optic axis. For this reason no attempt was made to record their Raman spectra. These crystals did, however, have natural rhombohedral faces which could be used for infrared reflection experiments. The optic axis forms an angle with respect to the natural rhombohedral faces. If the crystal is aligned so that the optic axis is in a plane perpendicular to the plane defined by the incident and reflected radiation, then reflection with the electric field polarized parallel to the plane of incidence will produce reflectivity from pure E symmetry phonons while polarization perpendicular to the plane of incidence will produce reflectivity from oblique phonons.

Figures (6-10) & (6-11) show the polarized infrared reflectivity spectra of the ν_1 - ν_3 spectral region of ClO₃⁻ for the mixed crystals grown by slow evaporation. These spectra were recorded using natural rhombohedral crystal faces. Using the inflection points as a measure of the transverse

and longitudinal frequencies, the frequency vs. concentration curves shown in figure (6-12) were obtained. The frequency of the $\nu_3(E_T)$ mode of ClO_3^- did not change over the concentration range accessible, which agrees with the Raman data using microcrystalline samples. The frequency of the $\nu_3(E_L)$ mode was found to have a non-linear shift to lower frequencies upon dilution, although the curvature was not as great as with the microcrystalline data. In the experimental reflection geometry used here, reflectivity from an oblique phonon is observed for ν_1 . The frequency of this mode remained constant within experimental error over the complete concentration range.

Figures (6-13) & (6-14) show the polarized infrared reflectivity spectra of the ν_1 - ν_3 spectral region of BrO_3^- for several of these single crystals. These spectra exhibit pronounced dips in the T-L band gaps of the $\nu_3(E)$ modes. These dips could be due to surface damage, however the corresponding ClO_3^- modes do not show such a pronounced behavior. Another explanation could be that the $\nu_3(E_T)$ mode couples with the $\nu_2 + \nu_4$ density of states producing a reflectivity loss similar to that observed in $\text{Na}^{14}\text{NO}_3$ as described in chapter 2. Frequency vs. concentration curves for the ν_1 - ν_3 region of BrO_3^- are shown in figure (6-12). Over the accessible concentration range the $\nu_3(E_L)$ mode was found to vary linearly with concentration. The $\nu_3(E_T)$ mode was found to decrease in frequency by $\sim 12\text{cm}^{-1}$ to $\sim 777\text{cm}^{-1}$ at $\sim 70\%$ BrO_3^- and then increased in frequency to $\sim 785\text{cm}^{-1}$ at $\sim 20\%$ BrO_3^- . An oblique phonon originating at 789cm^{-1} in pure RbBrO_3 was found to decrease in frequency to $\sim 785\text{cm}^{-1}$ at $\sim 25\%$ BrO_3^- . Another oblique phonon originating at 798cm^{-1} in pure RbBrO_3 was found to decrease in frequency to $\sim 793\text{cm}^{-1}$ at 25% BrO_3^- . These frequency vs.

Figure (6-10). Infrared reflectivity spectra of $\text{RbClO}_3\text{-RbBrO}_3$ single mixed crystals. Natural rhombohedral crystal faces were used with the optic axis being in a plane perpendicular to x.

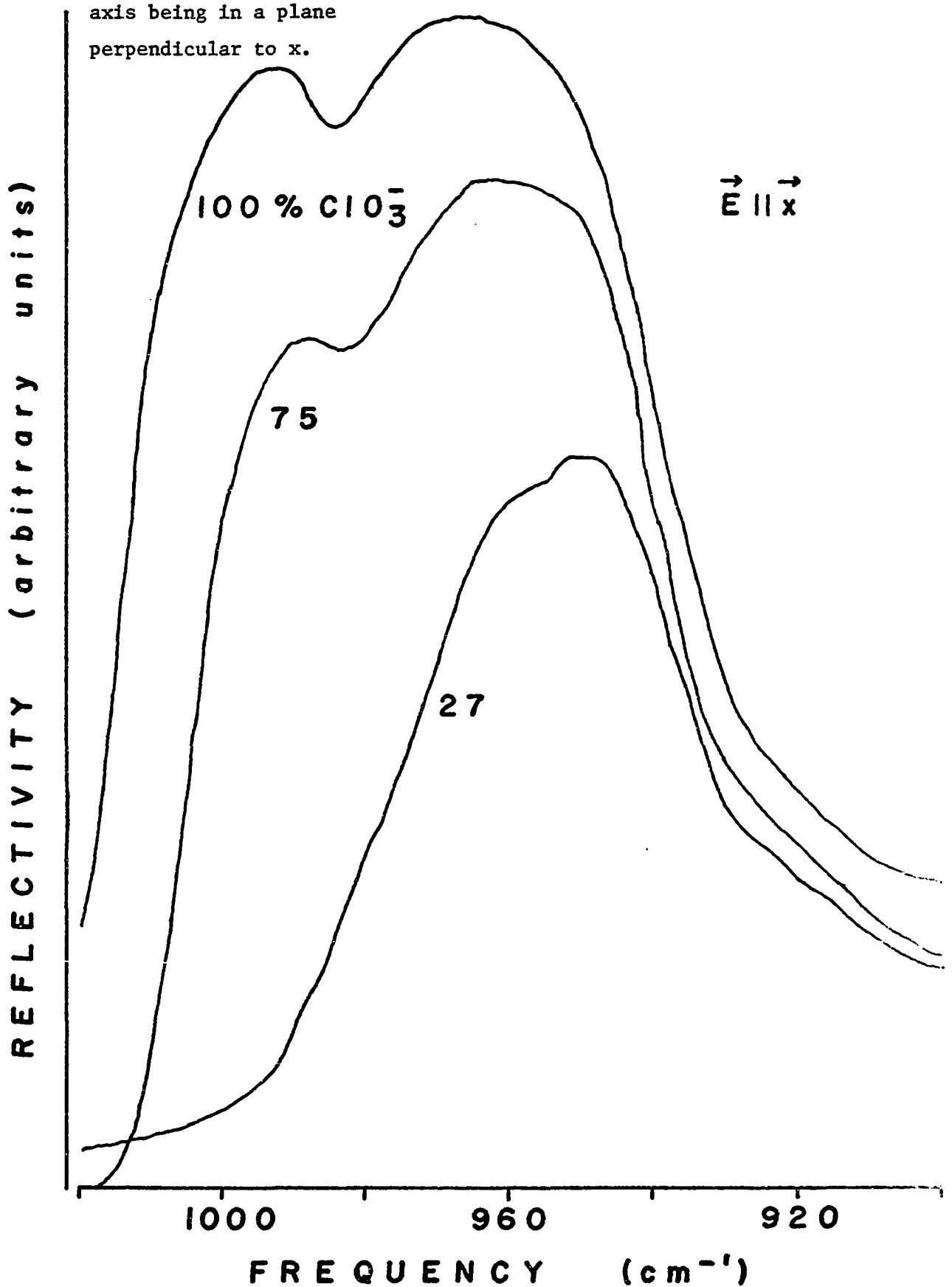


Figure (6-11). Infrared reflectivity spectra in the ν_1 - ν_3 spectral region of ClO_3^- for RbClO_3 - RbBrO_3 single mixed crystals. Natural rhombohedral crystal faces were used with the optic axis being in the plane perpendicular to x .

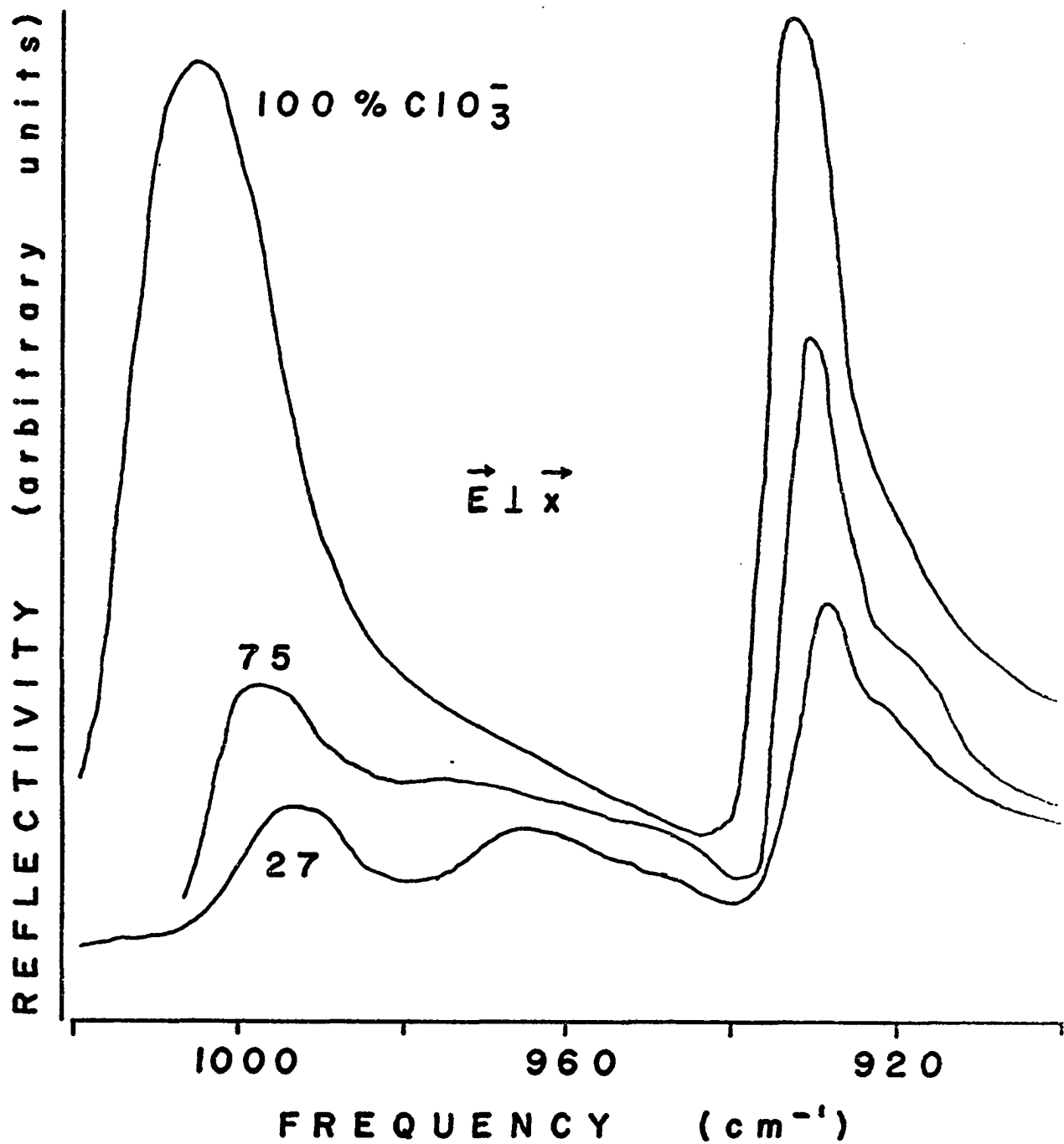


Figure (6-12). Graph of infrared frequencies as a function of ClO_3^- concentration for the ν_1 - ν_3 spectral regions of BrO_3^- and ClO_3^- in RbClO_3 - RbBrO_3 single mixed crystals. Inflection points were used for the transverse and longitudinal frequencies.

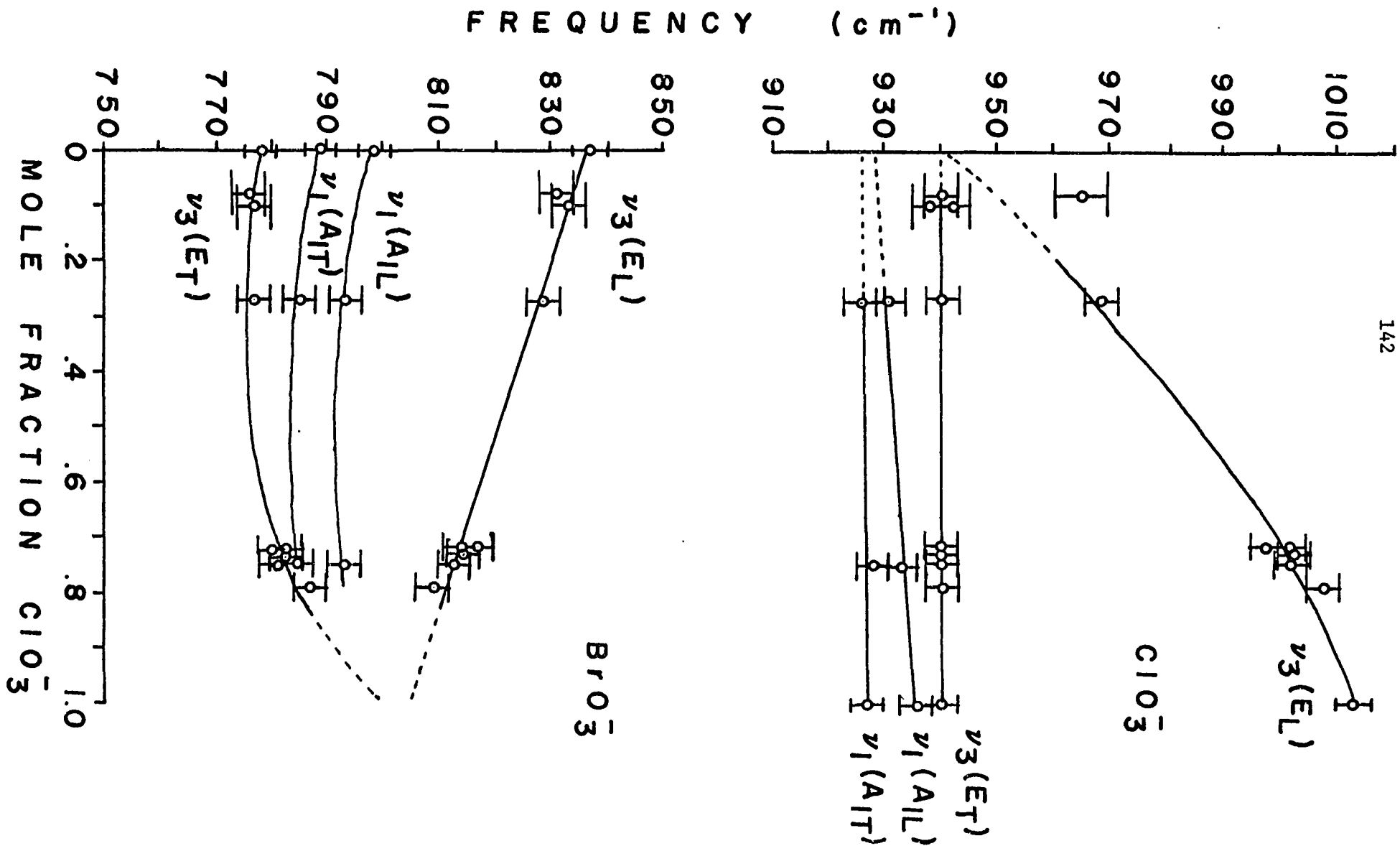


Figure (6-13). Polarized near normal incidence infrared reflectivity spectra for the ν_1 - ν_3 spectral region of BrO_3^- in the RbClO_3 - RbBrO_3 single mixed crystals. Natural rhombohedral crystal faces were used with the optic axis being in a plane perpendicular to x .

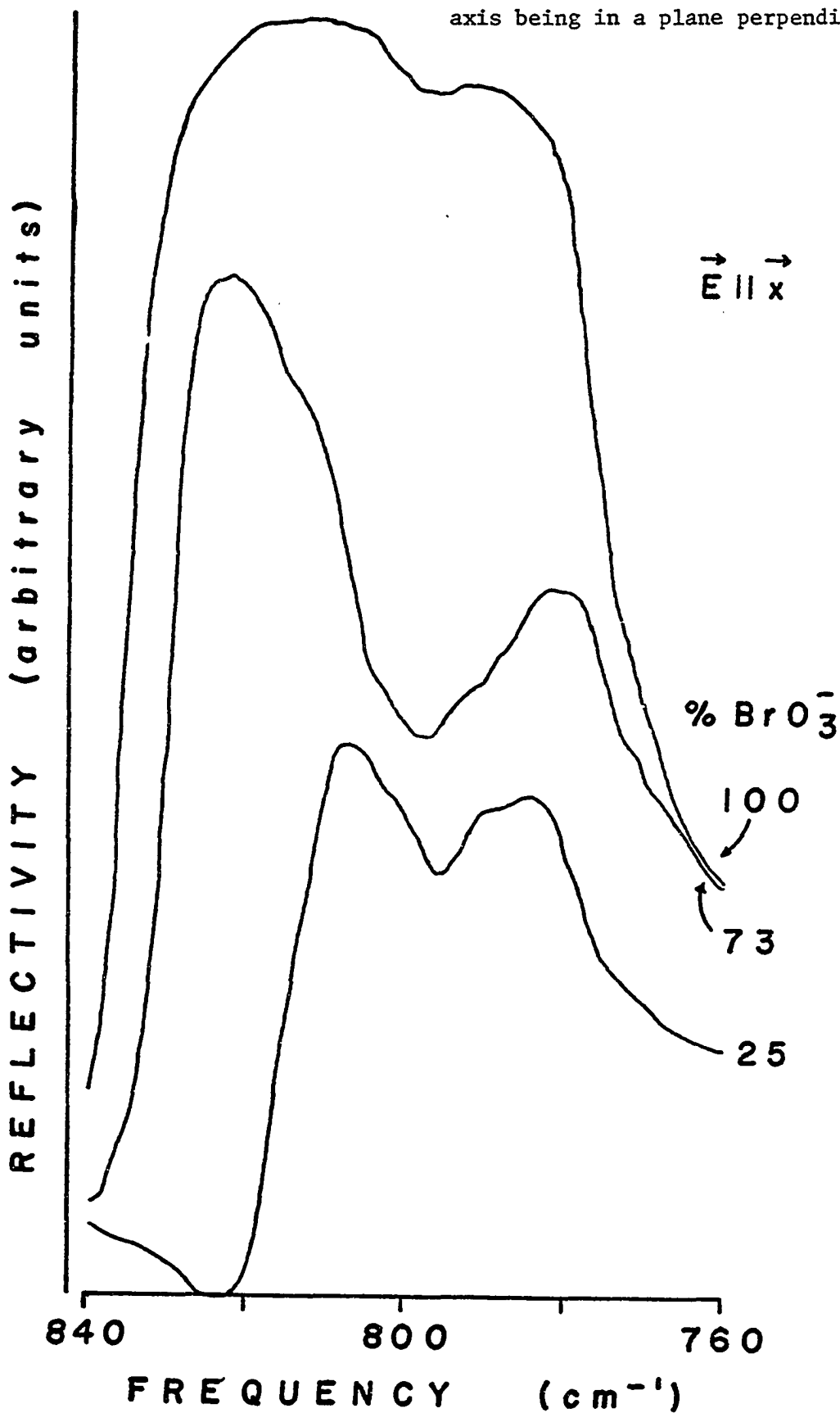
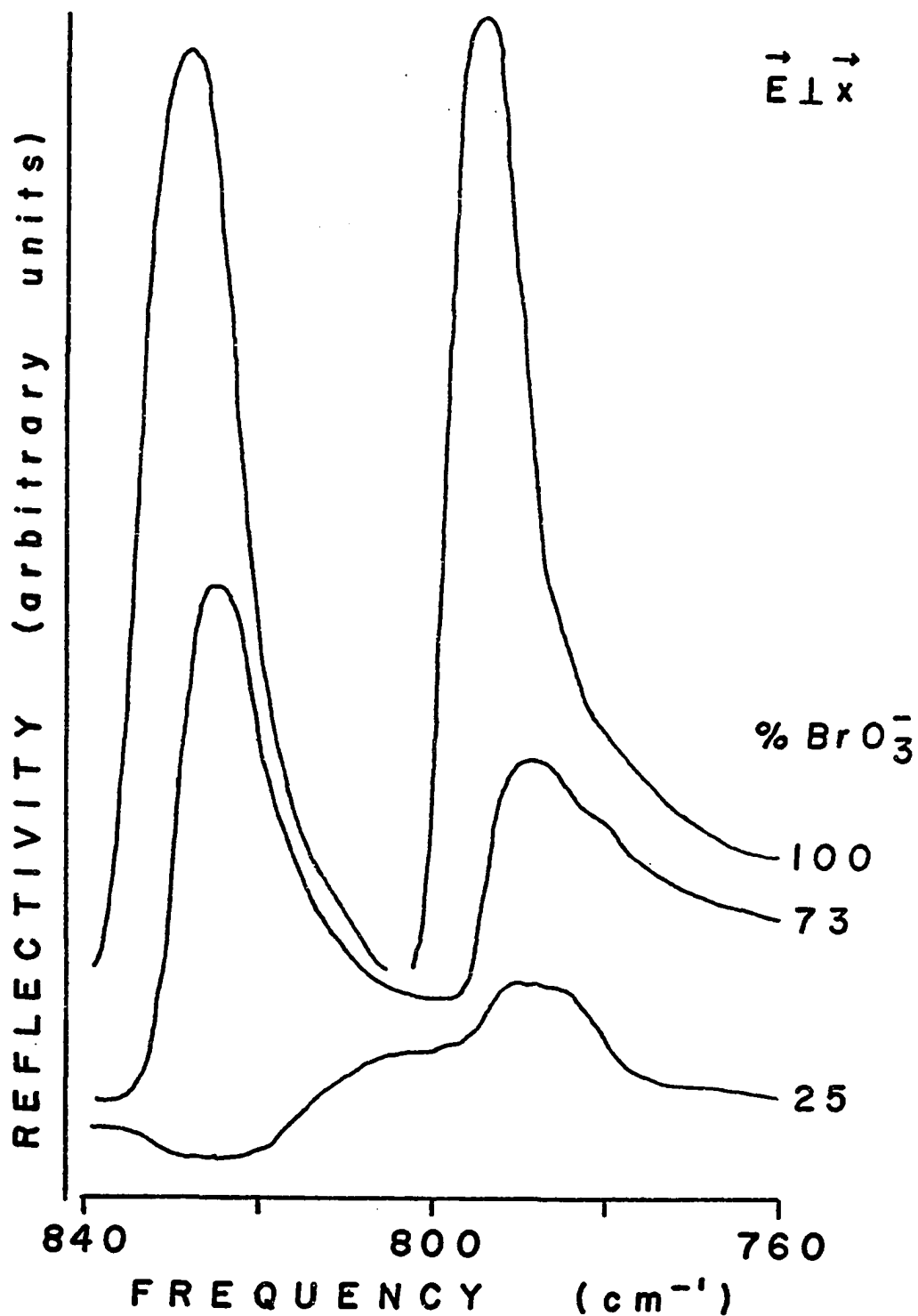


Figure (6-14). Polarized near normal incidence infrared reflectivity spectra for the ν_1 - ν_3 spectral region of BrO_3^- in the RbClO_3 - RbBrO_3 single mixed crystals. Natural rhombohedral crystal faces were used with the optic axis being in a plane perpendicular to x.



concentration curves are in agreement with those obtained with the microcrystalline Raman data.

Nujol mull spectra were obtained for the microcrystalline samples. Since NaCl windows were used, only the ν_1 - ν_3 spectral regions of BrO_3^- and ClO_3^- could be studied.

Spectra of small microcrystals suspended in a nujol mull should yield spectra which are not entirely due to absorption processes but should also exhibit microcrystalline reflectivity behavior. In the spectral region of an intense infrared active fundamental, microcrystalline reflectivity can produce spectra which are almost identical to those obtained from unpolarized single crystal reflection. This was shown in chapter 3 and explained as being due to high reflectivity from the microcrystal surfaces in the spectral region of a strong infrared active fundamental. Due to the sampling geometry, both absorption and reflection will remove part of the incident radiation in the nujol samples. Random orientation of the uniaxial microcrystals and any changes in absorptivity or reflectivity by mixing will further contribute to the difficulty of interpreting the spectra.

Figure (6-15) shows the nujol mull spectra for the ν_1 - ν_3 region of BrO_3^- in the microcrystalline samples. Using absorption maxima as an estimation of transverse frequencies and the high frequency inflection point as an estimation of the longitudinal mode of ν_3 , the graph of frequency vs. concentration shown in figure (6-16) was obtained. The longitudinal mode of the pure RbBrO_3 sample could not be estimated from the nujol mull spectrum. These curves agree favorably with those obtained from single crystal reflectivity data. The ν_1 (A_{1T}) mode is seen to drop

in frequency to $\sim 787\text{cm}^{-1}$ at 60% ClO_3^- . Between 70 and 80% ClO_3^- the $\nu_1(\text{A}_{1\text{T}})$ mode appears to increase in frequency by $\sim 10\text{cm}^{-1}$. This is consistent with the Raman intensity changes in this concentration region. The $\nu_3(\text{E}_{\text{L}})$ mode appears to be essentially linear over the complete concentration range. The $\nu_3(\text{E}_{\text{T}})$ mode was found to increase in frequency from $\sim 784\text{cm}^{-1}$ in pure RbBrO_3 to $\sim 787\text{cm}^{-1}$ at 10% BrO_3^- . Below 10% BrO_3^- the $\nu_3(\text{E}_{\text{T}})$ mode increased sharply in frequency to $\sim 800\text{cm}^{-1}$ at 1% BrO_3^- .

Using the method developed by Miller and Decius for determining the symmetries of matrix isolated ions, the symmetry of matrix isolated BrO_3^- or ClO_3^- in this crystal system should be $\text{C}_{3\text{v}}$.⁸ Shown in figure (6-17) is the Raman spectrum of the ν_1 - ν_3 spectral region of BrO_3^- of a micro-crystalline sample containing 1% BrO_3^- . Two modes are found at 799 and 806cm^{-1} with the mode at 799cm^{-1} having the greater intensity. The most intense mode is identified as being ν_1 . Figure (6-17) also shows the infrared transmission spectrum of this sample in a nujol mull. As the ν_3 mode should have the greater infrared intensity it is assigned at 800cm^{-1} , the center of the band. The mode at 806cm^{-1} found in the Raman spectrum corresponds to the high frequency inflection point of the band found in the infrared spectrum.

The transverse-longitudinal frequency separation arises from the electric field induced by the collective motion of like ions throughout the crystal. As the concentration of these ions is decreased, the collective nature of the motion is progressively destroyed and the T-L frequency separation should decrease. In the matrix isolation limit only one mode should be observed for each of the pure crystal fundamentals. It is somewhat surprising that even at 1% BrO_3^- the $\nu_3(\text{E})$ T-L splitting is still $\sim 6\text{cm}^{-1}$.

Figure (6-15). Infrared transmission spectra of the ν_1 - ν_3 spectral region of BrO_3^- for RbClO_3 - RbBrO_3 mixed microcrystals supported in nujol mulls.

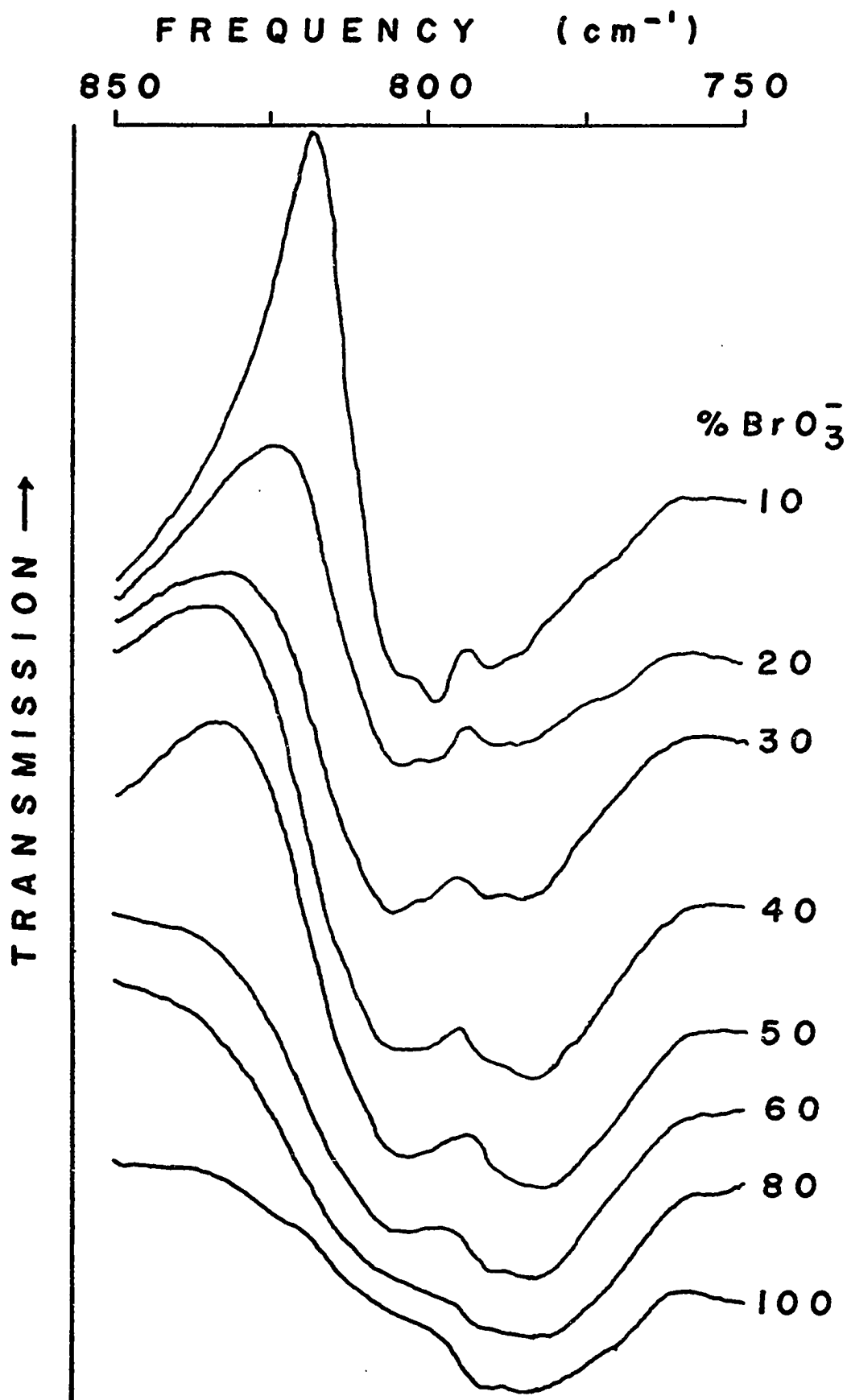
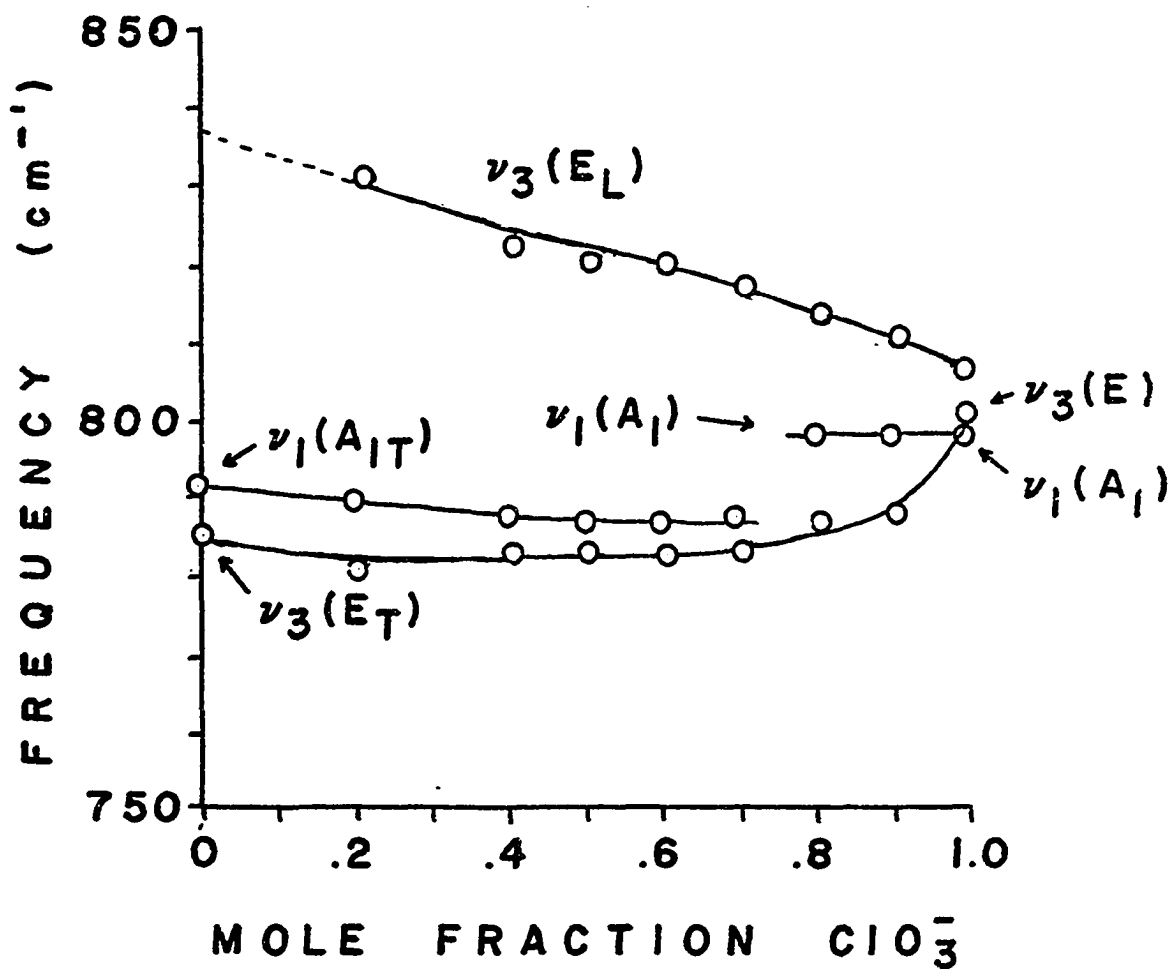


Figure (6-16). Graph of infrared frequencies as a function of ClO_3^- concentration in the ν_1 - ν_3 spectral region of BrO_3^- for RbClO_3 - RbBrO_3 mixed microcrystals supported in nujol mulls. Absorption maxima were used for transverse frequencies and the high frequency inflection points were used for longitudinal frequencies.



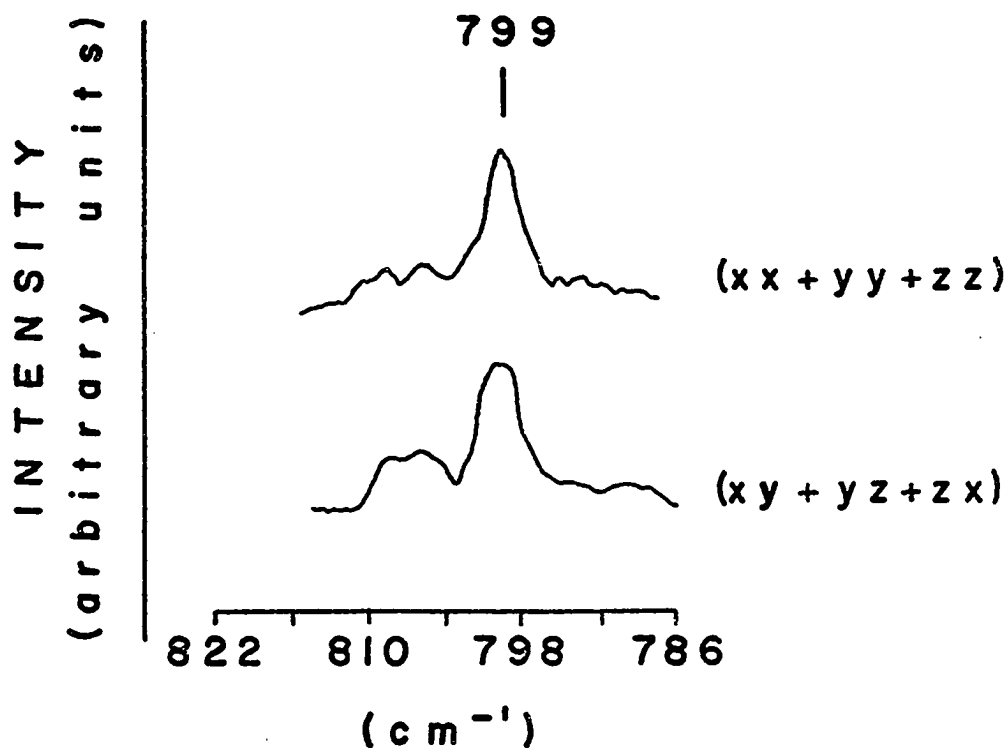
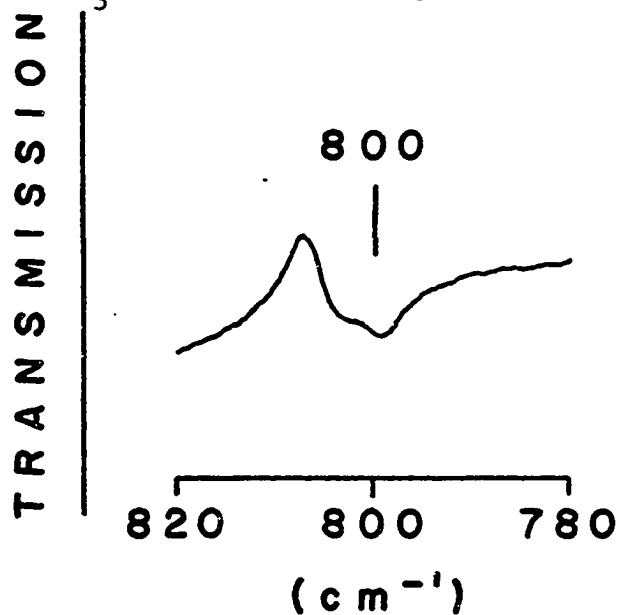


Figure (6-17). Polarized Raman spectra (above) of $\text{RbClO}_3\text{-RbBrO}_3$ mixed microcrystals containing 1% BrO_3^- in the $\nu_1\text{-}\nu_3$ spectral region of BrO_3^- . Infrared transmission spectrum (below) of microcrystals containing 1% BrO_3^- supported in a nujol mull.



With decreasing BrO_3^- concentration, the ν_1 mode seems to disappear at one frequency and reappear at another frequency. One explanation is that the vibrational mode followed in the Raman and infrared experiments is not the true $\nu_1(\text{A}_{1\text{T}})$ mode, but rather, is due to oblique phonons. The Raman experiments on the microcrystals should exhibit scattering from oblique phonons in all directions as all crystal orientations are sampled. As the angle between the optic axis and the direction of phonon propagation is varied from 0° to 90° , the phonon frequency shifts continuously from the $\nu_3(\text{E}_{\text{T}})$ frequency to the $\nu_1(\text{A}_{1\text{T}})$ frequency. The frequency of the $\nu_3(\text{E}_{\text{T}})$ mode itself does not change, but rather, scattering occurs from different phonons having different frequencies. The oblique phonons should exhibit both ν_1 and ν_3 character, with the dominant character being dependent upon the direction of phonon propagation. The directional dispersion in KBrO_3 , which should be very similar to RbBrO_3 , has been shown by Unger and Haussühl⁵ and by Frech⁷ to have two relatively flat regions, with respect to the direction of propagation, at frequencies very close to $\nu_3(\text{E}_{\text{T}})$ and $\nu_1(\text{A}_{1\text{T}})$. There are many phonons with frequencies very near the frequencies of the $\nu_1(\text{A}_{1\text{T}})$ and $\nu_3(\text{E}_{\text{T}})$ modes which should produce Raman spectra which closely resemble that which would be expected for scattering from pure transverse and longitudinal phonons. As the concentration of BrO_3^- is decreased, the $\nu_1(\text{A}_{1\text{T}})$ mode of the pure crystal should become the $\nu_1(\text{A}_1)$ mode in the $\text{C}_{3\text{v}}$ matrix isolation limit while the $\nu_3(\text{E}_{\text{T}})$ mode should become the $\nu_3(\text{E})$ mode in this limit. The scattering intensity of these two modes, however, may be much less than the combined scattering intensity of the oblique phonons occurring at frequencies very near to the $\nu_1(\text{A}_{1\text{T}})$ and $\nu_3(\text{E}_{\text{T}})$ frequencies. Disordering the crystal by dilution will destroy the

collective nature of these modes so that the intensity due to the oblique phonons should decrease. In the matrix isolation limit the intensities of the $\nu_1(A_1)$ and $\nu_3(E)$ modes should be the only observable spectral features, involving scattering from isolated ions with no cooperative intermolecular effects. The dominant spectral features in the pure RbBrO_3 microcrystals should be due to oblique phonon processes while at low BrO_3^- concentrations the spectral features should be attributed to the scattering from matrix isolated ions. The $\nu_1(A_{1T})$ mode could exhibit a shift to higher frequencies at intermediate concentrations which could be hidden by the intensity of the oblique phonon scattering. It is coincidental that the matrix isolation frequency of $\nu_1(A_1)$ occurs at the pure crystal $\nu_1(A_{1L})$ frequency and that the matrix isolation frequency of the $\nu_1(A_1)$ and $\nu_3(E)$ modes are almost degenerate.

The unusual behavior of the BrO_3^- modes in the $\nu_1-\nu_3$ spectral region can be attributed to the frequency ordering of the $\nu_1-\nu_3$ transverse and longitudinal modes. This unusual behavior was observed in both the $\text{Na}(\text{ClO}_3)_x(\text{BrO}_3)_{1-x}$ system, discussed in chapter 5, and the $\text{Rb}(\text{ClO}_3)_x(\text{BrO}_3)_{1-x}$ system discussed in this chapter. In both of these systems, only the $\nu_1-\nu_3$ spectral region of BrO_3^- exhibited unexpected and complicated behavior.

Figures (6-18) & (6-19) show the Raman spectra of the $\nu_2-\nu_4$ spectral region of ClO_3^- and BrO_3^- , respectively, in the microcrystalline samples. Frequency vs. concentration curves are shown in figure (6-20). The $\nu_2(A_{1T})$ mode of ClO_3^- was found to shift linearly to lower frequencies as the concentration of ClO_3^- decreased. The $\nu_2(A_{1L})$ mode of ClO_3^- decreased in frequency and merged with the $\nu_2(A_{1T})$ mode at $\sim 70\%$ ClO_3^- . The $\nu_4(E_T)$ mode did not exhibit any concentration dependent frequency shifts although the

Figure (6-18). Raman spectra of $\text{RbClO}_3\text{-RbBrO}_3$ mixed microcrystals in the $\nu_2\text{-}\nu_4$ spectral region of ClO_3^- .

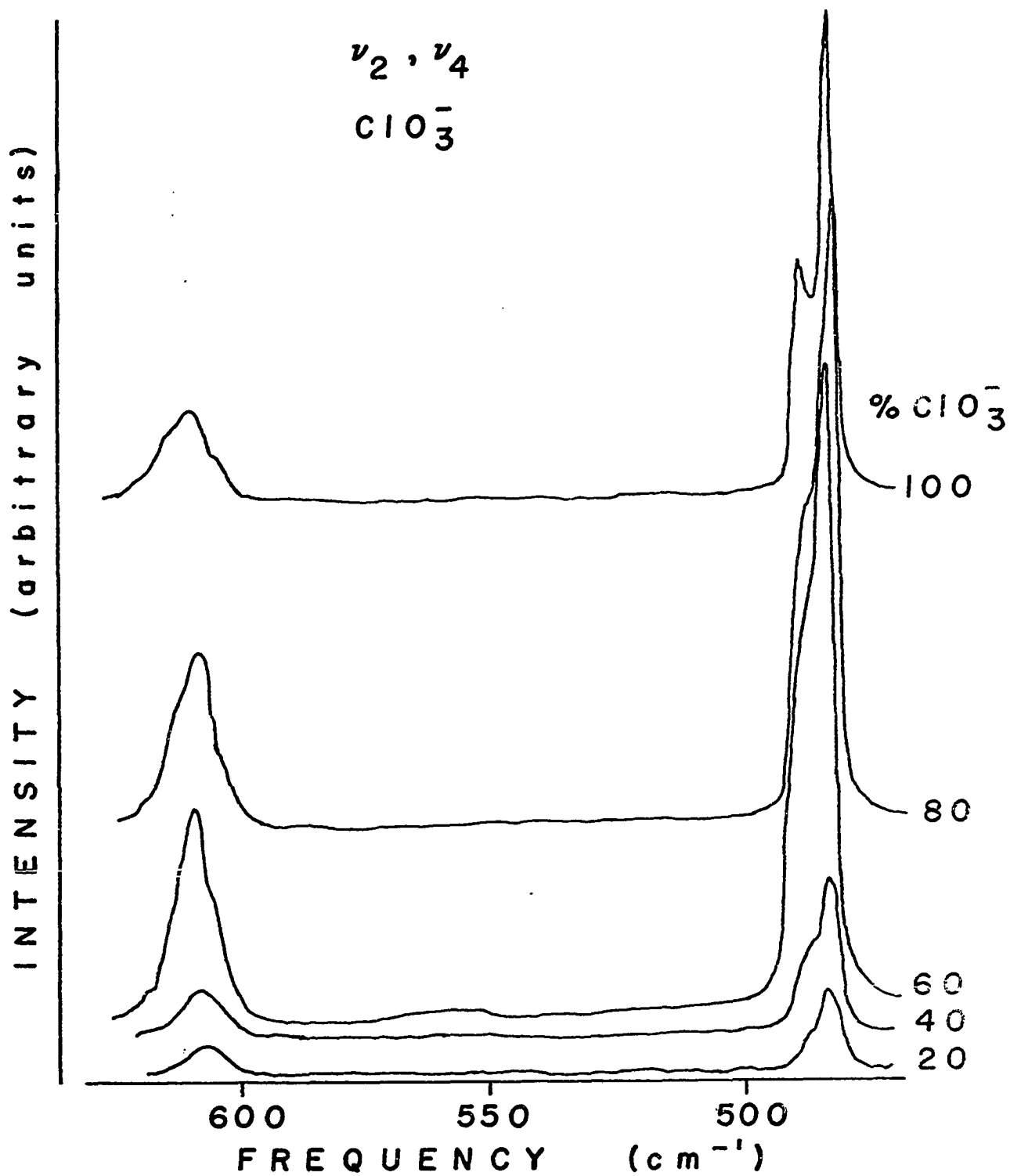
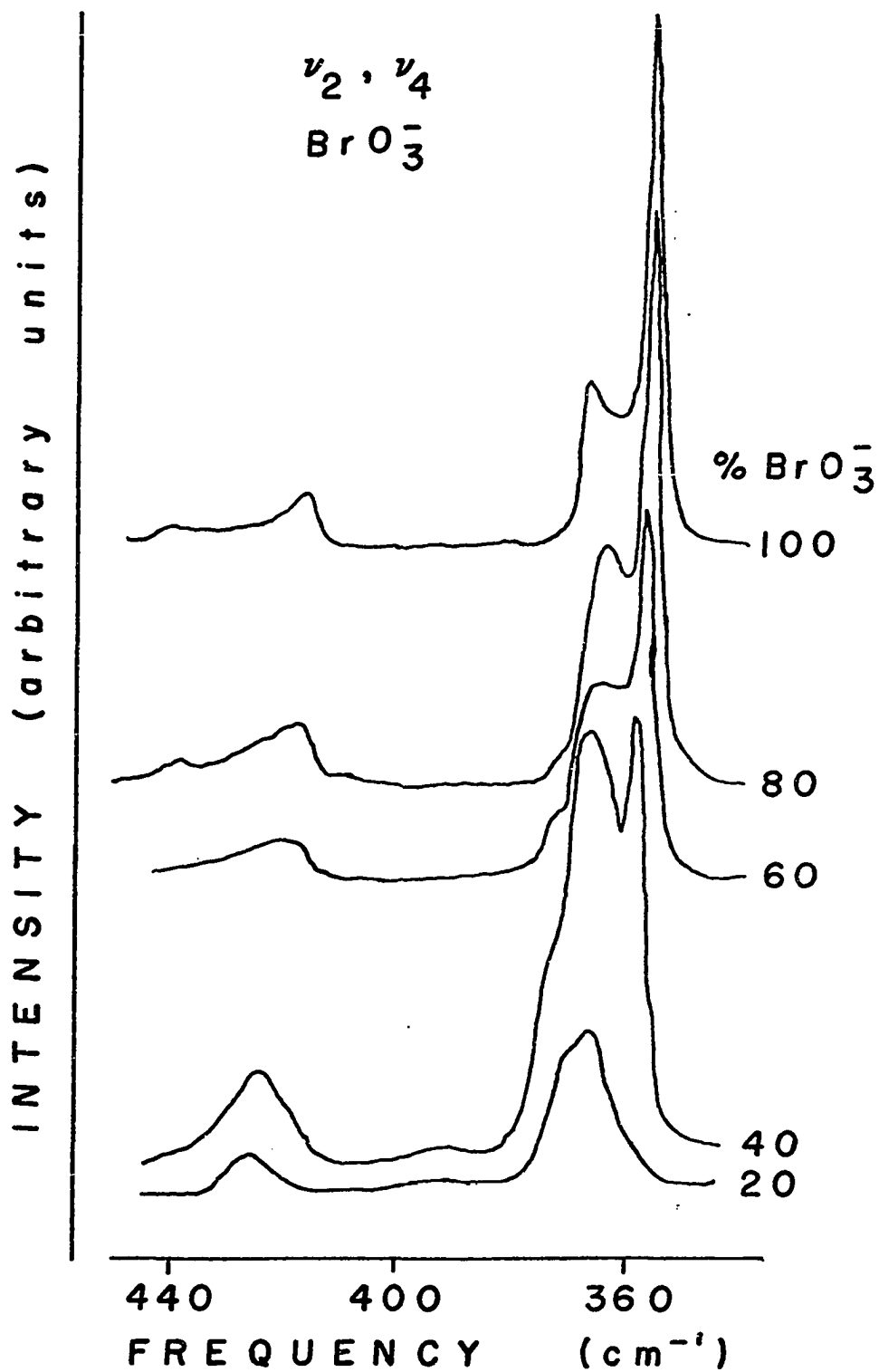
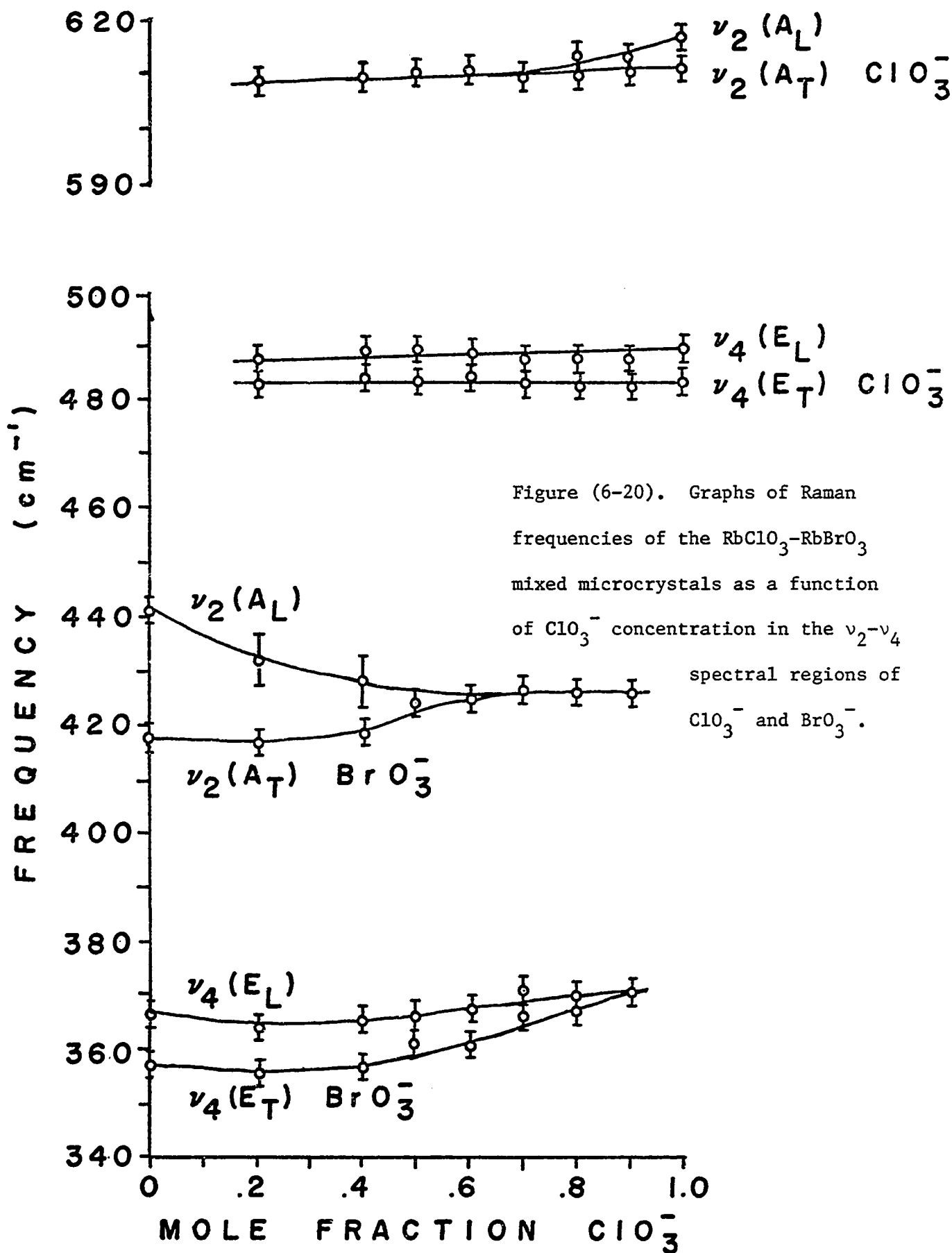


Figure (6-19). Raman spectra of $\text{RbClO}_3\text{-RbBrO}_3$ mixed microcrystals in the $\nu_2\text{-}\nu_4$ spectral region of BrO_3^- .





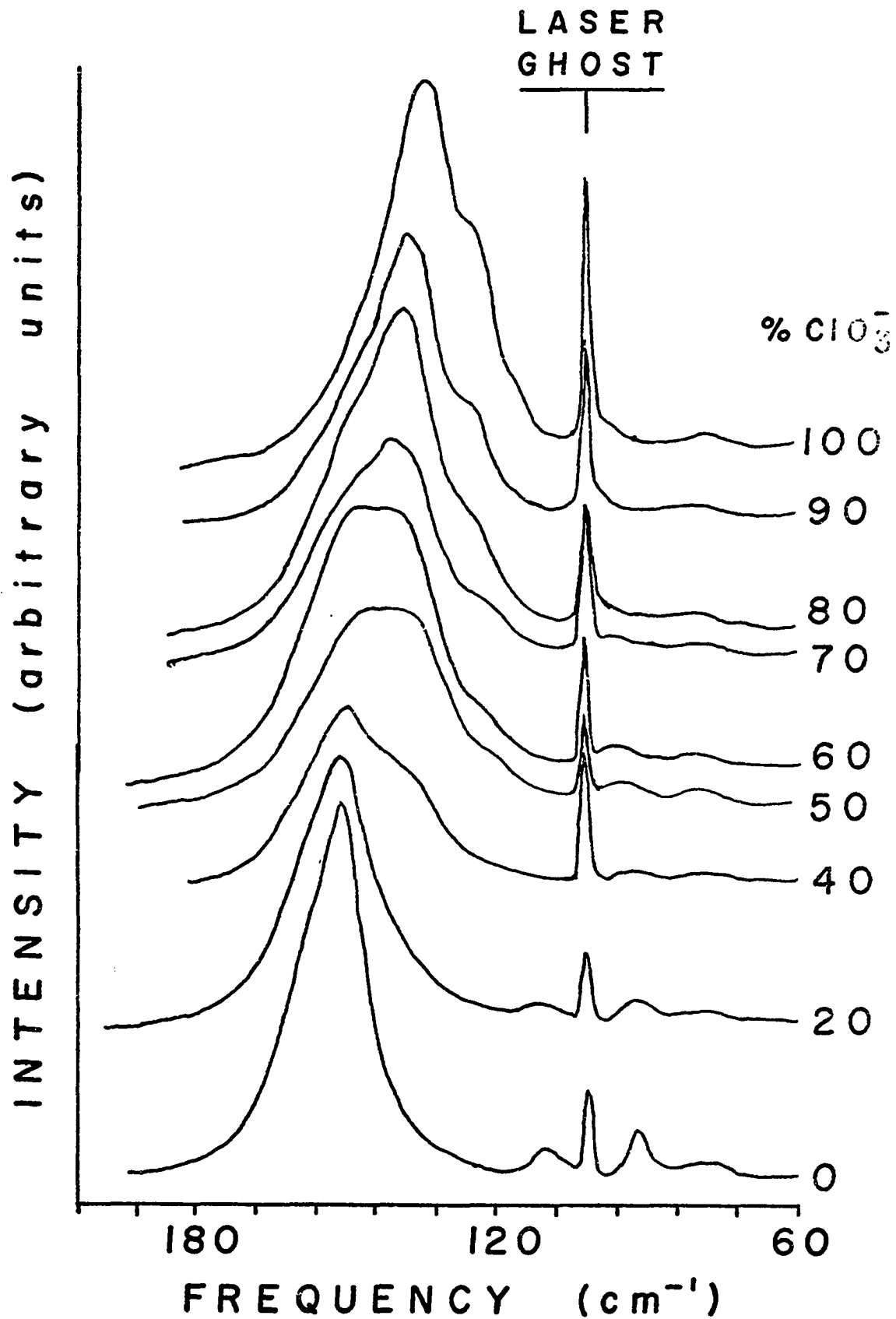
$\nu_4(E_L)$ mode shifted by $\sim 1-2\text{cm}^{-1}$ to lower frequency at 20% ClO_3^- . The $\nu_4(E_T)$ and $\nu_4(E_L)$ modes of ClO_3^- were not found to merge as the concentration of ClO_3^- decreased, although at 20% ClO_3^- it is probable that the matrix isolation limit was not achieved.

The $\nu_2(A_{1T})$ mode of BrO_3^- increased in frequency while the $\nu_2(A_{1L})$ mode decreased in frequency as the concentration of BrO_3^- decreased. These two modes merged at $\sim 40-50\%$ BrO_3^- . The $\nu_4(E_T)$ mode of BrO_3^- exhibited a non-linear increase in frequency as the concentration of BrO_3^- decreased. The $\nu_4(E_L)$ mode was found to decrease in frequency during the initial stages of dilution, followed by an increase in frequency as the BrO_3^- concentration dropped below $\sim 50\%$. These two modes were found to merge at $\sim 10\%$ BrO_3^- .

External Optic Modes in Microcrystals

Figure (6-21) shows the Raman spectra of the external optic modes in the microcrystalline samples. Since this spectral region was complicated by the presence of a laser ghost, both the 4880 and 5145Å excitation lines were used. There are three Raman active external modes in the pure crystals with the lowest frequency mode being of A_1 symmetry in both RbClO_3 and RbBrO_3 . This mode was found to exhibit one-mode behavior as the concentration of the microcrystals was varied, as shown in figure (6-22). With the addition of BrO_3^- , the A_{1T} mode underwent an initial decrease in frequency of $\sim 3\text{cm}^{-1}$ from 80cm^{-1} in pure RbClO_3 to $\sim 77\text{cm}^{-1}$ at 85% ClO_3^- . This was followed by an increase in frequency to $\sim 82\text{cm}^{-1}$ at 65% ClO_3^- and another decrease in frequency to $\sim 79\text{cm}^{-1}$ at 50% ClO_3^- . The mode retained this frequency below 50% ClO_3^- to the pure RbBrO_3 limit. Although the estimated errors in frequency would allow linear behavior, it is believed these frequency fluctuations are real.

Figure (6-21). Raman spectra of $\text{RbClO}_3\text{-RbBrO}_3$ mixed microcrystals in the external optic mode spectral region. Excitation wavelength was 4880\AA .



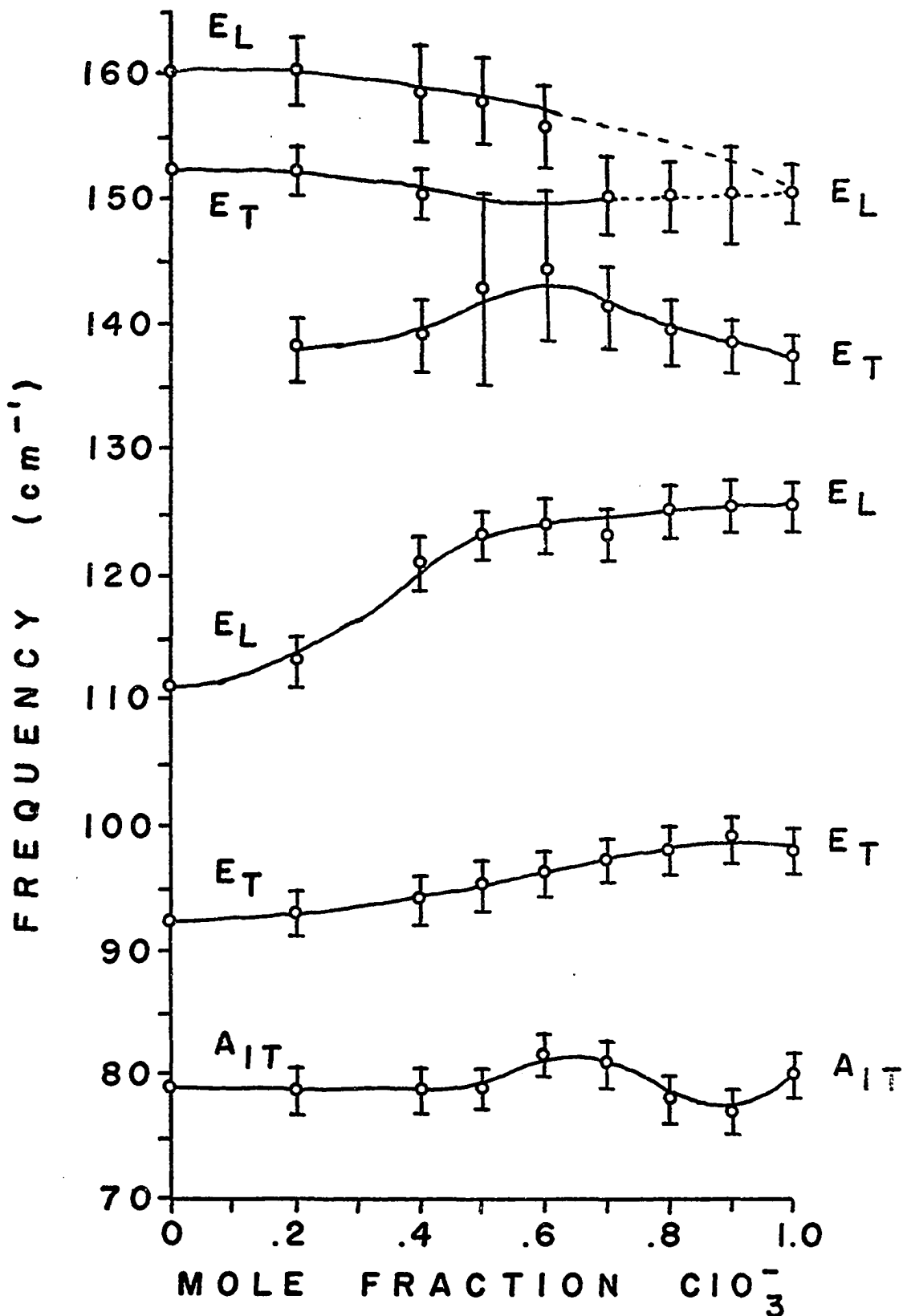


Figure (6-22). Graphs of Raman frequencies of $\text{RbClO}_3\text{-RbBrO}_3$ mixed microcrystals as a function of ClO_3^- concentration in the external optic mode spectral region.

The E_T mode at 93cm^{-1} in RbBrO_3 was found to exhibit one-mode behavior by shifting smoothly, but not linearly, to the RbClO_3 frequency of 98cm^{-1} . A mode at 111cm^{-1} in RbBrO_3 exhibited one-mode behavior by increasing in frequency to the RbClO_3 frequency of 125cm^{-1} . The major frequency shift occurred below 50% ClO_3^- . This is believed to be an E_L mode.

The highest frequency external mode is of E symmetry. The E_T component in the RbBrO_3 microcrystalline sample was found at $\sim 152\text{cm}^{-1}$ while the corresponding mode in the RbClO_3^- microcrystalline sample occurred at $\sim 137\text{cm}^{-1}$. It is somewhat surprising that this mode would be at a higher frequency in RbBrO_3 . The external modes involve a movement of the whole ion so that motions involving the more massive BrO_3^- ion would be expected to occur at lower frequencies than the ClO_3^- ion. As the concentration of BrO_3^- decreases, the E_T mode originating at 152cm^{-1} in RbBrO_3 was found to decrease in frequency by $\sim 2\text{cm}^{-1}$ at 40% ClO_3^- , whereas the mode originating at 137cm^{-1} in pure RbClO_3 shifts to higher frequencies upon dilution with BrO_3^- . In the concentration range 50-60% ClO_3^- , only one broad band could be found in the Raman spectrum. A shoulder was found in the 20 and 40% ClO_3^- samples at 138 and 139cm^{-1} respectively which was not found in the pure RbBrO_3 sample. Assigning this mode to E_T of ClO_3^- suggests that the high frequency external E_T modes of RbClO_3 and RbBrO_3 exhibit two mode-behavior. The criteria for one-mode and two-mode behavior developed by Chang and Mitra⁹ predicts one-mode behavior as $m_{\text{ClO}_3^-} > \mu_{\text{RbBrO}_3}$ and $m_{\text{BrO}_3^-} > \mu_{\text{RbClO}_3}$, where m is the mass of the ion and μ is the reduced mass of the ion pair. Another criterion, which is that if the T-L band gaps of the two pure components overlap then one-mode behavior will result, appears to hold here. The

E_T mode was found at 158cm^{-1} in the pure RbBrO_3 crystal which places it above the E_L mode of RbClO_3 , which was found at 150cm^{-1} by Hwang and Solin.⁴

A shoulder found at 160cm^{-1} in the pure RbBrO_3 sample is attributed to the E_L mode. This mode decreased in frequency as the concentration of BrO_3^- decreased and its frequency is extrapolated in figure (6-23) to converge with the E_T mode of BrO_3^- . The E mode of matrix isolated BrO_3^- is seen in figure (6-23) to have a near accidental degeneracy with the E_L mode of RbClO_3 at 150cm^{-1} . This E_L mode is believed to decrease in frequency as the concentration of ClO_3^- decreases to merge with its corresponding E_T mode, which originates at 134cm^{-1} .

Discussion

In chapter 5, arguments were presented to expand the definition of two-mode behavior to encompass behavior which might be found in mixed crystal systems having internal optic modes. The term "separated-mode" behavior was used to describe a mixed crystal mode whose frequency changed smoothly from a pure crystal frequency of one component to the matrix isolation frequency of that component. In the mixed crystal system studied here, the two lowest frequency external optic modes exhibited one-mode behavior while all other optic modes exhibited separated-mode behavior.

References for Chapter VI

1. Ralph W. G. Wyckoff, Crystal Structures, vol. 2 (Interscience Publishers, New York, 1960).
2. NBS Circular 539, vol. 8.
3. D. M. Hwang and S. A. Solin, Phys. Rev. B 7, 843 (1973).
4. D. M. Hwang and S. A. Solin, Appl. Phys. Lett. 20, 181 (1972).
5. B. Unger and S. Haussühl, Phys. Stat. Sol. B 54, 183 (1972).
6. W. Otaguro, E. Wiener-Avneer, C. A. Arguello, and S. P. S. Porto, Phys. Rev. B 4, 4542 (1971).
7. Roger Frech, J. Chem. Phys. 67, 952 (1977).
8. Ralph E. Miller and J. C. Decius, J. Chem. Phys. 59, 4871 (1973).
9. I. F. Chang and S. S. Mitra, Phys. Rev. 172, 924 (1968).

Appendix A

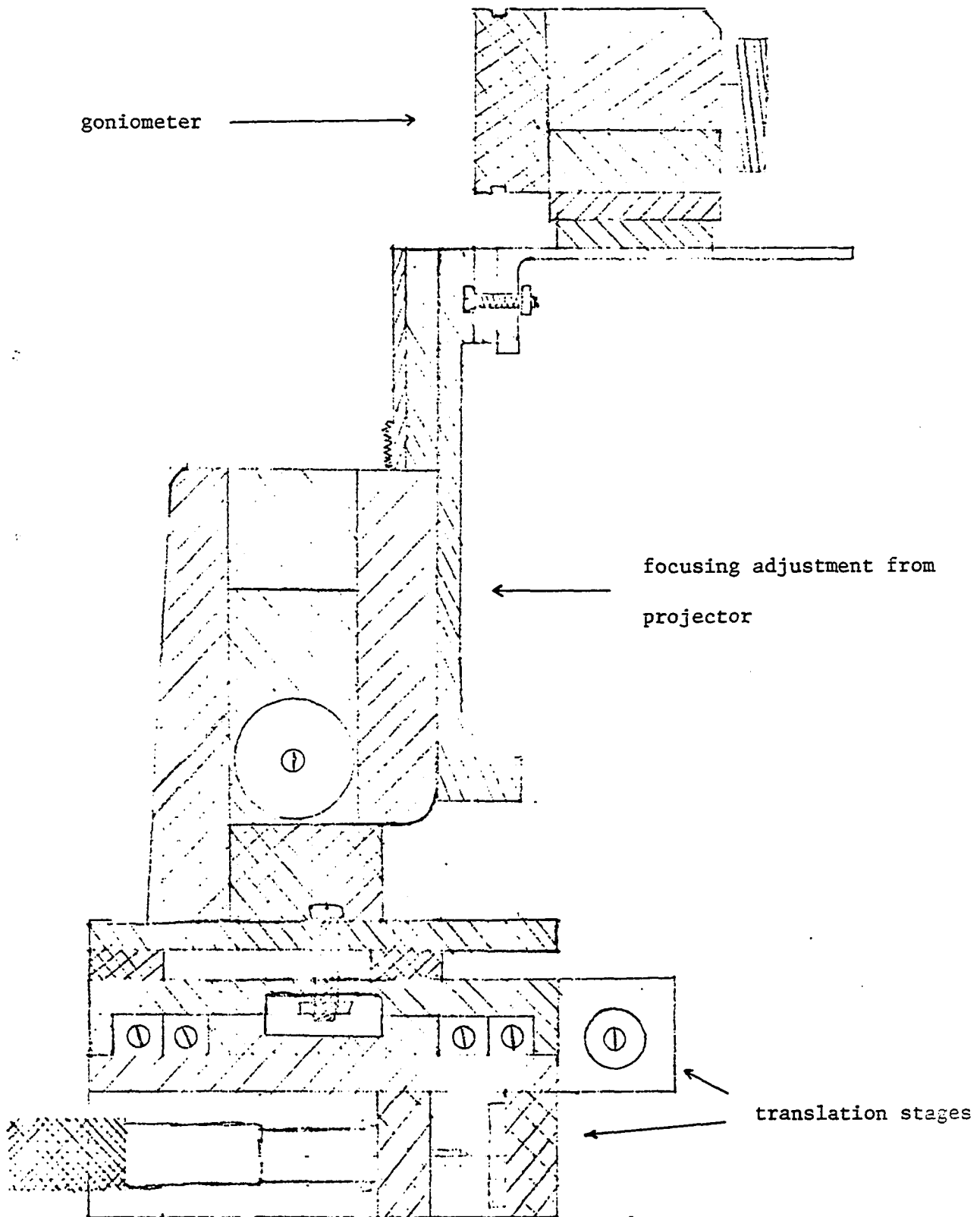
Sampling Accessories

In the course of this study several accessories were made to solve several sampling problems in the Raman studies. Two of these accessories are discussed here.

A translation accessory was built to position the sample at the optimum sampling point of the instrument. A schematic of this device is shown in figure (A-1). The x-y translations are obtained by using ordinary translation stages while the z translation used the focusing adjustment from an old projector. This piece has a coarse and fine adjustment. A goniometer is mounted on a platform on top of the z translator which, along with a goniometer head, allows a 360° rotation around one axis combined with two arc adjustments.

A second attachment was made for backscattering experiments. A dielectric coated pierced mirror allows the laser light to hit the sample while reflecting the back scattered radiation into the collection optics. A schematic showing the principle of operation is presented in figure (A-2). The mirror is mounted at 45° on a plastic block which can be set on the specimen stage of an old microscope such that it is allowed to rotate about the z direction. The stage allows a limited x-y translation and was mounted on the microscope focusing adjustment. The focusing adjustment was rigidly mounted to the spectrometer to allow translation in the z direction.

Figure (A-1). Translation accessory used in Raman experiments.



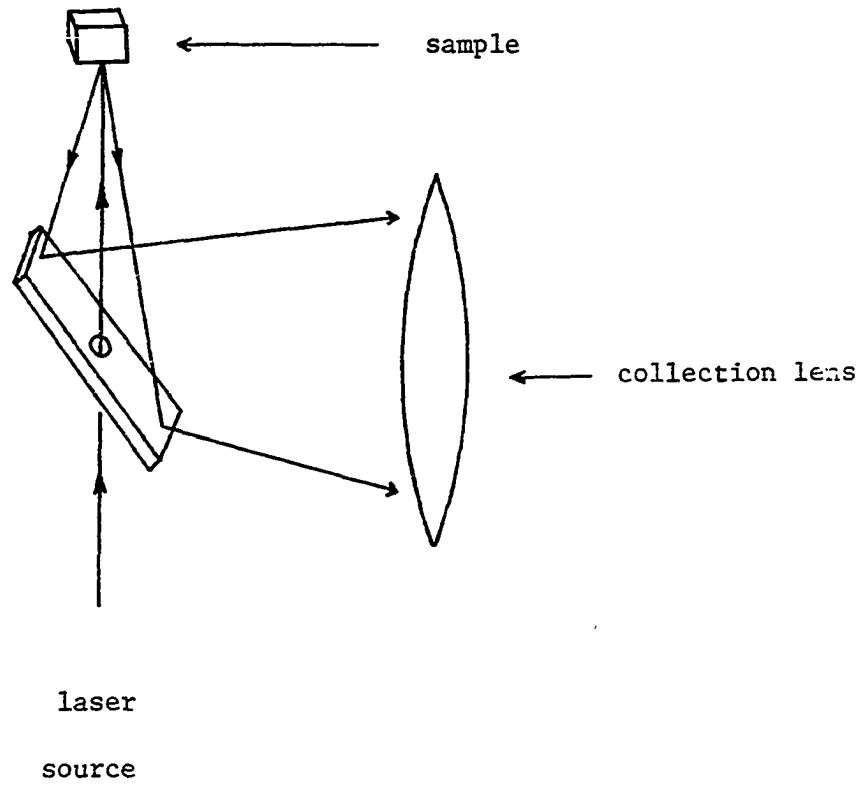


Figure (A-2). Schematic of back scattering accessory used in Raman experiments